

# Length Sensing and Control of a Prototype Advanced Interferometric Gravitational Wave Detector

Thesis by  
Robert L. Ward

In Partial Fulfillment of the Requirements  
for the Degree of  
Doctor of Philosophy



California Institute of Technology  
Pasadena, California

2010  
(Defended February 24, 2010)



# Acknowledgements

First and foremost, I would like to thank my advisor, Alan Weinstein. His guidance was invaluable, and if I learned anything during this process, it was that whenever we argued, he would turn out to be right. It is not possible to describe in words the debt I owe to Rana Adhikari. By example, he showed me how to think, what to measure, and how to enjoy the process. Thanks for everything.

Many thanks to Osamu Miyakawa, who first showed me how to not blind myself with a laser, Seiji Kawamura who gave me my first lesson in control theory, and to Steve Vass, who has always been, and always will be, a true pleasure to work with. Sam Waldman showed me how the perfect is the enemy of actually finishing something. Stefan Ballmer graciously let me take over the radiometer. Matt Evans and Hartmut Grote both helped tremendously during critical periods. Thanks also go to all my other friends and colleagues at the 40 m, for making it such a great place to work: Bob Taylor, John Miller, Yoichi Aso, Koji Arai, Jenne Driggers, Kirk McKenzie, Bram Slagmolen, Kiwamu Izumi, Alberto Stochino, Joe Betzweiser, and Tobin Fricke. Then there's David Yeaton-Massey, Aidan Brooks, Zack Korth, and Alastair Heptonstall, who never let me write in peace.

The CDS crew, Ben and Rich Abbott, Rolf Bork, Jay Heefner, and Alex Ivanov, was invaluable. Without their support, nothing at the 40 m would have ever worked. Thanks to Mike Smith for his help with the OMC.

My family has always been supportive, and I especially want to thank my parents for always letting me do whatever I wanted.

My most excellent friends at Caltech deserve much blame for the length of this work. They made this place too much fun to leave. The usual suspects were Dan, Brad, Christie, James, Keiko, Andrew, Meredith, John, Spanish Jon, Jack, Lindsey, Dylan, Emily, Jan, Katerina, Kirk, Ella, Tommy, and Nicola. They and all the other Friends of the BWMA made Pasadena home. Everybody always had a good time, and nobody ever got hurt.

And of course, Marie-Hélène. You really are the center of the universe.

Finally the boilerplate: LIGO was constructed by the California Institute of Technology and Massachusetts Institute of Technology with funding from the National Science Foundation and operates under cooperative agreement PHY-0757058. This work was also supported by the NSF Graduate Research Fellowship. This thesis has LIGO document number LIGO-P1000018.

# Abstract

There is a worldwide effort to directly detect gravitational radiation. The Laser Interferometer Gravitational Wave Observatory (LIGO) operates three kilometer-scale interferometric gravitational wave detectors at two sites: two in Hanford, WA and one in Livingston, LA. A significant upgrade, called Advanced LIGO, is planned for these detectors. The core work of this thesis involves using a 40 m prototype interferometer on the Caltech campus to study length and sensing and control techniques for Advanced LIGO. The principal results are the development of a lock acquisition protocol for an advanced detector and a comparison of noise couplings between two gravitational wave signal extraction techniques, called RF and DC readout.

In addition, a search in LIGO data was carried out for broadband, long-duration stochastic gravitational waves emitted from point sources. The results of this search are presented.

# Contents

<b>Acknowledgements</b>	<b>iii</b>
<b>Abstract</b>	<b>iv</b>
<b>1 Introduction</b>	<b>1</b>
<b>2 Gravitational Waves</b>	<b>3</b>
2.1 Gravity . . . . .	3
2.2 Gravitational Waves . . . . .	5
2.2.1 The Evidence: PSR B1913+16 . . . . .	6
2.3 Sources of Gravitational Waves and Detection Strategies . . . . .	6
2.3.1 The Stochastic Background of Gravitational Radiation . . . . .	6
2.3.2 Continuous Wave Sources . . . . .	7
2.3.3 Compact Binary Coalescences . . . . .	8
2.3.4 Unmodeled Short-Duration Sources . . . . .	8
2.4 Gravitational Wave Detection . . . . .	8
2.4.1 Terrestrial Gravitational Wave Detectors . . . . .	9
2.4.1.1 Resonant Mass Antenna . . . . .	9
2.4.1.2 Optical Interferometers . . . . .	9
2.5 LIGO . . . . .	10
2.5.1 The LIGO Scientific Collaboration . . . . .	10
2.6 A New Window on the Universe . . . . .	11
<b>3 Interferometric Gravitational Wave Detection</b>	<b>12</b>
3.1 Principle of Operation . . . . .	12
3.2 Noise . . . . .	13
3.3 Mathematical Notations for Mirrors, Fields, and Spaces . . . . .	15
3.4 The Michelson Interferometer as a Gravitational Wave Detector . . . . .	17
3.5 Signal Extraction . . . . .	19

3.5.1	Optical Heterodyne Detection . . . . .	20
3.5.1.1	Schnupp Asymmetry for Michelson Length Sensing . . . . .	22
3.5.2	Optical Homodyne Detection . . . . .	23
3.6	Fabry-Pérot Cavities . . . . .	23
3.6.1	Cavity Spatial Modes . . . . .	25
3.6.2	Transfer Functions of a Fabry-Pérot Cavity . . . . .	27
3.6.3	The Pound-Drever-Hall Technique . . . . .	28
3.7	Adding Fabry-Pérot Cavities to the Arms of a Michelson Interferometer . . . . .	30
3.8	Coupled Cavities . . . . .	31
3.8.1	Antiresonant Short Cavity . . . . .	32
3.8.2	Resonant Short Cavity . . . . .	33
3.8.3	Detuned Short Cavity . . . . .	33
3.9	Recycling . . . . .	35
3.9.1	Power Recycling . . . . .	35
3.9.2	Signal Recycling . . . . .	37
3.10	Resonant Sideband Extraction . . . . .	38
3.11	Detuned RSE . . . . .	39
3.11.1	Two-Photon Formalism . . . . .	39
3.11.2	The RSE Response Function . . . . .	40
3.11.3	Detuned RSE Interferometers as Optical Springs . . . . .	42
3.11.3.1	Dynamical Instability . . . . .	43
3.11.3.2	Anti-spring . . . . .	43
3.11.4	The Detuned Resonant Sideband Extraction Interferometer with Power Recycling . . . . .	44
3.12	Feedback Control . . . . .	44
3.12.0.1	Noise reduction . . . . .	46
3.12.0.2	Transduction linearity . . . . .	46
3.13	The Advanced LIGO Design . . . . .	46
<b>4</b>	<b>Gravitational Wave Signal Extraction</b> . . . . .	<b>49</b>
4.1	RF Readout . . . . .	50
4.2	DC Readout . . . . .	51
4.3	Considerations . . . . .	51
4.3.1	Laser Noise Couplings . . . . .	52
4.3.2	Spatial Overlap . . . . .	54
4.3.3	Output Mode Cleaner . . . . .	54

4.3.3.1	OMC noise mechanisms . . . . .	54
4.3.4	Oscillator Noise . . . . .	55
4.3.4.1	Oscillator amplitude noise . . . . .	55
4.3.4.2	Oscillator phase noise . . . . .	56
4.3.5	Flicker Noise . . . . .	56
4.3.6	Unsuppressed Signal . . . . .	56
4.3.7	Shot Noise . . . . .	57
4.3.8	Signal Linearity . . . . .	57
4.4	Decision . . . . .	57
<b>5</b>	<b>The Caltech 40 m Prototype Interferometer</b>	<b>59</b>
5.1	Prototyping . . . . .	59
5.2	Vacuum and Seismic Isolation . . . . .	61
5.3	Suspensions . . . . .	61
5.4	Electronics and Digital Controls . . . . .	62
5.5	Pre-Stabilized Laser . . . . .	63
5.5.1	MOPA . . . . .	63
5.5.2	Power Stabilization . . . . .	64
5.5.3	Frequency Stabilization . . . . .	64
5.5.4	Pre-Mode Cleaner . . . . .	65
5.6	Input Optics . . . . .	65
5.6.1	Phase Modulations . . . . .	65
5.6.1.1	A Mach-Zehnder interferometer for non-cascaded RF sidebands . . . . .	65
5.6.2	Input Mode Cleaner . . . . .	66
5.6.3	Input Isolation, Mode Matching, and Steering . . . . .	66
5.7	The Common Mode Servo . . . . .	67
5.8	Interferometer . . . . .	67
5.9	Output Optics . . . . .	67
5.9.1	Output Mode Cleaner . . . . .	69
5.9.1.1	OMC Length Sensing and Control . . . . .	69
5.9.2	Output Steering . . . . .	69
5.9.3	Output Mode Matching . . . . .	69
5.9.4	Higher Order Mode Content at Asymmetric Port . . . . .	71
5.9.5	Photodetectors . . . . .	71
5.10	The Future . . . . .	71

<b>6</b>	<b>The Length Sensing and Control Scheme</b>	<b>73</b>
6.1	Principle . . . . .	73
6.2	Resonance Profile . . . . .	74
6.3	Sensing . . . . .	76
6.3.1	Signal Selection: Ports, Frequencies, and Quadratures . . . . .	76
6.3.2	Double Demodulation . . . . .	76
6.3.3	Sideband Imbalance and Offsets . . . . .	77
6.3.3.1	Measuring Demodulation Phases . . . . .	77
6.3.4	Configuration Space and the Operating Point . . . . .	79
6.3.5	Discriminants . . . . .	79
6.3.5.1	Frequency dependence . . . . .	80
6.3.5.2	Position dependence . . . . .	82
6.3.5.3	Example matrix at operating point . . . . .	82
6.3.5.4	SPOB . . . . .	83
6.3.5.5	Non-resonant sideband . . . . .	83
6.4	Control . . . . .	83
6.4.1	Matrices and Bases . . . . .	84
6.4.1.1	Input Matrix . . . . .	86
6.4.2	Feedforward Corrections . . . . .	86
6.5	Discussion . . . . .	87
<b>7</b>	<b>Calibration of a Detuned RSE Interferometer</b>	<b>89</b>
7.1	Calibration in Initial LIGO . . . . .	89
7.1.1	Free Swinging Michelson . . . . .	90
7.1.2	ITM Calibration . . . . .	90
7.1.3	ETM Calibration . . . . .	91
7.1.4	DARM calibration . . . . .	91
7.1.4.1	Tracking . . . . .	91
7.1.4.2	Comment . . . . .	92
7.2	Calibrating the 40 m Detuned RSE Interferometer . . . . .	92
7.2.1	Actuator Calibration . . . . .	92
7.2.2	DARM Calibration . . . . .	93
7.2.3	Modeling . . . . .	94
7.2.4	Tracking . . . . .	95
7.3	Calibration for Advanced LIGO . . . . .	97

<b>8</b>	<b>Lock Acquisition</b>	<b>100</b>
8.1	Lock Acquisition: The Path to Control . . . . .	100
8.2	Lock Acquisition of a Resonant Cavity . . . . .	101
8.2.1	Threshold velocity . . . . .	101
8.2.2	Normalized PDH locking . . . . .	102
8.2.3	Loop Triggering . . . . .	102
8.2.4	Offset locking . . . . .	102
8.3	Lock Acquisition of Coupled Cavities . . . . .	103
8.3.1	Lock Acquisition for Initial LIGO and Virgo . . . . .	104
8.4	Lock Acquisition of a Detuned Resonant Sideband Extraction Interferometer with Power Recycling . . . . .	105
8.5	Bootstrapping . . . . .	105
8.5.1	Interferometer subsets . . . . .	105
8.5.2	Alignment . . . . .	106
8.5.3	Double Demodulation signals . . . . .	107
8.6	The Lock Acquisition Procedure for the Caltech 40 m Interferometer . . . . .	108
8.6.1	Initial Acquisition . . . . .	108
8.6.2	The spring and the anti-spring . . . . .	110
8.6.2.1	Locking the spring and the anti-spring . . . . .	110
8.6.3	The Protocol . . . . .	112
8.6.4	Adaptive compensation filter: the moving zero . . . . .	116
8.6.5	Other Protocols . . . . .	119
8.6.6	Scripting Tools . . . . .	121
8.7	Deterministic Locking . . . . .	121
8.7.1	The Future: It's easy being green . . . . .	123
8.7.1.1	Envisioned lock acquisition procedure . . . . .	124
8.7.1.2	Advantages of this technique . . . . .	125
8.7.1.3	Alternative Technique . . . . .	125
8.8	Discussion . . . . .	126
<b>9</b>	<b>Measurement of Laser and Oscillator Noise Couplings in RF/DC Readout</b>	<b>127</b>
9.1	DC Readout Experiment . . . . .	127
9.1.1	Noise Injections . . . . .	128
9.1.1.1	Laser Amplitude Noise . . . . .	128
9.1.1.2	Laser Frequency Noise . . . . .	128
9.1.1.3	Oscillator Noise . . . . .	129

9.2	Power Recycled Fabry-Pérot Michelson Interferometer . . . . .	129
9.2.1	Simulation . . . . .	129
9.2.2	Laser Amplitude Noise . . . . .	130
9.2.2.1	DC Readout . . . . .	130
9.2.2.2	RF Readout . . . . .	130
9.2.3	Laser Frequency Noise . . . . .	131
9.2.4	Oscillator Phase Noise . . . . .	131
9.2.5	Oscillator Amplitude Noise . . . . .	133
9.3	Detuned RSE Interferometer . . . . .	135
9.3.1	Length Offsets . . . . .	135
9.3.1.1	Cyclical dependencies . . . . .	135
9.3.1.2	Mode cleaner length . . . . .	136
9.3.1.3	Effect on DARM calibration . . . . .	136
9.3.2	Simulation . . . . .	136
9.3.2.1	Feedback and Offsets . . . . .	137
9.3.3	The simulated noise traces . . . . .	137
9.3.3.1	Effects not included . . . . .	138
9.3.3.2	Auxiliary loop coupling . . . . .	138
9.3.4	Laser Amplitude Noise . . . . .	138
9.3.4.1	DC Readout . . . . .	138
9.3.4.2	RF Readout . . . . .	139
9.3.5	Laser Frequency Noise . . . . .	140
9.3.5.1	DC Readout . . . . .	140
9.3.5.2	RF Readout . . . . .	141
9.3.6	Oscillator Phase Noise . . . . .	141
9.3.6.1	DC Readout $f_1$ . . . . .	142
9.3.6.2	DC Readout $f_2$ . . . . .	142
9.3.6.3	RF Readout $f_1$ . . . . .	143
9.3.6.4	RF Readout $f_2$ . . . . .	143
9.3.7	Oscillator Amplitude Noise . . . . .	144
9.3.7.1	DC Readout $f_1$ . . . . .	144
9.3.7.2	DC Readout $f_2$ . . . . .	145
9.3.7.3	RF Readout $f_1$ . . . . .	145
9.3.7.4	RF Readout $f_2$ . . . . .	145
9.4	Conclusions . . . . .	149

<b>10 A Directional Cross-Correlation Search for Stochastic Gravitational Waves Using Data from the Fifth LIGO Science Run</b>	<b>150</b>
10.1 Stochastic Gravitational Waves . . . . .	150
10.2 Detecting stochastic gravitational waves . . . . .	151
10.2.1 Isotropic strategy . . . . .	152
10.2.2 Segmenting Data and Optimal Combination . . . . .	153
10.2.3 Gravitational Wave Radiometry . . . . .	155
10.2.4 The Point Spread Function . . . . .	156
10.3 Analysis Pipeline . . . . .	156
10.4 Limits on Gravitational Waves . . . . .	158
10.4.1 Detection . . . . .	158
10.4.2 The Data . . . . .	161
10.4.3 Data Quality . . . . .	161
10.4.3.1 Frequency Masking . . . . .	161
10.4.3.2 Delta-Sigma Cut . . . . .	161
10.4.4 Posterior Distributions and Upper Limits . . . . .	162
10.4.5 Gravitational Wave SkyMap . . . . .	164
10.4.5.1 Injection . . . . .	164
10.5 Frequency and Location Resolved Searches . . . . .	165
10.5.1 Upper Limit on gravitational waves from Sco X1 . . . . .	165
10.5.2 The Galactic Center . . . . .	166
10.5.3 Globular Clusters . . . . .	167
10.5.4 Untargeted Narrowband Search on the Whole Sky . . . . .	175
10.5.5 Injection . . . . .	175
10.6 Future Work . . . . .	176
10.6.1 Detection Thresholding . . . . .	176
10.6.2 Multi-baseline Radiometry . . . . .	177
10.6.3 Transient Searches . . . . .	177
10.6.4 Clustering . . . . .	178
10.7 Discussion . . . . .	178
<b>11 Summary and Conclusion</b>	<b>179</b>
<b>A Acronyms</b>	<b>181</b>
<b>B Quantum Noise in RSE interferometers</b>	<b>184</b>

<b>C</b>	<b>Laser Noise Coupling Formulae</b>	<b>187</b>
C.1	Asymmetries and Couplings . . . . .	187
C.2	Laser noise coupling to asymmetric port . . . . .	187
<b>D</b>	<b>Resonant Cavity Formulae</b>	<b>195</b>
D.1	Statics . . . . .	195
D.2	Equilibrium Frequency Response . . . . .	196
D.3	Coupled Cavities . . . . .	198
<b>E</b>	<b>Feedback</b>	<b>200</b>
E.1	Linear Control: Loopology . . . . .	200
E.2	Servo Stability . . . . .	202
E.2.1	Bode gain-phase relationship . . . . .	202
E.2.2	Conditional Stability . . . . .	202
E.3	Servo Bandwidth . . . . .	203
E.4	Feedback Filter Design . . . . .	203
E.4.1	MIMO control . . . . .	203
E.4.1.1	Cross Coupling . . . . .	205
<b>F</b>	<b>Interferometer Modeling</b>	<b>206</b>
F.1	Modeling Tools . . . . .	206
F.1.1	FINESSE . . . . .	206
F.1.2	GWINC . . . . .	206
F.1.3	Optickle . . . . .	207
F.1.4	Looptickle . . . . .	207
F.1.5	E2E: End to End . . . . .	207
F.1.6	FFT . . . . .	207
F.2	MATLAB code . . . . .	208
F.2.1	The RSE response function . . . . .	208
	<b>Bibliography</b>	<b>209</b>

# List of Figures

2.1	Effect of a GW on a circle of test particles. . . . .	7
3.1	Input and output fields of a mirror mass . . . . .	16
3.2	Michelson based interferometer topologies for gravitational wave detection. . . . .	18
3.3	A Fabry-Pérot Cavity with overlapping waves. . . . .	25
3.4	Cavity gain vs. bandwidth. . . . .	29
3.5	A schematic of a typical PDH length sensing setup . . . . .	29
3.6	The PDH signals for a single cavity. . . . .	30
3.7	A three mirror coupled cavity . . . . .	31
3.8	Effect of adding a third mirror with a short cavity on the bandwidth of the coupled system. . . . .	33
3.9	A Power Recycled Fabry-Pérot Michelson Interferometer. . . . .	36
3.10	A Dual Recycled Fabry-Pérot Michelson Interferometer. . . . .	38
3.11	Changing the detuning of the signal cavity . . . . .	42
3.12	Frequency response in different readout quadratures . . . . .	43
3.13	Measurement of the opto-mechanical RSE response. . . . .	44
3.14	Measurement of the opto-mechanical RSE response in an anti-spring configuration . . . . .	45
3.15	Projected sensitivity for possible operating modes of Advanced LIGO. . . . .	48
4.1	Phasor diagram of the asymmetric port in an RF readout scheme. . . . .	50
4.2	Phasor diagram of the asymmetric port in a DC readout scheme. . . . .	52
5.1	The layout of the 40 m. . . . .	60
5.2	A MOS suspension. . . . .	63
5.3	Real time control network example. . . . .	64
5.4	The laser frequency stabilization system. . . . .	68
5.5	An example EPICS control screen . . . . .	70
5.6	Mode scans of the AS port . . . . .	72
5.7	The DC Readout sensing chain. . . . .	72

6.1	The length sensing and control scheme. . . . .	75
6.2	Demod phase errors will lead to offsets . . . . .	78
6.3	Modeled and measured response of a differential demodulation error signal . . . . .	79
6.4	Frequency dependent magnitude of the OMC DC row of the matrix of discriminants. . . . .	81
6.5	Output of signals as SRCL is varied. . . . .	82
6.6	Block diagram of length sensing and control system. . . . .	85
7.1	Feedback loop block diagram. . . . .	90
7.2	Feedback loop block diagram. . . . .	93
7.3	An example DARM open loop transfer . . . . .	96
7.4	Ratio of the opto-mechanical response to nominal with given parameter variation . . . . .	97
7.5	An example DARM open loop transfer . . . . .	98
7.6	DARM noise spectra for a detuned RSE interferometer. . . . .	99
8.1	Error signals for a single Fabry-Pérot cavity. . . . .	103
8.2	Signals and DOFs for bootstrapping . . . . .	107
8.3	A typical initial acquisition . . . . .	109
8.4	Histogram of waiting times to acquire initial control of five length degrees of freedom. . . . .	111
8.5	The sequence of error signal usage and transitions in the lock acquisition process . . . . .	113
8.6	DARM demodulation phase rotation . . . . .	115
8.7	The optical response (magnitude only) of the CARM DOF at several CARM offsets. . . . .	117
8.8	Interferometer power during lock acquisition . . . . .	118
8.9	dB magnitude of the CARM (sensed at) open-loop opto-mechanical frequency response . . . . .	118
8.10	Bode plots of the opto-mechanical frequency response of . . . . .	119
8.11	Dynamic compensation filter used in the CARM loop . . . . .	120
8.12	CARM cavity response and open loop transfer functions . . . . .	120
8.13	The flow of the main watch script used for locking. . . . .	122
8.14	The hierarchy of scripts . . . . .	122
9.1	Laser intensity noise coupling for the 40 m Fabry-Pérot Michelson interferometer with power recycling. . . . .	132
9.2	Laser frequency noise coupling for the 40 m Fabry-Pérot Michelson interferometer with power recycling. . . . .	132
9.3	Oscillator phase noise coupling for the 40 m Fabry-Pérot Michelson interferometer with power recycling. . . . .	133
9.4	Oscillator amplitude noise coupling for the 40 m Fabry-Pérot Michelson interferometer with power recycling. . . . .	134

9.5	DC readout laser amplitude noise coupling . . . . .	139
9.6	RF readout laser amplitude noise coupling . . . . .	140
9.7	DC readout laser frequency noise coupling . . . . .	141
9.8	RF readout laser frequency noise coupling . . . . .	142
9.9	DC readout $f_1$ oscillator phase noise coupling . . . . .	143
9.10	DC readout $f_2$ oscillator phase noise coupling . . . . .	144
9.11	RF readout $f_1$ oscillator phase noise coupling . . . . .	145
9.12	RF readout $f_2$ oscillator phase noise coupling . . . . .	146
9.13	DC readout $f_1$ oscillator amplitude noise coupling . . . . .	146
9.14	DC readout $f_2$ oscillator amplitude noise coupling . . . . .	147
9.15	RF readout $f_1$ oscillator amplitude noise coupling . . . . .	147
9.16	RF readout $f_2$ oscillator amplitude noise coupling . . . . .	148
10.1	The estimate of the variance for each data segment is calculated using data from neighboring time segments to avoid biasing the estimator. . . . .	154
10.2	Radiometer point spread function. . . . .	157
10.3	The radiometer analysis. . . . .	157
10.4	The radiometer pipeline. . . . .	159
10.5	Representative strain noise curves from the 4 km LIGO detectors during the fifth LIGO science run. . . . .	162
10.6	Upper limit map from S5 run. . . . .	165
10.7	An injected broadband point source. . . . .	166
10.8	Limits on gravitational radiation from Sco-X1. . . . .	167
10.9	Limits on gravitational radiation from the galactic center. . . . .	168
10.10	Results from GC1. . . . .	168
10.11	Results from GC2. . . . .	169
10.12	Results from GC3. . . . .	169
10.13	Results from GC4. . . . .	169
10.14	Results from GC5. . . . .	170
10.15	Results from GC6. . . . .	170
10.16	Results from GC7. . . . .	170
10.17	Results from GC8. . . . .	171
10.18	Results from GC9. . . . .	171
10.19	Results from GC10. . . . .	171
10.20	Results from GC11. . . . .	172
10.21	Results from GC12. . . . .	172

10.22	Results from GC13. . . . .	172
10.23	Results from GC14. . . . .	174
10.24	Results from GC15. . . . .	174
10.25	Injected point source. . . . .	177
C.1	Laser amplitude noise coupling paths in DC readout . . . . .	191
C.2	Laser amplitude noise coupling paths in RF readout . . . . .	192
C.3	Laser amplitude noise coupling in RF readout . . . . .	192
C.4	Laser frequency noise coupling paths in DC readout . . . . .	193
C.5	Laser frequency noise coupling paths in RF readout . . . . .	193
C.6	Laser frequency noise coupling in RF readout . . . . .	194
D.1	Indexed fields in a resonant cavity . . . . .	195
D.2	Reflected and transmitted fields through a cavity. . . . .	197
E.1	Schematic idealization of a canonical feedback loop. . . . .	201
E.2	Example feedback loop. . . . .	204
E.3	A $2 \times 2$ MIMO control system . . . . .	205

# Chapter 1

## Introduction

There is a worldwide effort to detect gravitational waves using laser interferometers. This thesis describes work toward the development of second generation laser interferometric gravitational wave detectors. These are highly complex instruments that are at the frontier of precision measurement science and interferometry, and their successful commissioning and operation require detailed study.

The direct detection of gravitational radiation is a primary goal of the community devoted to the experimental study of gravitation. The currently operating gravitational wave detectors, which include the Laser Interferometer Gravitational Wave Observatory (LIGO [1]) in the U.S., GEO600 [2] in Germany, Virgo [3] in Italy, and TAMA300 [4] in Japan, are the most sensitive such devices ever built, but have not yet detected a clear signal. This situation was not unexpected, and plans for a second generation of instruments, the so-called advanced detectors, are already well underway; indeed, Advanced LIGO [5] is already under construction. Advanced LIGO is expected to make regular detections and to open the field of gravitational wave astronomy. The work in this thesis is centered on experimentally prototyping a length sensing and control scheme for an advanced interferometric detector such as Advanced LIGO.

Chapter 2 is a short introduction to gravitational waves. Chapter 3 provides a brief overview of interferometric gravitational wave detection, and the motivation for the topology planned for advanced detectors; chapter 4 discusses the choice of how to extract a gravitational wave signal from the interferometer.

Chapter 5 describes the prototype facility for the experiments; chapter 6 describes the length sensing and control scheme for the prototype; and chapter 7 discusses the calibration of the prototype.

To validate an operational control scheme in a suspended-mass interferometer, first a process must be developed by which the interferometer can be brought from its uncontrolled state to a controlled one: the interferometer must be locked. In general, this is a difficult problem. Chapter 8 describes a lock acquisition protocol developed and used for the prototype.

Chapter 9 contains measurements of several important noise couplings (laser and oscillator noises) in two different gravitational wave signal extraction schemes, using the prototype.

Finally, chapter 10 describes a study done using data acquired during LIGO's fifth data taking run, which represents the most sensitive strain data taken to date in the frequency band around 100 Hz. This study, using a radiometer analysis technique, placed limits on point source emission of long-duration, broadband gravitational radiation, from any direction. In addition, upper limit amplitude spectra are presented which place limits on gravitational radiation in the band from 40 Hz to 1 kHz from the directions of the 15 nearest globular clusters. The results presented in chapter 10 use data from the LIGO detectors, but have not been reviewed or endorsed by, and do not represent the scientific opinion of, the LIGO Scientific Collaboration.

## Chapter 2

# Gravitational Waves

This chapter contains a short introduction to gravity, gravitational waves, possible sources of gravitational waves, and the effort to detect gravitational waves with the LIGO.

### 2.1 Gravity

The first mathematical exploration of the nature of gravity came in 1687 from Isaac Newton in *Philosophiæ Naturalis Principia Mathematica*. Newton proposed a theory that described gravity as a force that acts on all matter, and between each pair of particles. The mathematical definition of this force,  $\vec{F}_G$ , is Newton's Law of Universal Gravitation,

$$\vec{F}_G = G \frac{m_1 m_2}{\|\vec{r}_2 - \vec{r}_1\|^3} (\vec{r}_2 - \vec{r}_1), \quad (2.1)$$

where  $m_1$  and  $m_2$  are the masses of the particles undergoing the force, and  $r_1$  and  $r_2$  are the position vectors of the particles, the term  $G = 6.63 \times 10^{-11} \frac{\text{N}}{\text{m}}$  is a constant which is the same throughout the universe. This is an example of a  $\frac{1}{r^2}$  law. Applying Newton's Law immediately solved several puzzles of the day, including the elliptical nature of planetary orbits. The theory was remarkably successful for almost 300 years.

By the early 20<sup>th</sup> century, however, Newton's theory was found wanting. In 1916 [6] Albert Einstein published the theory of general relativity as an alternative mathematical description of gravity. Rather than invoking a field which involves action at a distance, or describing a force, this theory describes gravity as a curvature in the fabric of space-time. The apparent attraction of particles under the influence of gravity results from the fact that these particles are travelling through a space-time that is warped by nearby massive objects. This remarkably elegant theory immediately explained the long-standing puzzle regarding the precession of the perihelion of the orbit of Mercury, and since then has been experimentally confirmed numerous times, beginning in 1919 with Eddington's expedition [7] and continuing to this day.

In the limit where gravity is relatively weak (a situation that comprises most of human experience), general relativity is approximately similar to Newtonian theory; however when masses become very large (or dense), or great precision is required, Newtonian theory fails to adequately explain the results of precision experiments. General relativity has not failed to explain any experiments. For a recent review of the relationship between experiments and general relativity, see [8].

The central result of general relativity is the Einstein field equation, which relates the presence of matter and energy to the warpage of nearby space, all in the language of differential geometry:

$$G^{\mu\nu} = 8\pi T^{\mu\nu}. \quad (2.2)$$

$T^{\mu\nu}$  is the local stress-energy tensor familiar from relativistic electrodynamics (see, e.g., [9]), and  $G^{\mu\nu}$  is the Einstein tensor, which is related to the local curvature of space-time in the following manner: the Einstein tensor  $G^{\alpha\beta}$  is related to the Ricci tensor  $R^{\alpha\beta}$  by

$$G^{\alpha\beta} \equiv R^{\alpha\beta} - \frac{1}{2}Rg^{\alpha\beta}, \quad (2.3)$$

where  $g_{\alpha\beta}$  is the space-time metric,  $R$  is the scalar curvature formed by contraction of the Ricci tensor with the metric,

$$R = g^{\alpha\beta}R_{\alpha\beta} \quad (2.4)$$

and the Ricci tensor  $R_{\alpha\beta}$  is itself a contraction of the Riemann curvature tensor  $R^{\gamma}_{\alpha\beta\gamma}$ ,

$$R_{\alpha\beta} = R^{\gamma}_{\alpha\beta\gamma}. \quad (2.5)$$

Given a distribution of matter/energy, the Einstein field equations are solved in order to find the metric  $g_{\alpha\beta}$ , which encapsulates the geometry of space-time. This space-time metric then describes how freely falling (influenced only by gravity) test particles will move.

Because the Einstein field equations are nonlinear, analytic solutions to them are difficult to find; there are, however, two notable examples of exact solutions for static and symmetric configurations. These are the Schwarzschild [10] and Kerr [11] metrics, which describe space-time around a non-spinning spherically symmetric mass distribution and a spinning, spherically symmetric mass distribution, respectively.

Given that it is so difficult to solve the field equations directly for any dynamical (or nonsymmetric) system, the bulk of progress has been in numerical relativity, where the equations are solved using numerical methods. Recent advances in numerical relativity, where the Einstein field equation is solved computationally using numerical methods, have led to a rapid growth in our understanding of general relativity and the dynamical behavior of system with strong gravity. A major success

included the first simulation of a binary black hole merger [12].

## 2.2 Gravitational Waves

One prediction of Einstein's theory is gravitational radiation, typically referred to as *gravitational waves* [13, 14] (GW). These waves are small, fluctuating perturbations in the metric which travel at the speed of light. Gravitational waves are generated by changing matter/energy distributions, in a manner somewhat analogous to the generation of electromagnetic waves by changing charge distributions. One important difference is that the leading term in the generation of gravitational waves is the time-varying component of the mass-quadrupole moment. This means that leading candidates for generating large-amplitude gravitational waves must be significantly non-spherical.

Compared to the other fundamental forces, the interaction strength of gravity is small, so gravitational radiation undergoes significantly less scattering than other types of radiation as it propagates throughout the universe [15]. What this means is that the universe is essentially transparent to gravitational radiation, making it an excellent candidate for a carrier of astrophysical information.

Moreover, because gravitational radiation is generated in such a different manner to electromagnetic radiation (i.e., GWs come from the coherent motion of large masses, unlike EM waves which come from the incoherent motion of many charges), gravitational waves are very likely to carry complementary information to their EM counterparts which are currently used for studying the universe and the large objects within it; see [14] for a quick discussion.

The small interaction comes with a catch, however: it makes these waves extremely difficult to detect. The leading term in the generation of gravitational radiation is the time-varying component of the mass quadrupole moment, and the frequency of the gravitational radiation is twice the angular frequency of the changing quadrupole. A simple formula can describe the scales involved, as an order-of-magnitude estimate of the amplitude of gravitational waves for a given source term:

$$h \simeq \frac{G}{c^4} \frac{\ddot{Q}}{r}, \quad (2.6)$$

where  $Q$  is the mass quadrupole moment of the source system, and  $\ddot{Q}$  is its second time derivative,  $c$  is the speed of light,  $r$  is the distance to the source, and  $h$  is a perturbation in the local space-time metric, which can be thought of as a time-varying strain in space.

For two ice skaters in a pair spin, at a distance of a mile, this amplitude is  $\sim 10^{-45}$ . For two 1.4 solar mass neutron stars in the final stages of inspiral, about to collide while orbiting each other at  $\sim 0.3c$ , from a distance of 30 million light-years, the amplitude is closer to  $\sim 10^{-21}$ . Because a strain is a fractional change in length, the latter amplitude can be thought of as a length change of about one ten-thousandth of the diameter of a proton over a distance of a kilometer.

The gravitational waves themselves are transverse quadrupole waves; this is best understood by inspecting their effect on a ring of freely falling (affected only by gravity) test particles, in an imaginary location where the local space-time is basically flat. We assume that the wavelength of the gravitational radiation is much larger than the length scale (diameter) of the particle ring. Then for a wave passing into (or out of the page), the effect of a passing gravitational wave is depicted in figure 2.1. The quadrupolar nature of the waves means that they effect both spatial directions transverse to the propagation direction; the two possible gravitational wave polarizations ( $+$ ,  $\times$ ) are also shown. In this figure, the light-colored grid can be thought of as the background metric in the absence of gravitational waves. As the wave affects the particles, so will it affect the metric, although this latter effect is not shown here.

The work in this thesis is part of a worldwide effort to detect gravitational waves.

### 2.2.1 The Evidence: PSR B1913+16

Gravitational waves have not yet been directly detected. The most convincing, though indirect, evidence for the existence of gravitational radiation comes from the binary pulsar system **PSR B1913+16**. This system, discovered in 1974 by Hulse and Taylor, has evolved since then in precise agreement with predictions from general relativity [16, 17]. It is thus deduced that the binary system is losing energy as it emits the gravitational radiation predicted by general relativity. The radiation emitted from this system is far too weak and too low in frequency, however, for direct detection by current gravitational wave detectors.

## 2.3 Sources of Gravitational Waves and Detection Strategies

Although gravitational radiation can be emitted from any massive system with an accelerating mass-quadrupole moment, the search for gravitational waves is in large part motivated by the search for signals of astrophysical origin. Such signals are, moreover, the only signals likely to be of sufficient magnitude to be detectable with ground-based techniques using foreseeable technology. These astrophysical signals which are candidates for ground-based detection are typically divided into four categories, based on the time-frequency morphology of the signals. This then shapes the strategies employed to detect them in the low signal to noise regime.

### 2.3.1 The Stochastic Background of Gravitational Radiation

A stochastic background of gravitational radiation may be of cosmological origin (such as gravitational waves generated during the inflationary period after the Big Bang) or of astrophysical origin (such as a large number of weak astrophysical sources, superimposed to form a stochastic signal)

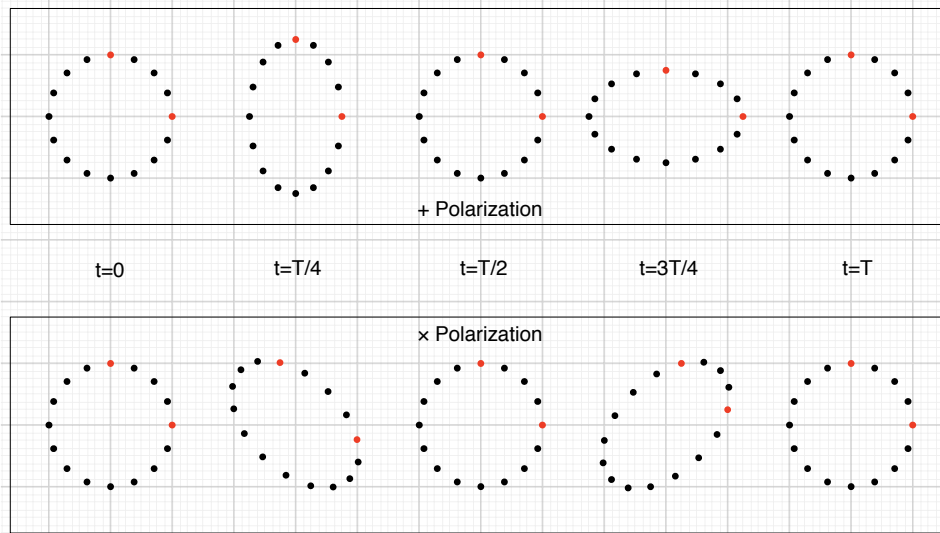


Figure 2.1: Effect of a GW on a circle of test particles. Shown are the effects of a + polarized wave and a  $\times$  polarized wave, for a wave passing into the plane of the page. The positions of the particles are shown at  $1/4$  intervals of the gravitational wave period  $T$ . The red colored particles indicate possible fiducial test masses in an interferometric gravitational wave detector.

[18, 19]. A gravitational wave background of cosmological origin would provide penetrating observations of the birth of the universe, as it would not be limited to times after recombination (as all electromagnetic based observations are), and might yield information about very early times in the universe.

Because such a signal is presumed to be much smaller than the noise floor of the detector, the detection strategy is to look for excess correlation (integrated over long periods) in the otherwise uncorrelated outputs of two gravitational wave detectors. Such a strategy relies on the assumption that the only possible correlation between two detectors comes from a signal. This is assumed to be the case for widely separated detectors, such as the H1-L1 pair of LIGO 4 km detectors (separated by 3000 km).

A directional search for stochastic gravitational waves is described in chapter 10.

### 2.3.2 Continuous Wave Sources

A pulsar (a rotating neutron star) with any asphericity will emit gravitational radiations as it spins [20, 21]. This continuous wave radiation is an “always on” type of source.

Because gravitational wave detectors have non-uniform antenna patterns, the detected signal from a pulsar will be modulated as the earth (and the detector) rotates. In addition to this amplitude modulation, the gravitational radiation will also be Doppler shifted as the earth rotates on its axis and orbits the sun. Searching for unknown pulsars is thus a straightforward, but computationally demanding undertaking. The program Einstein@Home [22] utilizes spare computer cycles on

participants' computers to carry out some of this processing.

### 2.3.3 Compact Binary Coalescences

Massive compact objects, such as black holes and neutron stars, are the typical examples of objects which exhibit strong gravity. This, combined with their supposed abundance in the universe, makes them interesting candidates for detection. As a pair of massive compact astronomical objects (a binary system) orbit each other, they will emit gravitational radiation [23]. This radiation carries energy away from the system, causing the orbits to decay and the objects to fall in toward each other. As these orbits decay, the objects inspiral until they collide and coalesce. As the objects inspiral, the orbital period decreases, with a corresponding rise in the frequency of the emitted gravitational radiation. The resulting waveform is a chirp during the inspiral phase, followed by the merger phase, then by a ringdown as the new, single, body settles into a spherical shape (non-spherical oscillatory modes are effectively damped by the emission of gravitational radiation).

The detection strategy for a such a signal relies on accurate modeling of the waveforms combined with matched filtering of the data stream [24]. Thus, a bank of templates is produced which spans the expected physical parameter space, and each template is compared to the data to find a possible match.

### 2.3.4 Unmodeled Short-Duration Sources

Also expected are unmodeled sources of short duration: bursts. These might result from such events as the (relatively) poorly understood merger phase of binary inspirals [23], aspherical supernova collapse [25], gamma-ray bursts [26], or other unforeseen astrophysical events. This type of event has rich prospects for totally new discoveries [27, 28, 29].

As the waveforms of such events cannot be foreknown, detection relies primarily on a coincidence of excess power seen in multiple detectors, and possibly near coincidence with other types of astronomical detectors (e.g., radio, optical, or high energy telescopes).

## 2.4 Gravitational Wave Detection

In the long-wavelength regime (where the wavelength of the GW is much larger than the scale of the detector:  $\lambda \gg L$ ), the local, time varying effect of a passing gravitational wave will be a *strain*, transverse to the direction of propagation of the wave. The detection of gravitational waves thus relies on the sensitive detection of strain. Any strain detector will suffice, provided it has sufficient sensitivity and low enough noise. The strain is the proportional change in length:

$$strain \equiv \frac{\delta L}{L}. \tag{2.7}$$

If the length (or distance,  $L$ ) over which the measurement will be taken is known, then it is sufficient to measure the displacement  $\delta L$  of the relative endpoints.

The largest expected amplitude (on Earth) of gravitational waves of astrophysical origin correspond to a strain of about  $10^{-21}$  [14]; a wave with such an amplitude might occur from a few times a year to once every few years [30]. This number, which sets the scale for the target sensitivity for a gravitational wave detector, is based on estimates of how frequently significant gravitational wave generating events may occur in a given volume of the universe, given our current knowledge of the astrophysical populations. Events in our own Milky Way galaxy would have a much larger amplitude when they reach Earth, but are expected to occur so infrequently that it is unreasonable to wait for one.

## 2.4.1 Terrestrial Gravitational Wave Detectors

### 2.4.1.1 Resonant Mass Antenna

The first operational gravitational wave detectors were resonant mass antennae built by Weber in the 1960s [31]. These antennae were solid masses which essentially would ring like a bell when a gravitational wave passed through, temporarily putting a stress on the mass. Small displacement sensors are attached to the mass in order to measure the amplitudes of several normal modes of the mass; when a gravitational wave passes through the mass, these amplitudes will change momentarily as the wave excites the antenna. Because the sensitivity depends greatly on the resonant, bell-like ringing of the test masses, these types of detectors can never be broadband detectors, and can only attain meaningful sensitivity in a narrow frequency band around the resonant frequency of the mass.

### 2.4.1.2 Optical Interferometers

An optical interferometer can also be used as a gravitational wave detector, an idea first studied in detail by Weiss [32]. The essential operating principle is to use interferometric techniques to measure the relative displacement of two test masses ( $\delta L$ ), which can be converted into a strain via equation (2.7). Such devices are relatively broadband in nature, with the upper limit of their sensitivity band determined by detector scale (which must be smaller than the GW wavelength) and the lower limit generally determined by insurmountable sources of noise.

A discussion of several interferometer configurations for gravitational wave detection is in chapter 3. Many of the limits to interferometer sensitivity (the noise sources) presented in Weiss' original study are still significant today; for a summary of the noises and the strategies employed to mitigate them, see [33]. Saulson's book [34] provides an excellent introductory overview to the techniques involved in using interferometers as gravitational wave detectors.

## 2.5 LIGO

LIGO has been constructed by Caltech and MIT with the support of the U.S. National Science Foundation as part of an effort to detect gravitational waves and to open the field of gravitational wave astronomy. LIGO is composed of three kilometer-scale interferometers at two sites, separated by 3000 km. The three interferometers are the Hanford, WA 4 km (H1), Hanford 2 km (H2), and Livingston, LA 4 km (L1). The widely separated pair (H1-L1) can increase confidence that a detection is genuine, as few sources of noise will be correlated between two detectors separated by 3000 km. The co-located pair (H1-H2) can provide additional confirmation with an exactly coincident arrival time and a 2:1 amplitude ratio in the detected signal, whereas local displacement noise sources should have a 1:1 amplitude.

The LIGO detectors are long baseline optical interferometers, enclosed in a vacuum envelope, and with aggressive isolation from seismic noises. They are capital facilities, with a schedule of operation and upgrades planned from Initial LIGO, which was the predicted state of the art at the time of its conceptual design, through Advanced LIGO [5], a planned upgrade which is the predicted state of the art now. Initial LIGO was decommissioned in 2008 for a partial upgrade to Enhanced LIGO [35], which began taking data in mid 2009 with a best effort goal of a factor of two sensitivity improvement over Initial LIGO. Advanced LIGO is currently under construction, and will be installed beginning in 2012. Advanced LIGO is expected to provide approximately 10 times better sensitivity to gravitational radiation than Initial LIGO, and should thus detect events approximately 1000 times more frequently. It is expected that Advanced LIGO will have regular detections, and will open the field of gravitational wave astronomy.

The work in this thesis was done as part of the effort to build Advanced LIGO.

### 2.5.1 The LIGO Scientific Collaboration

As of this writing, the LIGO Scientific Collaboration (LSC) is made up of over 700 scientists from 60 institutions and 11 countries. It is dedicated to the first detection of gravitational waves and the opening of the field of gravitational wave astronomy, through the development of gravitational wave detectors and the exploitation of their output. The LSC operates multiple subgroups dedicated to detector characterization, advanced detector research, detector calibration, and dedicated search groups which analyze the detector output to search for the four signal types: stochastic, burst, inspiral, and continuous wave.

The LSC has produced several white papers which outline the future directions for the field of gravitational wave detection. The work in this thesis, in particular chapters 6, 8, and 9 was specifically called out in the instrument science white paper; the work in chapter 10 was called out in the separate data analysis white paper.

## 2.6 A New Window on the Universe

The detection of gravitational waves will be exciting, and will allow further confirmation of general relativity through verification of its prediction for GW properties: transverse, with two polarizations, and traveling at the speed of light. Even more exciting however, will be the opening of the field of gravitational wave astronomy. The four types of sources listed here represent those anticipated to be detectable with ground based interferometric detectors, but it is possible that this categorization will cease to be meaningful once detections are made regularly. When that happens the field will transform from one focused on detection to one focused on astronomy, with gravitational radiation being the messenger allowing the study of populations and systems, as well as detailed astrophysics of systems which can not be studied in any other way. For example, complete information regarding the space-time structure around a black hole is encoded in the waveform of the gravitational radiation emitted as a relatively small body inspirals and infalls [36, 37]. The study of gravitational waves will open a new window on the universe, and perhaps revolutionize our understanding of the cosmos.

## Chapter 3

# Interferometric Gravitational Wave Detection

In this chapter we discuss the basic concepts of interferometric gravitational wave detection, including a brief review of important noise sources and some standard interferometer topologies. We also mention the need for feedback control in interferometers, and briefly describe the Advanced LIGO design.

### 3.1 Principle of Operation

The most sensitive gravitational wave (GW) detectors currently operating are *laser interferometer gravitational wave detectors*, which will be frequently referred to as simply “interferometers.” In order to be sensitive to gravitational waves in the long-wavelength limit ( $\lambda_{GW} \gg L$ , the case considered from here on), an interferometer must contain masses which are free to follow geodesics (at least in one direction). A geodesic is the path followed by a particle moving through spacetime, when gravity is the only force acting on the particle. Such particles following geodesics are said to be *freely falling*. The free masses in an interferometer are known as test masses (TMs).

We can see how an interferometer can be used as a gravitational wave detector by writing down the total accumulated phase of a light beam which travels between two freely falling masses separated by  $L$ , given by the integral of the spacetime metric along the way,

$$\phi = \frac{\omega_0}{c} \int_0^L g dx, \quad (3.1)$$

where  $\phi$  is the accumulated phase,  $\omega_0$  is the angular frequency of the light ( $1.78 \times 10^{15}$  rad/s for light with wavelength  $\lambda = 1064$  nm), and  $g$  is the metric. Replacing the metric  $g$  with a flat background metric  $\eta$  plus a small time varying perturbation  $h$ ,

$$g = \eta + h(t), \quad (3.2)$$

we can split the integral into a constant piece and a time varying piece:

$$\phi(t) = \frac{\omega_0}{c}L + \frac{\omega_0}{c} \int_0^L h(t) dx. \quad (3.3)$$

Ignoring the constant term, we can see that the time variations in the phase of a light beam traveling between two freely falling masses contain information about time variations in the metric between them. For the case where the light travel time  $L/c$  is much smaller than the timescale of the variations in the metric  $L/c \ll 1/f_{gw}$ , the variable metric term  $h(t)$  can be considered approximately constant over the length of the integral. The time dependent phase then becomes

$$\phi(t) = \frac{\omega_0 L}{c} h(t). \quad (3.4)$$

By attaching mirrors to the test masses, one can use them as the endpoints in an interferometer, with the fluctuations in the metric arising from GWs being imprinted on the phase of the light beams traversing the detector. This is the basis of interferometric gravitational wave detection, and it permits the use of techniques developed for precision interferometry to measure optical phase. Several configurations of interferometers which can be used as gravitational wave detectors are discussed in this chapter.

Just to set the scale for the discussion, it helps to have some numbers. The LIGO interferometers have arms that are 4 km long. For a strain of  $10^{-22}$ , this corresponds to a displacement of  $4 \times 10^{-19}$  m. Compare this to the diameter of a proton, which is approximately  $10^{-15}$  m. For  $\lambda = 1064$  nm, this is less than one part in  $10^{12}$  of a wavelength.

## 3.2 Noise

In order for an interferometer to accurately detect gravitational waves, the test masses must be freely falling. Of course, no system exists in complete isolation, and so what we mean by freely falling is that any forces *other than those due to gravitational waves* must be sufficiently small to not degrade the signal to noise ratio of the interferometer output. At the level of  $10^{-19}$  m, there are abundant sources of noise which could mask a signal. Interferometer design is strongly motivated by the need to avoid and/or mitigate noise, and so we begin our discussion of interferometers with a quick mention of several of the types of noise that can limit the sensitivity of these devices. A thorough discussion of noise in interferometers, and the strategies employed to mitigate them in LIGO, can be found in [33].

There are two distinct types of noise: displacement noises, which actually move the test masses; and sensing noises, which do not move the test mass but appear in the detection channel. Nonetheless, when referring to noises of mixed provenance, we will say displacement noise. In the gravita-

tional wave detection community, noises are frequently classified as either ‘technical’ or ‘fundamental.’ The fundamental noises include the following.

**Seismic noise** is a primary concern for terrestrial detectors. At  $\sim 100$  Hz, where the LIGO interferometers are most sensitive, the motion of the ground is approximately  $10^{-12} \frac{\text{m}}{\sqrt{\text{Hz}}}$ , seven orders of magnitude above the desired sensitivity. Seismic noise limits the sensitivity of interferometers at low frequencies (40 Hz and below for LIGO, 10 Hz and below for Advanced LIGO). This noise is mitigated through the use of multistage passive and active seismic isolation [38].

**Thermal noise** arises due to the random thermal fluctuations of the individual particles which comprise the test mass, the mirror attached to it, and the suspension system. Thermal noise in the mirror coating is expected to limit the Advanced LIGO sensitivity around 100 Hz [39]. The thermal fluctuations are related to the loss in the materials [40], so this noise is mitigated by using low-loss materials. In all cases, high-Q materials are used to limit the thermal noise to a narrow frequency band around the resonant acoustic modes; those frequency bands are then excluded from the measurement band.

**Quantum noise** is due purely to quantum effects of the light in the interferometer, and not due to any quantum mechanical motion of the test masses themselves [41]. The quantum noise of the light comprises different problems in two regimes: at low frequencies and high laser power *radiation pressure noise* will physically buffet the test masses; at higher frequencies and low laser power *photon shot noise* will limit sensitivity. Shot noise is an example of a *sensing noise*, which is a noise that appears in the sensing channel, but does not actually displace the test masses. Shot noise will limit Advanced LIGO sensitivity at high frequencies, and radiation pressure noise may limit sensitivity at low frequencies as well. Unless otherwise stated, for a given interferometer configuration the shot noise and radiation pressure noise can be considered as uncorrelated.

The technical noises include, but are not limited to, the following.

**Light source noise** or laser noise (both in amplitude and phase), can also pollute the signal [42], generally as a sensing noise (although amplitude variations in the light source can cause radiation pressure noise of a technical origin).

**Control noise** is a general term comprising self-inflicted noise caused by auxiliary control systems (e.g., alignment control). This type of noise limited the low frequency sensitivity of initial LIGO, and may also limit the low frequency sensitivity of Advanced LIGO. This can include noise generated in both the sensing for auxiliary systems and the actuation. Much of the design and commissioning effort in gravitational wave detection is directed at reducing control noise.

**Environmental noise** coupling into the interferometer is mostly due to acoustic perturbations of the sensing systems at the output port, rather than the test masses themselves. Other couplings, such as magnetic fields from the power mains lines are of course also possible. These are mitigated as much as possible through isolation of the sensing systems.

### 3.3 Mathematical Notations for Mirrors, Fields, and Spaces

It is useful to review some notation that will ease our discussion of interferometers. Interferometers are composed of mirrors and fields, with the main source of the field being given by a laser. Light coming from the laser will have an electric field given by

$$E(z, t) = E_0 e^{i(\omega_0 t - kz)}, \quad (3.5)$$

where  $E_0$  is the field amplitude (a complex number),  $k$  is the wave number ( $\frac{2\pi}{\lambda}$  for wavelength  $\lambda$ ),  $\omega_0$  is the angular frequency of the laser light, and  $z$  is the distance along the direction of travel of the light source. The  $e^{i\omega_0 t}$  term will be common to all fields, and so generally we will suppress it. We also generally work in a single polarization, and so we can suppress that as well. Because the gravitational waves which we hope to detect are at audio frequencies (10 Hz—10 kHz), we will also frequently refer to ‘audio sidebands,’ which will be caused by either gravitational waves (cf. equation (3.4), from which we can see that gravitational waves will create phase modulation sidebands, and [43] for a complete description) or they will be caused by noise. We will use a subscript  $a$  to refer to audio sidebands about the carrier at angular frequency  $\omega_0 + \omega_a$ .

We adopt the notation,

$$E_{port} = E(z_{port}), \quad (3.6)$$

to indicate the field at a given port, where the port is right at the mirror surface. A mirror  $i$  ( $m_i$ ) is characterized by an amplitude reflectivity (lowercase  $r_i$ ) and amplitude transmissivity (lowercase  $t_i$ ). The corresponding quantities in power (indicated by uppercase letters) are the squares of the amplitude factors. Mirrors can also be lossy (with the fractional power loss denoted by  $L_i$ ). These relations are summarized by

$$\begin{aligned} T_i &= t_i^2, \\ R_i &= r_i^2, \\ 1 &= T_i + R_i + L_i. \end{aligned} \quad (3.7)$$

Because a mirror has two sides, it can be considered to behave as a four-port object, with two input fields and two output fields (cf. figure 3.1), and a corresponding  $2 \times 2$  transfer matrix. The

quantities  $r_i$  and  $t_i$  are, in general, complex; the matrix elements must have some relative phase in order for the mirror to conserve energy, but there are several possible choices which allow this, all of which can yield fully self-consistent results. One possible energy-conserving choice for this matrix which is particularly simple is

$$\begin{bmatrix} -r_i & t_i \\ t_i & r_i \end{bmatrix}, \quad (3.8)$$

which we can implement by considering one surface of the mirror (usually we will pick the ‘back’ surface) to have a negative amplitude reflectivity. Then the input-output relations for the fields in figure 3.1 are given by

$$\begin{pmatrix} E_{bo} \\ E_{fo} \end{pmatrix} = \begin{bmatrix} -r_i & t_i \\ t_i & r_i \end{bmatrix} \begin{pmatrix} E_{bi} \\ E_{fi} \end{pmatrix}. \quad (3.9)$$

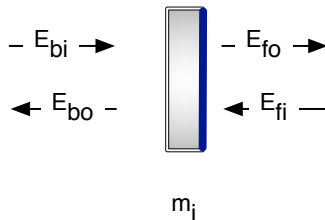


Figure 3.1: Input and output fields of a mirror mass. The mirror is composed of a substrate (grayish block) and a reflective coating (dark blue). The coated side is considered the ‘front’ of the mirror.

We will decompose the spaces between mirrors into macroscopic and microscopic lengths, with the macroscopic length always being an integer multiple of the laser wavelength  $\lambda$  and the microscopic length being the residual. So, the distance  $d_{AB}$  between two locations at  $A$  and  $B$  can be written

$$d_{AB} = L_{AB} + \Delta L_{AB} + \delta L_{AB}, \quad (3.10)$$

where

$$kL_{AB} = 2\pi n, \quad (3.11)$$

for integer  $n$ ,  $\Delta L_{AB}$  is the static residual, and  $\delta L_{AB}$  is a fluctuating residual. For the most part, this will also allow us to suppress macroscopic cavity lengths in equations when we are only interested in timescales such that  $\tau \gg L/c$ .

The mirror operator in equation (3.9) and the propagation operator in equation (3.5) are enough to determine the static (equilibrium) response of an arbitrary interferometer configuration—all that is required is to use these operators to write down all the field relationships and solve the resulting system of coupled linear equations. The process can be repeated for each frequency desired (as  $k$  changes with frequency) to calculate a frequency response. This is the approach taken by frequency

domain modeling tools (more in appendix F).

### 3.4 The Michelson Interferometer as a Gravitational Wave Detector

Figure 3.2(a) shows a Michelson interferometer, which is composed of a beamsplitter and two retro-reflecting mirrors, illuminated by a laser. Light  $E_{IN}$  approaches from the laser, is split by the beamsplitter (which we will consider to be a 50-50 beamsplitter, reflecting half the incident light and transmitting half the incident light), travels the length of the two arms, is reflected from the two end mirrors, and returns to recombine at the beam splitter. We can write the field at the asymmetric port of this interferometer (the side of the beamsplitter not facing the laser)

$$\begin{aligned} E_{AS} &= E_{IN} (t_{bs}r_{bs}e^{i2k\Delta l_x} - t_{bs}r_{bs}e^{i2k\Delta l_y}) \\ &= E_{IN}t_{bs}r_{bs}(r_x e^{i2k\Delta l_x} - r_y e^{i2k\Delta l_y}), \end{aligned} \quad (3.12)$$

where  $l_x$  and  $l_y$  are the lengths of the two arms, and  $r_x$ ,  $r_y$  the reflectivity of the end mirrors, which we will assume to be perfect. The field at the asymmetric port can vary from zero (called the dark fringe) when the two arms are of equal length to  $E_{IN}t_{bs}r_{bs}(r_x + r_y)$  when the arms lengths differ by  $\lambda/4$ . Any signal derived from the asymmetric port field is sensitive only to differential motion of the two end mirrors. Common motions appear at the symmetric port; more importantly, for the case when  $\Delta x = \Delta y$ , fields entering from the symmetric port ( $IN$ ) do not couple to the asymmetric port to first order, which means that a perfect Michelson effectively rejects noise originating in the laser.

We will find it useful on occasion to think of the Michelson as a complex mirror—that is, a mirror that has an amplitude reflectivity and also rotates the carrier optical phase. The Michelson reflectivity from the symmetric side is

$$r_{mich-sym} = r_{bs}^2 r_x e^{i2k\Delta l_x} + t_{bs}^2 r_y e^{i2k\Delta l_y}. \quad (3.13)$$

From the asymmetric side it is

$$r_{mich-asym} = t_{bs}^2 r_x e^{i2k\Delta l_x} + r_{bs}^2 r_y e^{i2k\Delta l_y}. \quad (3.14)$$

Examining figure 2.1, let us imagine using the red particles in the ring as our test masses. It would be possible to construct many types of interferometers which would sense the relative motions

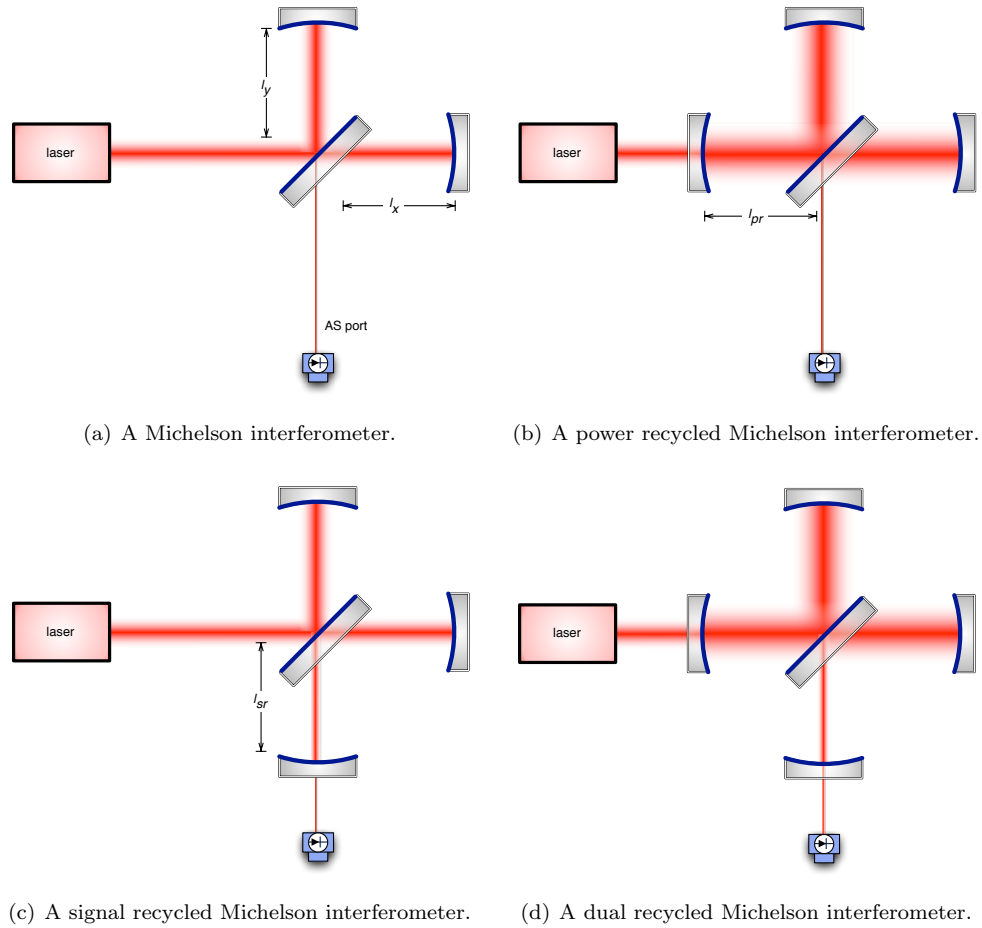


Figure 3.2: Michelson based interferometer topologies for gravitational wave detection.

of these two test masses, but if we limit ourselves to the  $+$  polarized wave, Weiss' original choice of a Michelson based interferometer is very sensible. By placing the beamsplitter at the center of the ring, and mirrors on the two red particles, we can see that the  $+$  polarization precisely excites the differential mode of our Michelson, and so we should be able to extract a signal at the asymmetric port. We lose sensitivity to the  $\times$  polarized waves, which only excite the common mode, but gain immunity to light source noise—a worthwhile trade-off. Of course, the immunity is not perfect; any asymmetries between the two Michelson arms will allow light source noise to couple to the asymmetric port. For a simple Michelson, these asymmetries include arm length differences and end mirror reflectivity mismatches.

If we define the Michelson differential length (MICH),

$$l_- = l_x - l_y, \quad (3.15)$$

then near the dark fringe the field derivative at the  $AS$  port is

$$\left. \frac{dE_{AS}}{d\delta l_-} \right|_{\Delta l_- = 0} = i2kE_{in}t_{bs}r_{bs}(r_x + r_y), \quad (3.16)$$

which will define the signal gain for a given displacement. Increasing the gain for a given strain can be accomplished by either increasing the length of the arms (cf. equation (3.4)) or by illuminating the interferometer with a more powerful laser (as  $E_{in} = \sqrt{P_{in}}$ ).

### 3.5 Signal Extraction

It is important that the Michelson be operated on a dark fringe in order to reject laser noise, but we here confront the fact that we cannot actually directly detect the electric field at the asymmetric (output) port, and certainly not at the frequencies of oscillation used in current interferometers (where the laser field has angular frequency  $\omega_0 \approx 10^{15}$  rad/s). What we can actually detect is the average power, using (for IR and visible light) a photodetector. The power is given generally by

$$P = E^* E, \quad (3.17)$$

where  $E^*$  is the complex conjugate of  $E$ . We will also lazily consider the power at the photodetector to be our final output, although this is not strictly true. The photodetector converts the power hitting it (with some efficiency) into an electrical current or voltage; it is this electrical signal which is actually measured, but the distinction is not terribly important for this discussion.

The power transmitted to the asymmetric port of a Michelson interferometer with perfect end mirrors is

$$P_{AS} = 4|E_{IN}^2|(t_{bs}r_{bs})^2 \sin^2 \phi_-, \quad (3.18)$$

where the differential phase  $\phi_-$  is  $k(2\Delta l_x - 2\Delta l_y) = k\Delta l_-$ .

The signal gain we expect is proportional to the derivative  $\frac{dP_{AS}}{d\phi_-}$ ,

$$\frac{dP_{AS}}{d\phi_-} \propto 2 \sin \phi_- \cos \phi_-, \quad (3.19)$$

which is zero when  $\phi_- = 0$ . Thus, for small deviations around the dark fringe, we have no signal. This is a common situation, and much of interferometer design is concerned with how to solve this problem. However, there is a straightforward solution: we can use a different field, co-incident on the photodetector, as a local oscillator  $E_{LO}$ . In this case the field and detected power at the

photodetector become

$$\begin{aligned}
 E_{PD} &= E_{LO} + E_{SIG} \\
 P_{PD} &= |E_{PD}^* E_{PD}| \\
 &= |(E_{LO} + E_{SIG})^* (E_{LO} + E_{SIG})|,
 \end{aligned} \tag{3.20}$$

where the cross terms in the product,  $E_{SIG}^* E_{LO} + E_{SIG} E_{LO}^*$ , can allow us to recover a linear signal around  $\phi_- = 0$  even when  $|E_{SIG}| = 0$  at  $\phi_- = 0$ , for the proper choice of local oscillator field. The two sections which follow describe two of the possible choices for such a local oscillator.

Classically this signal will be limited by shot noise, the fluctuations in laser power due to photon counting statistics (for a quantum mechanical discussion, refer to [44]). The shot noise level is given by the power incident on the photodetector:

$$\delta P_{shot} = \sqrt{\frac{2hc}{\lambda} P_{inc}}. \tag{3.21}$$

If we set up our interferometer such that our local oscillator field is proportional to the input field  $E_{LO} \propto E_{in}$ , then (cf. equation (3.16)) the shot noise limited signal-to-noise ratio will scale as:

$$SNR_{shot} \propto \sqrt{P_{in}}. \tag{3.22}$$

This is a fairly general result, and explains why increasing the power illuminating the interferometer can improve the sensitivity.

### 3.5.1 Optical Heterodyne Detection

One possible choice for a local oscillator is a frontal phase modulation sideband. The usual setup includes an electro-optic phase modulator installed with the input beam (cf. figure 3.5). These devices (also called Pockels cells) can be used to apply a sine wave modulation of depth  $\Gamma$  and angular frequency  $\Omega_m$  on the phase of the input light  $E_0 e^{i\omega_0 t}$  yielding the field incident on the interferometer,

$$E(t) = E_0 e^{i[\omega_0 t + \Gamma \cos(\Omega_m) t]}. \tag{3.23}$$

We can use the Jacobi-Anger expansion which relates trigonometric exponentials in terms of Bessel functions [45],

$$e^{i\Gamma \cos(\Omega) t} = \sum_{n=-\infty}^{\infty} i^n J_n(\Gamma) e^{in\Omega t}, \tag{3.24}$$

yielding (keeping only terms to first order):

$$E(t) = E_0 e^{i\omega_0 t} [J_0(\Gamma) - iJ_{-1}(\Gamma)e^{-i\Omega_m t} + iJ_1(\Gamma)e^{i\Omega_m t} + \dots], \quad (3.25)$$

which for  $\Gamma \lesssim 0.5$  is approximately

$$E(t) \simeq E_0 e^{i\omega_0 t} \left[ \left(1 - \frac{\Gamma^2}{4}\right) + \frac{i\Gamma}{2} e^{-i\Omega_m t} + \frac{i\Gamma}{2} e^{i\Omega_m t} \right]. \quad (3.26)$$

Then the first-order modulation sidebands can function as local oscillators. This scheme is known as *heterodyne detection*, because the local oscillator is at a different frequency from the carrier field. After photodetection, there is a beat signal in the photocurrent at the difference frequency (in this case,  $\Omega_m$ ). The desired readout signal (in this case, the Michelson length) appears as a modulation of this beat signal. The modulation sidebands are typically at radio frequency (RF), and this technique is thus sometimes known as RF readout. We will refer to the RF local oscillator fields as ‘RF sidebands.’

We can consider the case where we have audio sidebands on the carrier field and on the RF sideband fields we are using as a local oscillator. If we let, e.g.,  $F_\omega$  indicate the complex amplitude of a field oscillating at frequency  $\omega_0 + \omega$ , the field at the photodetector can be written

$$E_{PD} = e^{i\omega_0 t} (F_{-\Omega_m} e^{-i\Omega_m t} + F_{\Omega_m} e^{i\Omega_m t} + F_{-\omega_a} e^{-i\omega_a t} + F_{\omega_a} e^{i\omega_a t}) \quad (3.27)$$

$$+ F_{-(\Omega_m \pm \omega_a)} e^{-i(\Omega_m \pm \omega_a)t} + F_{(\Omega_m \pm \omega_a)} e^{i(\Omega_m \pm \omega_a)t} + F_0), \quad (3.28)$$

where we have again only kept first-order terms at each modulation, and we have lumped together the audio sidebands on the RF sidebands. Applying equation (3.17) yields 49 terms. We will ignore terms at  $2\Omega_m$  and  $2\omega_a$ , and collect terms around  $\omega_a$ ,  $\Omega_m$ ,  $\Omega_m \pm \omega_a$ , and at DC:

$$P(\omega = 0) = F_{-\Omega_m} F_{-\Omega_m}^* + F_{\Omega_m} F_{\Omega_m}^* + F_{-\omega_a} F_{-\omega_a}^* + F_{\omega_a} F_{\omega_a}^* + F_0 F_0^* \quad (3.29a)$$

$$P(\omega \approx \Omega_m) = 2 \times \text{Re} \left\{ [F_{-\omega_a} e^{-i\omega_a t} + F_{\omega_a} e^{i\omega_a t} + F_0] \times [F_{-\Omega_m} e^{-i\Omega_m t} + F_{\Omega_m} e^{i\Omega_m t}]^* \right\} \quad (3.29b)$$

$$+ 2 \times \text{Re} \left\{ F_0 \times [F_{-(\Omega_m \pm \omega_a)} e^{-i(\Omega_m \pm \omega_a)t} + F_{(\Omega_m \pm \omega_a)} e^{i(\Omega_m \pm \omega_a)t}]^* \right\}$$

$$P(\omega \approx \omega_a) = 2 \times \text{Re} \left\{ F_0 \times [F_{-\omega_a} e^{-i\omega_a t} + F_{\omega_a} e^{i\omega_a t}]^* \right\}, \quad (3.29c)$$

where  $\text{Re}$  indicates taking the real part of a complex number. Equation (3.29a) is the total light power on the photodetector. Equation (3.29c) is essentially homodyne detection (discussed more in section 3.5.2). Equation (3.29b) is the heterodyne signal. We can now *demodulate* the signal

by using an electronic mixer to multiply the photodetector output by a  $\cos(\Omega_m t)$  (the mixer really multiplies by a square wave but the distinction is not critical) and low-pass filtering the mixer output to eliminate components remaining at  $\Omega_m$  and  $2\Omega_m$ . The in-phase mixer output  $M_I$  is

$$M_I = \text{Re} \{ F_0^* F_{\Omega_m} + F_0 F_{-\Omega_m}^* \} \quad (3.30a)$$

$$+ \text{Re} \{ (F_{-\omega_a}^* F_{\Omega_m}^* + F_{-\omega_a}^* F_{-\Omega_m}^* + F_{\omega_a} F_{\Omega_m} + F_{\omega_a} F_{-\Omega_m}) e^{i\omega_a t} \} \quad (3.30b)$$

$$+ \text{Re} \left\{ (F_0 F_{-(\Omega_m+\omega_a)}^* + F_0^* F_{-(\Omega_m-\omega_a)} + F_0^* F_{(\Omega_m+\omega_a)} + F_0 F_{(\Omega_m-\omega_a)}^*) e^{i\omega_a t} \right\}. \quad (3.30c)$$

Multiplying by a  $\sin(\Omega_m t)$  for the quadrature phase output  $M_Q$  would give us the negative of the imaginary part instead:

$$M_Q = -\text{Im} \{ F_0^* F_{\Omega_m} + F_0 F_{-\Omega_m}^* \} \quad (3.31a)$$

$$- \text{Im} \{ (F_{-\omega_a}^* F_{\Omega_m}^* + F_{-\omega_a}^* F_{-\Omega_m}^* + F_{\omega_a} F_{\Omega_m} + F_{\omega_a} F_{-\Omega_m}) e^{i\omega_a t} \} \quad (3.31b)$$

$$- \text{Im} \left\{ (F_0 F_{-(\Omega_m+\omega_a)}^* + F_0^* F_{-(\Omega_m-\omega_a)} + F_0^* F_{(\Omega_m+\omega_a)} + F_0 F_{(\Omega_m-\omega_a)}^*) e^{i\omega_a t} \right\}. \quad (3.31c)$$

One convenient improvement is to use a so-called *I&Q* demodulator which simultaneously multiplies the photodetector output by both a  $\cos \Omega_m t$  (the in-phase) and a  $\sin \Omega_m t$  (the quadrature-phase), yielding the  $I_0$  and  $Q_0$  phased outputs. Then these outputs can be combined using a rotation matrix to achieve an arbitrary demodulation phase  $\phi_D$ , such that  $I_{\phi_D}$  is equivalent to mixing the PD output with  $\cos(\Omega_m t + \phi_D)$ ,

$$\begin{pmatrix} I_{\phi_D} \\ Q_{\phi_D} \end{pmatrix} = \begin{bmatrix} \cos \phi_D & -\sin \phi_D \\ \sin \phi_D & \cos \phi_D \end{bmatrix} \begin{pmatrix} I_0 \\ Q_0 \end{pmatrix}. \quad (3.32)$$

Generally, the I-phase signal will contain information about the relative optical phase of the  $F_0$  and  $F_{\pm\Omega_m}$  fields; the Q-phase signal will contain information about the imbalances in the  $F_{\pm\Omega_m}$  fields (see [43] for a derivation).

### 3.5.1.1 Schnupp Asymmetry for Michelson Length Sensing

We can transmit the RF sidebands to the asymmetric port of a Michelson interferometer using a Schnupp asymmetry [46], which is a macroscopic length difference between the arms of the Michelson. We recall the Michelson length asymmetry (macroscopic) as

$$l_- = l_x - l_y. \quad (3.33)$$

We will as usual denote microscopic deviations from the condition  $l_- = n\lambda$  by  $\Delta l_-$ . If the arms of the Michelson are of equal length ( $l_- = 0$ ), and moreover  $\Delta l_- = 0$ , then all frequencies of light will

undergo the same destructive interference at the asymmetric port. If the arms are of unequal length ( $l_- \neq 0$ ), however, only at those wavelengths for which  $\phi_- = n\pi$  will the asymmetric port actually be dark.

We can apply a frontal phase modulation to the input beam at  $\Omega_m$ . The transmission for the modulation sidebands to the asymmetric port is

$$T_{mich} = \sin^2 \left( \frac{\Omega_m l_-}{c} \right). \quad (3.34)$$

We can recover a linear sensing function for the Michelson displacement by using this transmitted pair of RF sideband field as a local oscillator in an RF heterodyne detection scheme. This technique allows us to operate a Michelson on a carrier dark fringe.

### 3.5.2 Optical Homodyne Detection

A technique complementary to heterodyne detection (cf. section 3.5.1) is *homodyne detection*. For homodyne detection, the local oscillator employed to downconvert the audio frequency sidebands is a field oscillating at the same frequency as the carrier field. In this case, the audio sidebands are directly downconverted to DC by the photodetection process (cf. equation (3.29c)), and can simply be read out from the photocurrent. This technique is generally simpler than heterodyne detection, because it requires less in the way of electronics and altogether avoids the modulation/demodulation process, but in most cases it is more vulnerable to several types of noise—especially laser noise and the so-called 1/f or flicker noise that plagues basically all electronics at frequencies near DC. We will revisit homodyne detection in the context of DC readout in chapter 4.

## 3.6 Fabry-Pérot Cavities

A Fabry-Pérot cavity is composed of a pair of partially reflecting surfaces facing each other (cf. figure 3.3), such that light can bounce back and forth between them, returning along the same path after one or more round trips. If the distance between the surfaces is a half-integer multiple of the wavelength of the light, and the light has a coherence length much longer than the cavity, then light which has made a round trip through the cavity can interfere constructively with light coming fresh from the light source. When this condition, known as *resonance*, occurs, light can build up in the cavity. The mirrors which make up the cavity have reflectivity  $r_i$  and  $r_e$  and  $L$  is the distance between the mirrors.

For input field  $E_{in}$ , the field circulating in the cavity is

$$E_{circ} = E_{in} \frac{t_i}{1 - r_i r_e e^{2ik(L+\Delta L)}}, \quad (3.35)$$

and the reflected field is given by

$$E_{refl} = -r_i E_{in} + t_i r_e E_{circ} e^{2ik(L+\Delta L)}. \quad (3.36)$$

The field circulating in the cavity on resonance is

$$E_{circ} = g_c E_{in}, \quad (3.37)$$

where we have used the cavity field gain,  $g_c$ ,

$$g_c = \frac{t_i}{1 - r_i r_e}. \quad (3.38)$$

At zero frequency, the cavity reflectivity on resonance is

$$r_0 = \frac{-r_i + r_e(R_i + T_i)}{1 - r_i r_e} \simeq \frac{r_e - r_i}{1 - r_i r_e}. \quad (3.39)$$

Any number of wavelengths can resonate in the cavity, and the frequency separation between these longitudinal modes is the *free spectral range*:

$$\nu_0 = \frac{c}{2L}. \quad (3.40)$$

When the cavity is held on resonance for the carrier, we can write the cavity pole,  $\nu_c$ , which is the offset from the carrier frequency at which the circulating optical power in the cavity falls by 3 dB (or 1/2):

$$\nu_c = \frac{\nu_0}{2\pi} \frac{1 - r_i r_e}{\sqrt{r_i r_e}}. \quad (3.41)$$

This is the cavity half-bandwidth. A related quantity is the cavity storage time,

$$\tau \equiv \frac{2\pi}{\omega_c} = \frac{4FL}{c}, \quad (3.42)$$

where we have used the cavity finesse  $\mathcal{F}$ , given by

$$\mathcal{F} \simeq \frac{\pi}{2} \frac{(r_i r_e)^{1/4}}{1 - \sqrt{r_i r_e}}. \quad (3.43)$$

The finesse is defined as the full width half max (FWHM) divided by the free spectral range,

$$\mathcal{F} = \frac{2\nu_c}{\nu_0}. \quad (3.44)$$

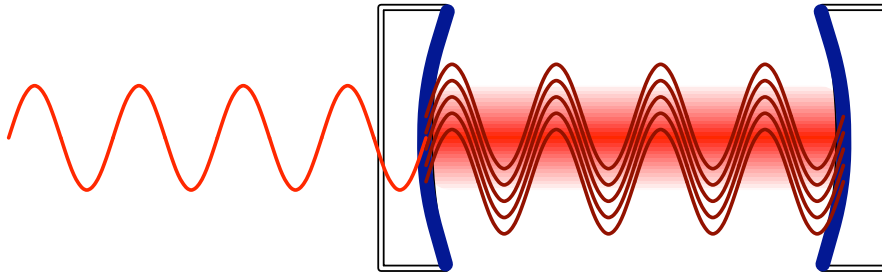


Figure 3.3: A Fabry-Pérot Cavity with overlapping waves. When the distance between the cavity mirrors is a half-integer multiple of the wavelength of the light, light which completes a round trip can interfere constructively with new light entering the cavity, resulting in a buildup of power circulating in the cavity.

### 3.6.1 Cavity Spatial Modes

Laser beams in general have a spatial profile transverse to the direction of propagation. The most important example of a transverse profile is a two-dimensional Gaussian, which is generally referred to as the fundamental mode. Such a mode can be characterized by a complex beam parameter  $q$ , which changes as the beam propagates along a  $z$ -axis as

$$q(z) = q_0 + z. \quad (3.45)$$

We often write  $q$  in terms of two real beam parameters, the transverse spot size  $w$  (the distance from the propagation axis at which the amplitude has fallen by  $1/e$ ), and the radius of curvature  $R$  (the radius of curvature of the wavefront where it intersects the propagation axis):

$$\frac{1}{q} = \frac{1}{R} - i \frac{\lambda}{\pi w^2}. \quad (3.46)$$

A lens (or mirror) of focal length  $f$  (mirror curvature  $R = 2f$ ) in the beam path changes the beam parameter according to

$$\frac{1}{q_2} = \frac{1}{q_1} - \frac{1}{f}. \quad (3.47)$$

In order for a cavity to resonate a laser field, the field's beam parameter must be the same after each round trip (or some half-integer number of round trips), which is what occurs for a cavity *eigenmode*. For the simple case of a cavity of length  $L$  and mirrors of curvature  $R$ , this is the condition  $q_1 = q_2$  in

$$\frac{1}{q_2} = \frac{1}{q_1 + L} - \frac{2}{R}. \quad (3.48)$$

This is a quadratic equation in  $q$ , and we are only interested in solutions where the spot size  $w$  is real. The waist for the cavity is the minimum spot size of this eigenmode, and it occurs directly

between the mirrors. It is

$$w_0^2 = \frac{\lambda}{2\pi} \sqrt{L(2R - L)}. \quad (3.49)$$

The Rayleigh range is the distance along the propagation axis where the area of the cross section has doubled; it is given by

$$z_R = \frac{\pi w_0^2}{\lambda}. \quad (3.50)$$

The beam spot size at a distance  $z$  from the waist location is

$$w(z) = w_0 \sqrt{1 + \left(\frac{z}{z_R}\right)^2}. \quad (3.51)$$

To optimally pump this cavity with a laser, the incident laser field must have the same beam parameter as the cavity: the waist size and location should be the same. This condition is called perfect mode-matching. Mode-matching is generally quantified by doing an overlap integral of the two fields, and then squaring the result to get the power. The mode-matching of two beams can be calculated by

$$MM = 4 \frac{z_{R1} z_{R2}}{(z_1 - z_2)^2 + (z_{R1} + z_{R2})^2}, \quad (3.52)$$

where  $z_1$  and  $z_2$  are the waist locations. The mode matching is 1 for identical beams. Imperfect mode-matching generally causes a reduction in signal amplitude, either through reduced power coupling into an interferometer or reduced interference (whether constructive or destructive) where it occurs.

A more general Gaussian beam can be written as a sum of the fundamental mode plus higher-order modes (HOMs), the most common basis for which is a Hermite-Gaussian basis (see [47] for details). These modes are denoted by  $\text{TEM}_{nm}$ , where  $n$  and  $m$  indicate the order in the two transverse directions. A Fabry-Pérot cavity can resonate any of these higher order modes (see [48] for an excellent discussion), simultaneously in the case of a degenerate cavity, and separately in the case of a non-degenerate cavity, where the modes will actually resonate at slightly different lengths (corresponding to different resonant frequencies). The modes resonate at different lengths because as a Gaussian beam propagates, it accumulates an extra phase in addition to the  $e^{ikz}$  term. This extra phase is known as the Gouy phase, is defined on the beamline (at the center of the transverse profile), and represents the additional phase of a Gaussian beam when compared to a plane wave:

$$\Phi(m, n; z) = (m + n + 1) \arctan \frac{\lambda z}{\pi w_0^2}, \quad (3.53)$$

where  $w_0$  is the beam waist. In terms of the cavity parameters, we can also write the cavity resonant frequencies as

$$\nu/\nu_0 = q + 1 + \frac{1}{\pi}(m + n + 1) \arccos \sqrt{1 - L/R}. \quad (3.54)$$

Here  $\nu_0$  is the cavity free spectral range,  $q$  is the longitudinal mode number (not the beam parameter), and  $R$  is the mirror radius of curvature.

Interferometers are generally designed to operate in the fundamental mode, and so the inevitable presence of higher-order modes usually represents a problem. We will normally ignore them unless they present a specific problem, but when thinking about interferometers it is important to keep them in mind.

### 3.6.2 Transfer Functions of a Fabry-Pérot Cavity

Considering only the Gaussian TEM<sub>00</sub> spatial mode, Fabry-Pérot cavities act as low pass filters for signals imposed on the light. This is because the cavities have a certain linewidth; signals whose bandwidth lies within the linewidth can resonate in the cavity and thus build up enough optical power to transmit the mirrors which form the cavity. Signals which are outside the linewidth do not build up, and thus are either reflected from the cavity (if they are generated outside the cavity) or only weakly transmitted (if they are generated inside the cavity).

If we adopt the cavity pole notation [49]:

$$s_c \equiv \frac{i\omega_a}{\omega_c}, \quad (3.55)$$

then when  $\frac{\omega_a}{2\pi} \ll \frac{c}{2l}$  the field circulating in the cavity is

$$E_{circ}(\omega_a) = E_{in}(\omega_a) \left[ g_c \frac{1}{1 + s_c} - 2ik\Delta L \frac{r_i r_e g_c}{(1 - r_i r_e)(1 + s_c)^2} \right]. \quad (3.56)$$

The audio frequency-dependent cavity reflectivity (on resonance) can be computed with the help of equation (3.36):

$$r_c = r_0 \frac{1 + s_c/r_0}{1 + s_c}. \quad (3.57)$$

We will generally consider gravitational waves to move the end mirror by  $\delta x = hL$ , rather than directly phase modulate the circulating light; this approximation is valid when  $\lambda_{GW} \ll L$  (see [50] for a discussion of cavity response when this approximation breaks down). When the end mirror moves by  $\delta x$  at frequency  $\omega_a$ , the reflected light is a phase modulated version of the input beam:

$$E_{refl} = r_e E_{inc} e^{i2k\delta x \cos \omega_a t} \quad (3.58)$$

$$\simeq r_e E_{inc} (1 + ik\delta x e^{i\omega_a t} + ik\delta x e^{-i\omega_a t}). \quad (3.59)$$

For the purposes of gravitational wave detection, the cavities are a method for ‘folding’ the arms of the Michelson—as the light beam bounces back and forth between the cavity mirrors, it samples

the metric many times, coherently adding signal. Relative to no cavity (i.e., just an end mirror with no input mirror), the cavity gain for a gravitational wave at  $\omega_a \ll c/2L$  is

$$G_c(\omega_a) \simeq g_c^2 \frac{e^{i\omega_a L/c}}{1 + s_c}. \quad (3.60)$$

This has increased the detector's transduction gain, but reduced its bandwidth: the gain-bandwidth trade-off. We could increase the cavity gain at DC by increasing the mirror reflectivities which would increase  $g_c$ , but this would move the cavity pole  $\omega_c$  down in frequency, and so we would lose signal gain at higher frequencies. Figure 3.4 shows the case of a LIGO size detector ( $L = 4$  km), where we assume the end mirror has perfect reflectivity ( $r_e = 1$ ). There is only one remaining parameter:  $r_i$ , which determines both the detector gain and the detector bandwidth.

### 3.6.3 The Pound-Drever-Hall Technique

In [51] the authors present a technique for laser phase stabilization using a resonant cavity. Such a technique assumes that the cavity can provide a stable reference; if one instead assumes that the laser can provide a stable reference, then this technique can be used to stabilize the length of a cavity, which allows one to measure disturbances to the cavity length. In either case, this technique provides a sensitive measure of the mismatch between the length of the cavity and the laser wavelength, and has become a standard in the field of precision laser interferometry.

The Pound-Drever-Hall (PDH) technique allows phase sensitive detection at optical frequencies by using a pair of RF sidebands as a stable reference, as discussed in section 3.5.1, and shown diagrammatically in figure 3.5. The RF modulation frequency is chosen such that the RF sidebands are as far as possible from a resonance (at a free spectral range of the cavity), also without having the  $J_2$  term in the expansion in equation (3.24) fall on a resonance. The RF sidebands are thus reflected from the cavity, and provide a local oscillator in a heterodyne detection scheme as in section 3.5.1. Using equation (3.36) to calculate the cavity reflectivity for the three incident fields (carrier and RF sidebands), we can use equation (3.30a) to get the PDH signal at DC. Equation (3.56) and equation (3.30b) can be used to calculate the frequency response.

Figure 3.6 shows the PDH signals as the cavity length is swept through  $\sim \frac{\lambda}{2}$ . The cavity error signal is in the I-phase signal, which goes through zero at the carrier and sideband resonances. The signal has a linear range of about  $\frac{\lambda}{4\mathcal{F}}$ , centered around the resonances. Within the linear range the signal can be used to sense the cavity length. The Q-phase signal is zero everywhere but at the sideband resonances; this signal is a measure of the sideband imbalance at the photodetector.

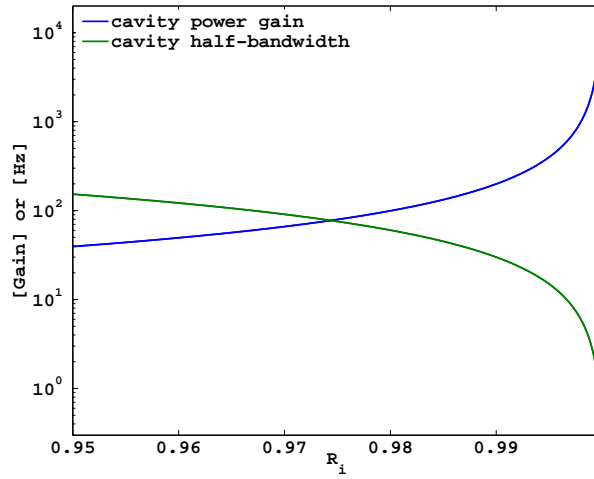


Figure 3.4: The power gain and cavity pole frequency of a 4 km cavity (with a perfect end mirror) vary with the input mirror reflectivity. Note that the  $y$ -axis is showing two different quantities—it is a coincidence that we can get them on the same plot for a 4 km cavity.

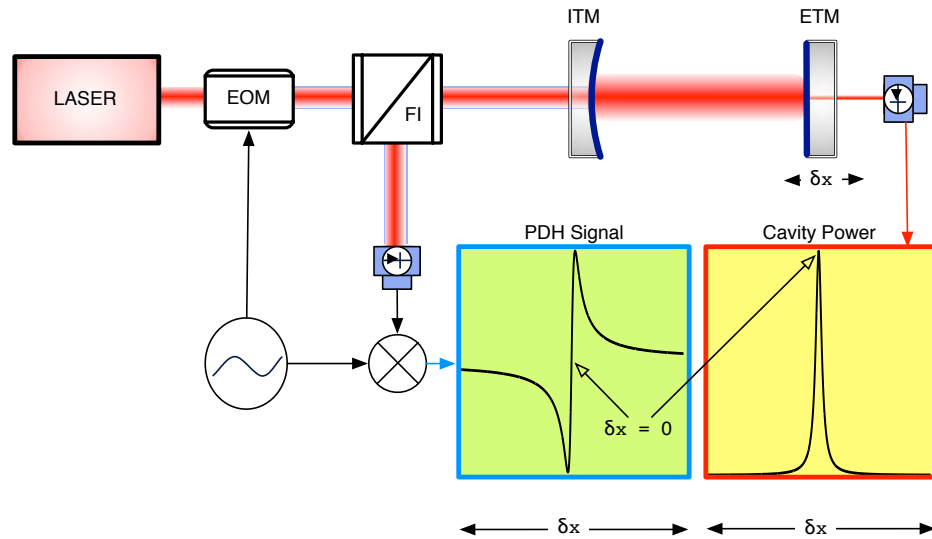


Figure 3.5: A schematic of a typical PDH length sensing setup for a resonant cavity composed of an input test mass (ITM) and an end test mass (ETM). The beam is modulated with an electro-optic modulator (a Pockels cell), goes through a Faraday-Isolator (which separates the forward beam from the return beam), and is input to the cavity. The RF sidebands (in light blue) are reflected from the cavity and the FI directs them (along with any reflected carrier light) to the photodetector. As the cavity is swept through resonance, the output of the mixer (plus an unseen low-pass filter) is an error signal which goes through zero at the resonance. Also shown is the transmitted power, which is at a maximum at resonance, measured using a separate photodetector.

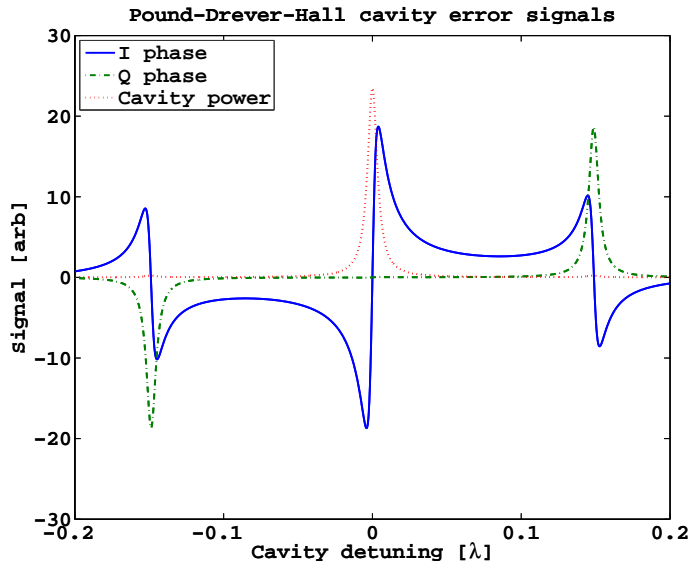


Figure 3.6: The PDH signals for a single cavity. The I-phase signal can be used as an error signal in a feedback loop to keep the cavity resonant for either the carrier or an RF sideband; switching the sign of the feedback loop will select between the two. Which RF sideband is resonating (upper or lower) can then be selected by using the Q-phase signal as a trigger, since it has a different sign for each of the two sidebands.

### 3.7 Adding Fabry-Pérot Cavities to the Arms of a Michelson Interferometer

By placing partially reflecting mirrors in the arms of a Michelson interferometer, one arrives at a configuration known as a Fabry-Pérot Michelson interferometer. Such an interferometer behaves as a Michelson interferometer with end mirrors that have complex, frequency dependent reflectivity (see appendix D for details). So, by adding cavities to the arms of our Michelson, we have increased the phase gain of the interferometer, but reduced the bandwidth. Adding two arm cavities adds two degrees of freedom to the interferometer—the length of the two cavities. We denote these as  $L_x$  and  $L_y$ . We will typically rewrite these as

$$L_- = L_x - L_y, \quad (3.61a)$$

$$L_+ = \frac{L_x + L_y}{2}, \quad (3.61b)$$

and refer to  $L_-$  as DARM (Differential ARM) and  $L_+$  as CARM (Common ARM).

Signal sidebands in the arm cavities can be rewritten according to equation (3.61); following that, signals which appear in CARM are transmitted to the symmetric port of the Michelson, and signals which appear in DARM are transmitted to the asymmetric port. The reverse also applies: signals from the symmetric port are transmitted to CARM, and from the asymmetric port are transmitted

to DARM. We will thus refer to DARM as the asymmetric mode and CARM as the symmetric mode. Note that these concepts of symmetric mode and asymmetric mode apply only to signal (or noise) sidebands—the power buildup of the carrier field is, of course, the same in both modes.

The cavities in the arms also introduce more possible asymmetries. The cavity reflectivities on resonance may be different. Differing losses in the two cavities will cause a fundamental mode static contrast defect  $\xi$ , approximately  $\xi \simeq 2\Delta\epsilon/T_i$ , where  $\epsilon$  is the round trip cavity loss and  $T_i$  is the ITM power transmissivity. Also, the cavity input mirrors may have mismatched reflectivities, which causes a cavity pole mismatch ( $\Delta\omega_c$ , also the finesse imbalance  $\Delta\mathcal{F}$ ). These asymmetries allow noise sidebands to couple to the dark port, since they experience slightly different filtering and thus no longer perfectly cancel at the asymmetric port. To first order, the differential arm cavity reflectivity is [52]

$$\Delta r_c = \frac{\xi}{1 + s_c} + \frac{2s_c}{(1 + s_c)^2} \frac{\Delta\mathcal{F}}{\mathcal{F}} + \frac{2i}{(1 + s_c)^2} \frac{\omega_0 \Delta L_-}{\omega_c L}. \quad (3.62)$$

### 3.8 Coupled Cavities

A short detour here will prove useful. We will consider the case of a three-mirror coupled cavity, such as the one depicted in figure 3.7. Of particular interest is the frequency response of such a cavity, considered in three distinct but interesting cases. In order to keep this discussion relevant to gravitational wave detectors, we will limit ourselves to the coupling of a long (arm) cavity with a short (recycling) cavity, where in each case the long (length  $L$ ) cavity is held at a length such as to be resonant with the laser carrier field (the primary optical frequency), and the mirror reflectivities are ordered such that  $r_r < r_i < r_e$ . We will continue to use a subscript  $c$  for the long cavity, while introducing a subscript  $r$  for the short cavity (the  $r$  is for ‘recycling,’ discussed in section 3.9).

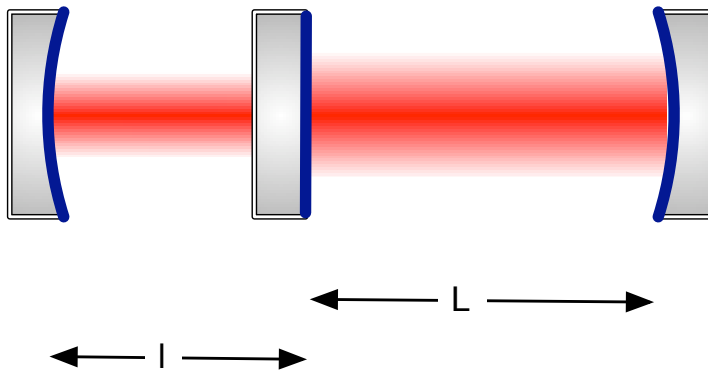


Figure 3.7: A three mirror coupled cavity

Replacing  $r_e$  with  $r_c$  in equation (3.38), we can write down the field in the recycling cavity,

$$E_r = E_{in} \frac{t_r}{1 - r_r r_c e^{2i\phi}}, \quad (3.63)$$

where  $\phi$  is the one-way phase in the recycling cavity. We note here that for the case of the overcoupled long cavity,  $r_c$  will have opposite sign to  $r_i$ .

The three cases, which encapsulate possible resonant conditions for the carrier in the short cavity, are discussed in the following sections.

### 3.8.1 Antiresonant Short Cavity

As depicted in figure 3.7, the recycling cavity is antiresonant when  $\phi = 0$  (because of our convention that the back surface of a mirror has negative reflectivity). Because on resonance for the arm cavity  $r_c$  is opposite in sign to  $r_i$  (thus  $r_c$  is positive), this actually represents the configuration with maximum power buildup in the recycling cavity, and thus also in the arm cavity (since the power in the short cavity is effectively the input power to the arm cavity). Thus, an anti-resonant recycling cavity means the coupled system has a greater finesse than the arm cavity, with a consequently lower bandwidth. This is the situation employed in the technique known as power recycling, described in section 3.9.1, and also in signal recycling, described in section 3.9.2.

With the help of equation (3.63) and [49], we can write down the frequency response of this coupled system with the updated definitions of the field amplitude gain,

$$g_r = \frac{t_r}{1 + r_r r_c}, \quad (3.64)$$

the coupled cavity pole,

$$\omega_{cc} = \frac{1 + r_r r_0}{1 + r_r} \omega_c, \quad (3.65)$$

and defining

$$s_{cc} = i \frac{\omega_a}{\omega_{cc}}, \quad (3.66)$$

we have the field in the recycling cavity:

$$E_{cc} = E_{in} g_r \frac{1 + s_c}{1 + s_{cc}}. \quad (3.67)$$

Note that these represent the transfer function from outside the recycling mirror to just inside the mirror. For an anti-resonant short cavity,  $s_{cc} < s_c$ , and this bandwidth reduction means that the coupled cavity acts as a low-pass filter on the light in excess of the filtering provided by the arm cavity alone, as shown in figure 3.8(a). The presence of  $s_c$  in the numerator represents a zero in this transfer function at the arm cavity pole frequency; physically, sidebands above this frequency are

no arm resonant in the arm cavity, and thus fall out of resonance in the recycling cavity as well since they do not experience a phase flip on reflection from the arm cavity. For a source field in the arm cavity, there is no zero at the arm cavity pole frequency; it would instead appear at the pole frequency of the short cavity.

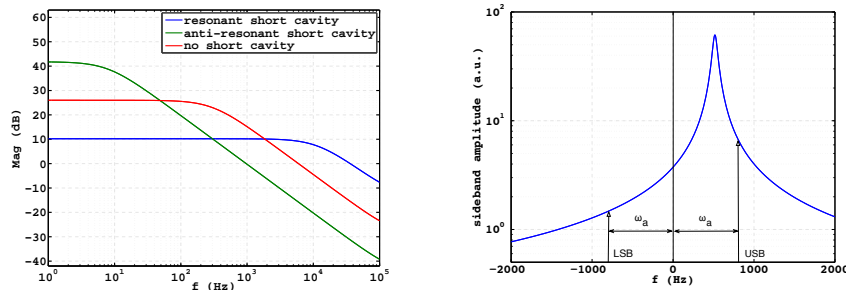
### 3.8.2 Resonant Short Cavity

In this case, the finesse of the coupled system is lowered, and so the bandwidth is higher than that of the arm cavity alone (cf. figure 3.8(a)). This is because, when viewed from the arm cavity, the reflectivity of the recycling cavity is lower than  $r_i$ , which lowers the overall finesse. This situation is useful in the technique known as resonant sideband extraction, described in section 3.10.

### 3.8.3 Detuned Short Cavity

A detuned cavity is neither resonant nor anti-resonant for the carrier, which implies that the system is resonant for some other frequency of light. Cavity detunings are typically specified as a carrier optical phase  $\phi$ , which specifies how far the cavity is from a carrier resonance. The specific details of the system (mirror reflectivities, cavity lengths) can then be used to determine the frequency at which the system will resonate; since that frequency will typically be shifted from the carrier by an audio frequency, such a system can be characterized as having an audio frequency optical resonance. What this means is that the response of the system can be tuned to have a maximal response to a certain audio frequency.

Figure 3.8(b) depicts a typical profile for a resonant system, with the frequency axis shifted such that the origin (the carrier frequency) is not at the center of the resonance. This represents the situation under discussion. When a phase modulation is produced by test mass motion at  $\omega_a$ , a pair of sidebands at  $\pm\omega_a$  appear. One of these sidebands will be closer to resonance than the other, and



(a) A short additional cavity can increase or (b) Detuning the short cavity affects upper decrease the system bandwidth, compared to and lower signal sideband amplitudes differ- no additional cavity. entially.

Figure 3.8: Effect of adding a third mirror with a short cavity on the bandwidth of the coupled system.

the total response of the system as a function of  $\omega_a$  will have a resonant peak in the response. We thus encounter the first delicate issue with detuning: sideband imbalance. In general, upper and lower signal sidebands will be imbalanced, and the RF sidebands used as local oscillators can also be imbalanced. One particular effect of this RF sideband imbalance is a reduction of cancellation efficiency for some noises on the sidebands, due to the differing amplitudes on the upper and lower sidebands.

There is another delicacy that we have neglected up to this point. We have been fortunate in being primarily concerned with cavities on resonance or anti-resonance, where  $\frac{dP}{dt} = 0$ ; this has allowed us to ignore the effects of radiation pressure, which in cavities detuned from resonance can affect the dynamics in significant ways.

The force due to radiation pressure is due to the momentum change of photons upon reflection from a mirror; it is given by the average number of photons per second striking a mass, times the momentum change experienced by each:

$$F = N \times 2 \frac{\hbar\omega}{c} = \frac{2P}{c}, \quad (3.68)$$

where  $P$  is the average power. If we take  $x$  to be the position of one of the cavity mirrors, we can define an effective spring factor,

$$\frac{dF}{dx} = \frac{2}{c} \frac{dP}{dx}, \quad (3.69)$$

which is the optical rigidity of a light beam in a cavity, and is frequency dependent. We can show heuristically why this matters by doing a rough estimate of this rigidity for a cavity with parameters relevant to LIGO: length 4 km, with 100 kW of circulating power, when held at the point of half-max-power (the maximum rigidity), for a system with a finesse of  $\sim 18000$ . The DC radiation force is  $\sim 600 \mu\text{N}$ , but the effective spring constant at DC is  $\frac{dF}{dx} \sim \frac{2}{c} \frac{PF}{\lambda} \rightarrow 10^7 \text{ N/m}$ . For comparison, the Young's modulus of diamond is 1220 GPa and so this light beam is about as stiff as an equivalent length of diamond rod with diameter 20 cm. If we attach a 10 kg mass, the system would have a resonant frequency of about 160 Hz. This cannot be ignored.

These two concerns, the sideband imbalance and the radiation pressure, are also related: at a given audio frequency  $\omega_a$ , the audio sidebands beat with the carrier field, resulting in a power fluctuation at  $\omega_a$ . This power fluctuation pushes on the mirror, creating further phase modulation at  $\omega_a$ . The optical fields and mirror positions are thus linked at all audio frequencies, and the upper and lower audio sidebands must be calculated together to correctly determine the radiation pressure force on the mirror. This complicates the derivation of frequency responses of coupled systems, because now, instead of just considering the fields in the interferometer at a single frequency, we must simultaneously consider two frequencies ( $\pm\omega_a$ ) and the mirrors; the resulting algebra becomes inconvenient enough that, for analytical work, it is simpler to work in the two-photon formalism

developed for quantum optics by Caves and Schumaker [53, 54]. This will be discussed more in section 3.11, and more details can also be found in appendix D.

### 3.9 Recycling

Consider the Michelson with Fabry-Pérot arm cavities (FPMI), when the Michelson is held on a dark fringe and the arm cavities are on resonance. Then from the symmetric side, the FPMI reflectivity is

$$r_{FPMI-sym} = r_{bs}^2 r_X e^{i2k\Delta l_x} + t_{bs}^2 r_Y e^{i2k\Delta l_y}, \quad (3.70)$$

where  $r_X$  and  $r_Y$  are the reflectivity of the X and Y arm cavities. From the asymmetric side it is

$$r_{FPMI-asym} = t_{bs}^2 r_X e^{i2k\Delta l_x} + r_{bs}^2 r_Y e^{i2k\Delta l_y}. \quad (3.71)$$

The arm cavity reflectivities are complex and frequency dependent, and so the FPMI reflectivity is also complex and frequency dependent. This situation is intentionally similar to the one outlined in section 3.8, where we considered the long cavity to behave as a complex mirror.

Treating the FPMI as a mirror, we can place another partially reflecting mirror on the symmetric side to form a cavity, a technique known as power recycling, because the primary effect is to increase the power incident on the Michelson, by recycling the light reflected from the FPMI.

If we place a mirror at the asymmetric side to form a cavity, it is called signal recycling. In this case, gravitational wave signal light *is transmitted* through the Michelson, and we reflect it back into the asymmetric mode, where it can constructively interfere with more signal light and build up resonantly.

#### 3.9.1 Power Recycling

Power-recycling topologies (sometimes referred to in the older literature as simply *recycling*) are shown in figures 3.2(b) and 3.9. We have now added another degree of freedom to this interferometer,  $l_r$ , which is the recycling cavity length (PRCL) and is defined as

$$l_r \equiv \frac{l_x + l_y}{2} + l_{pr}, \quad (3.72)$$

where  $l_{pr}$  is the distance between the power recycling mirror and the beamsplitter.  $l_r$  will be known as PRCL (Power Recycling Cavity Length).

We arrange the power recycling mirror so that the power recycling cavity is anti-resonant for the carrier, congruent to the situation described in section 3.8.1. This has several beneficial effects in

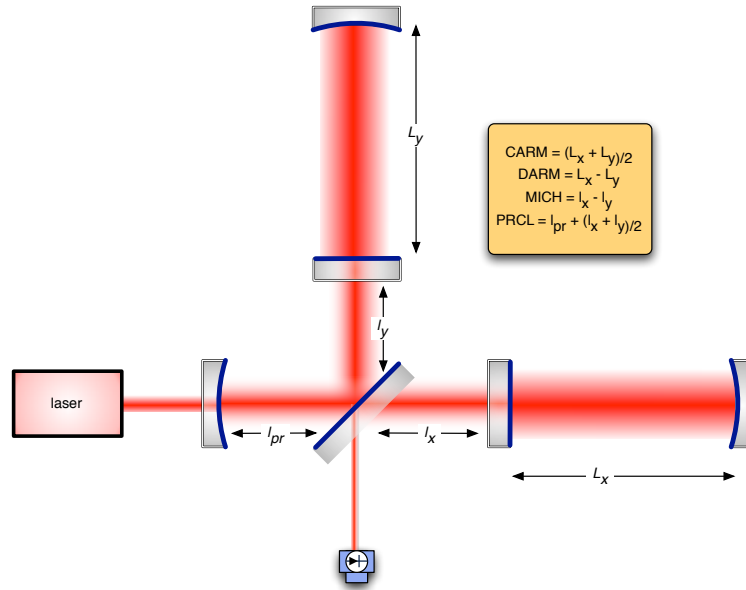


Figure 3.9: A Power Recycled Fabry-Pérot Michelson Interferometer.

our quest to increase the SNR. First, the power illuminating the Michelson increases, by the factor of the recycling gain:

$$G_r = g_r^2. \quad (3.73)$$

This yields an increase in signal gain and shot noise limited SNR. Second, the signal bandwidth in the symmetric mode is reduced (cf. equation (3.65)), while the signal bandwidth in the asymmetric mode remains unchanged (since the asymmetric mode is unaffected by the presence of a mirror on the symmetric side). This has the important effect of reducing susceptibility to laser noise. The laser noise sidebands appear on the symmetric side, and thus see the decreased bandwidth of the coupled cavity pole, which acts as a low pass filter. Gravitational wave signal sidebands in the asymmetric mode are filtered only by the arm cavities, and so this causes a net reduction in laser noise coupling. For Advanced LIGO, the corner frequency of this low-pass filter will be about 100 mHz, and so this is a significant advantage.

It would thus seem that the higher the recycling gain, the better, but that is not really the case. For a given interferometer size (cavity length), the DC strain signal transduction gain can be increased by increasing the power circulating in the arm cavities, which can be accomplished in three ways: (1) using a more powerful laser; (2) increasing the power recycling gain; (3) increasing the DC gain in the arm cavities. Each of these options has drawbacks.

Using a more powerful laser and increasing the recycling gain both increase power circulating in the central part of the interferometer, where it must pass through the substrates to which the mirrors are attached (specifically, the beamsplitter and the two input test masses). These substrates

will necessarily absorb some fraction of the laser power as heat. Since neither the absorption nor the laser power are uniform across the substrate, this will result in a temperature gradient in the substrate and an optical deformation given by the change in index of refraction with temperature ( $dn/dT$ ). This deformation will cause the substrate to behave as a lens, distorting the wavefronts in the interferometer in a manner detrimental to the sensitivity. There are possible technical solutions to mitigate this problem, including using a Thermal Compensation System [55] to add more heat to the substrate with an additional laser and thus even the thermal load, but it is better to simply avoid the problem if possible.

The third option, increasing the DC gain in the arm cavities, will reduce the bandwidth of the detector. It thus seems, that for a given amount of power in the arm cavities (and thus gain), we have to choose between high thermal loads at the beamsplitter, or a greatly reduced detector bandwidth (cf. figure 3.4). We can partially avoid both, however using resonant sideband extraction, discussed in section 3.10.

### 3.9.2 Signal Recycling

The technique known as *signal recycling*, studied by Meers [56], is a dual technique to power recycling that involves placing a partially reflecting mirror at the output port of the interferometer. An example of a signal recycled Michelson interferometer is shown in figure 3.2(c), and the usual form, which is a combination of signal and power recycling, is in figure 3.2(d). This additional mirror recycles the signal carrying light by sending it back into the interferometer to interfere constructively with the signal carrying light still circulating in the interferometer. When referring to *signal recycling*, we usually mean an anti-resonant short cavity; this is completely analogous to the power recycling discussed in section 3.9.1, but in the asymmetric mode rather than the symmetric mode. This amplifies the signal at low frequencies but reduces the bandwidth of the detector (cf. figure 3.8(a)). This bandwidth reduction, however, only increases the signal gain at low frequencies, where the sensitivity of interferometers is already limited by seismic noise and thermal noise. Since these are displacement noises (and not sensing noises), signal recycling does not yield any increase in SNR relative to these noises. For these reasons the signal recycling with anti-resonant short cavities are not considered further.

We have now added a fifth length degree of freedom,

$$l_s \equiv \frac{l_x + l_y}{2} + l_{sr}, \quad (3.74)$$

where  $l_{sr}$  is the distance from the SRM to the beamsplitter.  $l_s$  will be known as SRCL (Signal Recycling Cavity Length). A five degree-of-freedom, dual recycled Fabry-Pérot Michelson interferometer, is depicted in figure 3.10.

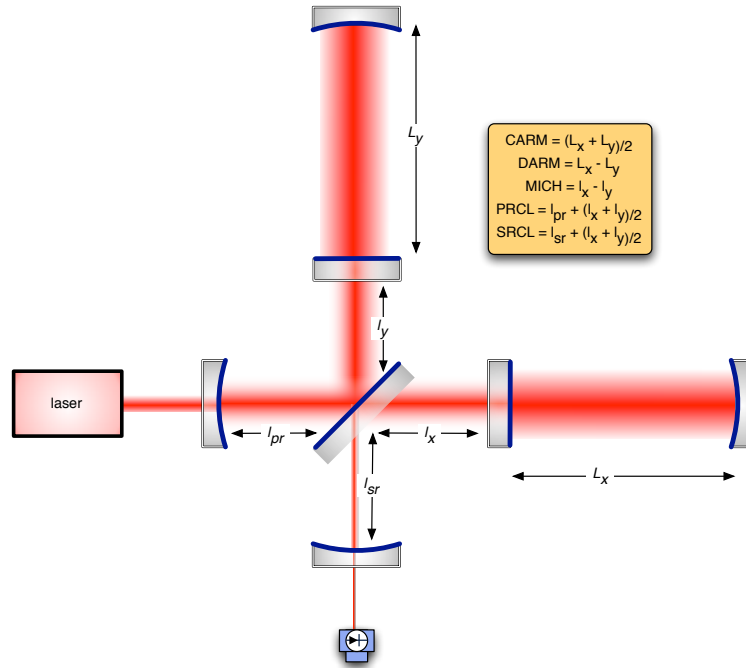


Figure 3.10: A Dual Recycled Fabry-Pérot Michelson Interferometer.

### 3.10 Resonant Sideband Extraction

A counterpart to signal recycling is resonant sideband extraction (RSE), first described by Mizuno [57], which also involves placing a partially reflecting mirror at the output port of the interferometer. This mirror is still (confusingly) called the signal recycling mirror (SRM), but is now placed such that the signal cavity is resonant for the carrier. As discussed in section 3.8.2, this increases the bandwidth of the asymmetric mode, at the cost of DC gain (cf. figure 3.8(a)). This technique is more useful than signal recycling however, because the increase in bandwidth yields an increase in SNR at high frequencies, where the limiting noise source is actually a sensing noise (shot noise) and not a displacement noise. More importantly, RSE allows us to decouple the relationship between the DC gain and the detector bandwidth expressed in equation (3.60) and figure 3.4, in a way that reduces the impact of another problem, that of thermal load in the central part of the interferometer (cf. section 3.9.1).

This situation, with a resonant short cavity and increased bandwidth, is called RSE in this thesis. Elsewhere, it is sometimes known as ‘broadband RSE’ or ‘tuned RSE.’ Furthermore, sometimes the signal recycling mirror (SRM) is called a ‘signal extraction mirror,’ and the cavity is the ‘signal extraction cavity.’ In this thesis we use the terms ‘signal recycling cavity’ and ‘signal cavity’ interchangeably.

### 3.11 Detuned RSE

A signal cavity which is neither resonant nor anti-resonant for the carrier is *detuned*. We will refer to any such detuning as a form of ‘detuned RSE’ (and never to ‘detuned signal recycling’).

The detuned RSE interferometer is significantly more complicated than any of the configurations considered to this point. In the configuration of LIGO (a power recycled Fabry-Pérot Michelson), only one parameter ( $r_i$ ) determined the detector bandwidth. In a detuned RSE interferometer, the concept of ‘detector bandwidth’ becomes less simple, as the resonant frequency is no longer DC; it makes more sense to talk about a frequency response. There are now (at least) three obvious parameters which affect the frequency response:  $r_i$ ,  $r_s$ , and the detuning phase  $\phi$ . These can be chosen to craft a frequency response (cf. figure 3.8(b)) which maximizes the detector response at a certain frequency; this would be useful for a targeted search (such as for a known pulsar).

Moreover, as discussed in section 3.8.3, radiation pressure effects must be considered, and upper and lower signal (or noise) sidebands must be computed together. These complications are not insurmountable, and it is possible to keep track of everything simultaneously (indeed, this is the approach taken in the numerical interferometer simulation software Optickle [58], appendix F). Nonetheless, as a short hand we will briefly describe enough of the two-photon formalism to enable us to write down the frequency response of a detuned RSE interferometer in a relatively simple manner.

#### 3.11.1 Two-Photon Formalism

The two-photon formalism [53, 54] rewrites the field due to two photons (one for each of the upper and lower sidebands) at frequencies  $\omega_0 \pm \omega_a$ ,

$$E = E_{\omega_a} e^{i\omega_a t} + E_{-\omega_a} e^{-i\omega_a t}, \quad (3.75)$$

as

$$E = E_1 \cos(\omega_a t) + E_2 \sin(\omega_a t), \quad (3.76)$$

where  $E_{1,2}$  are now the *quadrature field amplitudes*, and we have as usual suppressed the terms varying at the carrier frequency  $\omega_0$ . The two-photon formalism was created for quantum optics, but here we are using it for classical field amplitudes.

Each quadrature field amplitude is a complex number and contains partial information about

the upper and lower sideband amplitudes. These fields are related by

$$E_1 = \frac{E_{\omega_a} + E_{-\omega_a}^*}{\sqrt{2}}, \quad (3.77)$$

$$E_2 = \frac{-iE_{\omega_a} + iE_{-\omega_a}^*}{\sqrt{2}}. \quad (3.78)$$

The field  $E_1$  is known as the amplitude quadrature and the field  $E_2$  is known as the phase quadrature. Note that (cf. equation (3.26)) a phase modulation only appears in the phase quadrature, as should be expected.

A given pair of quadrature fields can be written as a vector,

$$\mathbf{E} = \begin{pmatrix} E_1 \\ E_2 \end{pmatrix}. \quad (3.79)$$

Switching to the frequency domain, we write the field in a given quadrature  $\zeta$  at  $\omega_a$  as

$$E_\zeta(\omega_a) = E_1(\omega_a) \sin \zeta + E_2(\omega_a) \cos \zeta, \quad (3.80)$$

which implicitly defines the meaning of  $\zeta$ .

For homodyne detection, the output of a photodetector at  $\omega_a$ ,

$$PD = \mathbf{E}_{\text{LO}} \cdot \mathbf{E}(\omega_a), \quad (3.81)$$

where the  $\cdot$  indicates an inner product. Alternatively, we can write

$$PD = E_{\text{LO}} E_\zeta(\omega_a), \quad (3.82)$$

when the local oscillator is in quadrature  $\zeta$ .

### 3.11.2 The RSE Response Function

For non-detuned interferometers (cf. sections 3.7, 3.9.1, 3.9.2), the detector response to gravitational waves (or displacement noise) at frequencies well below the arm cavity FSR can be characterized by a simple pole at the detector half-bandwidth; the detector behaves as a low-pass filter. For non-signal recycled interferometers, this bandwidth is determined only by the ITM reflectivity; for non-detuned signal recycled interferometers, it is the combination of the ITM and SRM reflectivities, along with the choice of resonant or anti-resonant signal cavity.

For a detuned interferometer, this is not the case, as the detuning creates an optical resonance, while the effect of radiation pressure creates an opto-mechanical resonance; this was first realized

in the papers [59, 60, 61]. There, the focus was on the effects of these features on the quantum-noise limited noise spectral density of the resulting configuration (more in appendix B); in this section we focus instead on the response, to be better able to control and calibrate the output of the interferometer.

Rearranging equation 2.20 of [61], we can write the RSE signal response function in quadrature  $\zeta$  as

$$E_\zeta = h * \frac{t_s e^{i\beta} [(1 - r_s e^{2i\beta}) \cos \zeta \cos \phi - (1 + r_s e^{2i\beta}) \sin \zeta \sin \phi]}{1 + r_s^2 e^{4i\beta} - 2r_s e^{2i\beta} [\cos 2\phi + \frac{\mathcal{K}}{2} \sin 2\phi]} \sqrt{2I_{bs} \frac{\omega_0^2}{(\omega_c^2 + \omega_a^2)}}, \quad (3.83)$$

where

$$\mathcal{K} = \frac{8I_{bs}}{mL^2} \frac{\omega_0}{\omega_a^2 (\omega_c^2 + \omega_a^2)}, \quad (3.84)$$

and  $\beta$  is the phase delay in the arm cavity  $\beta = -\arctan \frac{\omega_a}{\omega_c}$ . This response function can be seen to depend on  $\zeta$ ,  $I_{bs}$ ,  $r_s$ ,  $\phi$ , and  $\omega_c$ , where  $\omega_c$  of course depends on  $r_i$  and  $L$ . It should be noted that this function is not exact—it depends (as usual) on the condition  $\lambda_{gw} \ll L$ , but it also breaks down at the arm cavity free spectral range. Moreover, this expression of the function ignores the effect of the finite signal recycling cavity length, which is a tiny correction.

Figure 3.11 shows (in Bode form) a set of these response functions as the detuning phase  $\phi$  is varied from 0 to  $\pi/2$ , for the 40 m prototype parameters (cf. table 5.1) and figure 3.12 shows a set as the quadrature  $\zeta$  is varied. A MATLAB routine which implements equation (3.83) is in appendix F. Both the magnitude and phase of this function must be well understood in order to design appropriate control systems and to accurately calibrate the detector (more in chapter 7). In general, the response is characterized by two peaks: an optical resonance and an opto-mechanical resonance. The optical resonance is just the one described in section 3.8.3 and shown in figure 3.8(b): the coupled cavity system is detuned from a zero-frequency resonance. The opto-mechanical resonance arises from the radiation pressure restoring force, and is a form of optical spring. Table 3.1 describes roughly what aspects of the frequency response are affected by the parameters.

Parameter	Effect
$r_i$	frequency of both resonances
$r_s$	Q of optical resonance
$\phi$	frequency of both resonances
$I_{bs}$	Overall magnitude,
	frequency of opto-mechanical resonance
$\zeta$	‘tilts’ response about optical resonance
L (ARM)	frequency of optical resonance

Table 3.1: Approximate effect of parameters on the RSE response.

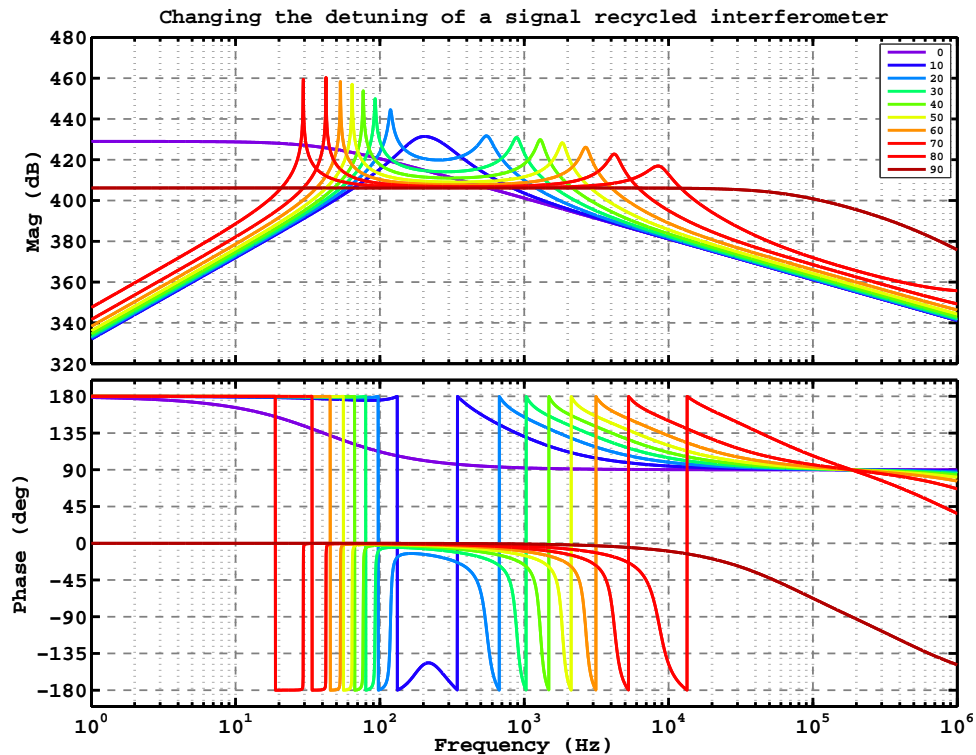


Figure 3.11: Changing the detuning of the signal cavity in a Fabry-Pérot Michelson Interferometer with a signal recycling mirror yields changing opto-mechanical response functions. As the signal recycling cavity goes from resonant for the carrier (brown) to anti-resonant for the carrier (violet), the bandwidth of the detector increases at a cost of overall gain. When the signal cavity is neither resonant nor anti-resonant for the carrier, a pair of resonances appear in the response—an optical spring and an optical resonance. The legend indicates the signal cavity detuning in degrees of carrier phase.

### 3.11.3 Detuned RSE Interferometers as Optical Springs

The fact that a detuned RSE interferometer would behave as an optical spring was first realized by Buonanno and Chen [60], although Braginsky et al. had previously developed the idea of an ‘optical bar’ detector [62].

The salient features of the spring are the resonant peak, which is always lower in frequency than the optical resonance, and the low frequency response, which is rising like  $f^2$ . This is a real effect, and it means that the interferometer responds very weakly to gravitational waves below the spring frequency. It also responds weakly to displacement noise, however, so this is not a real problem: terrestrial detectors are dominated by seismic noise at low frequencies in any case.

The springlike behavior was first demonstrated at the Caltech 40 m interferometer as part of the work for this thesis, and previously reported in [63]. Measurements are also shown figure 3.13 and figure 3.14.

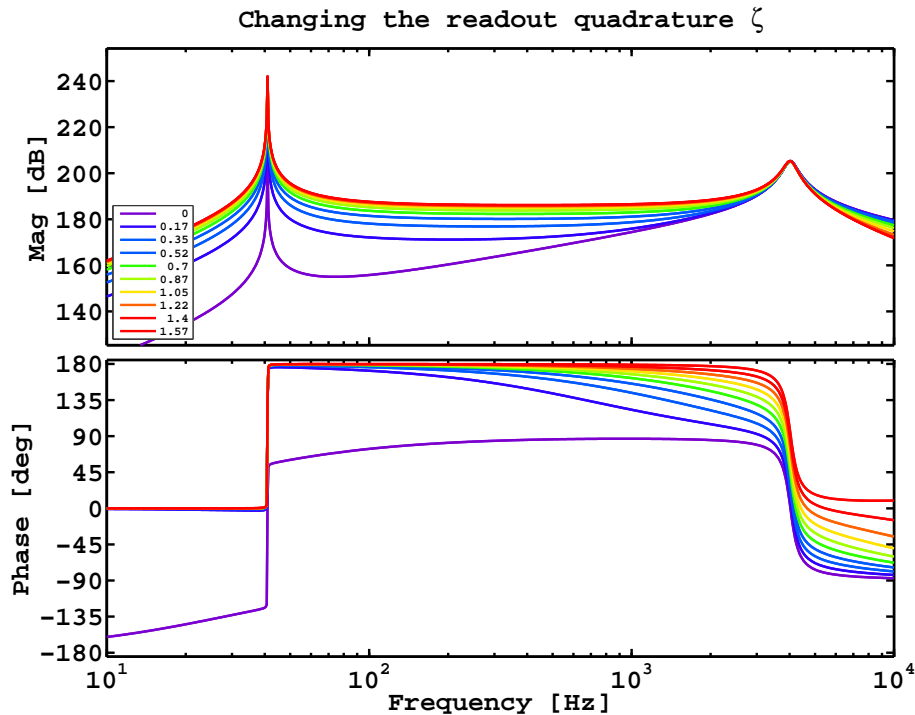


Figure 3.12: Frequency response in different readout quadratures. The legend indicates the readout quadrature in radians.

### 3.11.3.1 Dynamical Instability

The opto-mechanical resonance is a dynamically unstable resonance; perturbations grow with time rather than being naturally damped [60]. To quench the instability, we must introduce an appropriate control system [60], but this would be necessary in any case (more in section 3.12). The optical spring complicates the design of the control system, but not in any way that cannot be anticipated by careful examination of equation (3.83) and plots like figure 3.11. The RF sideband imbalance that results from detuning is a bigger controls problem (more in section 6.3.3).

### 3.11.3.2 Anti-spring

For values of  $\phi < 0$ , the radiation pressure force at DC is not restoring and there is no opto-mechanical resonance—this is called an anti-spring. The low frequency reduction in the response is still present, just as in the spring case; the difference is purely the absence of the resonant peak and the resulting smoother phase profile. One can imagine a situation where this detuning might actually be preferable: in the case where any dip in the noise spectrum would be completely obscured by a displacement noise (such as mirror thermal noise), operating in the anti-spring mode would provide the dual benefits of a simpler controls problem and not having a large peak in the raw (uncalibrated) noise spectrum, which would be the result of the mirror thermal noise exciting the opto-mechanical

resonance.

### 3.11.4 The Detuned Resonant Sideband Extraction Interferometer with Power Recycling

Combining detuned RSE and power recycling yields an interferometer with 5 length (longitudinal) degrees of freedom, and which is usually called a dual-recycled Fabry-Pérot Michelson interferometer (DRFPMI). Such a topology, which combines the benefits of power recycling with those of RSE, is shown in figure 3.10. This is the configuration of the Caltech 40 m prototype interferometer, which is described in chapter 5; it was also the baseline design for Advanced LIGO, but this is no longer the case, due in part to the prototyping effort at the 40 m (more in chapters 6 and 9).

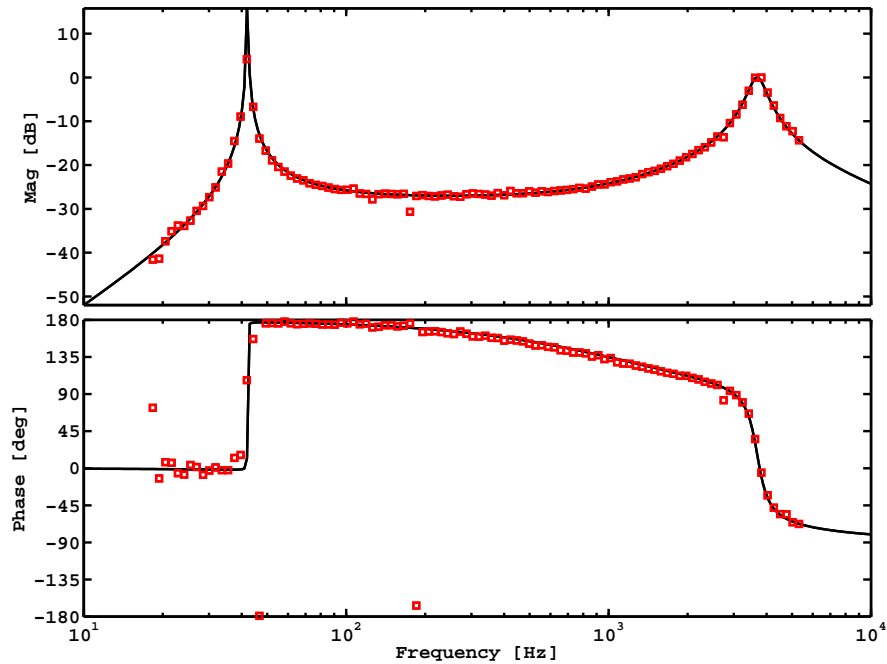


Figure 3.13: Measurement of the opto-mechanical RSE response. The magnitude has been scaled so the optical resonance is at 0 dB.

## 3.12 Feedback Control

For successful operation, the interferometers described in this chapter depend critically on the optical cavities being on resonance; considering the level of seismic disturbances present (which will cause the optics to move by more than a wavelength at low frequencies), this will not happen without an active control system. Thus, interferometric gravitational wave detectors typically operate as actively

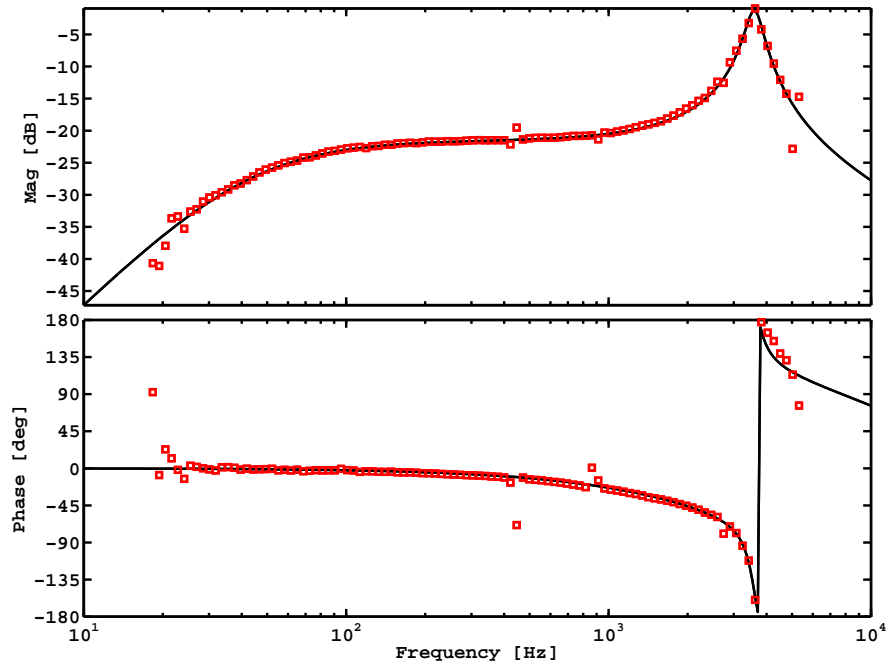


Figure 3.14: Measurement of the opto-mechanical RSE response in an anti-spring configuration. The magnitude has been scaled so the optical resonance is at 0 dB. The measurements at high frequencies (above 5kHz) and low frequencies (below 30Hz) generally have poor measurement coherence, due to large (unrelated) noise amplitudes at these frequencies. The disagreement at 440 Hz and 880 Hz are also from poor measurement coherence, due to known mechanical resonances.

nulled detectors, kept at the null point by a control system. This control system must sense the *deviation* of the degrees of freedom of the detector from their nominal operating points (information about this deviation is contained in the *error signals*) and apply the appropriate restoring forces to cancel these error signals. This technique is known as *feedback control*. An introduction to feedback is in appendix E, and a short description of a control system is in chapters 5 and 6.

It is important to keep in mind that the linear control systems (sometimes called *servos* or *servomechanisms*) we will use act to suppress the error signals; the degree to which the deviations themselves are canceled depends on the information contained in the error signals. Depending on the design, the error signals may not contain complete information about the deviations, or may include information not related to the deviations (more in section 6.3.5). In these cases, the control system will not perfectly cancel the deviations.

Feedback control in interferometric gravitational wave detectors serves two principal purposes: to reduce and mitigate the deleterious effects of noise, and to preserve the linearity of the gravitational wave transduction from strain to volts.

### 3.12.0.1 Noise reduction

The first, reduction of noise, concerns all aspects of the system which are auxiliary to the detection (seismic isolation, suspensions, interferometric DOFs other than DARM, angular DOFs, etc.). These noises can be coupled into DARM by various mechanisms, and they will mask a gravitational wave signal. The effect of these noises can be reduced by eliminating the source of noise, reducing the coupling of the noise to DARM, or suppressing the noise with feedback. Nearly all of the considerable infrastructure of LIGO is devoted to at least one of these three techniques. Sometimes the techniques are related—if the coupling of one noise source to DARM depends on a third degree of freedom, then applying feedback to that third degree of freedom can reduce the specified noise coupling.

### 3.12.0.2 Transduction linearity

The second, linearity of transduction, concerns the DARM degree of freedom which is sensitive to gravitational waves. Here, any noise that arises in DARM, from any source, will reduce the sensitivity to gravitational wave by mimicking a signal. A control system can apply feedback to DARM to suppress this noise, but this system can have no method of distinguishing between noise and signal. Even though the noise cannot be reduced at this stage, a control system for DARM still serves an important purpose because the signal transduction from DARM motion to volts is non-linear (cf. section 3.6.3, chapter 4). If the noise amplitudes are not sufficiently small, this nonlinearity will invalidate the linear methods which comprise the bulk of the signal processing techniques used to study the output of a gravitational wave detector. The goal of the DARM control system is thus to keep these disturbances small enough that linear spectral techniques can be applied. Thus, even though disturbances from seismic noise will probably prevent earth-based detectors from operating below 10Hz, a control system can be used to prevent such low-frequency noise from being non-linearly upconverted to higher frequencies, which would spoil a much larger frequency band.

Feedback control is a rich subject, which will not be explored in greater depth than necessary in this thesis. More complete introductory materials can be found in [64] and [65]. The concepts helpful for a complete understanding of the work done for this thesis include linear control, servo bandwidth, and servo stability, and are reviewed in appendix E.

## 3.13 The Advanced LIGO Design

Advanced LIGO is a next-generation interferometer, with upgraded subsystems relative to Initial and Enhanced LIGO.

**Dual-recycled configuration.** The interferometer will be a power and signal-recycled Michelson

interferometer with Fabry-Pérot arms, operable in multiple signal cavity detunings (including a zero detuning).

**Seismic isolation.** An active system with ground motion sensors, feedback and feedforward noise reduction, and hydraulic actuators both external to the vacuum envelope and within the vacuum envelope, will isolate the optical tables housing the core optics.

**Multiple pendulum suspensions.** The core optics of the interferometer will be suspended from a set of triple and quadruple pendulum systems, providing additional seismic isolation. These pendulums will be actively sensed and locally damped in all degrees of freedom. They will also provide a capability for global feedback control.

**High power laser.** A 180 watt CW 1064 nm laser will provide the single frequency light source for the interferometer, under stringent requirements for frequency and amplitude stability.

Each of these subsystems will be integral to the success of Advanced LIGO in achieving the designed sensitivity, and each subsystem will represent the state of the art. Table 3.2 shows the Advanced LIGO optical parameters as of this writing, along with several parameters from a previous reference design. These parameters were changed in part due to lessons learned during the work described in this thesis.

Parameter	Value	Previous Reference Design
$T_{ITM}$	0.014	0.005
$T_{ETM}$	5 ppm	10 ppm
$T_{PRM}$	0.03	0.07
$T_{SRM}$	0.20	0.07
$ROC_{ITM}$	1934 m	
$ROC_{ETM}$	2245 m	
L (ARM)	3994.5 m	
PRCL	57.656 m	8.4 m
SRCL	56.008 m	9.1 m
Schnupp asy	0.05 m	.42 m
$f_1$	9.1 MHz	9 MHz
$f_2$	45.5 MHz	180 MHz
PRC $\Phi_{Guoy}$	25°	
SRC $\Phi_{Guoy}$	19°	

Table 3.2: The primary Advanced LIGO optical parameters.

Figure 3.15 shows the projected sensitivity for several operating modes of Advanced LIGO; these various modes can be achieved by changing the detuning phase and the input power. The projected noise levels due to seismic noise and mirror coating thermal noise can be inferred from this plot: the most sensitive curves below 10 Hz are limited by seismic noise, and the most sensitive curve from 30 Hz to 300 Hz is limited by thermal noise. The variation in sensitivity, which allows optimization for specific astrophysical sources, is the primary motivation for adding a signal recycling mirror.

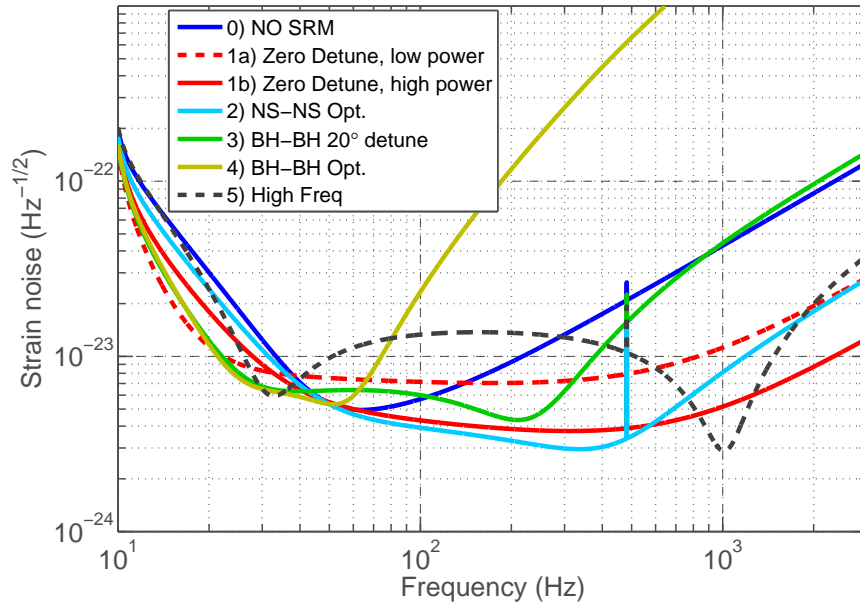


Figure 3.15: Projected sensitivity for possible operating modes of Advanced LIGO. The blue curve shows the sensitivity with no SRM. The other curves can all be achieved by changing a combination of the detuning phase and the input power. All the curves are limited by quantum (shot) noise at high frequency. The best low frequency sensitivity curve (zero detune, low power) is limited by seismic noise at low frequency, the others are limited by quantum (radiation pressure) noise. The NS-NS optimized curve is limited in the middle frequency band (30 Hz to 300 Hz) by mirror coating thermal noise. The different modes are optimized for various astrophysical targets (black hole binaries, neutron star binaries, etc.)

In the next chapter, we will discuss the choice between two methods of gravitational wave signal extraction.

## Chapter 4

# Gravitational Wave Signal Extraction

The techniques described in the previous chapter centered around three principle concerns:

**Shaping the gravitational wave signal frequency response** using the technique of signal recycling/RSE.

**Amplifying the GW transduction gain** by using resonant cavities to increase the amplitude of the circulating laser field which samples the metric.

**Reducing extraneous sources of noise** by carefully employing symmetries which reduce the influence of noise, especially laser noise.

These all work towards increasing the fidelity of the optical carrier phase with the strain (cf. equation (3.4)), with the additional possibility of emphasizing certain frequency bands. We now have to convert this optical phase to a measurable quantity, which is the subject of this chapter.

As discussed in section 3.5.1, there are two ways to convert an optical phase to a measurable signal (current or voltage) using a photodetector: heterodyne detection and homodyne detection. We now discuss these options in more detail as pertained to gravitational wave signal extraction, where the choice is between *RF readout* (heterodyne) and *DC readout* (homodyne), terms which refer only to the GW channel (DARM). Signal extraction for the other degrees-of-freedom (MICH, PRCL, SRCL, CARM) is by heterodyne detection, as it provides more options for non-degenerate sensing of these auxiliary DOFs [66].

For audio frequency gravitational waves incident on the interferometer, the gravitational wave signal takes the form of audio sidebands around the laser carrier light. We now need to detect these audio sidebands at the output port. The choice between RF readout and DC readout is just the choice of local oscillator used to downconvert those audio sidebands to an electronically tractable frequency.

## 4.1 RF Readout

In order to sense and control the length degrees-of-freedom of a complex interferometer, a sophisticated variant of the Pound-Drever-Hall technique (cf. section 3.6.3) is employed. This involves using a set of frontal (upstream of the interferometer) phase modulation sidebands on the laser carrier field. The carrier and modulation sidebands experience different resonant conditions in different subsections of the interferometer; this is the resonance profile (more in chapter 6). By optically heterodyning the fields exiting various ports of the interferometer, we can extract non-degenerate signals about the various length degrees of freedom [43, 67]. A detailed discussion of this technique for a power-recycled Fabry-Pérot Michelson interferometer is in [68]; an overview of a technique for a detuned RSE interferometer is in chapter 6. Since the length sensing and control system relies on heterodyne detection for all the auxiliary (non-DARM) degrees of freedom, it is convenient to use the same technique for DARM. This is what has been done in the first generation of detectors (LIGO, Virgo, TAMA, GEO600).

Figure 4.1 shows the fields at the asymmetric port, after demodulation. The rightmost portion of the phasor diagram is basically a picture of equation (3.30a) and equation (3.31a), with the fields represented by arrows. It is worth noting that the interpretation of the I-phase and Q-phase signals is reversed here from what was mentioned in section 3.5.1 (i.e., now the Q-phase signal gives the carrier optical phase, while the I-phase signal contains the sideband imbalance); this is a common convention for the asymmetric port. The left panel shows the resultant LO-field vectors after demodulation, for the two demodulation phases; the middle panel shows both carrier field vectors reflected from the arm cavities, which ideally should sum to zero at the asymmetric port. DARM motion counterrotates the two vectors, resulting in a vector field pointing along the horizontal axis. The third panel combines the two, showing how the I-phase signal is a combination of the carrier contrast defect (due to unequal reflectivities of the two arm cavities), while the Q-phase signal contains DARM motion.

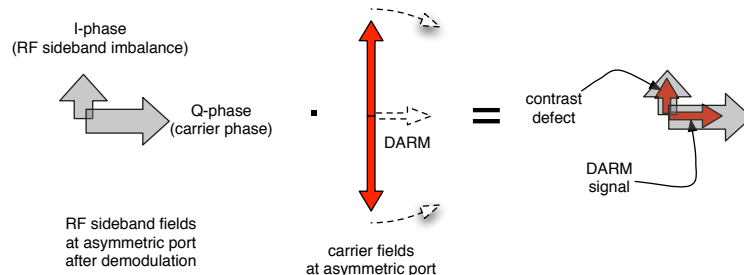


Figure 4.1: Phasor diagram of the asymmetric port in an RF readout scheme.

A common feature of heterodyne schemes is that the RF sidebands used as local oscillators for the DARM signal are transmitted to the asymmetric port using a Schnupp asymmetry (cf. section 3.5.1),

and these sidebands do not resonate in the arm cavities. This means that the RF sidebands do not undergo any significant filtering by  $s_c$  or  $s_{cc}$ , and any noise on the modulation sidebands (whether from the laser itself or the modulator) thus passes essentially unchanged to the detection port of the interferometer. Once there, amplitude and phase noise on the modulation sidebands can pollute the signal when these sidebands are used as a local oscillator (cf. equation (3.30c), also appendix C). These noisy sidebands are the principal drawback of RF readout.

## 4.2 DC Readout

A complementary technique for gravitational wave signal readout is to arrange the optics of the interferometer in such a way that the power present at the output port of the interferometer is directly proportional to gravitational wave strain. This technique is a form of optical homodyne detection known as DC readout, in which laser carrier light that has circulated in the interferometer serves as a local oscillator, rather than RF modulation sidebands. This makes sense for a kilometer-scale gravitational wave detector, where carrier light enters the kilometer-scale arm cavities and thus undergoes passive low-pass filtering by the interferometer (cf. equation (3.67), [49]). The laser light circulating in the interferometer is, literally, the quietest laser light in the world at the frequencies where the interferometer is most sensitive. It makes sense to use it as a local oscillator field if we can.

In its simplest form, DC readout involves intentionally causing a small offset ( $\sim 10^{-11}$  m) in the DARM degree of freedom, which slightly spoils the destructive interference at the asymmetric side of the beamsplitter. This causes a small amount of light ( $\sim 100$  mW for Advanced LIGO) that has circulated in the arm cavities to leak out the asymmetric port, where it can be used as a local oscillator. This is shown in figure 4.2, where it can be seen that the resultant local oscillator is actually formed from a combination of the fields caused by the carrier contrast defect (in the amplitude quadrature) and the intentional DARM offset (in the phase quadrature). The angle of this resultant field relative to the phase quadrature is the homodyne angle  $\zeta$ . For a non-detuned interferometer, gravitational wave signals always appear at  $\zeta = 0$ ; in a detuned interferometer, both signals and noises will appear in all homodyne angles with differing amplitudes, and so the choice of homodyne angle is more complicated, as different homodyne angles will give different frequency responses (cf. section 3.11).

## 4.3 Considerations

There are several things to consider in choosing between an RF and a DC readout scheme; each technique involves trade-offs of implementation complexity and noise susceptibility. Here we review

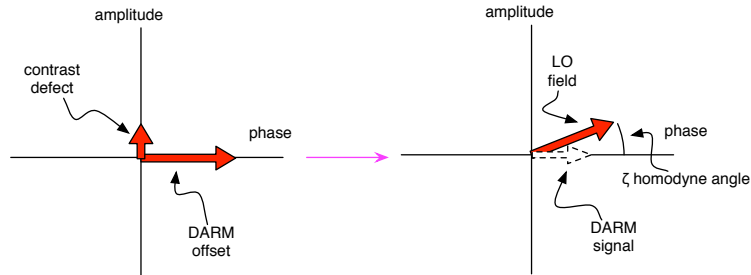


Figure 4.2: Phasor diagram of the asymmetric port in a DC readout scheme.

the major issues.

### 4.3.1 Laser Noise Couplings

Noise (amplitude or frequency) of the laser appears in both the input carrier field and the RF sidebands. The noise on the RF sidebands does not experience any significant filtering, and passes directly to the asymmetric port. The noise on the carrier is filtered in the interferometer, and couples to the asymmetric port through interferometer asymmetries (specifically, mismatches in the arm cavity parameters). In DC readout the carrier noise is, in principle, the only noise, while in RF readout there is additional noise from the RF sidebands that beats with static carrier fields at the asymmetric port.

Following [52], we write the Fourier components of the laser noise fields as the quadrature fields  $l_1$  and  $l_2$ ; at the input to the interferometer these are

$$\begin{aligned} l_1 &= \frac{E_{in}}{\sqrt{2}} \frac{\delta P}{2P}, \\ l_2 &= \frac{E_{in}}{\sqrt{2}} \frac{2\pi}{\omega_a} \delta\nu, \end{aligned} \tag{4.1}$$

where the laser RIN (relative intensity noise) is as usual  $\frac{\delta P}{P}$  and the laser frequency noise in Hz is  $\delta\nu$ .

Laser noises will couple to the asymmetric port through interferometer asymmetries. In particular we are concerned with the differential arm cavity reflectivity (cf. section 3.7 and equation (3.62)), but there is also a beamsplitter imbalance ( $\sigma = r_{bs}^2 - t_{bs}^2$ ) and a mass imbalance ( $\Delta m$ , generally negligible). Using the results from [42], we can write the fields due to laser noise at the *asymmetric*

side of the beamsplitter by combining equation (4.1) with equation (3.67) to get  $a_1$  and  $a_2$  [52]:

$$\begin{aligned}
a_1 &= -\frac{\pi\delta\nu}{\sqrt{2}\omega_a} \frac{2}{(1+s_{cc})(1+s_c)} \frac{\omega_0\Delta L_-}{\omega_c L} \\
&\quad + \frac{1}{4\sqrt{2}} \frac{\delta P}{P} \left\{ \frac{\xi}{1+s_{cc}} + \frac{2s_c}{(1+s_{cc})(1+s_c)} \frac{\Delta\mathcal{F}}{\mathcal{F}} \right\} \\
a_2 &= \frac{\pi\delta\nu}{\sqrt{2}\omega_a} \left\{ \frac{\xi}{1+s_{cc}} + \frac{2s_c}{(1+s_{cc})(1+s_c)} \frac{\Delta\mathcal{F}}{\mathcal{F}} \right\} \\
&\quad + \frac{1}{4\sqrt{2}} \frac{\delta P}{P} \frac{1}{(1+s_{cc})(1+s_c)} \left\{ \frac{2\omega_0\Delta L_-}{\omega_c L} \right. \\
&\quad \left. + \mathcal{K}(1+s_c)^2 \times \left[ \sigma + \frac{\Delta\omega_c/\omega_c}{(1+s_c)^2} + \frac{\Delta m}{2m} \right] \right\}.
\end{aligned} \tag{4.2}$$

Note that we have normalized these noise fields by the static field amplitude on the symmetric side of the beamsplitter ( $g_{pr}E_{in}$ ).  $a_1$  and  $a_2$  are the laser noise fields around the carrier. Also note that this equation does not include the effect of radiation pressure noise due to frequency noise, which will appear when the arm cavities are differentially detuned (as they will be for DC readout). This effect can be significant when the circulating power is very large.

Examining equation (4.2), we can see that noise in the amplitude quadrature includes frequency noise coupling through the DARM offset, and intensity noise coupling through the contrast defect and the finesse imbalance. In the phase quadrature, frequency noise couples through the contrast defect and finesse imbalance, while intensity noise couples through the DARM offset and the beamsplitter, cavity pole, and mass imbalances. The latter three coupling terms are the ‘technical radiation pressure’ noise. We can see that all the noise terms are filtered by the coupled cavity pole ( $s_{cc}$ ). The intentional DARM offset in a DC readout state can increase the laser carrier noise couplings, and so a detailed study must be done to determine which is actually better for any given case. In general, for kilometer-scale detectors DC readout will have a net lower laser noise coupling, as the filtering due to the coupled cavity pole will bring this noise level below that caused by the RF sidebands. An analysis of laser noise couplings in RF/DC readout schemes [52] is reviewed in appendix C, and measurements using a prototype interferometer are in chapter 9. Specific coupling mechanisms are also described in chapter 9.

In a signal recycled interferometer, the noises in equation (4.2) are partially reflected by the SRM into the interferometer anti-symmetric mode. This further complicates the frequency response (details are in appendix C), but it suffices to say that in a detuned interferometer, all the noises, with all the couplings, will appear in all quadratures. The noise transfer functions will be quadrature dependent (much like the GW signal transfer function, equation (3.83)), and so the total laser noise coupling will be quadrature dependent (more in appendix C).

### 4.3.2 Spatial Overlap

The spatial overlap refers to the mode-matching between the carrier field and the local oscillator field. In RF readout the RF local oscillator may not have perfect overlap with the signal field emitted from the arms, which will reduce the signal gain. In addition, the part of the local oscillator field which extends beyond the signal field also contributes shot noise without increasing the signal. There are thus significant gains in overall SNR to be realized from improving the overlap. In DC readout, as both the local oscillator and the signal are coming from the same place (i.e., the arm cavities of the interferometer), they are in the same transverse spatial mode and thus have perfect spatial overlap at the photodetector. The spatial overlap can be improved with an output mode cleaning filter cavity, called an *output mode cleaner*.

### 4.3.3 Output Mode Cleaner

The spatial overlap, and resulting shot noise limited SNR, can be improved with the use of a filter cavity at the output of the interferometer, designed to reject any light that is not either the local oscillator field or the signal carrier field. This is the output mode cleaner (OMC). Specifically, such cavities are most useful for their rejection of ‘junk light,’ which is all the spatial HOM content of the field of the asymmetric port, at any frequency.

In RF readout, such a cavity would resonate both the carrier and the RF sidebands; this can be accomplished by either building a cavity such that  $\Omega_m \lesssim \omega_c$  or  $\Omega_m = \omega_{FSR}$ . For DC readout, in addition to rejecting junk light, the OMC must also reject the RF sidebands.

The output mode cleaner must be coupled to the interferometer’s output port, adding another layer of complexity; it thus can introduce new sources of noise.

#### 4.3.3.1 OMC noise mechanisms

The OMC needs to be:

- Resonant with the carrier light.
- Mode matched to the carrier field in the arms.
- Aligned to the carrier field in the arms.

Any static deviation from these conditions will lead to a decrease in signal amplitude. Small dynamic deviations (e.g., at frequency  $f_n$ ) will generate noise in the output signal, with a coupling level determined by the static deviation. Large dynamic deviations are obviously unacceptable. Thus, the OMC length and the alignment of the OMC to the interferometer must be actively controlled. An example of an OMC control system is described in section 5.9.1.

The actual noise couplings from the OMC will of course depend on whether DC or RF readout is used. In DC readout, the formulae in chapter 3 can be simply applied; it is, after all, just a cavity and there is only one transmitted power. The linear noise arising from the deviation of a generic quantity  $\alpha$  (which represents the deviation from nominal of either length or alignment) is given by

$$N = \frac{dP}{d\alpha} \delta\alpha. \quad (4.3)$$

Any sensible OMC design will have

$$\left. \frac{dP}{d\alpha} \right|_{\alpha=0} = 0 \quad (4.4)$$

for all the noise mechanisms, so the coupling will be second order in the noise.

In RF readout, the transmission of the RF sidebands must also be considered, along with differential effects — this complicates noise coupling mechanisms. A review of the couplings in RF readout is in [69] and [70].

### 4.3.4 Oscillator Noise

In an RF readout scheme, the electronic oscillators used to apply phase modulations are not perfect. In principle, this noise should not be a problem, since it appears at both modulation and demodulation; in reality noise on these oscillators (in both amplitude and phase) will couple to the output signal, sometimes in devious ways.

The coupling mechanisms will be different for RF and DC readout. In both cases, however, these noises can create sensing noise in the auxiliary degrees-of-freedom (especially MICH), since the signal extraction for these degrees-of-freedom is by heterodyne detection. The control system can impose this sensing noise on that auxiliary DOF, causing additional noise in the gravitational wave channel. Since this control-loop based path is the result of a sensing noise, it can be cancelled (or at least substantially reduced) through the use of feedforward loop correction (more in section 6.4.2).

#### 4.3.4.1 Oscillator amplitude noise

In DC readout the first order coupling is actually laser intensity noise, since changing the modulation depth  $\Gamma$  also changes the carrier field strength which goes as  $J_0$  (cf. equation (3.24)). The laser amplitude noise is related to the oscillator amplitude noise by:

$$\frac{\delta J_0}{J_0} \simeq -\frac{\Gamma^2}{2J_0} \frac{\delta\Gamma}{\Gamma}. \quad (4.5)$$

This noise can also couple via leakage through the OMC, and via auxiliary degree-of-freedom control systems; the last is the dominant term, as we will see in chapter 9.

In RF readout, oscillator amplitude noise places amplitude noise on the RF sidebands. It also

places noise on the electronic local oscillators, but these are ideally at sufficient strength to saturate the electronic mixers, so it should have no effect there. Thus, this noise should appear primarily as a gain modulation of the signal in RF readout, in addition to the laser intensity noise term described above.

#### 4.3.4.2 Oscillator phase noise

In principle, oscillator phase noise should cancel, since it appears at both modulation and demodulation, unless there is a significant time of flight difference between the optical and electronic paths. It does not cancel in real interferometers. The main difference in the paths is due to the filtering of the input mode cleaner (cf. chapter 5), but this did not actually explain the coupling level first seen in Initial LIGO, which proved to be a limiting noise source in the third science run. One explanation given in [71] is that RF sideband HOMs can undergo significant filtering in the interferometer since they have different resonance conditions than the RF sideband fundamental mode (cf. equation (3.54)), which is designed to be nearly anti-resonant in the arm cavity. This filtering in the optical path means the noise will not be cancelled at demodulation.

This mechanism makes a general analysis difficult, since it depends in detail on the HOM content of the input beam and the resonance profiles of those modes in the interferometer; both of these will depend strongly on interferometer imperfections, and can vary substantially with small changes (by small, we mean changes that appear to have a tiny/no effect on the sensitivity if only the fundamental mode is considered). As a result, this noise coupling has turned out to be basically unpredictable; the best solution so far has been to use oscillators with very low phase noise (from Wenzel Associates, Inc.).

In DC readout, this noise can couple via the OMC, which for off-resonant fields will act like a phase to amplitude converter, and also via auxiliary degree-of-freedom control systems. The latter coupling is dominant, as we will see in chapter 9.

#### 4.3.5 Flicker Noise

The well-known  $1/f$  (or flicker) noise that effects electronics at low frequency is one argument against DC readout, since it will directly appear as noise in the measured photocurrent. However, given the DC readout local oscillator power in Advanced LIGO ( $\sim 100$  mW), it will not be difficult to design a photodetector circuit where  $1/f$  noise will not be limiting.

#### 4.3.6 Unsuppressed Signal

In RF readout, at the asymmetric port only one RF quadrature (confusingly called the Q-phase in this particular case) is sensitive to gravitational waves; the I-phase signal is sensitive to quantities not

normally directly controlled (it is a product of the carrier contrast defect and sideband imbalance) and thus has no control system to suppress it. This means that there is an RF photocurrent that grows with the optical gain; eventually it will cause some electronics in the photodetector to saturate or otherwise behave non-linearly. To circumvent this, the output field must be split among many photodetectors. Such an unsuppressed signal is not present in DC readout. Note that while this so-called ASI signal was a significant problem in initial LIGO, where the RF sideband imbalance was unintentional, it will only get worse in a detuned interferometer.

### 4.3.7 Shot Noise

The shot noise limited SNR in homodyne detection is better than standard heterodyne detection [72]. Classically, this is due to cyclostationary noise; quantum mechanically, it is due to additional vacuum fields at  $\omega_0 \pm 2\Omega_m$ , which beat against the RF sideband fields at  $\omega_0 \pm \Omega_m$ . The net result is that the shot noise limited SNR in heterodyne readout will be worse than homodyne by a factor of at least  $\sim 1.22$ .

### 4.3.8 Signal Linearity

In DC readout, the signal is non-linear to a greater extent than in RF readout. This places stricter limits on the low-frequency noise tolerance than an RF readout system, to prevent non-linear up-conversion.

## 4.4 Decision

The decision of which readout technique to use must include all of these factors. Neither option is perfect, but DC readout has been chosen as the baseline for Advanced LIGO. The lower shot noise level of DC readout is a strong motivating factor—the major drawbacks of DC readout are technical limitations arising from noise mechanisms in the output mode cleaner, but the LIGO lab has a good history of taking on technical challenges. In any case, in Advanced LIGO an output mode cleaner would probably have been necessary for RF readout as well, so the better shot noise limited sensitivity, reduced laser noise couplings (for long-baseline interferometers), and reduced oscillator noise couplings, sway the decision in favor of DC readout.

DC readout was also chosen for the intermediate upgrade to LIGO, Enhanced LIGO [35]. A first prototype system was developed at the 40 m (cf. chapters 5 and 9), and system in Enhanced LIGO improved on the 40 m design. The system in Enhanced LIGO has been reasonably successful, with the expected increase in optical gain due to the spatial overlap, reduction in shot noise, and elimination of ASI problems; it has not been without drawbacks, however. The interferometers

have been less stable than in Initial LIGO, and the output mode cleaner system (particularly the angular controls) has proved more difficult (noisy) than expected. The Enhanced LIGO system has served as a noise prototype for the Advanced LIGO DC readout system, a critical step in developing low noise techniques.

## Chapter 5

# The Caltech 40 m Prototype Interferometer

This chapter gives a brief overview of the 40 m interferometer, which is the apparatus used for the experiments and measurements described in chapters 6, 7, 8, and 9.

### 5.1 Prototyping

The Caltech 40 m interferometer is a test bed interferometer for prototyping upgrades to the LIGO interferometers. It is a fully instrumented engineering and controls prototype, with an emphasis on global control and systems integration. Generally, advanced subsystems (such as the Advanced LIGO seismic isolation systems) are not tested at the 40 m; the 40 m, however, is the only prototype with some version (in some instances rudimentary) of all the subsystems of a large scale interferometric gravitational wave detector. The primary mission of the 40 m is to function as a controls and configuration prototype; the 40 m is *not* a noise prototype. Achieving fundamental noise limited sensitivity is simply not the primary goal, and so great effort is not put into actually reducing noise.

A gravitational wave interferometer is a complicated system, with many independent servo loops (the 40 m has more than 60). At the 40 m, these servo loops can be broadly classed into local control systems (such as local damping for the suspended optics) or global systems, such as Interferometer Sensing and Control (ISC). ISC is further decomposed into Length Sensing and Control (LSC), and Angular Sensing and Control (ASC). Currently, the primary mission of the 40 m is to study the Length Sensing and Control scheme for Advanced LIGO. The optical parameters for the 40 m, which determine the optical response, are given in table 5.1. These parameters (including the mirror reflectivities) are different from the current Advanced LIGO parameters (cf. table 3.2); this is because the Advanced LIGO design has been changed, in part as a result of lessons learned at the 40 m while studying the previous reference design in table 3.2.

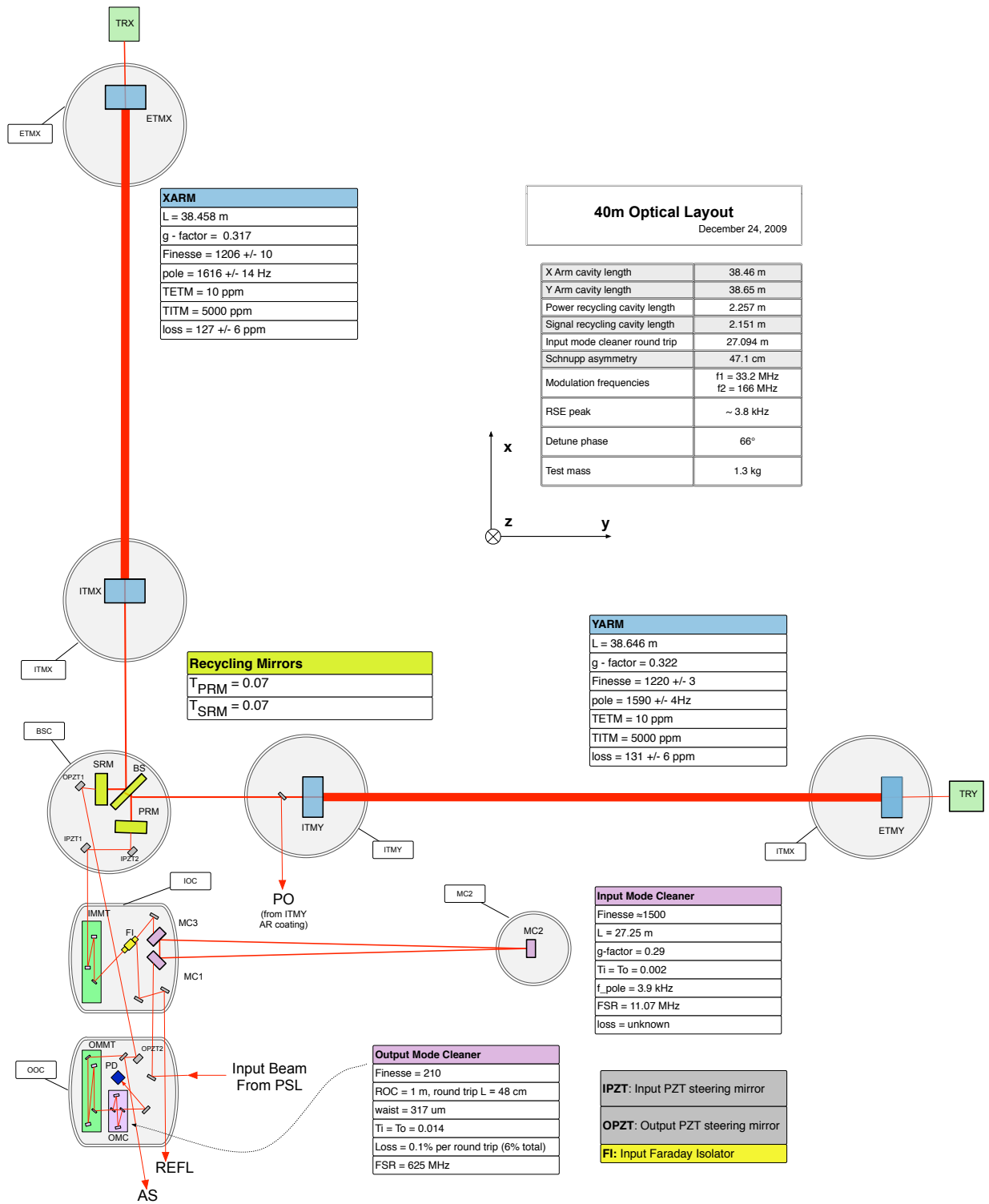


Figure 5.1: The layout of the 40 m.

Parameter	Value
$T_{ITM}$	0.005
$T_{ETM}$	10 ppm
$T_{PRM}$	0.07
$T_{SRM}$	0.07
$ROC_{ITM}$	> 4000 m
$ROC_{H-ETMX}$	$55.8957 \pm 0.0045$ m
$ROC_{V-ETMX}$	$56.7937 \pm 0.0038$ m
$ROC_{H-ETMY}$	$56.1620 \pm 0.0013$ m
$ROC_{V-ETMY}$	$57.3395 \pm 0.0011$ m
$ROC_{PRM}$	348 m
$ROC_{SRM}$	365 m
L (XARM)	$38.4583 \pm 0.0001$ m
L (YARM)	$38.6462 \pm 0.0003$ m
PRCL	2.257 m
SRCL	2.151 m
Schnupp asy	0.451 m
$f_1$	33.2 MHz
$f_2$	166.0 MHz
$\phi$	$\pm 67^\circ$

Table 5.1: The primary 40 m optical parameters.

## 5.2 Vacuum and Seismic Isolation

The 40 m facility has an L-shaped vacuum envelope with a total volume of approximately 35,000 liters and, naturally, 40 m long beam tubes. The internal pressure at normal operating conditions is about  $10^{-6}$  torr with a single maglev turbo pump. The 5 main optic chambers have internal, passive, multi-layer spring and mass (the springs are viton) seismic isolation stacks which are designed to provide an overall reduction of seismic noise above  $\sim 40$  Hz by  $f^{-8}$  [73]. These are three-leg, four-stage stacks topped with 1" bread-boarded optical tables. The remaining two chambers have single-leg, four-stage stacks topped with optical tables.

## 5.3 Suspensions

The 40 m has ten suspended optics, each a single pendulum stage suspended by a single loop of steel wire. Six of these optics (the three mode cleaner optics and the BS, PRM, and SRM) are LIGO small optic suspensions (SOS), and the four test masses are medium optic suspensions (MOS). Nominal

Object	Quantity	Size
beam tube (arms)	2	40 m L $\times$ 61 cm D
beam splitter chamber	5	124 cm D $\times$ 155 cm H
chamber	2	61 $\times$ 76 $\times$ 137 cm
beam tube (MC)	1	371" L $\times$ 8" D + 141" L $\times$ 10" D
chamber (MC2)	1	28" D $\times$ 36" H

Table 5.2: The 40 m vacuum chambers.

properties of these suspensions are summarized in table 5.3; figure 5.2 is a picture of an MOS.

Each optic has (at least) five cylindrical magnets attached: four to the rear face, plus another on the side. These magnets are paired with coil-current actuators and also function as flags in a shadow sensor. The combined coil and shadow sensor is called an OSEM (Optical Sensor and Electromagnetic Actuator); the OSEMs are fixed to the suspension cage. The five actuators allow the optic to be sensed and controlled in longitudinal (perpendicular to the optic face) position, pitch, yaw, and side (pendulum motion parallel to the optic face).

All suspensions are equipped with active local damping systems that also permit global interferometer control, both in position and alignment. The local damping damps only the pendulum resonance, with a bandwidth of  $\sim 2$  Hz, to reduce the effect of noise in the shadow sensor above this frequency from being imposed onto the optic motion by the control system. The suspension is controlled by the Digital Suspension Controller (DSC), which will be described in section 5.4.

## 5.4 Electronics and Digital Controls

As a fully instrumented systems engineering prototype for Advanced LIGO, the 40 m prototype facility is equipped with a digital control system nearly identical to that in use in the LIGO facilities. The LIGO system is described in [74] and the 40 m system in this section.

A set of  $\gtrsim 30$  computers is used to provide local and global controls and data acquisition for the detector. These computers are divided into two networks: the fast, real-time controls network, which communicates via a fiber based reflective memory network (RFM); and an asynchronous, slower monitoring network, which runs on the Experimental Physics and Industrial Controls System (EPICS [75]) and which communicates via Ethernet. EPICS also provides a user interface for the controls; an EPICS control screen (using MEDM) is shown in figure 5.5.

The digital signal processing is carried out by generic computers (most of which are in a VME form factor) running a real time operating system (either RTLinux or VxWorks) and LIGO Lab designed controls code. The various systems run at sampling rates of 2048, 16384, and 32768 Hz.

Figure 5.3 depicts a portion of the real-time controls network. Shown are a Digital Suspension

Parameter	SOS	MOS
optic diameter	75 mm	125 mm
optic thickness	25 mm	50 mm
mass	0.23 kg	1.3 kg
$f_{pos}$	1 Hz	0.8 Hz
$f_{pitch}$	0.744 Hz	0.5 Hz
$f_{yaw}$	0.856 Hz	0.6 Hz
$f_{bounce}$	16.7 Hz	11.6 Hz

Table 5.3: Nominal SOS and MOS parameters.

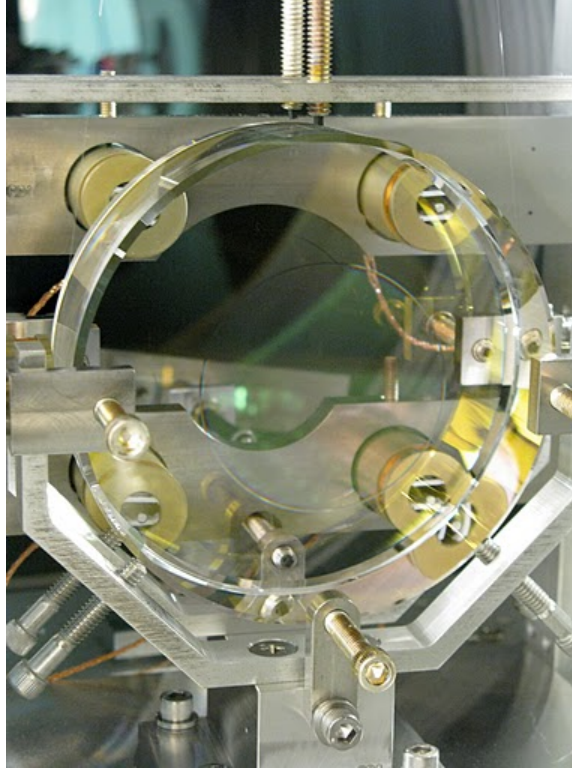


Figure 5.2: A MOS suspension. Visible are the optic, the OSEMs (behind the optic) and the suspending steel wire (a single loop, barely visible as a glint near the top of the photo). The various bolts pointing toward the optic are earthquake stops.

Controller (DSC), which is responsible for control of one or more suspended optics, the Length Sensing and Control computer, and the OMC controls computer. In this diagram, DARM signals are acquired in two places: the RF DARM signal is acquired by the LSC, and the DC readout signal (the OMC transmitted power) is acquired by the OMC computer. The OMC computer then transmits this signal via a fiber network, it is filtered in the LSC computer, and the control signal is sent to the digital suspension controller via fiber. The DSC then converts the signal to analog, and a force is applied to the optic.

The digital control system used for the DC readout chain (consisting primarily of OMC length and alignment controls) is of the type projected for use in Advanced LIGO, running at 32768 Hz. This machine is a PCIX architecture rather than VME.

## 5.5 Pre-Stabilized Laser

### 5.5.1 MOPA

The main laser is a Lightwave electronics 10 watt CW, 1064 nm Nd:YAG laser in a MOPA (Master Oscillator Power Amplifier) configuration. The master oscillator is a non-planar ring oscillator

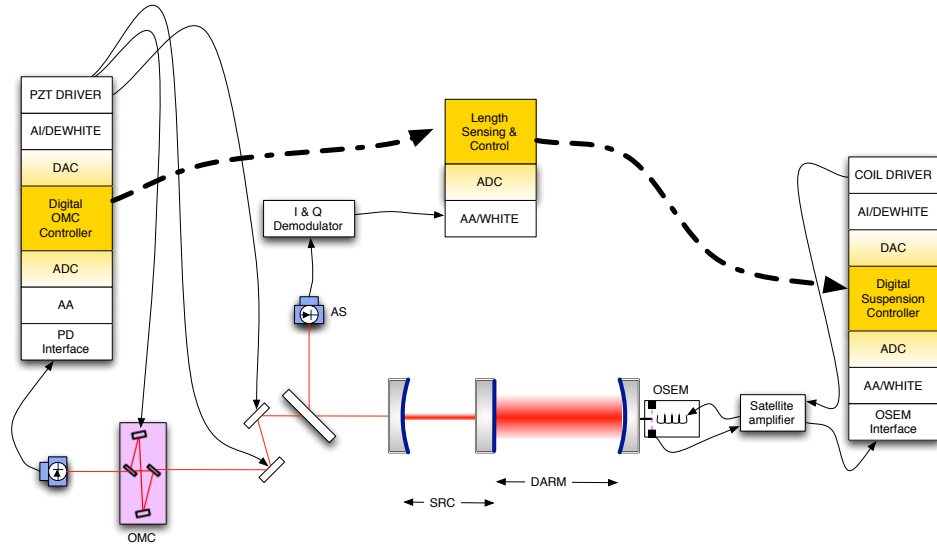


Figure 5.3: A simplified real-time digital control network diagram. The solid lines indicate analog signals, while the dashed lines indicate digital communication via the reflective memory network. Digital elements are yellow, analog elements are white, and the interfaces (ADC/DAC) are blended.

(NPRO), pumped by diodes emitting at 808 nm. The NPRO emits a single mode, linearly polarized Gaussian beam at 500 mW, which is double passed through four diode pumped amplifying rods in the power amplifier. Attached to NPRO are a Peltier device which provides a slow, large dynamic range frequency actuation ( $5 \text{ GHz/V}$ ,  $\lesssim 0.1 \text{ Hz}$ ) and a PZT which provides a faster actuation ( $5 \text{ MHz/V}$ ,  $\lesssim 100 \text{ kHz}$ ). The MOPA in the 40 m is currently operating at 2.7 W of output power, due to age related deterioration (most likely the PA pump diodes failing).

### 5.5.2 Power Stabilization

The laser power is stabilized by a system called the Intensity Stabilization Servo (ISS), which senses the power and feeds back via current-shunt that modulates the current supplying power to the pump diodes in the MOPA power amplifier. The bandwidth of this system is  $\sim 60 \text{ kHz}$ .

### 5.5.3 Frequency Stabilization

The laser frequency is stabilized by a hierarchical system of servos, including the Frequency Stabilization System (FSS), the mode cleaner servo (MC), and the common mode servo (CM). This system is shown schematically in figure 5.4. The FSS stabilizes the laser frequency to a frequency reference cavity (RC,  $\mathcal{F} \sim 9500$ ) a standard PDH setup, with the primary actuator being a Pockels cell (PC) at the output of the MOPA, up to a bandwidth of 250 kHz (although the system is designed for 500kHz). The PC has a limited range, so the loop also actuates on the PZT attached to the NPRO crystal, which provides the primary actuation below a few kHz. Finally, a perl script adjusts

the NPRO crystal temperature to prevent the PZT drive from saturating.

As shown in figure 5.4, a frequency shifting device (a double passed acousto-optic modulator) shifts the frequency of the beam going toward the reference cavity, with the shift frequency supplied by a voltage-controlled oscillator (VCO). Without any applied voltage the VCO oscillates at 80 MHz, and so the laser light entering the reference cavity is actually shifted in frequency from that of the main laser field by 160 MHz. By applying a voltage to the VCO the laser frequency can be shifted while the RC stays exactly on resonance. The FSS can then be used as a frequency actuator, limited by the FSS bandwidth, and with a range determined by the limits of the VCO ( $\pm 7$  MHz) rather than the linewidth of the RC ( $\sim 76$  kHz).

#### 5.5.4 Pre-Mode Cleaner

A triangular mode cleaning cavity with a fixed glass spacer serves to reduce the higher-order-mode content of the beam, and also passively filters noise out of the beam above the cavity pole, which is approximately 450 kHz. The main purpose of this cavity is to reduce laser noise at the frequencies where RF sidebands will be applied for interferometer sensing and control (cf. section 5.6.1).

## 5.6 Input Optics

### 5.6.1 Phase Modulations

A pair of New Focus model 4003 electro-optic modulators (EOMs) are used to apply phase modulation sidebands to the laser light for use in interferometer sensing and control. These phase modulation sidebands are used as local oscillator fields in the variants of PDH sensing used for global interferometer length sensing and control (more in chapter 6). The electrical signals used to drive the Pockels cells come from a set of IFR2023A signal generators which are kept in phase using the 10 MHz output of one as an external clock for the others. Two sets of RF sidebands are applied for the LSC, called  $f_1$  (at 33.2 MHz) and  $f_2$  (at 166 MHz). There are three more IFR2023A generators, which are used to provide modulations at 29.5 MHz (for the input mode cleaner, more in section 5.6.2) and at  $f_2+f_1$  (199 MHz) and  $f_2-f_1$  (133 MHz). The last two signals are used as electronic local oscillators for a heterodyne scheme; there are no RF sidebands at those frequencies.

#### 5.6.1.1 A Mach-Zehnder interferometer for non-cascaded RF sidebands

The length sensing and control scheme for the 40 m (described in chapter 6) depends on sensing the optical beats between different sets of RF sidebands (i.e.,  $f_1$  and  $f_2$ ); such signals are called *double demodulation* signals (DDM). DDM signals can be mixed down to the audio band (cf. section 3.5.1) by mixing sequentially at  $f_1$  and  $f_2$ , or by mixing at  $f_2+f_1$  and  $f_2-f_1$ .

Applying two phase modulations in series yields sidebands on the sidebands. This second set of sidebands appears, relative to the carrier frequency, at the difference frequency between the two sidebands. These sidebands-on-sidebands corrupt the purity of the DDM signals, causing them to be heavily influenced by carrier light, and thus less useful in isolating the short degrees of freedom from motion in the long degrees of freedom [76]. To avoid this, the phase modulation sidebands are applied in parallel, in the arms of a Mach-Zehnder interferometer. This means the RF sidebands are not true phase modulations (cf. equation (3.26)), as the carrier field is recombined at the output of the Mach-Zehnder but not the phase modulation sidebands. The resulting ‘modulation depth’ is a factor of 2 lower at the output of the MZ than in the arm. The resulting spectrum of light, which is injected into the mode cleaner, (next section) is cartooned in figure 6.1(a).

### 5.6.2 Input Mode Cleaner

The beam exiting the PSL is injected into the vacuum and passed through a suspended, triangular mode cleaning cavity. The mode cleaner cavity parameters are shown in figure 5.1.

The input mode cleaner serves two purposes: (1) it passively stabilizes the beam above the cavity pole frequency; (2) it provides further higher-order-mode suppression beyond that of the PMC; (3) it provides a quieter frequency reference than the RC above  $\sim 100$  Hz.

The mode cleaner servo stabilizes the mode cleaner to match the laser frequency below 100 Hz, by applying a force to the MC2 mirror. Above 100 Hz, the MC length error signal is fed back to the VCO in the PSL, thus stabilizing the laser frequency by matching it to the mode cleaner length (cf. figure 5.4). The bandwidth of the mode cleaner servo is  $\sim 60$  kHz.

The mode cleaner macroscopic length is roughly matched to the RF modulation frequencies, so that the RF sidebands fall on a free-spectral range of the mode cleaner and can thus be transmitted to the interferometer. The exact RF frequencies (down to  $\sim 5$  Hz) are then set to be exactly resonant in the mode cleaner, the precise length of which is measured using a technique similar to the one described in [77].

### 5.6.3 Input Isolation, Mode Matching, and Steering

The beam exiting the MC is passed through a Faraday Isolator (FI) and then through a fixed mode matching telescope which expands the beam to match the mode in the arm cavities. The beam is then reflected off two PZT actuated tip-tilt steering mirrors which provide input pointing to the interferometers. These PZT steering mirrors have in principle a useful actuation bandwidth up to  $\sim 800$  Hz; a series of mechanical resonances in the 1–10 kHz regime limit their utility above this frequency.

## 5.7 The Common Mode Servo

The Common Mode Servo is the final stage of frequency stabilization in the 40 m interferometer. It stabilizes the laser frequency to the symmetric mode of the interferometer, which includes the arm common mode (CARM) and the power recycling cavity (PRCL). During interferometer operation, this is the primary actuation for the CARM DOF. Figure 5.4 shows a block diagram of the common mode servo topology. The hierarchical nature of the system can be seen graphically in the nesting of the faster systems within the slower. Each nested box appears as a frequency actuator to the enclosing system, within the bandwidth of the nested system.

The common mode servo uses a PDH signal from the interferometer in reflection, and feeds the error signal to the input mode cleaner via two paths: a slower, digital path which actuates on the mode cleaner length (the MCL path), and a faster analog path called the AO path which *adds an offset* to the mode cleaner servo error signal. The result of the full servo is that at all frequencies where the servo has significant gain, the laser frequency is matched to the symmetric mode of the interferometer. At frequencies below  $\sim 100$  Hz, the laser light is also resonant in the mode cleaner. Above this frequency, the laser light can actually be slightly off resonant in the mode cleaner, but by an amount which is small compared to the mode cleaner linewidth of 8 kHz.

The bandwidths achieved at the 40 m are  $\sim 250$  kHz for the FSS, 60kHz for the MC, and 20kHz for the Common Mode servos. The high bandwidth of the common mode servo will be exploited during lock acquisition, discussed in chapter 8.

## 5.8 Interferometer

The interferometer is a detuned resonant sideband extraction interferometer with power-recycling. The interferometer has seven suspended optics, with five length degrees of freedom (cf. figure 3.10). The physical layout of the interferometer, including the arrangement of suspended optics on seismic stacks, is in figure 5.1. The optical parameters are in table 5.1.

## 5.9 Output Optics

The output optics of an interferometer are designed to direct the signal carrying light exiting the asymmetric port to the photodetector. For a DC readout system, these optics will ideally also reject any light that does not carry signal ('junk' light and the RF sidebands). The output optics described here are installed in the 40 m vacuum system to reduce seismic and acoustic noise. This system functioned as a prototype of the DC readout system in Enhanced LIGO. The DC readout sensing chain receives 60% of the light exiting the output port of the interferometer; the remaining

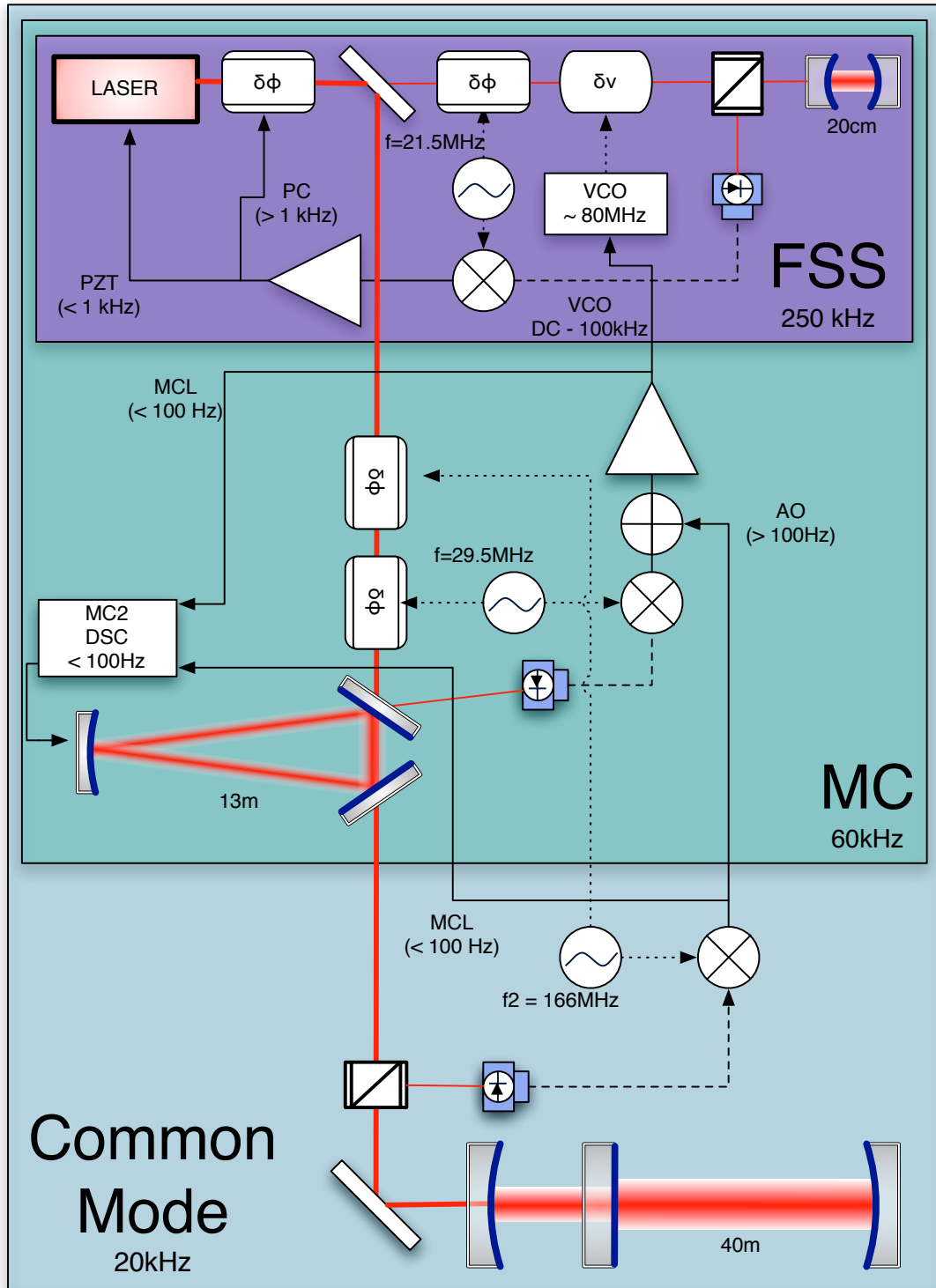


Figure 5.4: The laser frequency stabilization system.

40% immediately exits the vacuum and is sent to a traditional RF readout sensing chain to be used for lock acquisition, signal extraction of auxiliary degrees of freedom, and DC/RF comparisons.

### 5.9.1 Output Mode Cleaner

We use a monolithic, four-mirror bowtie shaped resonant cavity as a mode cleaning cavity for the output port of the interferometer. This output mode cleaner (OMC) serves to reject the RF modulation sidebands and ‘junk light’ exiting the output port of the interferometer, both of which contribute noise but not signal. The key parameters of the OMC are in table 5.4. The OMC power transmission (of light not rejected) is 94%; the remainder is lost intracavity.

#### 5.9.1.1 OMC Length Sensing and Control

The output mode cleaner is kept on resonance with the interferometer carrier light via PZT length actuation; one mirror of the cavity is bonded to a  $100\text{V}/\mu\text{m}$  PZT stack, which provides the necessary dynamic range (greater than one FSR) to ensure that the cavity can be locked. To sense the OMC length, the PZT is dithered at a frequency outside of the gravitational wave detection band (in this case, 12 kHz) and demodulated coherently. The dither signal and demodulation are done with a ‘digital lock-in’ system in the real-time digital controls system. The servo bandwidth is about 100 Hz.

### 5.9.2 Output Steering

The angular degrees of freedom of the OMC (beam tilt and displacement relative to the mode of interferometer) are controlled by a pair of PZT actuated steering mirrors situated between the output port of the interferometer and the OMC; sensing of these degrees of freedom is also via dithering. Limitations on the actuators (i.e., mechanical resonances) require that this dithering remain in the detection band, at 3–4 kHz for the four degrees of freedom. The two loops which stabilize the beam angle (near field) have bandwidth of  $\sim 20$  Hz, while the loops which stabilize the position (far field) have bandwidth below 1 Hz.

### 5.9.3 Output Mode Matching

There is a mode-matching telescope between the last PZT steering mirror and the OMC. This is a 4:1 beam reducing telescope designed to match the beam circulating in the interferometer (with a waist at the ITM) to the cavity mode of the OMC. The curved mirrors have radii  $\text{ROC1} = 618.4$  mm and  $\text{ROC2} = 150$  mm.

The mode matching is at least 95%. This is determined by measuring the OMC visibility in a bright-fringe Michelson with Fabry-Pérot arms, which is 92%. This configuration is a good estimate

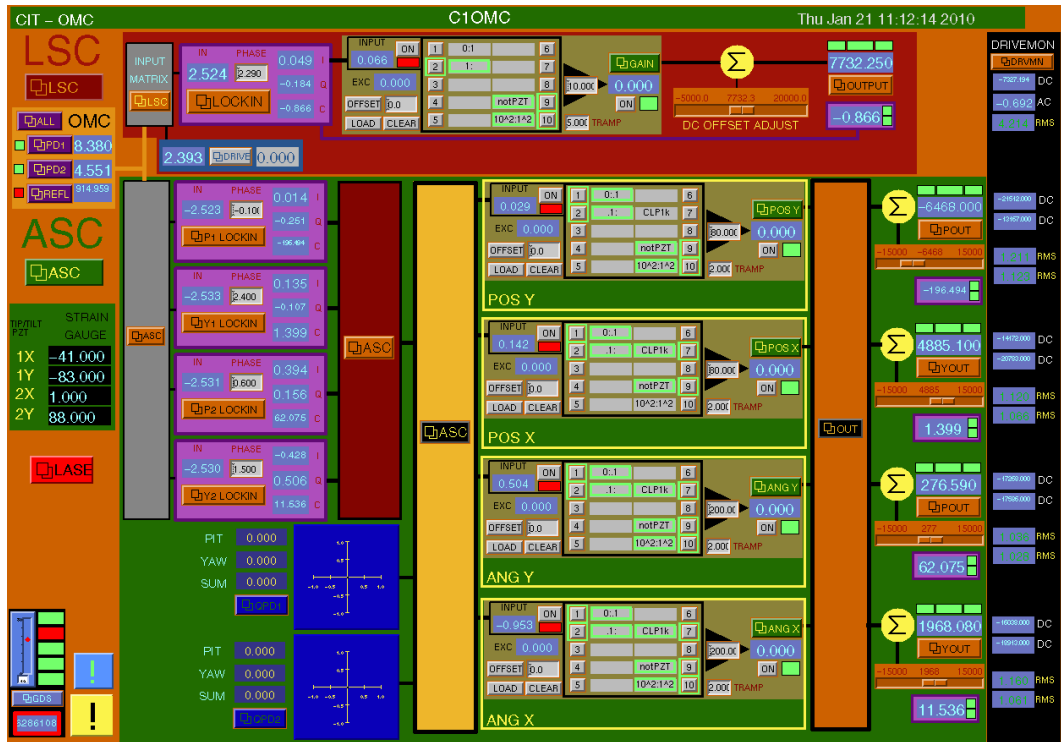


Figure 5.5: An MEDM (EPICS) screen for the output mode cleaner control system. Visible are depictions of the feedback filters for OMC LSC and ASC, several monitors, and the ‘digital lock-in’ detectors used to generate and demodulate the dither signals used for sensing and control of the OMC degrees of freedom.

Parameter	Value
length	48 cm
mirrors	4
g-factor	0.72
$w_0$	370 $\mu\text{m}$
FSR	625 MHz
$\mathcal{F}$	210
$T_{input}$	0.014
$T_{output}$	0.014
$ROC_{small}$	1 m
PZT	8.3 nm/V, $\sim 2 \mu\text{m}$ Range
loss	0.1% per round trip
spacer material	Cu
$f_{dither}$	12 kHz
$ G_L  = 1$	$\sim 100$ Hz

Table 5.4: Output mode cleaner parameters.

of the signal carrying mode: since the arm cavities are overcoupled, the reflected beam consists mostly of a leakage field from the arms. The recombination of the two beams in the Michelson then approximates the signal carrying mode. About 3% of the power in this beam is contained in RF sidebands which are promptly reflected by the arms and transmitted by the Michelson, so this establishes the lower bound on the mode matching.

#### 5.9.4 Higher Order Mode Content at Asymmetric Port

Both the RF and DC readout signals can be adversely affected by higher order mode content at the asymmetric port. Figure 5.6 is the result of using the OMC as a mode analyzer, with the interferometer locked in a detuned RSE configuration.

#### 5.9.5 Photodetectors

Light transmitted through the OMC is directed to a pair of photodetectors; the photodiodes are 2 mm InGaAs diodes, with the InGaAs surface exposed (no glass). They are reverse voltage biased and wired in series with  $250\ \Omega$  wire wound resistors which function as current-to-voltage converters; this signal is then amplified/whitened by an op-amp filter stage in a non-inverting configuration. A load resistor is used as the transimpedance stage rather than an op-amp so the op-amp will not have to source the full amount of the photocurrent; while this is not a major concern for the 40 m, it may be for Enhanced and Advanced LIGO. The photodiodes, series resistors, and amplification electronics are all housed in the vacuum, with the electronics housed in a separate vacuum nipple that was filled with Krypton gas for leak detection (it did leak).

The amplified photodetector signal is transmitted differentially through a vacuum feedthrough, further amplified, and acquired digitally for use in the digital control system and measurement of transfer functions.

### 5.10 The Future

The 40 m is currently undergoing a significant upgrade, to do a detailed test of the LSC scheme designed for the Advanced LIGO design in section 3.13. This involves the complete replacement of the real-time digital controls (just the computers and ADC/DACs, not the signal conditioning electronics), the procurement of new core optics (and some new suspensions), and the procurement of lock acquisition dedicated hardware (more in chapter 8).

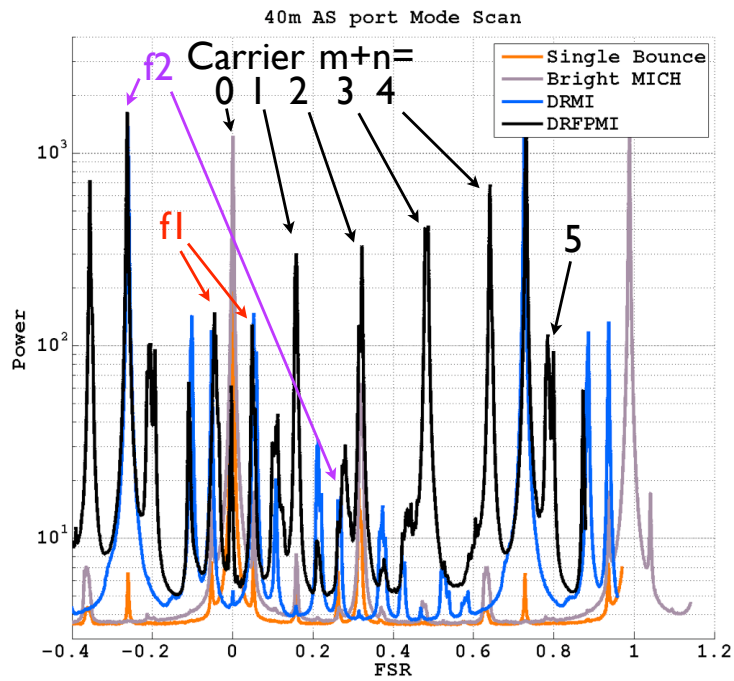


Figure 5.6: Mode scans of the AS port, using the OMC as a mode analyser. There is significant higher order mode content, which changes with interferometer alignment and with the thermal state. This is why we have an output mode cleaner.

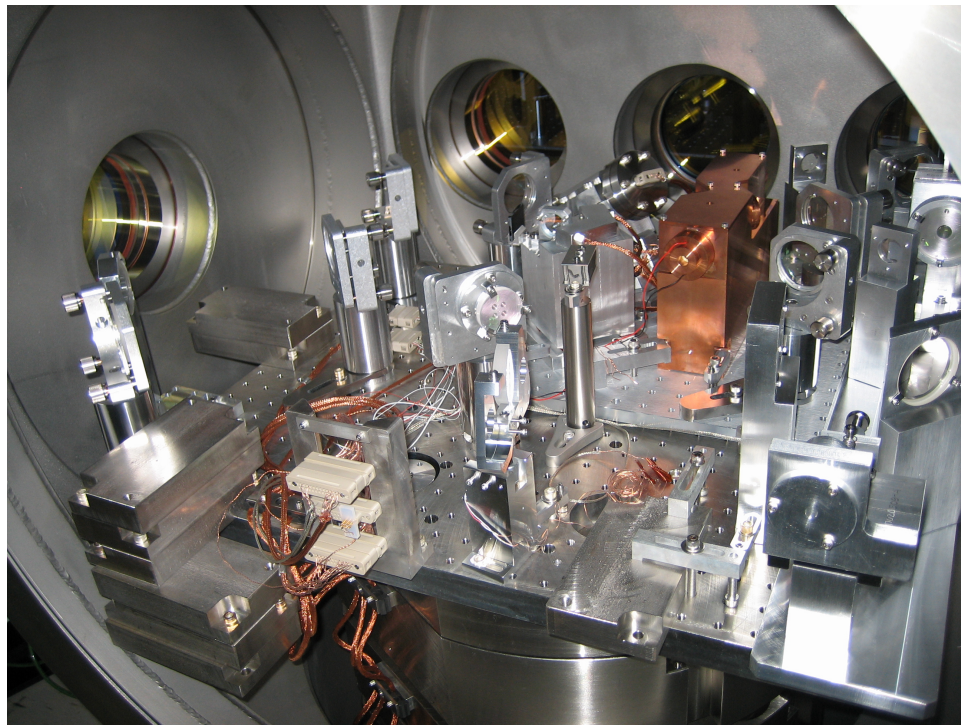


Figure 5.7: The DC readout sensing chain. Visible on the table are one PZT steering mirror, the mode matching telescope, the output mode cleaner (made of copper to damp vibrational modes), the DC photodetectors and other optics.

## Chapter 6

# The Length Sensing and Control Scheme

Without length measurement, interferometers are useless as gravitational wave detectors, and so the specific techniques used for length sensing and control (LSC) are a critical aspect of interferometry. Chapter 3 covered the motivations for using an interferometer with complex, coupled resonant systems; chapter 4 described the two rival techniques for sensing the gravitational wave channel. This chapter completes the picture by describing how to sense the other longitudinal degrees of freedom, and how we control all of them, focusing on the specific LSC scheme of the 40 m (already described in chapter 5).

### 6.1 Principle

Length sensing and control schemes rely on illuminating the interferometer with multiple frequencies of light; these different frequencies experience different resonant conditions in the interferometer, in what is called the resonance profile. By choosing appropriate demodulation frequencies, phases, and ports, one can extract non-degenerate information about the length DOFs in an interferometer. The signals are all variants of PDH signals (cf. section 3.6.3), and so are fundamentally non-linear in the optic positions, but we will focus on the small motion, linear regime centered around the operating point of the interferometer. How the interferometer is brought to the operating point is called lock acquisition, and is the subject of chapter 8. Calibration of the output signals is the subject of chapter 7 (which focuses on the DARM degree of freedom).

The initial LIGO LSC scheme is described in depth in [43] and [68]. It has a relatively simple philosophy, with a carrier field plus a single set of phase modulation sidebands incident on the interferometer. The carrier field is resonant everywhere (technically, it is anti-resonant in the PRC alone), the RF sidebands are resonant in the PRC, and the Schnupp asymmetry is set to allow a partial leakage of the RF sidebands to the asymmetric port.

The LSC configuration of the 40 m is designed to test a potential configuration for Advanced LIGO, in particular a detuned RSE interferometer. This needs to be more sophisticated, in particular for sensing the SRCL degree of freedom. Since the asymmetric port should be on (or near) the dark fringe for the carrier, sensing SRCL requires that a RF sideband be resonant (or nearly so) in the SRC; in order to discriminate between motion of SRCL, PRCL, and MICH usually requires at least two RF sideband frequencies. The 40 m scheme employs a pair of non-cascaded, frontal, RF, phase modulation sidebands to provide a suitably non-degenerate sensing matrix. The carrier plus two pairs of non-cascaded phase modulation sidebands can be represented as five frequencies of light incident on the interferometer (cf. figure 6.1(a)). The resonance profile of these five frequencies can be seen in figure 6.1(b) and is described in section 6.2. The error signals and frequency response are described in section 6.3. The controls are described in section 6.4.

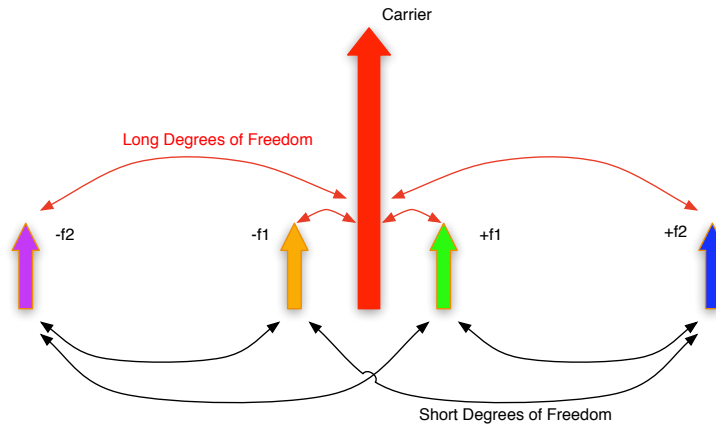
This scheme has also been briefly described in [78], [79], and [80]. Design principles for LSC schemes in dual recycled interferometers are discussed in [66], and bench-top demonstrations of specific schemes are reported in [81], [67], and [82]. This is the first demonstration of such a scheme in a suspended interferometer, and the first that has dealt with the effects of radiation pressure modifying interferometer dynamics.

## 6.2 Resonance Profile

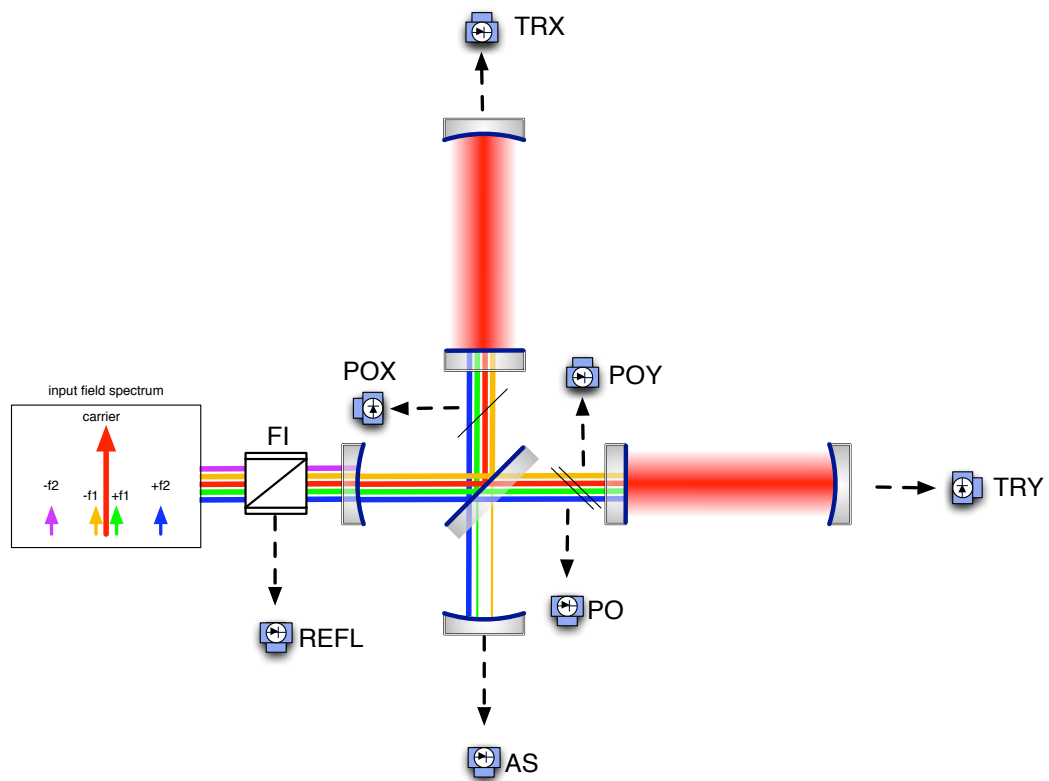
The RF sideband frequencies and the macroscopic cavity lengths are chosen to meet the following conditions, when the interferometer is at its operating point:

- The RF sidebands do not resonate in the arm cavities.
- The  $f_1$  (33 MHz) sidebands resonate in the power recycling cavity.
- The  $f_2$  (166 MHz) sidebands transmit the Michelson (Schnupp length).
- One  $f_2$  sideband resonates in the combined PRC + SRC.

These conditions are depicted in figure 6.1(b). The power recycling cavity macroscopic length is chosen so that when the carrier is anti-resonant, the  $f_1$  sidebands are resonant. The signal recycling cavity macroscopic length is chosen so that when the cavity is held at the desired carrier detuning, the  $+f_2$  sideband is resonant (but not the  $-f_2$  sideband). This sideband imbalance is a natural consequence of a detuned cavity. The  $f_1$  sidebands also have some Michelson transmittance; this causes them to also be somewhat imbalanced, a situation which can lead to offsets in demodulated error signals.



(a) The frequency spectrum of input laser light with the double demodulation philosophy.



(b) DC resonance profile in the 40 m detuned RSE interferometer and the location of signal ports.

Figure 6.1: The length sensing and control scheme.

## 6.3 Sensing

### 6.3.1 Signal Selection: Ports, Frequencies, and Quadratures

For a Michelson based interferometer, there are four natural ports where fields exit (or enter) the interferometer: the symmetric port, the asymmetric port, and the two transmitted ports. At the 40 m, these ports are called REFL, AS, TRX, and TRY, as indicated in figure 6.1(b). The REFL port is the rejected beam from the input Faraday isolator. Additional ports can be created by judicious placement of a partially reflecting mirror; at the 40 m the POX (Pick-Off XARM), POY (Pick-Off YARM), and PO (Pick-Off) ports are added in this manner. Although pick-off ports in figure 6.1(b) are depicted as separate elements, they are really the anti-reflective coatings on the back surface of the nearest optic. These have a typical power reflectivity of 600 ppm, although this can vary significantly. The actual values in the 40 m installed optics are not known.

A signal is created by directing a beam exiting a port to a photodetector, and electronically demodulating the resulting photocurrent (cf. section 3.5.1). Considering the number of ports and the possible demodulation frequencies, there is a large number of potential signals. At the 40 m, 31 of these signals are acquired digitally and used for interferometer control. They are listed in table 6.1. We give the signals unique identifiers by naming them with a simple convention that identifies the port, demodulation phase, and frequency. So the Q-phase signal from the  $f_1$  demodulation at the asymmetric port is AS Q1. P and M are used to indicate  $f_2+f_1$  and  $f_2-f_1$ , respectively. Table 6.3 has the names for most of the acquired signals in the first column.

Because the system is digital, more signals can be constructed through mathematical combination of the signals in table 6.1. This expands the total space of signals, and is exploited during lock acquisition (more in chapter 8).

### 6.3.2 Double Demodulation

Double-demodulation is a doubled optical heterodyne process—the photocurrent is first mixed with an electronic local oscillator at  $f_1$ , and then mixed again at  $f_2$ ; only after the second mixing is

Port	Frequency
PO	$2f_1, f_1 + f_2, f_1 - f_2, \text{DC}$
POX	$f_1, \text{DC}$
POY	$f_1, \text{DC}$
REFL	$f_1, f_2, f_1 + f_2, f_1 - f_2, \text{DC}$
AS	$f_2, f_1 + f_2, f_1 - f_2, \text{DC}$
TRX	DC
TRY	DC

Table 6.1: Signal availability for 40 m length sensing and control. For all demodulated signals, both quadratures are acquired.

the signal low-pass filtered. In the absence of oscillator noise, this is mathematically equivalent to mixing the photocurrent with a local oscillator at  $f_2+f_1$  and another at  $f_2-f_1$ , low-pass filtering both, and summing the resulting signals. The latter version is the one used at the 40m.

The LSC scheme at the 40 m relies heavily on double demodulation (DDM) to provide signals for the short degrees of freedom (MICH, PRCL, SRCL), because in principle these signals can be well isolated from signals imprinted on the phase of the carrier light by motions of the arm cavities. Since the RF sidebands do not resonate in the arm cavities, DDM signals which are comprised purely from beats of RF sidebands should not be affected by arm cavity motion.

### 6.3.3 Sideband Imbalance and Offsets

In section 3.5.1 it was noted that the Q-phase signal is sensitive to RF sideband imbalance, while the I-phase is sensitive to optical phases. This leads to a significant problem in a detuned RSE interferometer, where all the RF sidebands that couple to the detuned signal cavity (by, for example, Schnupp leakage) will be imbalanced. This will create offsets in the signals used to sense cavity lengths, rendering it impossible for the control system to keep the cavities exactly on resonance.

If we knew the precise demodulation phase, this would not be a real problem, as we could choose the demodulation phase where the offset is zero. Figure 6.2 shows the DC value of the AS QM signal, as the Michelson degree of freedom is swept through resonance, with multiple demodulation phases overlaid. We can see that at only one demodulation phase does the signal actually go through zero when the Michelson is at its operating point. The length offset is about 1 nm per degree of demodulation phase error. There is also a second point where the error signal goes through zero; a lock acquisition protocol (cf. chapter 8) must avoid such secondary lock points.

We typically do not know in advance the precise demodulation phase, however, since it depends on things we do not track precisely like cable lengths and RF signal connectors. So we have to measure it, and rely on it not changing significantly with time (it does—more on this is in section 9.3.1).

#### 6.3.3.1 Measuring Demodulation Phases

For a single cavity with a standard PDH sensing setup, this is a simple task. The usual method is to excite the cavity and measure the response in the two quadratures at the excitation frequency; the demodulation phase that yields the minimal response is the Q-phase. A demodulation phase can be measured to a precision better than  $1^\circ$  in this manner.

This technique does not work however, with DDM signals, as shown in figure 6.3. There, signal offsets do not go to zero at either the minima or maxima of the gain, and so this excitation technique fails. Possible solutions include setting the phase to get the maximum gain and digitally subtracting the offset, and setting the phase to get the minimum offset while temporarily using an alternate error signal (i.e., a single demodulation signal). The latter technique is the one used at the 40 m, because

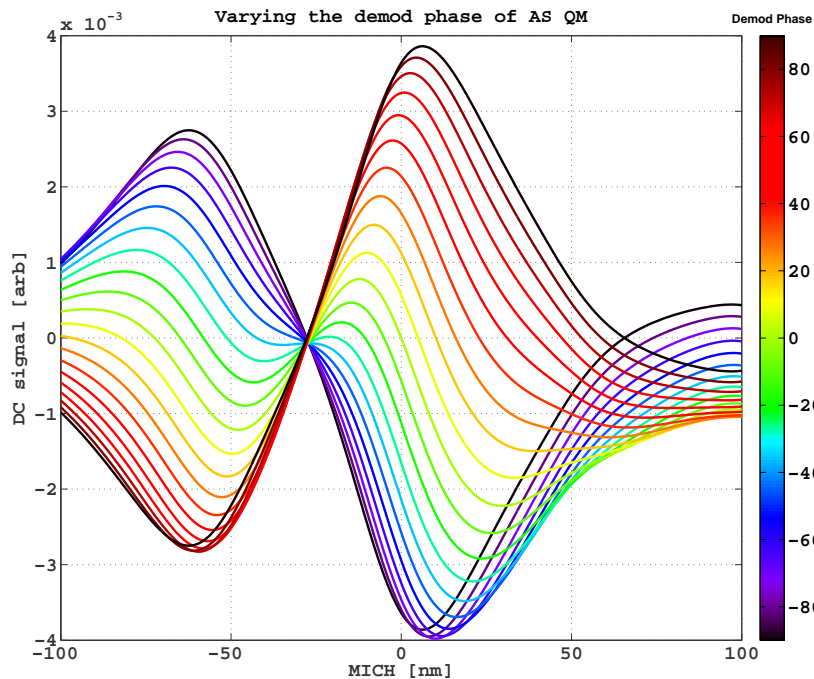


Figure 6.2: The signal at the AS QM ( $f_2 - f_1$ ) photodiode changes with the demodulation phase. Note that for most choices of demodulation phase, the signal does not cross zero when the Michelson degree of freedom is at its operating point. This is an error signal length offset.

it will be less sensitive to gain variations in the signal which will arise due to mirror alignment fluctuations. The actual process used to set the phases is described in section 8.5; that process is limited in the achievable accuracy, however, so there are still residual length offsets. This creates problems in predicting noise couplings (more in section 9.3.1).

All this means, if we do not want to digitally subtract offsets, we are restricted to one demodulation phase for each DDM signal. With this in mind, we simply choose whether to call the actually used demodulation phase I or Q; the names are meaningless, since there are really *two* demodulation phases for each DDM signal. Following a convention, the signals at the REFL and PO ports are the I-phases, and at the asymmetric port the Q-phase; these choices are shown in table 6.2.

Signal	Frequency
REFL DD	REFL IM + REFL IP
PO DD	PO IM + PO IP
AS DD	AS QM + AS QP

Table 6.2: Double demodulation signal definitions.

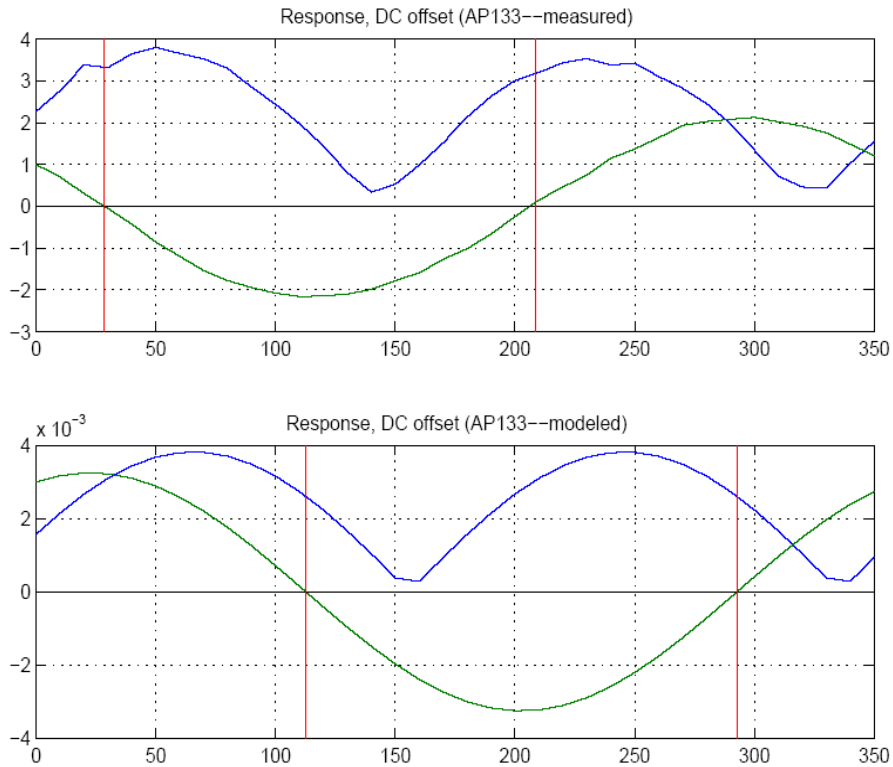


Figure 6.3: Modeled and measured response of a differential demodulation error signal, as the demodulation phase is changed. Shown are the gain (blue) and offset (green) of the signal, demonstrating that maximum gain does not occur at zero offset, in contrast to an ordinary PDH style single demodulation signal. The modeled and measured offsets do not go through zero at the same demodulation phases, because the origin of the demodulation phase axis in the measured plot (top) is arbitrary (as we do not track RF cable lengths); there is also a sign ambiguity in the demodulation phase.

### 6.3.4 Configuration Space and the Operating Point

We will define the term *configuration space* as the space spanned by the degrees of freedom of the interferometer (restricted in this discussion to length, although the real interferometer has many more angular degrees of freedom). Thus, the configuration space of the interferometer is a five-dimensional space. The *operating point* is defined as the point in configuration space where the interferometer has been designed to operate: all the degrees of freedom (except DARM when in a DC readout state) are at zero offset.

### 6.3.5 Discriminants

The derivative of a signal with respect to optic motion is called a discriminant. By writing down the derivatives of all the signal outputs with respect to motion of all the optics, one can evaluate the *matrix of discriminants*, also called a *sensing matrix* (see [83, 43, 84] for detailed discussions and

derivations). Each element of the sensing matrix is the optical gain of a given signal  $S_i$  in units of watts/meter with respect to the corresponding motion of a degree of freedom  $L_j$ . The matrix thus connects optic motion to signal output,

$$\vec{S} = \mathbb{M}\vec{L}. \quad (6.1)$$

In general, despite the best efforts of interferometer designers, the matrix can be well populated by off-diagonal terms. Moreover, all the elements are non-linear functions of the microscopic positions of every optic in the interferometer (i.e., the location in configuration space), and they also will vary with audio frequency  $\omega_a$ . Writing down a useful expression for a sensing matrix is thus a difficult task; so, to actually calculate a sensing matrix, we turn to the interferometer simulation tool Optickle (cf. appendix F). An example sensing matrix,  $\mathbb{M}_{ex}$ , is shown in table 6.3; this matrix gives the DC signal gains, with the interferometer *at its operating point* for DC readout (there is a 50 pm DARM offset). This particular matrix is calculated in the canonical basis (i.e., MICH, PRCL, etc.), but it could also of course be written in the optic basis (BS, PRM, etc.); these bases are related in a straightforward manner by the output matrix (more in section 6.4.1). We can see by inspecting table 6.3 that there are significant off-diagonal terms, and this is after the sensing scheme described here was designed with an effort to make this matrix as diagonal as possible.

### 6.3.5.1 Frequency dependence

The sensing matrix can vary with audio frequency  $\omega_a$ . To illustrate the variation with frequency, figure 6.4 shows the first row of  $\mathbb{M}_{ex}$  (magnitude only) as a function of frequency. We choose this row because, as the signal which is chosen to sense DARM (and hence GW) motion, it is a priori interesting—we need to know how motion of all the degrees of freedom might show up in the signal we are going to use as the GW channel. Inspection reveals that the curves in figure 6.4 are not trending at low frequency towards the values shown in the DC matrix (table 6.3). This is the result of radiation pressure modifying the interferometer dynamics, an effect included in figure 6.4 but not table 6.3. This is indicated in the  $y$ -axis units of figure 6.4, which are watts/meter\*, where the asterisk is used to indicate such modified dynamics (which is by radiation pressure in this case, but could also be by the control system). We choose this curious unit because it allows us to focus on what is interesting to us, which is ultimately the response of the interferometer signal outputs to the various disturbances which displace the optics. Thus, the unit meter\* does not indicate actual optic motion—it indicates *what the optic motion would have been in the absence of modification*. This allows us to simply input disturbances, and see the actual resulting signal, naturally including the effects of radiation pressure (or the control system, or both).

	PRCL	SRCL	MICH	CARM	DARM
OMC DC	-6.5e+03	-3.7e+03	3.9e+04	-2.4e+06	<b>3.1e+07</b>
AS Q2	5.5e+04	-1.2e+05	-1.8e+05	7.8e+07	<b>-1.4e+08</b>
REFL I1	-2.6e+07	-6.9e+05	5e+05	<b>-2.9e+09</b>	1.5e+08
REFL Q1	3.1e+06	1.5e+05	-2.2e+06	<b>2.1e+08</b>	-1.2e+07
REFL I2	3.3e+06	-5.8e+06	-2.7e+05	<b>3.7e+09</b>	-1.2e+08
REFL Q2	-3.9e+05	3.6e+04	-3.4e+05	<b>2.7e+08</b>	-4.2e+07
REFL IM	<b>1e+07</b>	2e+06	-8.4e+05	8.8e+05	-1e+05
REFL QM	2.1e+06	<b>2.2e+06</b>	4.1e+03	-8.3e+04	-3e+04
REFL IP	<b>-9.6e+06</b>	-1.8e+06	-3.6e+05	-1.5e+04	2.7e+03
REFL QP	<b>-2.5e+06</b>	-2.3e+06	1.1e+04	-1.3e+04	3.7e+03
AS IM	2.9e+05	<b>-5.3e+05</b>	5.5e+04	-5.1e+04	7.5e+04
AS QM	<b>-4.1e+05</b>	-1.2e+05	4.8e+04	1.4e+05	2.7e+04
AS IP	8.6e+04	<b>-5.5e+05</b>	-6.4e+04	-9.8e+02	6.9e+02
AS QP	<b>-5.6e+05</b>	2.5e+05	-4.8e+03	-2.2e+02	-5e+02
POB IM	6.9e+03	<b>-2.2e+04</b>	2.9e+03	8e+03	2.1e+02
POB QM	<b>-1.9e+04</b>	-1.8e+03	-1.6e+03	3.1e+03	-1.3e+02
POB IP	-1.3e+04	<b>2.6e+04</b>	2.6e+03	43	-39
POB QP	<b>2e+04</b>	1.2e+03	-9.9e+02	-14	-2
TRX DC	-1.6e+05	3.7e+04	-6.6e+04	<b>-6.3e+07</b>	-5.3e+07
TRY DC	-1.7e+05	-2.8e+04	3.1e+04	<b>-6.7e+07</b>	2.5e+07

Table 6.3: Example DC matrix of discriminants, computed for the 40 m. The signals are indicated by port, demodulation phase, and demodulation frequency. The P and M indicate  $f_2+f_1$  and  $f_2-f_1$ , respectively. The units are Watts/meter. The largest magnitude element in each row is bolded.

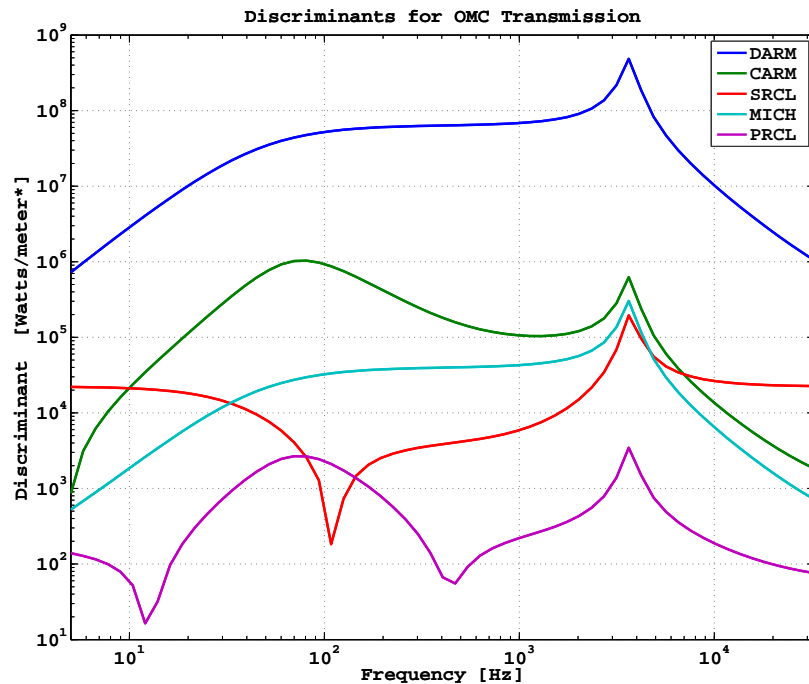


Figure 6.4: Frequency dependent magnitude of the OMC DC row of the matrix of discriminants. The units are Watts/meter\*, where the asterisk indicates the optic motion has been modified by radiation pressure. This plot shows the open-loop response (no control system).

### 6.3.5.2 Position dependence

The sensing matrix (including, of course, the frequency response) can also vary with microscopic optic position. In general, each element of the sensing matrix is a non-linear function of the position of all the interferometer optics. This is illustrated in figure 6.5, which plots the DC value of the signals in  $\mathbb{M}_{ex}$  as the signal recycling mirror is swept through 0.2 microns, centered on the operating point. The corresponding table column SRCL is the derivative of these signals at SRCL = 0. Similar plots can be made for all the columns of  $\mathbb{M}_{ex}$ .

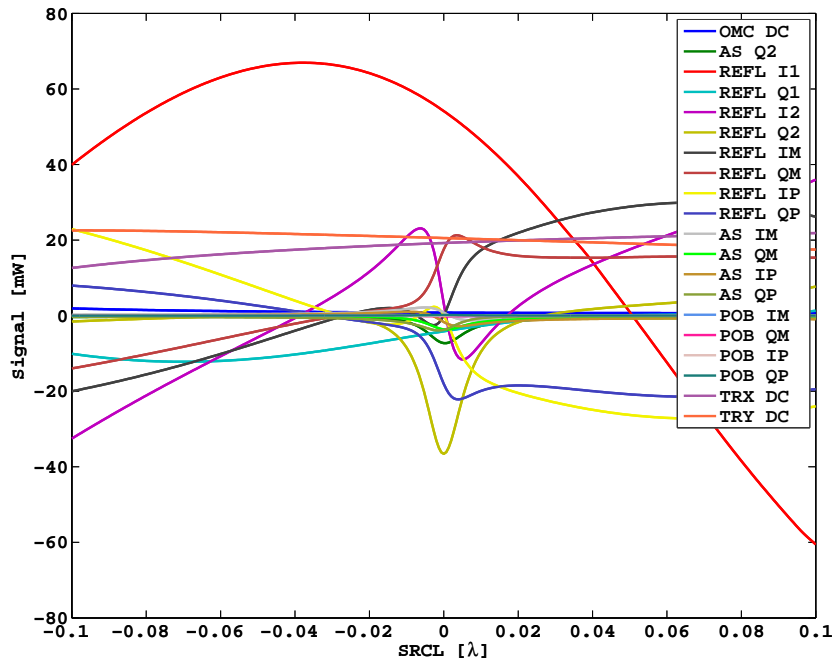


Figure 6.5: Output of signals as SRCL is varied.

### 6.3.5.3 Example matrix at operating point

The signals used at the operating point are a subset of the full sensing matrix; these are listed in table 6.4. This table shows the philosophy of the signal extraction scheme: the arm cavity signals (CARM and DARM) are sensed using single-demodulation signals (or the OMC transmitted light for DARM, when in DC readout), and the short degrees of freedom (MICH, PRCL, SRCL) are sensed using double demodulation signals. For each of the short degrees of freedom, all of the available DDM signals are used. This is done by measuring and inverting a subset of the sensing matrix, a process described in section 8.5.

DOF	Port	Demod
SRCL	PO, REFL, AS	DD
PRCL	PO, REFL, AS	DD
MICH	PO, REFL, AS	DD
CARM	REFL	$f_2$ I
DARM	AS	$f_2$ Q OMC DC

Table 6.4: Signal port and frequency selection for the 40 m length sensing and control scheme. The DD indicates a double-demodulation (DDM) signal; the PRCL, MICH, SRCL degrees of freedom are sensed through a combination of all the available DDM signals.

#### 6.3.5.4 SPOB

There is one additional signal which has not been discussed, but is extremely useful—the sideband product in the power recycling cavity. This signal is extracted from the PO port, and is the result of a demodulation at  $2 \times f_1$ . It is directly proportional to the RF sideband power, and so provides a convenient measure of the RF sideband power buildup. It is used in lock acquisition (more in chapter 8).

#### 6.3.5.5 Non-resonant sideband

One significant drawback of the 40 m scheme in general is the lack of a non-resonant sideband. Such a sideband, which would be nearly totally reflected from the power recycling mirror, would provide a stable phase reference for sensing common mode signals with no sideband imbalance. It can also provide a better shot noise limited SNR for common mode signals for interferometers with high PRM reflectivity, since no sideband light is ‘lost’ by being coupled into the interferometer. It could also be used in a double-demodulation scheme for a detuned interferometer, which would benefit from a stable phase reference. In short, this is a good idea that simplifies many aspects of length sensing and control; the only drawbacks are the (slight) reduction in carrier laser power and the additional complication of getting it through the input mode cleaner. All interferometer LSC designs should include a non-resonant sideband.

## 6.4 Control

As noted in section 3.12, we must also control the degrees of freedom of the interferometer using linear feedback (a brief introduction to feedback control is in appendix E). As described in section 5.4, all the length sensing and control systems are partially digital in nature. Figure 6.6 is a simplified control system diagram for the Length Sensing and Control subsystem. This diagram shows the basic philosophy, which is centered on using digital signal processing to diagonalize the multiple

input multiple output (MIMO) optical plant before applying servo filters. In the diagram, the optical plant is represented by a picture of an interferometer, with 8 inputs (the core optics length actuation signals, plus the a mode cleaner length actuator signal which represents control of the laser frequency—see section 5.7 for details about the common mode servo) and 31 outputs (the analog output signals which are either direct photodiode powers or outputs from I&Q demodulators). These signals are then digitally acquired and fed to the LSC computer. In the LSC computer, they undergo a basis transformation in the input matrix (ideally, this is the inverse of the sensing matrix  $\mathbb{M}$ ; more in the next section), are digitally filtered (the feedback filter in the feedback control loops) in the canonical degrees of freedom, and the resulting control signals are transformed to the optic basis before being sent to the digital suspension controllers, where they are converted to analog signals and fed to the optic coil drivers.

### 6.4.1 Matrices and Bases

Figure 6.6 shows 8 degrees of freedom (DARM, MICH, PRCL, CARM, SRCL, XARM, YARM, MC) available as choices for feedback filtering; this is to allow flexibility during lock acquisition (which is covered in detail in chapter 8). The interferometer, of course only has 5 length degrees of freedom—in normal operation we do not use XARM, YARM, or CARM (MC is used as a laser frequency feedback, cf. section 5.7). The physical meaning of these degrees of freedom is determined by the output matrix, which converts the control basis (MICH, PRCL, etc.) to the optic basis (BS, PRM, ETMX, etc.). We have purposely named the control basis to follow the canonical basis (cf. figure 3.10), because ideally they would be the same. In practice, they are not the same, for a few reasons. This can lead to confusion; in this thesis, references to the 40 m will always refer to the actual control basis unless otherwise specified. The one typically used is in table 6.5, where the actual values used which differ from the canonical basis are in parentheses. The only meaningful choice is how to control the MICH. We could actuate on the arm cavity mirrors (both ITMs and both ETMs), but we choose instead to actuate on the beamsplitter, and also feed the signal to the recycling mirrors to keep the recycling cavity lengths constant.

	ETMX	ETMY	BS	PRM	SRM	MC2
SRCL					1	
PRCL				1		
MICH			1	$\frac{1}{\sqrt{2}}$ (.588)	$\frac{1}{\sqrt{2}}$ (0.18)	
DARM	1	-1				
CARM	1	1				
MC						1

Table 6.5: The typical 40 m LSC output matrix. The actual values used in the control system are noted in parentheses when they differ significantly from the canonical basis.

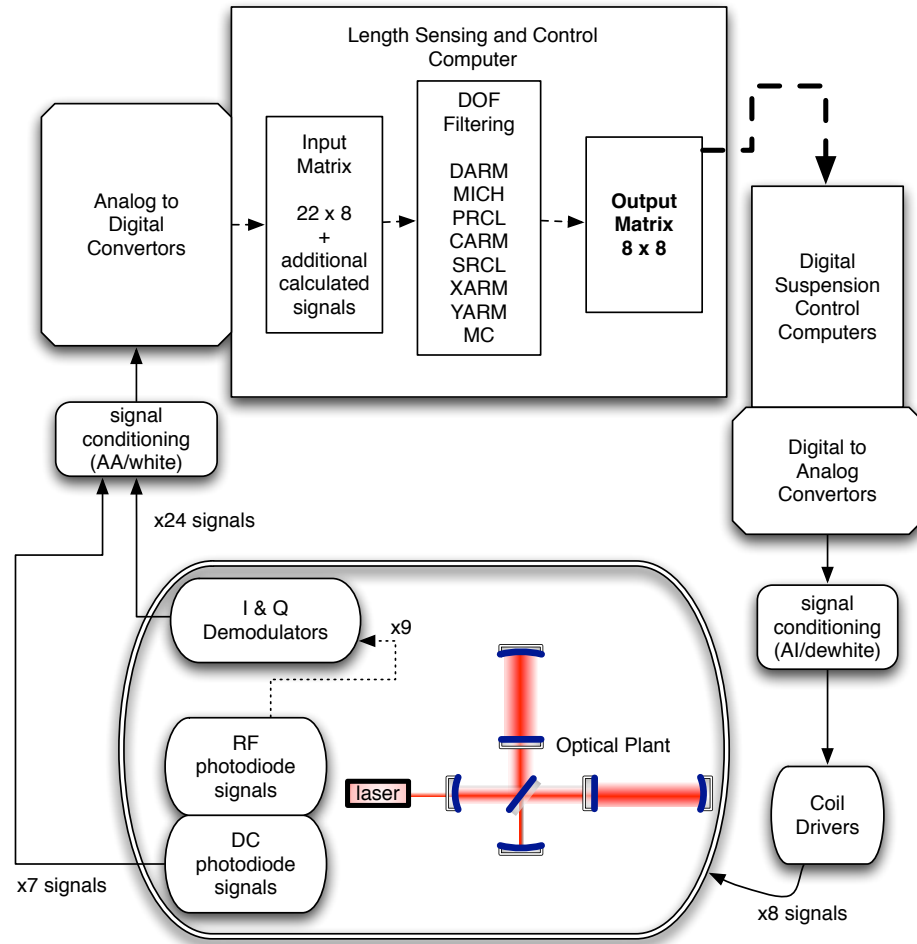


Figure 6.6: A simplified block diagram of the length sensing and control system. The optical plant is depicted here as an 8-input, 31-output analog system; this plant is a highly cross-coupled MIMO (multiple input multiple output) system. The length sensing and control subsystem block diagram shows the basic strategy, which is to combine the acquired signals in an input matrix, apply filtering in a certain basis, and then use the output matrix to convert the output/control signals to the actuator basis.

The first cause of the difference between the control and canonical bases is essentially a bootstrapping problem. Ensuring that the control basis is exactly the canonical basis requires precise calibration of the mirror actuators; this is not difficult for the ETMs (it is part of the calibration procedure in chapter 7). It is problematic, however, for the PRM and SRM. These optics can only be interferometrically sensed as part of a coupled system (i.e., they cannot be a part of a single DOF subset of the interferometer). In order to get a precise calibration, then, that coupled system would need a perfectly diagonal sensing matrix. Unfortunately, the sensing matrix at the 40 m is not really diagonal. This problem could probably be circumvented with additional hardware to determine accurate calibrations, but this was not deemed to be worth the effort. A reasonable technique is just to assume the BS, PRM, and SRM have the same calibration, and use simple geometry (the

knowledge that the BS is at a  $45^\circ$  angle to the PRM and SRM) to determine the output matrix. This then only requires the determination of the relative signs of the mirror actuators (which can be different depending on how the magnets were attached).

The second reason the control basis is different from the canonical basis has to do with lock acquisition (more in chapter 8). The particular lock acquisition protocol developed and regularly used at the 40 m worked better with the control basis in table 6.5, which is quite different from the canonical basis. This could be due to a radically different actuator strength in the SRM; it is not currently known if that is the case. In any case, attempts to write the canonical values into the output matrix proved unsuccessful: lock acquisition was slower, and the locks achieved were not stable.

#### 6.4.1.1 Input Matrix

The input matrix connects the photodiode signals to the feedback filters for the degrees of freedom. In an ideal system, the input matrix would be the inverse of the sensing matrix  $\mathbb{M}$ ; then the error signals for the control loops would only be sensitive to motion of their own degree of freedom. In principle, we should exactly measure the full sensing matrix  $\mathbb{M}$  at every frequency, invert it, and use that as the input matrix. In practice, we do not do this for a few reasons. First, it is difficult; at best, we generally measure and invert it at one frequency. Even then, we do not measure and invert the whole thing. At the 40 m, this measurement and inversion is only done for the MICH, PRCL, and SRCL degrees of freedom. The measurement and inversion of the input matrix (the part which connects the DDM signals to these DOFs) is done during the lock acquisition bootstrapping, described in section 8.5. The actual reason for doing this is purely to reduce cross-talk between these control loops; this complicates the analysis of control loop gain and stability, because the other loops become part of the plant for each loop (see section E.4.1.1). The effect of imperfect input matrix diagonalization is residual cross talk between the control loops.

The second reason we do not invert the complete matrix is sensing noise. It is simpler to use the signals with the most gain, and simply exclude signals with much lower SNR rather than add them to the mix.

#### 6.4.2 Feedforward Corrections

In addition to the servo loops which control the canonical degrees of freedom, it is also sometimes necessary to have correction paths that feed control signals from the auxiliary degrees of freedom directly to DARM. This can be seen by inspecting figure 6.4, where we can see that all the canonical degrees of freedom of the interferometer have some optical coupling to the output mode cleaner transmission, which is the DARM sensing signal. A similar statement can be made for RF readout.

This optical coupling represents a problem, since noise in these auxiliary degrees of freedom can pollute the DARM signal. The control system, of course is supposed to suppress *displacement noise* for these auxiliary DOFs, but it will not suppress *sensing noise*: it will instead impose the sensing noise on the auxiliary degree of freedom, and this will pollute the DARM signal via the optical coupling ( $\mathbb{M}$ ).

The solution, when the auxiliary degrees of freedom are sensing noise limited (usually the most important sensing noise in this case is shot noise, but we will see in chapter 9 that light source noise can also be a problem), is to simultaneously send the feedback signal to DARM, appropriately filtered and scaled. This is called feedforward loop correction, and is done in LIGO for MICH and PRCL. It has also been done at the 40 m for MICH in a power-recycled FPMI state, where it is especially simple, as the coupling factor is a constant  $\pi/2\mathcal{F}$ .

Figure 6.4 shows that in a detuned interferometer, the feedforward paths will need some filtering in order to be effective, especially for the SRCL and PRCL loops. These were never implemented because these length couplings never limited the noise of the interferometer, as other noise sources were dominant (specifically, digital to analog conversion noise for the test mass actuators).

Although sophisticated frequency-dependent feedforward loop corrections have not been tested for a detuned interferometer at the 40 m, they will prove crucial in Advanced LIGO, not just to reduce the effects shot of noise in the auxiliary loops, but as the measurements in chapter 9 will show, also for laser and oscillator noise.

The 40 m digital control system is currently being significantly upgraded (cf. section 5.10); the implementation of feedforward techniques should be a high priority. One technique that will be tested is the use of Wiener analysis (see [85] for a description) to determine the optimal filters for these correction paths.

## 6.5 Discussion

The LSC scheme described in this chapter has been demonstrated at the 40 m. This demonstration includes the development of a new technique for lock acquisition (chapter 8), locks lasting more than 3 hours, and the measurement of laser and oscillator noise couplings the gravitational wave channel (chapter 9). It works basically as advertised, which is to say, with difficulty. This work has already had a significant impact on the design of Advanced LIGO, which has been influenced by many of the lessons learned during the implementation of this scheme. The changes to the Advanced LIGO design include the following.

**Broadband RSE** rather than detuned RSE. The plethora of complications encountered in locking (chapter 8), controlling, and calibrating (chapter 7) a detuned RSE interferometer have altered the perspective of the relative merits of detuning. Advanced LIGO will instead be operable as

a broadband RSE interferometer, and will thus not be plagued by the sideband imbalances.

**Multiple modes of operation.** Although the baseline for initial operation is broadband RSE, the LSC scheme for Advanced LIGO will actually allow multiple modes, including detuned operation. This has been accomplished by designing the resonance profile such that the error signal for the SRCL has a broad linear range; an electronic offset can be added to change the signal cavity tuning. It is even conceivable that this detuning change could happen during a single lock, allowing the interferometer to track a coalescing binary.

**Lowering the arm cavity finesse** from 1250 to 450. Although this will increase the thermal load on the substrates in the recycling cavity, this will lessen the effect of anomalous losses in the optics, and simplify lock acquisition. At the 40 m, the interferometer as a whole is undercoupled because the high finesse arm cavities greatly increase the impact of optical losses in the arm cavities.

**No Mach Zehnder.** The LSC scheme has been designed to minimize the effects of sidebands on sidebands, and will thus work without the need for a Mach Zehnder (cf. section 5.6.1.1), which adds complexity to interferometer operation.

**Lower modulation frequencies.** This was not discussed in detail, but the experience with this scheme has shown that RF modulation frequencies above  $\sim 100$  MHz present significant technical challenges in electronics and photodetector design, particularly for the detection of sideband-sideband beats, which are at even higher frequencies than the modulation frequencies. Fast photodetectors must have a small active area; working with such small (1 mm diameter) photodetectors in a high-power, suspended interferometer proved challenging—several were destroyed during lock loss events. In addition, double demodulation places particular demands on photodetector frequency response; the previous Advanced LIGO design would have required a photodetector with resonances at 171 MHz and 189 MHz, and a notch at 180 MHz. Such a requirement is not practical. Furthermore, position sensitive, segmented photodetectors which operate well at such high frequencies were also believed to be very difficult to implement. The Advanced LIGO design was thus modified to limit the highest frequencies detected to less than  $\sim 100$  MHz.

**Lock acquisition.** The Advanced LIGO LSC scheme has been designed with lock acquisition in mind; a significant advantage over the scheme described here. In addition, there are plans for significant additional optical hardware whose primary purpose is to ease lock acquisition (more in chapter 8).

## Chapter 7

# Calibration of a Detuned RSE Interferometer

Calibration of the interferometer output requires a thorough understanding, through a combination of modeling and measurement, of the transduction process by which displacement (or strain) is converted to volts (and ultimately digital counts, here denoted by [cnt]). For Initial and Enhanced LIGO, this process is already fairly complicated, given the complexity of interferometric gravitational wave detectors. This situation will only be exacerbated by the use of a detuned optical configuration, with its more richly featured opto-mechanical response. Here we concern ourselves only with calibration of the DARM error signal in the frequency domain.

### 7.1 Calibration in Initial LIGO

One method used for calibrating the Initial LIGO detectors [86] involves a multistep process, based on the Schnupp sensing technique employed for the Michelson length DOF sensing. After demodulation and digital acquisition, the Schnupp technique yields an error signal for the Michelson length

$$MICH_{err} = A_0 \sin\left(\frac{4\pi l_-}{\lambda}\right), \quad (7.1)$$

where the amplitude  $A_0$  depends on many factors and so the easiest (and most accurate method) is to just measure it, using the laser wavelength  $\lambda$  as a reference. This procedure can be summed up as: ‘calibrate the actuator using a simpler system than the full interferometer, then excite the calibrated actuator and measure the response of the full system.’ This section outlines the calibration procedure.

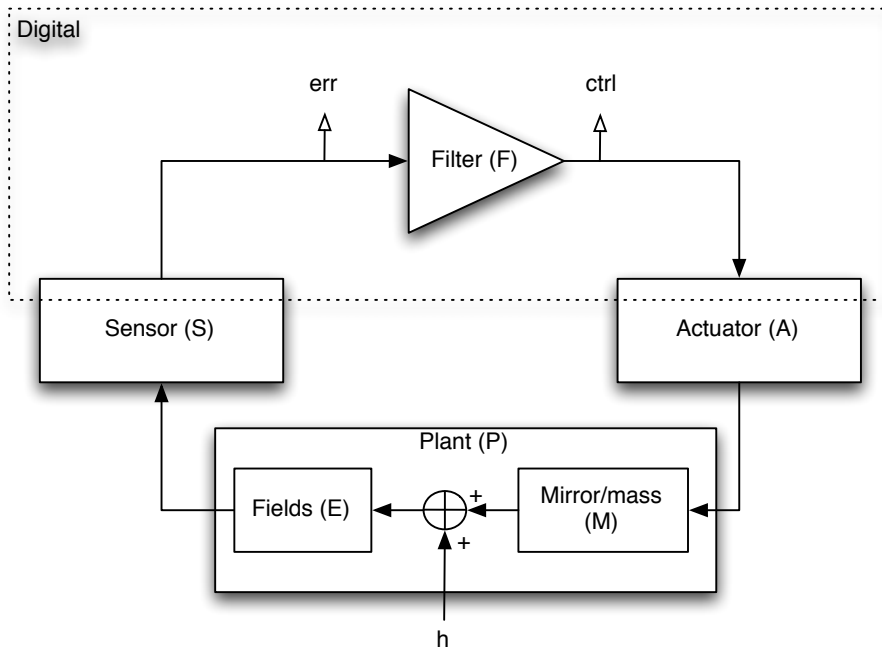


Figure 7.1: The MICH/XARM/YARM/DARM feedback loop model for non-signal-recycled interferometer. The transfer function  $E$  for these simple subsystems is just the arm cavity pole (or unity for the MICH). A gravitational wave signal  $h$  is modeled as an injection into the loop at the optical field  $E$ .

### 7.1.1 Free Swinging Michelson

With the interferometer optics aligned to create a simple Michelson, excite the optics in length and measure the peak to peak amplitude of the signal as the Michelson swings through complete fringes. The maximum amplitude is  $A_0$ . At the dark fringe, the Michelson error signal gain is then  $A_0 \frac{4\pi}{\lambda} [\frac{\text{cnt}}{\text{m}}]$ ; this is the calibration for the field+sensor transfer function  $E_{mich}S$  in figure 7.1, at DC. We assume  $S$  does not vary with frequency.  $E_{mich}$  is also constant with frequency. Thus, for a Michelson  $E_{mich}S$  can be used to write the error signal  $MICH_{err}$  in meters at all frequencies.

### 7.1.2 ITM Calibration

Lock the Michelson to a dark fringe, and excite the Michelson length by driving an input test mass (ITM) with a sine wave. Measure the swept sine transfer function from  $MICH_{ctrl}$  to  $MICH_{err}$ . Demodulate the response in the (now calibrated) Michelson length sensing output. This step measures the transfer function  $H_{mich/itm}$ ,

$$H_{mich/itm} = \frac{MICH_{err}}{MICH_{ctrl}} = \frac{A_{itm}M_{itm}E_{mich}S_{mich}}{1 + G_{mich}}, \quad (7.2)$$

where we have used the open loop gain  $G = FAMES$ . Since we already know  $E_{mich}S$ , after simply measuring the open loop gain  $G$ , we now also know  $A_{itm}M_{itm}$ .

$$A_{itm}M_{itm} = \frac{H_{mich/itm}}{E_{mich}S_{mich}}(1 + G_{mich}). \quad (7.3)$$

### 7.1.3 ETM Calibration

Lock a single arm cavity (say XARM), and measure the open loop gain  $G_{cav}$  and the transfer functions,

$$H_{cav/itm} = \frac{A_{itm}M_{itm}E_{cav}S_{cav}}{1 + G_{cav}}, \quad (7.4)$$

by exciting the ITM and

$$H_{cav/etm} = \frac{A_{etm}M_{etm}E_{cav}S_{cav}}{1 + G_{cav}}, \quad (7.5)$$

by exciting the ETM. Since  $E_{cav}S_{cav}$  is common to both transfer functions, and we already know  $A_{itm}M_{itm}$ , we can now easily determine  $A_{etm}M_{etm}$ :

$$A_{etm}M_{etm} = \frac{H_{cav/etm}}{H_{cav/itm}}A_{itm}M_{itm}. \quad (7.6)$$

### 7.1.4 DARM calibration

Lock the full interferometer, and measure the open loop gain  $G_{darm}$  and

$$H_{darm} = \frac{A_{etm}M_{etm}E_{darm}S_{darm}}{1 + G_{darm}}. \quad (7.7)$$

Then the sensing function is

$$C_{darm} = E_{darm}S_{darm} = \frac{H_{darm}(1 + G_{darm})}{A_{etm}M_{etm}}, \quad (7.8)$$

in units of  $[\frac{\text{cnt}}{\text{m}}]$ .

With  $C_{darm}$ , we can determine the magnitude of any signal  $h$  in meters by applying the calibration to the DARM error signal:

$$h = DARM_{err} \frac{1 + G_{darm}}{C_{darm}}. \quad (7.9)$$

The strain calibration is then just dividing by the arm length.

#### 7.1.4.1 Tracking

As the state of the interferometer changes (e.g., due to alignment fluctuations),  $C_{darm}$  and  $G_{darm}$  will in general only be affected in overall magnitude; the actual shape of their frequency responses will not change. It is thus sufficient to apply one calibration line which monitors this overall scaling

$\alpha$ , so that  $C_{darm}$  at a given time  $t$  is replaced by  $\alpha(t)C_{darm}$  in equation (7.9). Indeed, for calibration of initial LIGO  $C_{darm}$  is considered to be basically constant and is not dynamically corrected; it is measured perhaps several times over the course of a run, in contrast to  $\alpha(t)$  which is measured constantly and tracked in order to later reconstruct the calibration. A second calibration line can be applied as a consistency check and to get a better measurement of changes in the open loop gain  $G_{darm}$ .

#### 7.1.4.2 Comment

In this discussion, we have glossed over actually *understanding* the behavior of the actuators and sensors, in favor of simply measuring them. Part of the work of the LIGO scientific collaboration detector calibration subgroup is to also understand in detail all the smaller pieces of the model (i.e., the ADCs considered individually, the coil drivers, etc.), and make sure the subparts fit together properly. This is significantly more work, but gives added confidence to the calibration.

## 7.2 Calibrating the 40 m Detuned RSE Interferometer

As discussed in section 3.10, with the addition of a signal recycling mirror at the output port of the interferometer, the sensing function  $C_{darm}$  becomes more complicated. The salient features are the opto-mechanical resonance (the optical spring, the effect of which is shown in figure 7.2) and the optical resonance, higher in frequency than the spring peak. The nature of this opto-mechanical response is described thoroughly in [60] and [87], and some qualitative properties were also discussed in section 3.11. The details of these features (such as their frequency and Q) depend on interferometer parameters which, while set at the design phase, may vary dynamically during interferometer operation, and so a calibration procedure must be designed to track them. Figure 7.4 shows possible errors in the response function (in figure 7.2, this would be  $P_{darm}S_{darm}$ ) resulting from a small misestimation of several parameters which might vary during regular operation (circulating power, detune phase, and detection quadrature, all of which can potentially change with mirror alignment fluctuations).

### 7.2.1 Actuator Calibration

For calibrating the output of the 40 m detuned RSE interferometer, we employ a similar scheme to that described in section 7.1. This scheme involves first using the Schnupp technique and the free swinging Michelson to calibrate the ITM actuators, and then propagate that to the ETMs.

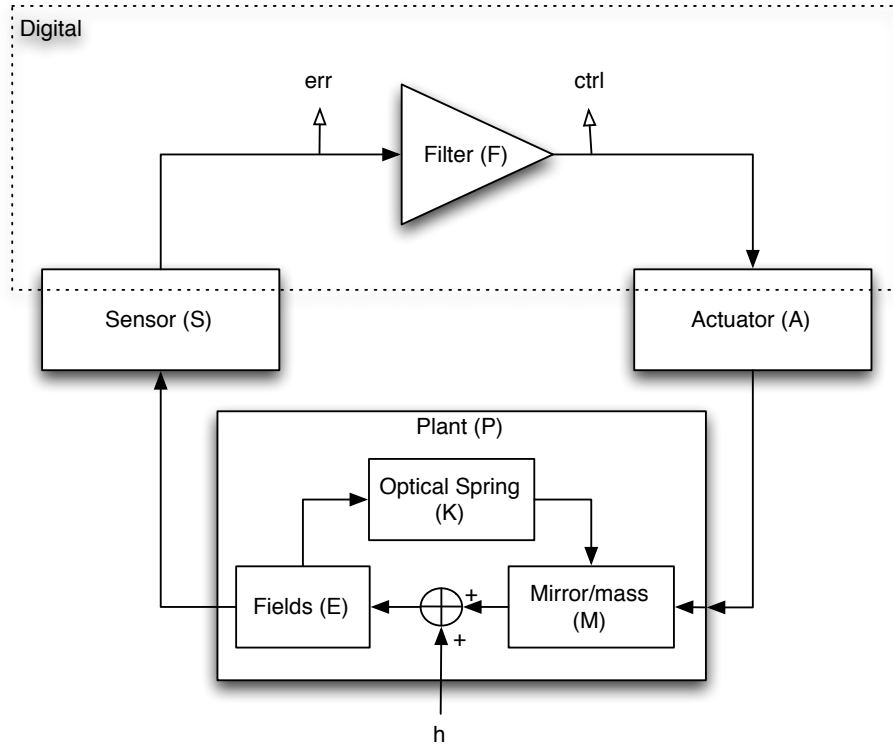


Figure 7.2: The DARM feedback loop model for a detuned RSE interferometer. The plant represents the opto-mechanical response, described in equation (3.83). A gravitational wave signal  $h$  is modeled as an injection into the loop at the optical field  $E$ .

### 7.2.2 DARM Calibration

Referring to figure 7.2, we then measure the open loop gain  $G$  (we will now omit the subscripts when referring to DARM; also  $AM$  will refer to the  $A_{etm}M_{etm}$ , measured previously using the method in section 7.1).

$$G = APSF, \quad (7.10)$$

where  $P$  is now the whole plant (we can no longer separate  $E$  and  $M$ , since they are both inside a feedback loop due to the radiation pressure). We can also measure

$$H = \frac{APS}{1 + G}. \quad (7.11)$$

Now, with some algebra, assumptions, and recalling that we measured the products  $A_{etm}M_{etm}$  and  $E_{cav}S_{cav}$  in section 7.1, we can isolate the response of the plant  $P$ ,

$$P = \frac{H}{A_{etm}S_{cav}a}, \quad (7.12)$$

where we have introduced an arbitrary scaling factor  $a$ , the value of which we also just measured. The assumptions for this last step were that  $M_{etm}$  is a pure (damped) pendulum response, that  $E_{cav}$  is a simple pole (cf. section 3.6.2), and that  $S$  can be written as  $aS_{cav}$ . These are all reasonable assumptions, that could also be verified (although they have not all been verified at the 40 m). The same photodetector is used to measure  $S$  and  $S_{cav}$ , so barring huge non-linearities in the PD or electronics the response should only differ by the optical power on the diode and the optical phase gain, both of which are included in the factor  $a$ .  $E_{cav}$  is the cavity response; this is simple enough that we can be confident in its behavior; it has also recently been measured. Assuming  $M_{etm}$  really behaves like a pendulum at the frequencies where radiation pressure matters (below 100 Hz) should not be controversial; it is the behavior of the actuators (i.e., the OSEMs) that are really in question, and that is mainly above a kHz.

The sensing function for  $h$  is then

$$C = \frac{PS_{cav}}{M_{etm}}a. \quad (7.13)$$

We can now calibrate  $DARM_{err}$  into meters:

$$h = DARM_{err} \frac{1+G}{C}. \quad (7.14)$$

### 7.2.3 Modeling

As discussed in section 7.2, the plant  $P$  and consequently the sensing function  $C$  can vary significantly with interferometer operation, with changes that cannot be described as simply an overall scaling. We can compensate for this by measuring the open loop gain  $G$  and using that measurement to determine  $C$ . Of course, for tracking purposes we cannot measure  $G$  at a large number of frequencies, since those frequencies would then have to be excluded from any analysis. We can track the behavior of  $P$  by measuring  $G$  at just enough frequencies to be able to fit the isolated  $P$  (cf. equation (7.12)) to a model (equation (3.83)).

We measure  $G$  at several frequencies (indexed by  $i$ ), and then isolate the plant  $P_i$  at those frequencies:

$$P_i = \frac{G_i}{A_{etm}SF}. \quad (7.15)$$

Since  $F$  is a digital filter, we know it precisely and do not have to measure it. The measurements of  $A_{etm}$  and  $S$  have been covered above.

We then minimize the function,

$$\left[ \sum_i \left| \frac{P_i}{M_{etm}} - RSEresp(f_i, I_{bs}, \phi, \zeta, g) \right|^2 \right]^{1/2}, \quad (7.16)$$

where  $RSEresp$  is simply equation (3.83) with hardcoded values for things that do not vary (like

$r_s$ ) and with an overall scale  $g$  included.  $M_{etm}$  is the theoretical pendulum response. The output from the minimization routine is then a set of estimates for the circulating power  $I_{bs}$ , detune phase  $\phi$ , detection quadrature  $\zeta$ , and overall gain  $g$ .

A model of the open loop gain  $G$  is then built using the output parameters from the fit and the theoretical opto-mechanical response (equation (3.83)), and the measured actuation/sensing product  $A_{etm}S$ . An example model, and the measured points, can be seen in Figure 7.3.

$$G_{mod} = RSEresp(f, I_{bs}, \phi, \zeta, g)A_{etm}M_{etm}SF. \quad (7.17)$$

Since the both the  $P_i$  and  $RSEresp$  are complex valued, this routine fits both magnitude and phase, and so a model of the overall delay must be included when removing the electronics (cf. equation 7.15) or the routine will get lost trying to match an impossible phase profile. The delay is digital, and so should be constant (it really is not, but it flips between several discrete values—this will be fixed in a future code upgrade). The minimization routine used can also easily get trapped in local minima, and so it must be primed with good guesses. One particular trap is that a  $\pi$  phase shift in the detection quadrature  $\zeta$  does not yield a simple sign change, as might be expected with a simpler system.

#### 7.2.4 Tracking

Doing occasional detailed measurements of the open loop gain such as in figure 7.3 is good to verify the validity of the modeling. The regular calibration, however, cannot be done with such detailed measurements of the open loop gain, as such measurements take many minutes to complete. For Advanced LIGO, as in initial LIGO, the calibration will be continuously tracked; the number of calibration lines must be kept as small as possible to avoid spoiling the data.

At the 40 m, we do not apply calibration lines continuously; instead, we just measure the open loop gain whenever a calibrated measurement needs to be made (such as a noise spectrum). We use 7 frequencies to determine the response. This number was determined by running the routine with fewer and fewer measured frequencies until the fit to the response was poor, and then adding back three points. The actual frequencies used can be seen in figure 7.5; these particular frequencies were selected to be at points where errors due to parameter misestimation should be large (cf. figure 7.4) while avoiding known mechanical resonances and frequencies with particularly poor noise performance.

In principle, these seven measurements are enough. In practice, at the 40 m, we add an additional measurement to get an overall scaling factor. This is because there are several length sensing and control parameters (gain settings) between the measurements for the DARM loop gain  $G$  and the

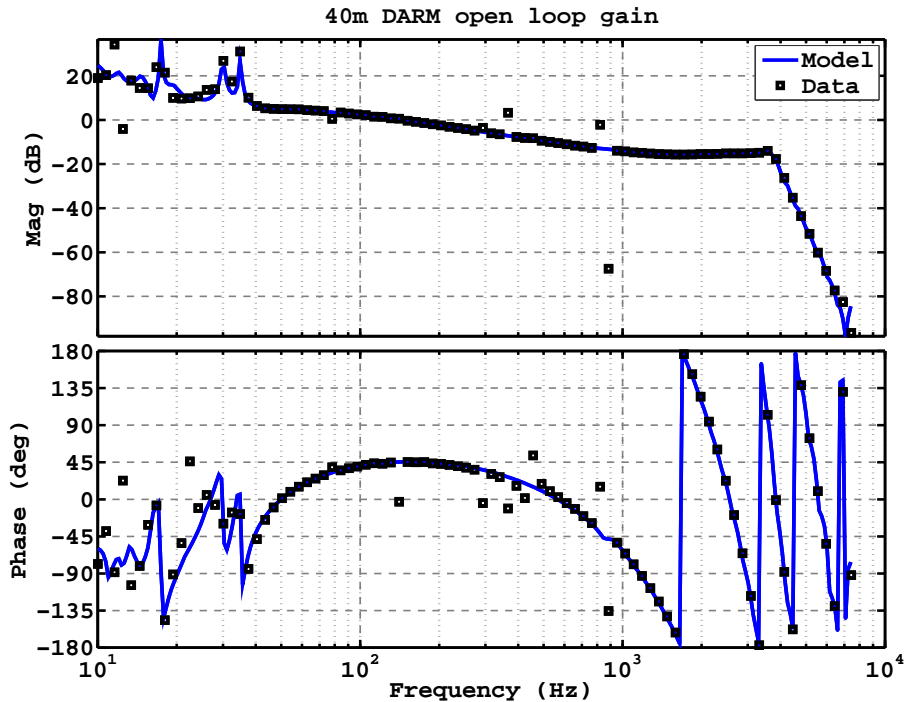


Figure 7.3: An example DARM open loop transfer such as is used for verification of modeling tools at the 40 m prototype. The squares represent measured data points, and the line is a model with four free parameters determined by a fit by eye. The large discrepancies at low frequencies are due to poor measurement coherence resulting from the large loop gain, and the isolated scattered points between 100 Hz and 1 kHz are due to unmodeled mechanical resonances (these points also have poor measurement coherence).

optic drive signal. To avoid tracking these, we use a separate excitation point whose calibration should not change. After building the open loop gain model, a calibrated excitation is performed by driving a ETM at a single frequency ( $f_{meas}$ ), and measuring the response in  $DARM_{err}$ . The response to this known excitation at one frequency can then be used to appropriately scale the sensing function  $C$ , by ensuring that  $C(f_{meas})$  is equal to the measured response.

A set of MATLAB functions has been written which automatically carries out the procedure described in this section by retrieving a set of data and taking the amplitude spectral density, measuring the open loop gain, applying a calibration line, and fitting a model to the measured open loop gain data. The model is then used to calibrate the amplitude spectral density. The calibration line and the open loop gain measurement excitations are not visible in the spectra because the data is not taken during these excitations, but rather approximately one minute before. Such a spectrum is in figure 7.6. The current version of this automated calibration routine actually applies an excitation to the ITM, simply leaving out the step of bootstrapping the ETM calibration. This leads to an error (due to the ITM also being part of the signal recycling cavities) of less than 0.2%, which is certainly negligible compared to other statistical and measurement errors.

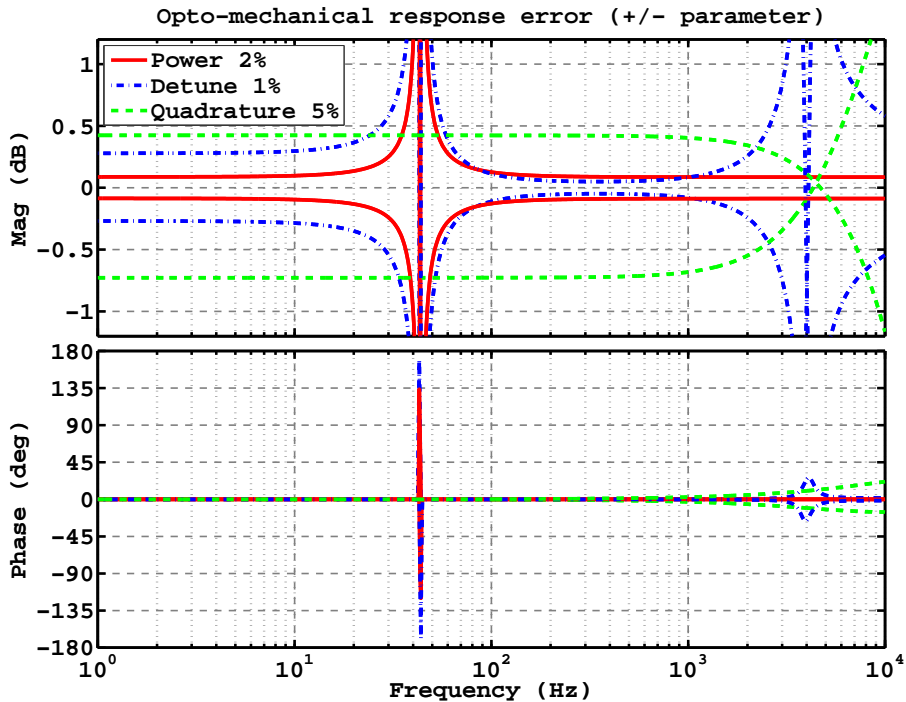


Figure 7.4: Ratio of the opto-mechanical response to nominal with given parameter variation, for a 40 m like RSE configuration. The red solid curves show the result of a  $\pm 2\%$  power variation, the blue dash-dot that of  $\pm 1\%$  detune phase variation, and the green dashed curves that of a  $\pm 5\%$  variation.

### 7.3 Calibration for Advanced LIGO

One of the possible operating modes of Advanced LIGO is in a detuned RSE configuration. The richness of the opto-mechanical response of a detuned RSE interferometer significantly complicates the determination of  $C(f)$ , a necessary step for the accurate calibration required to carry out the astrophysics goals of Advanced LIGO. Lindblom [88] concludes that a  $\sim 1\%$  calibration accuracy will be required to extract the maximum possible science; this should be compared with the  $\sim 10\%$  achieved in initial LIGO, the result of great effort on the part of the LIGO calibration team, and for a much simpler system.

For a detuned RSE interferometer, achieving such a calibration accuracy will likely require continuous tracking of the DARM response at several (at least 4, almost certainly more) frequencies to ensure an accurate estimation of the opto-mechanical response. Some of these tracking lines will also likely need to be in the detection band. It is conceivable that enough auxiliary information about the IFO can be collected to avoid the application of multiple calibration lines, but it is unknown whether enough information (such as microscopic details of auxiliary cavity lengths, mirror figures, alignments, and beam centering) can be tracked with enough precision and accuracy to reconstruct the opto-mechanical response; it is also unknown what effort such tracking might require, although

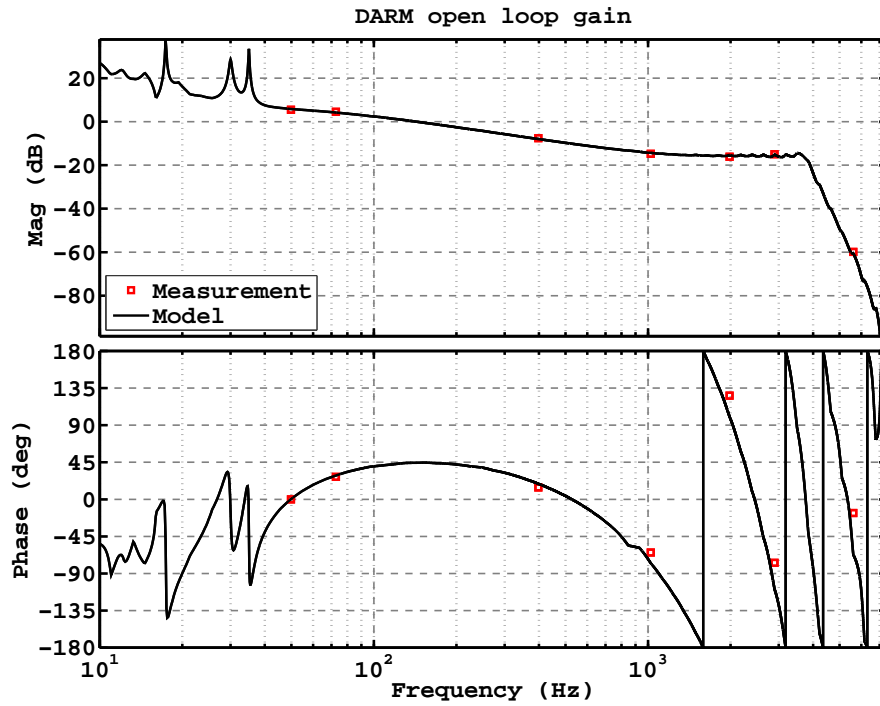


Figure 7.5: An example DARM open loop transfer such as is used for calibration of the DARM error signal into meters at the 40 m prototype. The squares represent measured data points, and the line is a model with four free parameters determined by a least squares fit—an overall gain, detune phase, circulating power, and detection quadrature.

it is surely significant.

Calibrating a non-detuned interferometer (such as a broadband RSE interferometer) avoids many of these issues and reduces the problem to one similar to that encountered in initial LIGO.

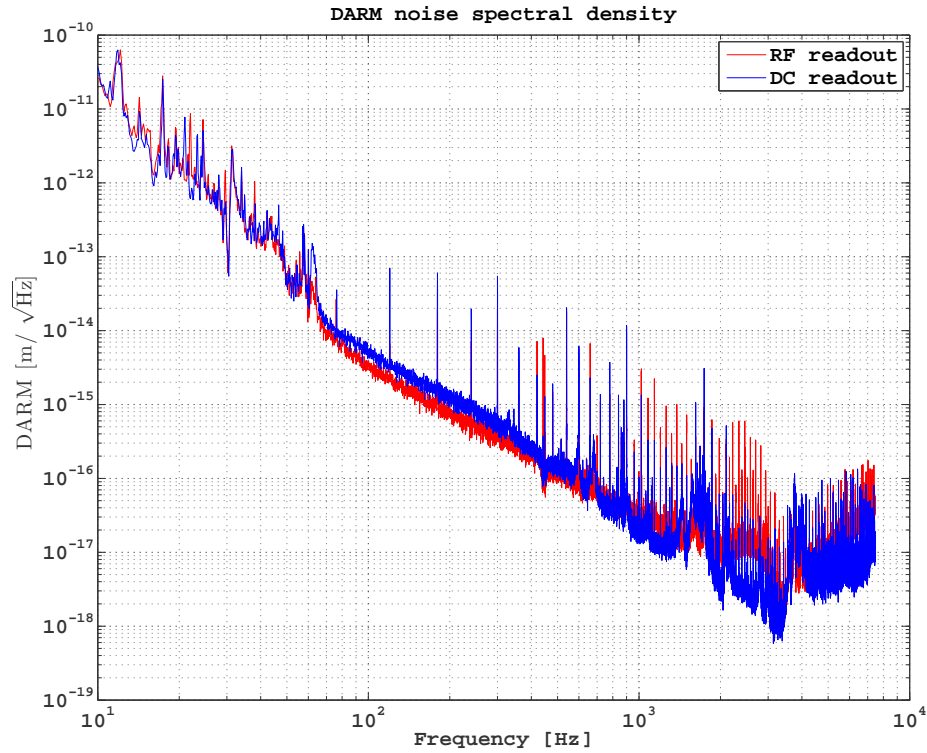


Figure 7.6: DARM noise spectra for a detuned RSE interferometer. The two traces are for RF (red) and DC (blue) readout. The noise below  $\sim 1\text{kHz}$  is common; any differences are due to calibration errors (probably uncertain estimates of the readout quadrature) from the auto-fit routine. There are many 60 Hz harmonics. At low frequencies, the structure is due to environmental noise couplings, both in the auxiliary length loops and the local damping loops. From 70 Hz to  $\sim 1$  kHz, the noise is from the digital-to-analog converters which drive the test mass actuators, above that it is sensing electronics noise. There are also two systems of apparently acoustic resonances around 1.6 kHz and 3.8 kHz. The source of the one at 1.6 kHz is unknown. The one at 3.8 kHz is suspected to be in the piezo-actuated input steering mirrors, but this has not been confirmed. The peaks at 3.8 kHz obscure the resonance in the DARM response at that frequency, which might otherwise be visible. RF readout has higher noise (due to the sensing electronics) above 1 kHz.

# Chapter 8

## Lock Acquisition

Interferometers do not come *prêt à porter*. The test masses (and many other auxiliary optics) in an interferometer are suspended; in the absence of control, they are moving at  $\mu\text{m}$  levels, and so the fields in the interferometer are changing rapidly and unpredictably. This renders the interferometer useless for gravitational wave detection, as the carefully constructed symmetries and frequency responses described in chapter 3 become invalid when the interferometer is not held by the control system at its operating point (to precision ranging from 1 nm to 1 pm, depending on the degree of freedom). Lock acquisition is the process of bringing the interferometer from the uncontrolled state to the controlled operating point. This decidedly difficult problem has been solved independently and differently for each of the interferometers around the world, a consequence of the uniqueness of each interferometer. In this chapter I describe a strategy that has been successfully used at the 40 m prototype to acquire lock of a detuned RSE interferometer. This is currently the only suspended interferometer with five length degrees of freedom (called here DARM, CARM, MICH, PRCL, SRCL) that has been locked, although the plans for advanced interferometers around the world generally include a signal recycling cavity, and so will be five length degree of freedom systems.

### 8.1 Lock Acquisition: The Path to Control

Lock acquisition is the process of bringing a plant from an uncontrolled state to a state controlled by a servo system, when the system is *locked*. For a simple, single control loop, this means that one degree of freedom (DOF) of the plant is being controlled. When the servo is unlocked, this DOF is free to take on any allowed value within its relevant configuration space. It is possible that the transfer functions of the plant ( $P$ ) and more commonly the sensor ( $S$ ) can vary with this DOF, meaning that the servo system may not be stable if the DOF to be controlled is not near the point at which the control system has been designed to keep it. This catch-22 is the problem of lock acquisition.

## 8.2 Lock Acquisition of a Resonant Cavity

With Pound-Drever-Hall (PDH) sensing for a resonant cavity, the proportion of the configuration space where linear error signals exist is about  $1/\mathcal{F}$ .

Thus, for high finesse cavities, the region of configuration space with useful control signals can be quite small. For one of the 40 m arm cavities, with a designed finesse of 1250, a free spectral range characterized by  $\lambda = 1064 \text{ nm}$ , and a typical velocity on the order of  $1 \frac{\mu\text{m}}{\text{s}}$ , the actuator has  $\sim 0.5 \text{ ms}$  to acquire lock; the actuator must be strong enough to apply the force necessary to bring a system in motion to rest within this time. When a cavity passes through a resonance (of the carrier or a sideband) without lock being acquired, the cavity (or light) is said to *flash*.

Some systems can be constructed such that when the cavity flashes, even if lock is not acquired, the motion of the degree of freedom can be slowed or damped. Knowing the functional form of the error signal can also allow one to invert it and then apply the appropriate force to either bring the system back to its resonant point or to brake the system in anticipation of it reaching a resonance at the next FSR. Such systems are typically referred to as guided lock acquisition systems, and have been shown to work for single cavities [89].

An alternative technique is to try to sense the position of the degree of freedom using another method that has a wider linear range; such signals are not always available, however, or may come with additional complications. One possible technique that may be employed in Advanced LIGO, which involves the use of a second laser beam, frequency doubled with respect to the main laser, is described in section 8.7. This technique requires significant additional optical hardware, but it will likely be worth the trouble and expense.

### 8.2.1 Threshold velocity

If we consider only one optic to be moving, the *threshold velocity* is the maximum velocity at which the optic can be moving before a length control based lock acquisition will fail regularly. It is a simple product of the cavity finesse, the mirror mass, and the maximum force an actuator can apply:

$$v_{\text{thresh}} < \sqrt{\frac{F_{\text{max}}\lambda}{2\mathcal{F}m}}. \quad (8.1)$$

This threshold does not apply when actuating on the laser frequency instead of the cavity length. For an interferometer with multiple degrees of freedom, however, that can only be used to acquire one DOF. The threshold velocity (or an even smaller one, due to the increased finesse of coupled cavities) applies to the rest.

### 8.2.2 Normalized PDH locking

The Pound-Drever-Hall error signal has a limited linear range, extending only to the linewidth (FWHM) of the cavity. This limited range can complicate the process of lock acquisition for high finesse cavities. By combining the PDH signal with other information, one can greatly extend the usable linear range of an error signal. The standard technique is a power normalization, in which the PDH error signal is divided by the power transmitted through the cavity, providing a linear slope over a range much broader than the cavity linewidth.

### 8.2.3 Loop Triggering

It is crucial that the control system does not *inject* noise during the lock acquisition process, as such noise is counterproductive and increases the time required to acquire lock. The noise injected by control systems trying to acquire lock is not random noise—it is correlated with the actual motion of the plant. When the sensing chain is nonlinear, this means it can pump energy into the plant much more rapidly than random noise would, and it can quickly make the acquisition impossible by pushing the mirror beyond its threshold velocity.

By triggering the loop (turning the feedback on and off at appropriate times), one can partially avoid this problem and greatly reduce lock acquisition time. For a Fabry-Pérot cavity, a useful monitor signal for triggering is the buildup of power in the cavity, which can be measured by detecting the power transmitted through the end mirror of the cavity. When the transmitted power exceeds a certain threshold, indicating the cavity is near resonance, the control is switched on. The control is switched off when the power falls below threshold. Use of a hysteretic trigger (i.e., Schmitt triggering) helps to eliminate the influence of noise on the switching process. The combination of normalization and loop triggering can reduce the time required to lock a single high finesse cavity by an order of magnitude, from a mean time to lock (MTTL) of minutes to one of seconds. At the 40 m, the triggers turn on the loops when the arm cavity power rises to 20% of its (single-arm) maximum value. An additional Schmitt trigger turns on low-frequency ‘boost’ filter stages when the arm cavity power passes 40% of its maximum.

### 8.2.4 Offset locking

A technique developed at the 40 m useful for acquiring control of high finesse suspended cavities involves using a calculated error signal based solely on the power buildup inside the cavity, which is monitored by measuring the transmitted power. The power in the cavity as a function of cavity length is

$$P = \frac{P_{in} t_i^2}{4r_i r_e} \frac{1}{\frac{\pi}{4\mathcal{F}^2} + \sin^2 \phi}. \quad (8.2)$$

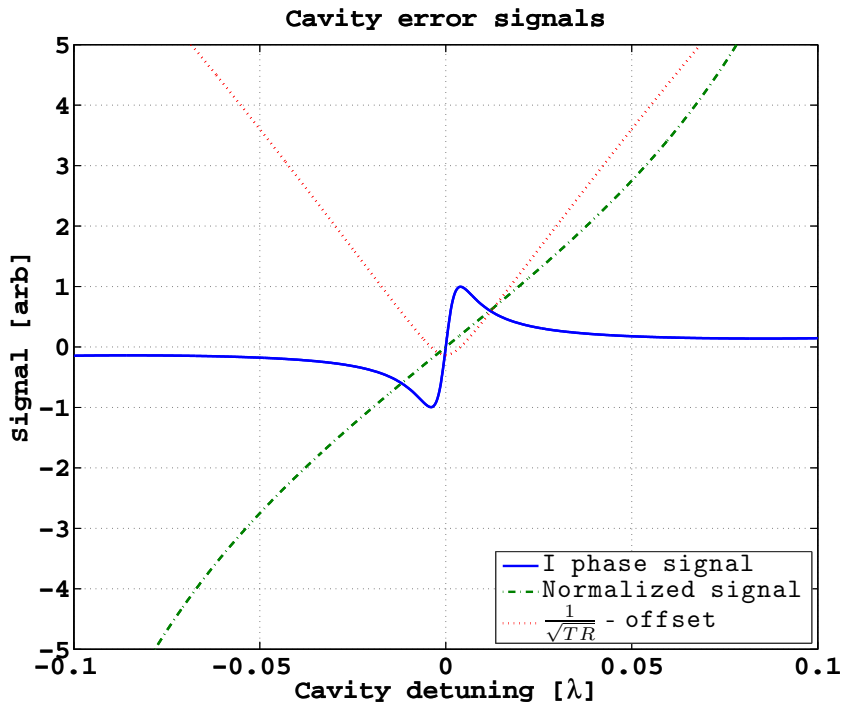


Figure 8.1: Error signals for a single Fabry-Pérot cavity. Shown are a standard PDH signal (solid), a power-normalized PDH signal (dash-dot), and a calculated signal (dash) based only on the transmitted power which passes through zero away from resonance, and which is not influenced by RF sideband light.

For high finesse cavities, the term  $\frac{\pi}{4\mathcal{F}^2}$  is small. Near resonance, where the round trip phase  $\phi$  is near (but not exactly) zero ( $2n\pi$ ), we can neglect the term  $\frac{\pi}{4\mathcal{F}^2}$ , expand the sine and rearrange terms to get

$$\phi \propto \frac{1}{\sqrt{P}}. \quad (8.3)$$

This gives a broad, flat signal adjacent to (but not exactly at) the cavity resonance, which can be seen in figure 8.1. This technique is well suited to locking the cavity at a point where the power buildup is half its maximum.

### 8.3 Lock Acquisition of Coupled Cavities

Lock acquisition of coupled resonant systems can be significantly more complicated than in single cavities. The coupling of the cavities causes each field to be sensitive to the round trip phase of each cavity, as described by the sensing matrix  $\mathbb{M}$  in section 6.3.5.

In order to take advantage of knowledge of a sensing matrix, which links the motion of DOFs to signal gains at optical ports, one must invert the matrix to apply control signals to the appropriate actuators. Inverting the sensing matrix amounts to diagonalizing the multiple input multiple output

(MIMO) control system (at least at a single frequency), which prevents control signals from one DOF from polluting another DOF. A non-diagonalized system with large cross couplings will have undesirable cross-talk between the control loops (cf. appendix E).

Generally, the functions which comprise  $\mathbb{M}$  will be strongly non-linear, making it problematic to invert this matrix for lock acquisition. The chicken-and-egg nature of lock acquisition complicates the inversion problem because a lack of knowledge of the state of the IFO implies a lack of knowledge of the sensing matrix, making it impossible to carry out an inversion.

### 8.3.1 Lock Acquisition for Initial LIGO and Virgo

The first general study of the problem of lock acquisition in coupled resonant systems was done in [84] and also reported in [90], which describes the method used for initial LIGO. Although this work was intended for a power-recycled Fabry-Pérot Michelson, the techniques are in principle extensible to systems with more than four length degrees of freedom. The approach taken is to use secondary signals (such as optical powers) to estimate the sensing matrix  $\mathbb{M}$  and dynamically invert this estimated sensing matrix to get an input matrix. This method brings the interferometer from an unlocked state directly to the operating point. The matrix is re-estimated and inverted continuously, with controls shut off when the matrix is singular. The IFO actually ‘cruises’ through a momentary singularity as power builds up in the interferometer, re-establishing feedback once the matrix is no longer singular. The matrix is calculated and inverted at a single frequency (corresponding to DC).

The process, when working, is dramatic. The IFO will pop about until lock is acquired, and power builds up in the interferometer in the time constant (about 1 s). It is, however, an all-or-nothing technique, and extremely difficult to debug when not working, as properly inverting the matrix relies on fairly precise knowledge of several parameters.

The Virgo lock acquisition protocol is different; it is reported in [91] and described in detail in [92]. Virgo also initially implemented the LIGO protocol of dynamic matrix inversion, but then settled on the variable finesse technique ([91]), which is in some sense a different philosophy: control is initially acquired at location in configuration space that is not the operating point of the interferometer, and the interferometer is then brought to its operating point while under control. This technique initially locks the interferometer with a slight misalignment of the power-recycling mirror, combined with a Michelson offset. Both of these factors serve to reduce the finesse of the interferometer, easing the problem. The Michelson offset is then reduced in a controlled way along with the PRM alignment until the interferometer is at its operating point.

While the dynamic matrix inversion was successful for LIGO, we explored other strategies for use in a detuned interferometer, which has a significantly more complicated control plant involving 5 degrees of freedom and signals with stronger cross-couplings and more complicated frequency response in the control band. The protocol described in the next section, like the Virgo variable-

finesse technique, also involves an initial acquisition which is not at the operating point followed by a controlled migration to the operating point; it was developed independently of the Virgo technique.

## 8.4 Lock Acquisition of a Detuned Resonant Sideband Extraction Interferometer with Power Recycling

One primary mission of the 40 m prototype interferometer is as an exploration testbed for lock acquisition procedures for advanced interferometers, with studies relevant to Advanced LIGO being the most important of these. The Advanced LIGO baseline design includes the use of a Signal Recycling Mirror (SRM) placed at the output port of the interferometer. This mirror couples another cavity to the interferometer, resulting in a significantly more complicated control plant.

The digital control system of the 40 m interferometer allows tremendous flexibility in operating feedback under different conditions in terms of signal routing, analysis, switching, and artificial signal construction (i.e., calculating error signals digitally which could not be simply produced by a purely analog system). This flexibility is extremely useful in constructing a lock acquisition procedure of significant complexity. The digital control system is described in further detail in section 5.4.

## 8.5 Bootstrapping

A crucial aspect of any lock acquisition procedure is the bootstrapping process, whereby one can start from a state with no knowledge of the interferometer, and via a predetermined sequence of steps, can measure or deduce the settings necessary to acquire lock. These settings include such things as DC optical alignment, control loop gains, and control loop triggering thresholds.

In order to lock a suspended interferometer with multiple length DOFs, hundreds of parameters must be determined. It is highly advantageous to be able to determine these settings in a manner which is automated and which does not have any cyclical dependencies, where more than one parameter must be deduced simultaneously.

In this section, we begin the discussion after some of the simpler bootstrapping has been done—this includes roughly aligning the mirrors, setting the demodulation phases (for the single demodulation signals), and determining the feedback filters and gains necessary for locking the subinterferometers (single arm cavity, Michelson, PRMI, DRMI).

### 8.5.1 Interferometer subsets

Bootstrapping depends upon using subsets of the interferometer which are simpler to understand and control. Subsets are created by temporarily grossly misaligning the optics not involved in the

subset. These subsets, along with simple length and alignment error signals, are in table 8.1. These are the signals used during the bootstrapping.

### 8.5.2 Alignment

The first stage is optimizing the interferometer alignment, which is done following the order shown in figure 8.2. Each stage has the minimum number of elements which must be varied to reach an optimum, the order is chosen such that there are no cyclical dependencies, and each stage is simple enough to be simply debugged. No stage has more than three DOFs which must be locked, nor more than one high finesse DOF; this is meaningful, as experience has shown that acquisition time increases dramatically as one goes from three DOFs to four DOFs or when combining independent, high finesse DOFs.

The alignment signals are all (by choice) quadratic in the alignment degree of freedom—they are at a minimum (or maximum) for optimal alignment. The best alignment is thus obtained through dithering an optic in angle at a low frequency (several Hz) and coherently demodulating the alignment signal; this then yields an error signal that is linear in the alignment, and goes through zero at the alignment optimum.

First the transmitted (XARM) arm is aligned; this establishes the input steering alignment and the alignment of ITMX and ETMX. Next is the YARM. This establishes the BS, the ITMY, and the ETMY. Following that is MICH, which can be used for a finer BS alignment, but also is used by locking MICH to bright fringe (instead of the usual dark fringe) to align the steering into the output mode cleaner. This then establishes the output alignment. Next is the PRMI, which uses a SPOB signal to establish alignment of the PRM, followed by the DRMI, which REFL 166Q to establish the alignment of the SRM. Recall that the Q-phase signal in reflection is proportional to the sideband imbalance; since only the  $+f_2$  sideband resonates in the SRC, this is a reasonable alignment signal.

IFO	DOFs	Length	Alignment
Single Arm	XARM	POX 33I	TRX
	YARM	POY 33I	TRY
MICH	MICH	AS 166Q	AS DC
PRMI	MICH	REFL 33I	
	PRC	REFL 33I	SPOB
DRMI	MICH	REFL 33Q	
	PRC	REFL 33I	
	SRC	REFL 166I	REFL 166Q

Table 8.1: Length and alignment error signals for bootstrapping. The length error signals are linear in the degree of freedom, while the alignment signals are quadratic. The best alignment is thus obtained through dithering at a low frequency (several Hz) and minimizing the spectral content of the alignment signal at that frequency.

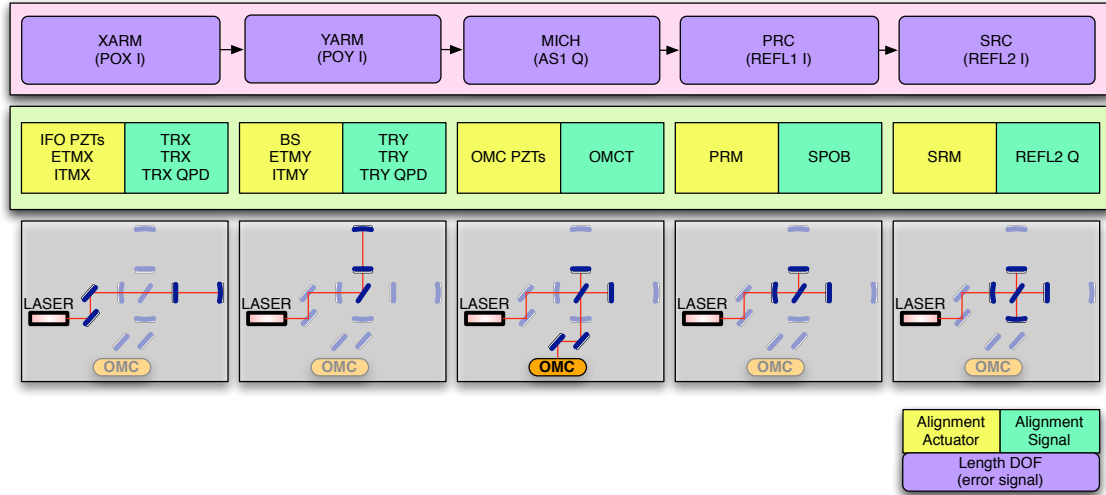


Figure 8.2: Signals and DOFs for bootstrapping the interferometer alignment prior to lock acquisition.

### 8.5.3 Double Demodulation signals

Once the DRMI optics have been aligned, it can be locked again using the initial acquisition signals (table 8.1). This permits the tuning of the double demodulation signals, which can only be done in a DRMI state. While the DRMI is locked using the initial signals, the DDM signal demodulation phases are adjusted to provide zero offset (in the error signal). Note that this is *not* actually the precise demodulation phase where the actual *length* offset will be zero (cf. section 6.3.3), because the single demodulation signals in table 8.2 *also* have offsets resulting from the detuned signal cavity (and RF sideband imbalance) at this point. There is no known way to get around this problem.

After the demodulation phases are set, the length degrees of freedom MICH, PRCL, and SRCL are successively excited at a frequency where the loop gains are low ( $\sim 3 \times \text{UGF}$ ) and the DDM signals are coherently demodulated. This yields a subset of the sensing matrix  $\mathbb{M}$  at the excitation frequency. This matrix subset can then be inverted and used as the input matrix for these degrees of freedom (cf. section 6.3.5).

DOF	Initial Signal	Final Signal
MICH	REFL 33Q	DDM signal matrix
PRC	REFL 33I	
SRC	REFL 166I	

Table 8.2: Hand off of short DOFs. The DDM signal matrix mixes the signals from REFL IM, REFL IP, PO IM, PO IP, AS QM, and AS QP.

## 8.6 The Lock Acquisition Procedure for the Caltech 40 m Interferometer

The lock acquisition procedure developed for the 40 m detuned RSE interferometer will form the basis of the lock acquisition procedure for Advanced LIGO (see [93]), and is presented in detail in this thesis for the first time. The basic scheme of the procedure is to first bring the interferometer into a controlled state at a location in phase space which may not be the final operating point, but can be smoothly connected via a known path (each point of which has useful control signals for all DOFs) to the operating point. The definitions of the DOFs can be seen in figure 3.10. This procedure is shown graphically in figure 8.5. The first demonstration of this approach was developed in the summer and fall of 2005 and briefly reported in [63] and [94]. This approach was chosen because it allows mostly independent sensing of all five degrees of freedom (i.e., the sensing matrix is mostly diagonal at the acquisition point), eliminating the need for a dynamically inverted sensing matrix.

### 8.6.1 Initial Acquisition

There are five DOFs to be acquired, each with an error signal as denoted in table 8.3. Each respective loop is controlled by a single error signal, and the output of each loop is switched on/off by a trigger. Thus, at this stage, each loop is essentially independent (although MICH and PRC are triggered by the same signal). The typical order of acquisition of these five DOFs can be seen in figure 8.5 to be (MICH/PRC, SRC, X/Y)—thus, typically the DRMI locks followed by the two ARMs, which lock individually. The three short DOFs (MICH, PRCL, SRCL) are locked at their operating point. The two ARMs are locked off-resonance (using the offset locking technique described in 8.2.4), by the same amount, each somewhat longer than nominal; the actual locking point is set to be one-half the single cavity buildup. A typical example of this acquisition is shown in figure 8.3. After this, the interferometer is locked at its *acquisition point*, which in this procedure differs from the operating point by a significant length offset in the CARM degree of freedom. Removing this CARM offset is the purpose of the rest of the protocol, described in section 8.6.3.

Note that none of the signals listed in table 8.3 are the same as the signals listed in table 6.4, which are used at the operating point. The initial signals were chosen for their independence of other DOFs, the existence of easily characterized and useful trigger signals, and the ability to easily bootstrap them. Also important is independent sensing for the two arm cavities — it is much easier to lock the arms independently than to try to lock CARM and DARM directly.

In the current implementation, this first stage is statistical in nature, with a non-deterministic period of waiting before all five DOFs can be brought under control. The distribution of times to wait for this stage to be completed is shown in figure 8.4. These waiting times apply during the night (from about 10 pm to 4 am, when anthropogenic noise is at a minimum); the wait is much

DOF	Control Signal	Trigger
SRC	REFL166 I	REFL166 Q
PRC	REFL 33 I	SPOB
MICH	REFL 33 Q	SPOB
XARM	$1/\sqrt{TRX}$ - offset	TRX
YARM	$1/\sqrt{TRY}$ - offset	TRY

Table 8.3: Control signals and loop triggers for initial lock acquisition of the 40m detuned RSE interferometer. These are the control signals used to bring the interferometer from an initially uncontrolled state to state A. The output of the control system for each DOF is independently switched on/off according to the value of the signal in the *Trigger* column.

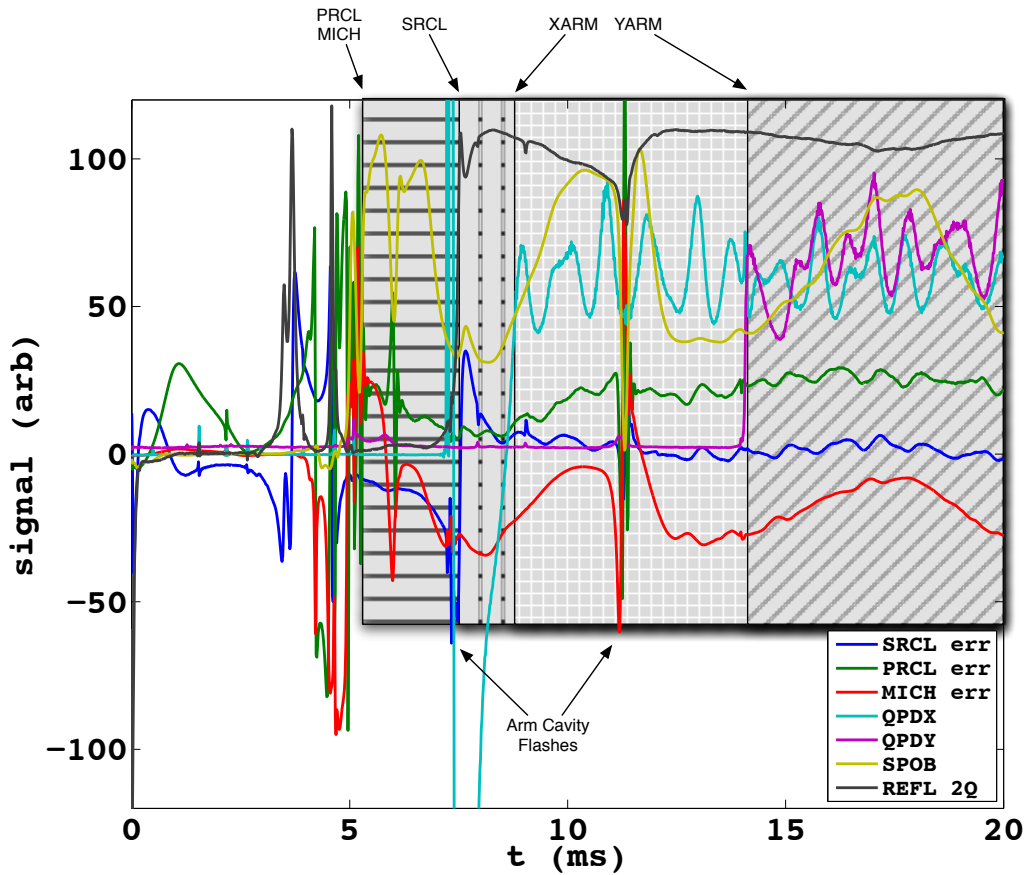


Figure 8.3: A typical initial acquisition (Step A of section 8.6). Shown are the error signals for MICH, PRCL, and SRCL, the trigger signals for MICH/PRCL and SRCL (SPOB and REFL 2Q, respectively), and the two arm cavity powers (QPDX and QPDY). The acquisition sequence is MICH/PRCL (indicated by the SPOB level), followed closely by SRCL (indicated by the REFL 2Q level), then the two ARM cavities (XARM and YARM). Also shown are two arm cavity flashes, which disturb the error signals for the short DOFs but do not destroy the lock; the bandwidths of the control loops for these are purposely kept low at this stage so that high-frequency signals (such as due to the high-finesse arm cavity flashes) will not destroy the lock.

longer during the daytime. The  $\sim 30$  second gap near zero wait is about how long it takes for some of the scripts which ‘reset’ the interferometer (more in section 8.6.6) to run; not all of these scripts always need to run, however, which is why there are a few times shorter than this.

Lock wait times which are longer than 15 minutes are excluded from the data, as that usually happens when something is broken or not reset properly, and so are not indicative of the statistical waiting times.

## 8.6.2 The spring and the anti-spring

For the DARM DOF, reversing the direction of the detuning in the SRC can change the optical response from one that is an optical spring to one that is an anti-spring (cf. section 3.11.3).

Switching the SRC detuning from positive to negative can be accomplished experimentally in this setup by choosing whether the upper or lower  $f_2$  RF sideband resonates in the SRC; we can choose between  $+f_2$  and  $-f_2$  by monitoring the sign of the REFL  $f_2$  Q-phase signal (cf. figure 3.6), which is conveniently used as the on/off trigger for the SRCL loop. This also requires sign changes in any loops whose error signals are derived from the  $f_2$  sideband (such as the DDM error signals). In addition, we must also lock with a CARM offset in the other direction, so the locking loops for the arm cavities, based on the offset locking signal in section 8.2.4, must also change sign.

Detuning the CARM DOF in different directions results in similar springlike behavior, with repercussions for the control of CARM (more in section 8.6.4). The particular set of lock acquisition signals for the initial acquisition listed in table 8.3 actually links the springs in CARM and DARM. By examining the points in configuration space where both ARM transmitted powers are at the nominal acquisition point (one-half the buildup achieved in a single arm state) and writing down a signal matrix for sensing the lengths of the two ARMs, derived from the transmitted powers, we can infer which of those points might be reasonable choices for locking. As can be seen in table 8.4, when the SRC is detuned to create a spring in DARM and the ARMs are detuned for a CARM anti-spring, the signal matrix is dominated by off-diagonal elements. This does not make the system impossible to control, but it does make it unlikely that lock of both degrees of freedom could be acquired. The upshot is that the procedure described in section 8.6.1 links the CARM and DARM springs, so that both must be dealt with at once, or neither.

### 8.6.2.1 Locking the spring and the anti-spring

During development of the lock acquisition procedure, it was discovered that the spring mode and the anti-spring mode (for DARM; more in section 8.6.2) have different statistics for initial acquisition. More specifically, the MTTL is much longer for the spring mode than for the anti-spring mode, a discrepancy which remains unexplained. Since the circulating power in the arms is very low at the acquisition point, radiation pressure effects are an unlikely culprit. Modeling work has not

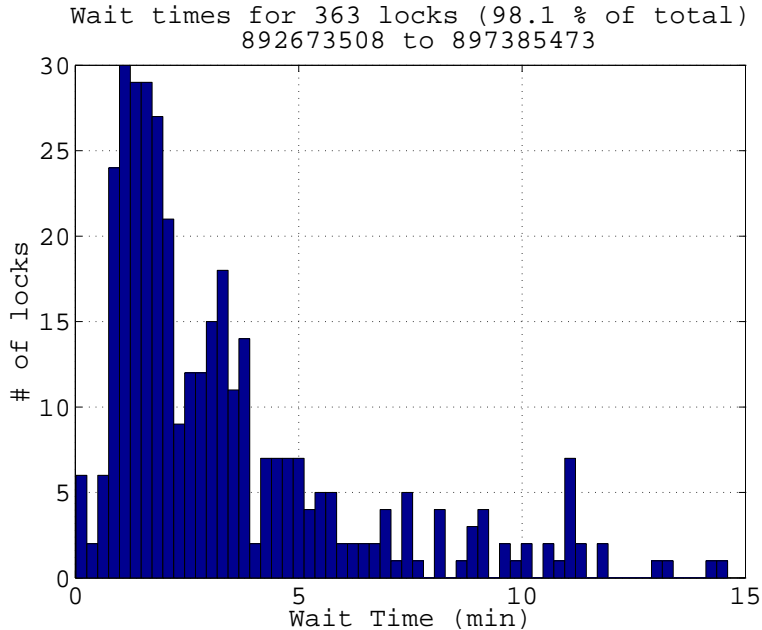


Figure 8.4: Histogram of waiting times to acquire initial control of five length degrees of freedom. Lock wait times longer than 15 minutes are excluded from the data. These statistics are for the anti-spring configuration; the spring configuration takes longer (cf. section 8.6.2). These waiting times were all measured between about 10 pm and 4 am on multiple nights.

		+detune		-detune	
		XARM	YARM	XARM	YARM
+CARM	TRX	2.8	5.3	4.7	3.1
	TRY	5.3	2.4	3.1	4.8
-CARM	TRX	4.6	3.2	2.7	5.3
	TRY	3.2	4.9	5.3	2.5

Table 8.4: Four sensing matrices for the individual arms (XARM and YARM) detected at the transmitted ports (DC). The numbers are in mWatts/pm, and the sensing matrices are at possible offset-lock points. Note that two matrices have larger diagonal elements, and two have larger off-diagonal elements.

confirmed the primary suspicion of higher-order modes of either the carrier or RF sidebands resonating differentially in the arms. The second suspect is higher-order modes in the recycling cavities; we do not know with any precision the Gouy phases of the recycling cavities, but with the design values there is a different modal structure in the signal recycling cavity for the two configurations. This hypothesis is also consistent with the strong sensitivity to alignment of locking wait times that has been observed in both configurations. In addition, it has been observed that the MTTL in a configuration even without arm cavities (DRMI) is slightly longer for the spring mode than the anti-spring mode. This lends further weight to the culprit being HOMs in the recycling cavities.

Methods which are more deterministic in nature (i.e., the MTTL is very short) are currently being studied at the 40 m and are discussed in section 8.7.

### 8.6.3 The Protocol

#### Step A: Acquire lock

The first step is to bring the interferometer under control; here the interferometer goes from a globally uncontrolled state (the local control systems are always operational) to a globally controlled state. This step has already been described in section 8.6.1.

#### Step B: Hand off control signals for short DOFs

Once all 5 DOFs of the interferometer are being actively controlled using the signals in table 8.3. The sensing of the short DOFs is now handed off to the signals shown in table 8.2, which are the final signals for these DOFs. These signal transitions are done digitally, enabling a smooth wipe. The gains of these short DOF loops are ramped up and low-frequency boosts are engaged.

#### Step C: $X_{DC} + Y_{DC}$ to $DARM_{DC} + CARM_{DC}$

Once the short DOFs are stably controlled, control of the arm cavities is switched from separately sensed (using  $X_{DC}$  and  $Y_{DC}$ ) and controlled lengths to the common and differential lengths (CARM and DARM). The CARM and DARM signals are closely related to the single arm signals, and are calculated in a similar manner using the transmitted power from the arm cavities:

$$X_{DC} = \frac{1}{\sqrt{TRX}} - \text{offset}, \quad (8.4)$$

$$Y_{DC} = \frac{1}{\sqrt{TRY}} - \text{offset}, \quad (8.5)$$

$$DARM_{DC} = \frac{TRX - TRY}{TRX + TRY}, \quad (8.6)$$

$$CARM_{DC} = X_{DC} + Y_{DC}. \quad (8.7)$$

This decomposition more closely resembles the final configuration, and making the transition at this stage simplifies the process of the bringing the arms into full resonance. Since the point reached in step A is one where both arm cavities are detuned from resonance in the same direction and by the same amount, there is effectively an offset in the CARM DOF. The rest of the lock acquisition process involves reducing and finally removing this CARM offset. The calculated signals can also be seen in the purple portion of figure 8.5. At this stage an adaptive compensation filter for the CARM servo loop is engaged; it is described in section 8.6.4.

#### Step D: Hand off control of DARM

The  $DARM_{DC}$  signal calculated from the arm cavity powers is a noisy signal and designed only for temporary use. Thus, at this earliest opportunity, we take advantage of the fact that

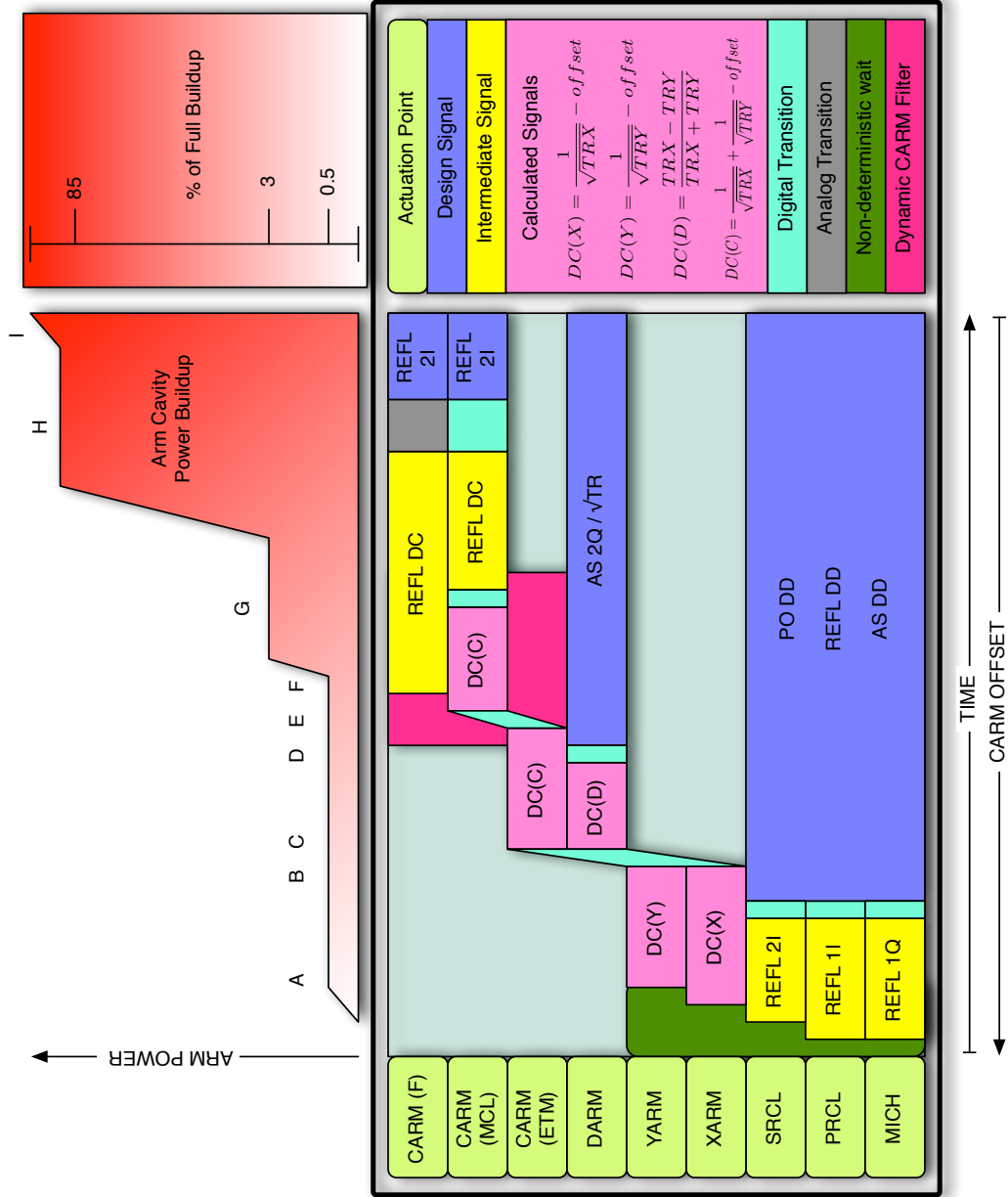


Figure 8.5: The sequence of error signal usage and transitions in the lock acquisition process developed for the 40 m RSE interferometer. The statistics of the non-deterministic stage (shown in green) can be inferred from figure 8.4. The letters refer to the descriptions of the procedures in the text in section 8.6

there is no offset in the DARM degree of freedom, and transition control of DARM directly to its final design signal. This can be the RF DARM or a DC Readout DARM (based on the transmission of an OMC). Each of these has advantages and disadvantages. As the CARM offset is reduced during the remainder of the lock acquisition process, the RF DARM signal will undergo a shift in demodulation phase as the CARM offset is reduced. This is because the CARM offset is primarily held constant by keeping the arm cavities off resonance, and the phases of the fields reflected from the arm cavities rotate as they approach resonance. The two arms rotate in such a way that at the asymmetric port of the IFO, the field amplitudes continue to cancel, but the phase angle at which a field due to DARM motion would appear is rotating. This is shown schematically using a phasor diagram in figure 8.6. The DC Readout DARM signal also undergoes changes as the CARM offset is reduced and the power in the IFO increases: the gain of the signal increases, and the DARM offset required for DC Readout changes if the setpoint in the DARM loop is determined by power transmitted through the OMC. If the setpoint is adjusted to keep the DARM offset the same, the increased power at the asymmetric port will cause the gain of any loops pertaining to controlling the OMC (in both length and alignment) to increase, and so some compensation will be required to keep these loops stable. We choose to use RF DARM for this stage, mainly because one offset (CARM) is simpler to keep track of (and model) than two (both CARM and DARM).

#### **Step E: Hand off control of CARM to MCL**

At this stage, the residual frequency noise of the laser is large enough to be problematic for maintaining control of the interferometer, in part because the signals used at this stage are more sensitive to laser frequency noise than the signals used at the operating point. To counter this, we begin the process of matching the laser frequency to the common arm length (CARM), using the Common Mode (CM) servo (cf. section 5.7). The first step in engaging the CM servo is to take the error signal which senses the CARM DOF and feed it back to the input mode cleaner length (MCL path). This ensures that the mode cleaner length and the common arm length share a common resonant frequency; as the laser frequency feedback is following the mode cleaner length, the laser frequency is now also matched to the common arm length, within the bandwidth of the MCL path ( $\sim 100$  Hz).

#### **Step F: Engage frequency path of CM servo**

Above  $\sim 100$  Hz, the suspended mode cleaner provides a quiet reference for the laser frequency, and thus the laser frequency is altered to match the mode cleaner length. The feedback of the high-frequency path of the CM servo injects a signal into the error point of the mode cleaner servo, generating an additive offset (AO). The mode cleaner servo then acts to suppress the sum of its error signal and the AO, causing a mismatch of the laser frequency and the mode

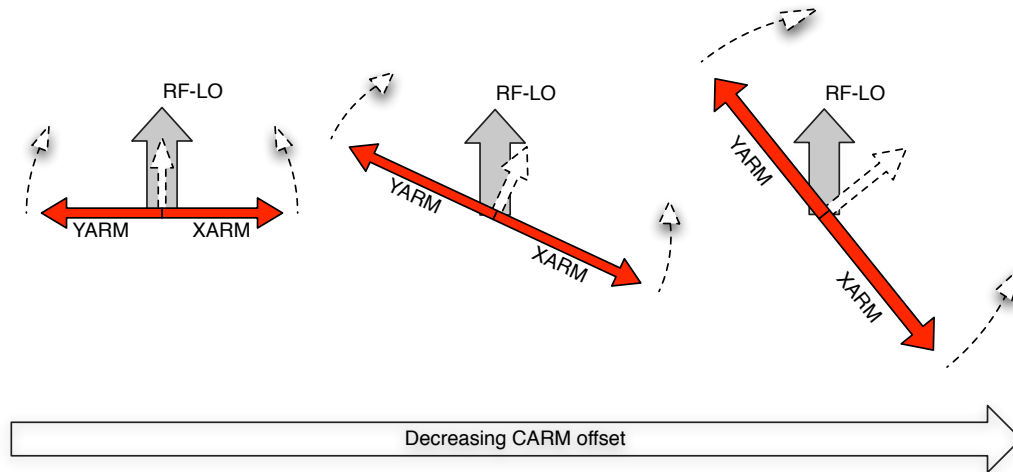


Figure 8.6: As the CARM offset is reduced, the arm cavities move closer to resonance, causing the phase of the reflected fields to rotate. Since the angle of the RF local oscillator is set by the demodulation phase, it does not rotate with the change in CARM offset. The dotted lines indicate arm cavity motion in a differential arm (DARM) mode.

cleaner length. The laser frequency is matched to the common arm length, however, within the bandwidth of the CM servo (several kHz). Once a high enough bandwidth is achieved, the adaptive CARM compensation (discussed in section 8.6.4) can be turned off. We need the frequency path (MCF-AO) to have a very high bandwidth, it is necessary to find an analog signal which has the appropriate properties (e.g., it is sensitive to the mismatch between the laser frequency and the CARM length, over a range of CARM offsets, with a frequency response that does not change radically). Calculated signals such as that used for length feedback to the ETMs ( $CARM_{DC}$ ) cannot be used because the sampling rate of the digital control system is too low (16384 Hz). One signal which meets these requirements is the reflected light-power level (known as  $REFL_{DC}$ ). Because the CARM DOF is offset from resonance, this signal is sensitive to the CARM-laser frequency mismatch. This signal is fed back to the laser frequency (after AC coupling, of course) to the AO path of the CM servo. It is necessary to appropriately match the relative gains of the frequency and length paths in order to ensure servo stability at the crossover frequency.

### Step G: Increase CM Servo bandwidth and reduce CARM offset

Once the bandwidth of the CM servo is significantly greater than the peak in the CARM optical response, the CARM offset can begin to be reduced. This increases the carrier light power circulating in the IFO, and so any control loop gains which are sensitive to the carrier

power must be adjusted to keep the loops stable. This includes the CM servo, as the gain in the AO path (sensed by  $REFL_{DC}$ ) will increase. The gain in the AO path can be reduced to compensate, or it can be set in step F such that there is enough headroom to accommodate the increase.

#### **Step H: Hand off CARM to RF**

Once the CARM offset has been reduced to the point where the buildup of power in the IFO is greater than half its final value, the standard, RF, PDH-style signals designed for sensing CARM will come within their linear range, and can be used for controlling CARM. Care must be taken at this stage to understand (through modeling) the frequency response of the DC and RF signals to ensure that they have compatible frequency response (the MCL-AO crossover must be stable for both signals). The MCL feedback can be transitioned to an RF based signal digitally, while the MCF feedback (which uses an analog signal) must be transitioned using a cross-fade amplifier; the latter is available in the common mode servo electronics. These transitions should happen approximately simultaneously; the scripts used at the 40 m transition the digital portion halfway, then transition the analog portion halfway, finish the digital portion and then finish the digital portion. Only the digital path has gain at DC, so it is not difficult to add an offset to the RF error signal to ensure a smooth signal transition without actually changing the offset in CARM; because the analog path has no gain at DC, it does not require an offset.

#### **Step I: Remove CARM offset**

Once the CARM loop (including the CM servo) is using the RF signal, the remaining CARM offset is removed and the IFO is brought to its operating point. At this stage the controls system is in its final configuration. All that remains is to apply any low-frequency boost stages that are not already engaged.

During this whole procedure, the primary observable change is a steady ramp in the power circulating in the interferometer, as shown in figure 8.8.

#### **8.6.4 Adaptive compensation filter: the moving zero**

While the interferometer is locked with a CARM offset, it is effectively operating as a low-power double detuned interferometer. Referring to figure 3.7, for DARM the detuning is in the short degree of freedom ( $l$ ), while for CARM the detuning is in the long degree of freedom ( $L$ ). The detune of the CARM degree of freedom creates a complex optical response which can impact the stability of the feedback loops which control the interferometer cavity lengths.

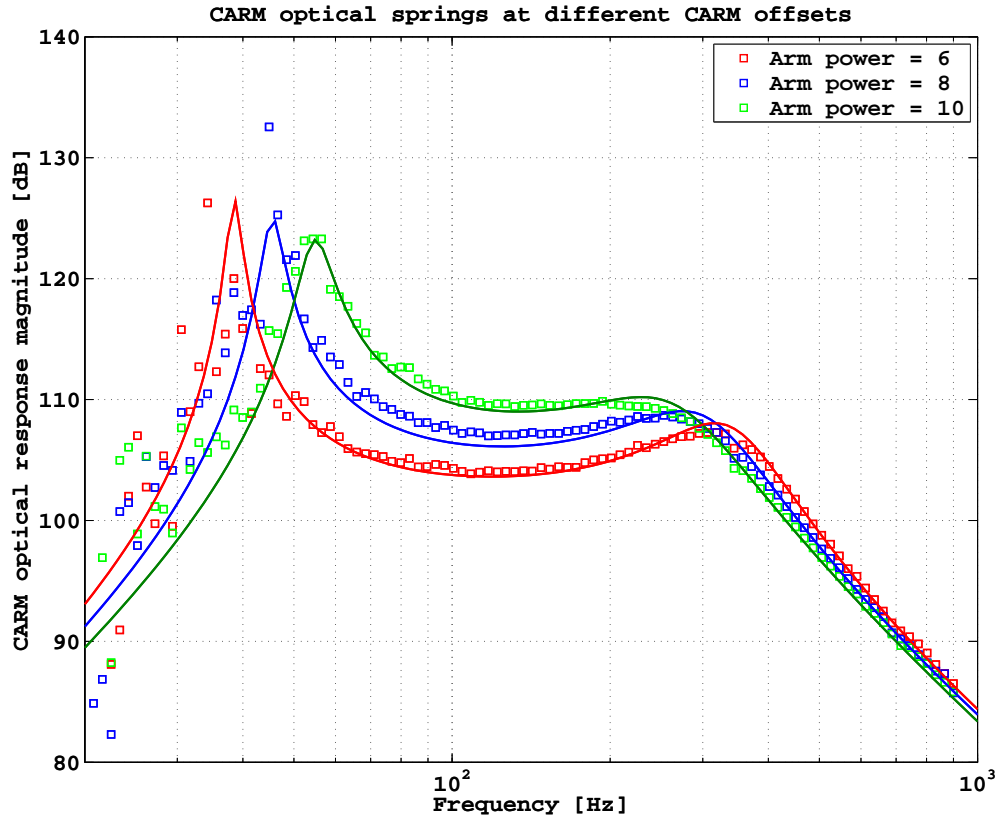


Figure 8.7: The optical response (magnitude only) of the CARM DOF at several CARM offsets. As the CARM offset is reduced and the circulating power increases, the peak in the optical response moves toward lower frequencies while the opto-mechanical spring resonance moves toward higher frequencies. Experimental data are shown in dots; the solid line is a simulation.

As the CARM offset is reduced, the detuning of the CARM degree of freedom changes, causing a change in the optical plant. This change takes the effect of a complex pole in the response function (the peak in the optical response) moving from a relatively high frequency (at  $\sim 1$  kHz) towards the on-resonance common mode coupled cavity pole (at  $\sim 100$  Hz). The digital control system at the 40 m (cf. section 5.4) generally limits UGFs to a maximum of about 400 Hz, so this particular sweep of frequencies carries this complex pole right through the UGF of the CARM loop. This creates an excess phase delay which degrades the stability of the control loop. To prevent this, a digital filter which adapts to the changing response was implemented. This filter is composed of a flat path summed with a path rising like  $f^2$ . The flat path is gain adjusted by being divided by the current buildup of power in the arm cavities. Thus, as the power builds in the interferometer, this division compensates the increasing optical gain. The path which rises like  $f^2$  is not gain compensated, however, and so as the power builds in the interferometer the crossover frequency of the  $f^0$  path and the  $f^2$  path moves downward in frequency along with the pole in the coupled cavity response.

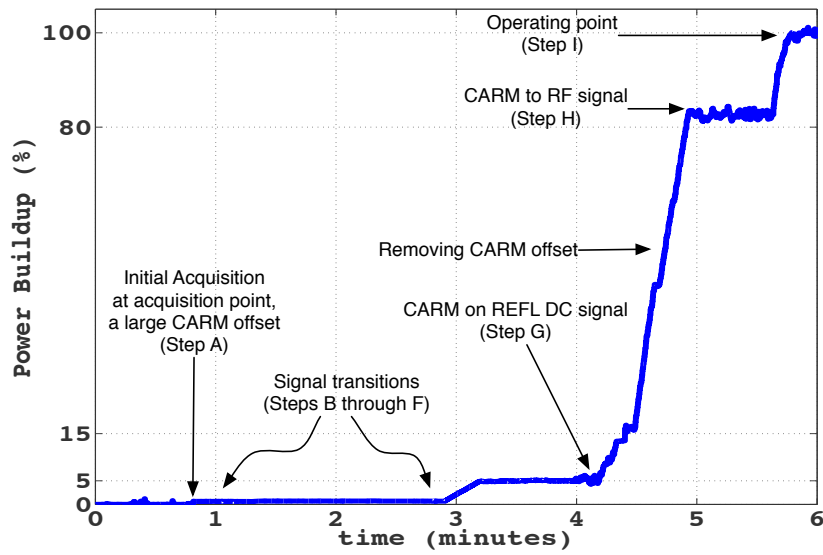


Figure 8.8: The power in the interferometer gradually increases as the CARM offset is reduced during the lock acquisition procedure. This plot is a time trace of the power in an arm cavity; compare to the top of figure 8.5.

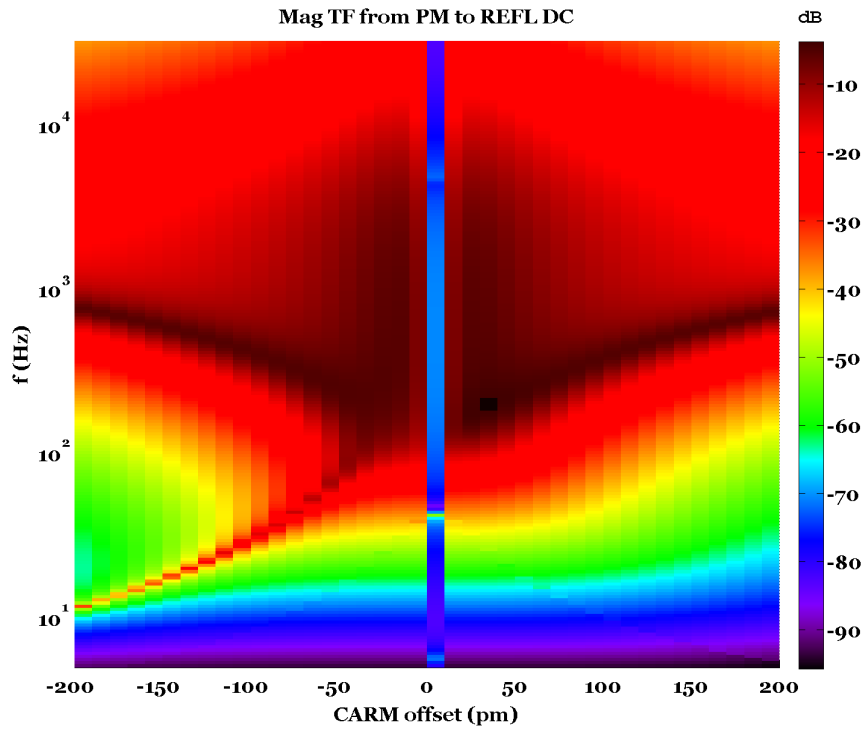


Figure 8.9: dB magnitude of the CARM (sensed at  $REFL_{DC}$ ) open-loop opto-mechanical frequency response to input laser phase noise shown as a function of CARM offset.

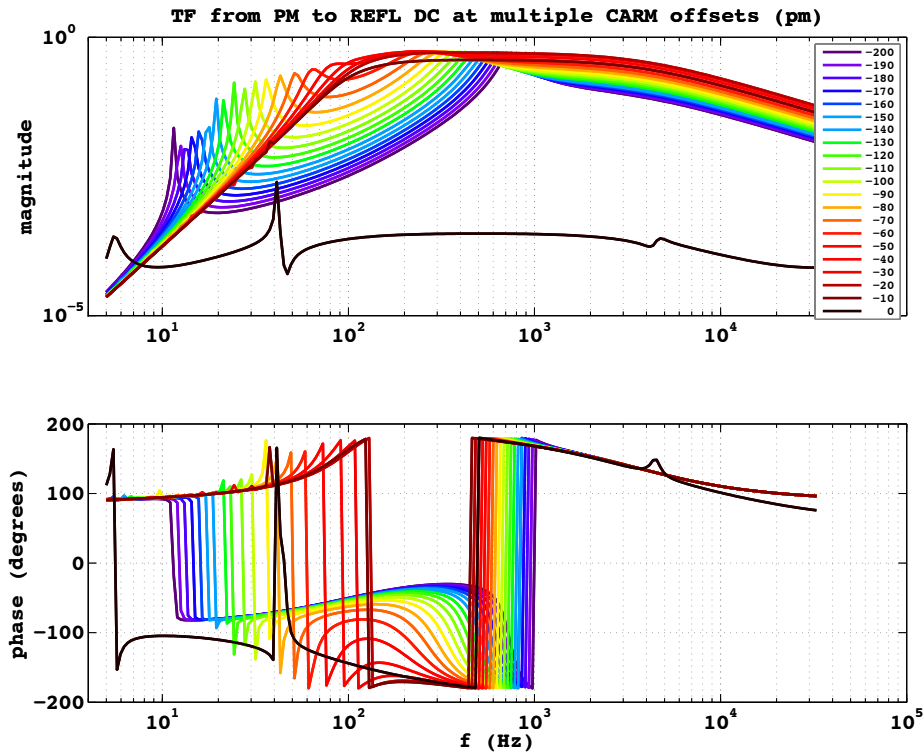


Figure 8.10: Bode plots of the opto-mechanical frequency response of  $REFL_{DC}$  to input laser phase noise, at various CARM offsets. This selection shows a series of offsets which lead to spring behavior in CARM; offsets from resonance in the other direction would exhibit anti-spring behavior.

Figure 8.12 shows the action of this compensating filter with several transfer function measurements detailing the CARM cavity optical response at different CARM offsets, along with open-loop transfer functions which show the action of the compensation filter (since they do not change significantly).

This technique is limited however; eventually the rising control signal amplitude at high frequencies will saturate the digital to analog converters. Thus, this compensation filter is only used until the AO path (Step F in section 8.6.3) has increased the CARM servo bandwidth enough that the phase delay at a few hundred Hz no longer impacts the overall loop stability. The period where it is applied is shown in figure 8.5.

### 8.6.5 Other Protocols

This protocol has proved successful; many others were tried, however. These other trials included numerous attempts at mis-alignment techniques such as that employed in Virgo (where the power-recycling mirror is slightly misaligned). It turns out, however, that the most important part of Virgo's variable-finesse technique is actually the Michelson offset which allows light to leak out the asymmetric port. In a signal recycled interferometer, such a MICH-offset technique does not actually

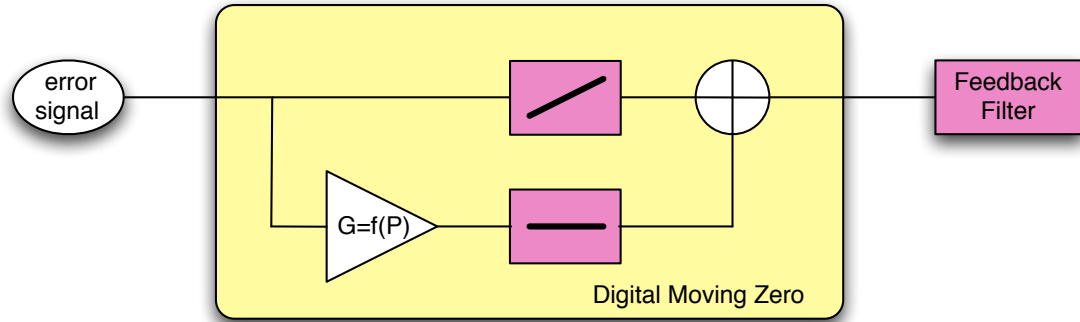


Figure 8.11: The topology of the compensation filter used in the CARM loop. A path rising like  $f^2$  is combined with a path having flat response; the sum is complex zero near the crossover frequency. This compensates the complex pole in the CARM optical response. The function  $G = f(P)$  is  $P_{tr}^{-1/2}$ , after  $P_{tr}$  has been heavily low-pass filtered.

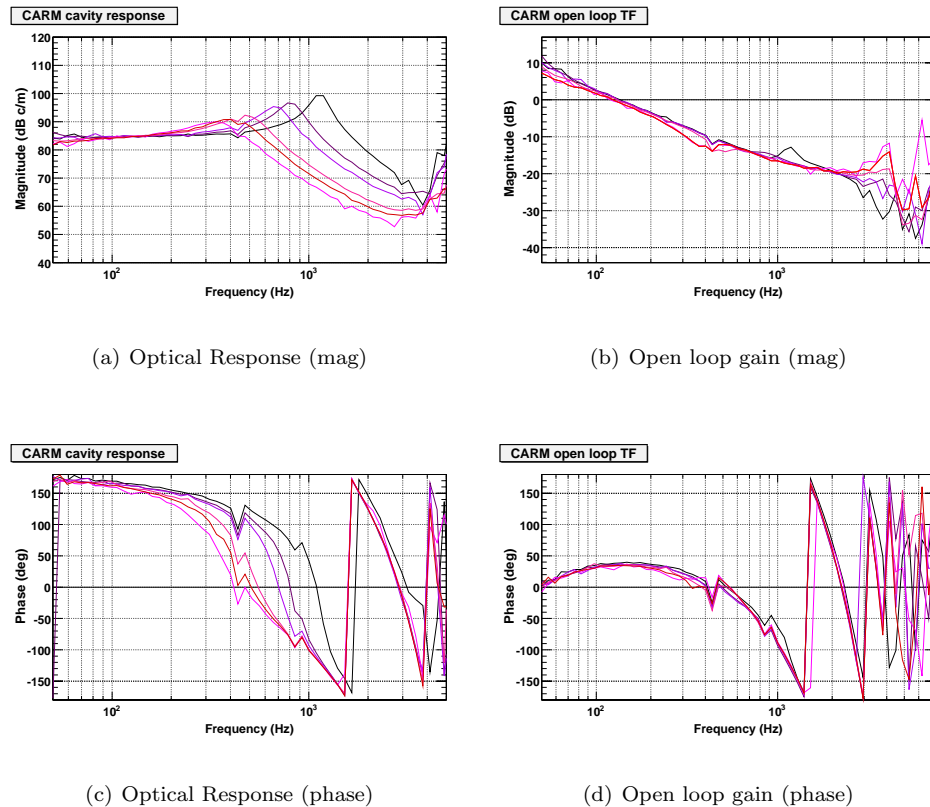


Figure 8.12: CARM cavity response and open loop transfer functions (near the UGF) for different CARM offsets. The dynamic cavity-pole compensation filter can be seen to be working, as the change in the open loop transfer function is much smaller than the changes in the optical response. The phase is plotted such that the loop is unstable at  $0^\circ$  (rather than the usual  $-180^\circ$ ).

reduce the finesse, since the leaked light is re-injected to the interferometer by the signal recycling mirror. In a detuned interferometer, it would only *increase* the cross-coupling of the degrees of freedom, which is exactly the opposite of what we want.

In a power-recycled configuration, both mis-alignment techniques and Michelson offset techniques showed early success for initial acquisition. A complete procedure based on these techniques was never developed, however, because: (1) there is little desire to change the technique used for Initial LIGO, and (2) even without them, the initial acquisition was very rapid (seconds rather than the minutes seen in figure 8.4 for a dual-recycled interferometer) for the CARM offset technique used for the signal recycled interferometer.

### 8.6.6 Scripting Tools

The lock acquisition procedure developed relies heavily on scripting tools to automate and coordinate repetitive and routine tasks. Figure 8.13 is a flow diagram of the master locking script, which calls subscripts as described in figure 8.14. The main script watches the transmitted powers in the arm cavities; when both arm powers are above threshold (meaning the IFO is at the acquisition point), it initiates the sequence to remove the CARM offset. When the arm powers fall below threshold, that means that lock has been lost and so the script initiates the re-setting of all the IFO parameters for initial acquisition.

## 8.7 Deterministic Locking

The long tail of the distribution of waiting times for acquiring initial lock shown in figure 8.4 motivated attempts to develop an alternate lock acquisition scheme which would be largely deterministic. Without continual, complete knowledge of the microscopic state of the interferometer, a truly deterministic lock acquisition process is impossible (and, moreover, unnecessary). *Deterministic locking* is thus a process which appears deterministic on human timescales—any statistical variations in process length are on the order of seconds rather than minutes. Such a process is a holy grail of lock acquisition, sought by gravitational wave interferometer scientists and commissioners the world over. It has many benefits, including reduced commissioning time (and consequently greater observation time), easier debugging of hardware and software, and much reduced frustration and boredom of detector operators. As discussed in section 8.6.5 some effort was expended at the 40 m to find a deterministic locking process for a power-recycled Fabry-Pérot Michelson interferometer (LIGO and Enhanced LIGO) configuration; promising candidates were found but not pursued, as the straightforward application of the procedure in section 8.6 was already quite fast. Furthermore, significant effort was expended at the 40 m to find a deterministic locking process for a dual recycled Fabry-Pérot Michelson interferometer, as such a technique could be very useful for Advanced LIGO. No

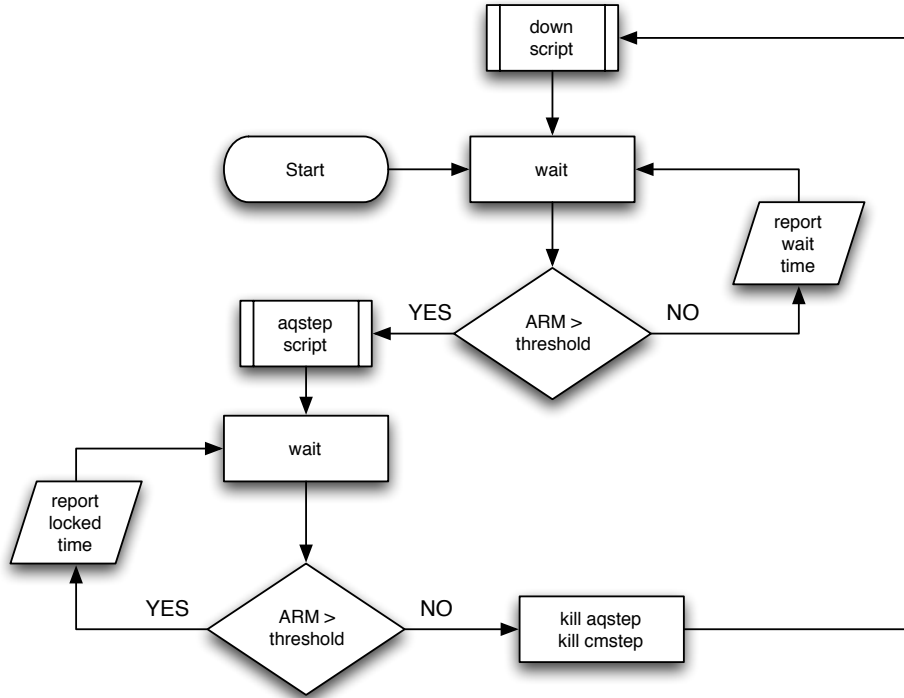


Figure 8.13: The flow of the main watch script used for locking.

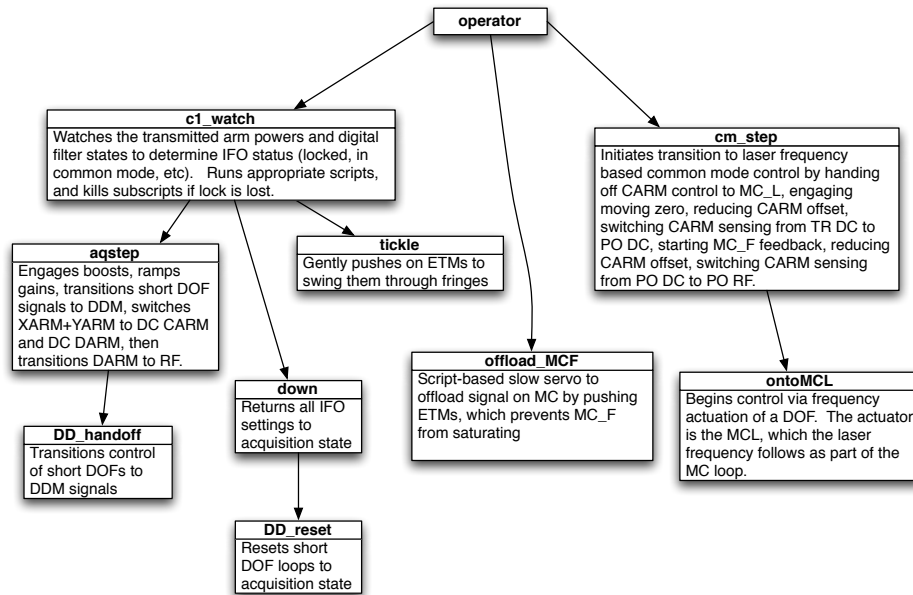


Figure 8.14: The hierarchy of scripts used for automating lock acquisition of the 40 m.

promising candidates were found, which serves to underline the added complexity in the controls plant introduced by the technique of signal recycling.

The failure to find a deterministic locking procedure for the 40 m has prompted the serious consideration of significant auxiliary hardware, such as secondary interferometers (operating in a different color or polarization) which are dedicated to providing signals for lock acquisition. The goal is to be able to sense robustly each single DOF without interference from the other DOFs, and without causing interference to the other DOFs. Such an approach, which strives to reduce the dimensionality of the initial, statistical stage of lock acquisition, can greatly reduce the MTTL. Essentially, the goal is to reduce the problem of inverting an  $n \times n$  matrix to inverting  $n$   $1 \times 1$  matrices. A promising candidate strategy is described in the next section, and it will soon be prototyped at the 40 m lab.

### 8.7.1 The Future: It's easy being green

The primary difference between the scheme proposed below and the scheme described in 8.6 involves replacing step A with a version which is deterministic in nature.

The 40 m experience has demonstrated that it is not difficult to lock a 3 DOF system such as the DRMI, provided there is an appropriate selection of signals and the recycling cavities are of sufficiently low finesse, which is the case for the current Advanced LIGO design. In order to have an essentially deterministic locking scheme for Advanced LIGO, it should thus be sufficient to improve the locking time of the arm cavities, which can be accomplished with the addition of some auxiliary hardware dedicated to lock acquisition.

The basic idea is to quadruple the number of laser fields. For a primary laser (i.e., the one that will be used during interferometer operation) operating at 1064 nm, we would add

- A laser field frequency doubled from the main (PSL) laser (so at 532 nm—green).
- Two additional 532 nm lasers at the transmitted ports of the two arm cavities.
- Dichroic coatings for the ETMs ( $T \sim 0.9$  for 532 nm).
- Dichroic coatings for the ITMs ( $T \sim 0.99$  for 532 nm).

The benefits of this additional hardware include (more details in the following)

- Multiple lasers allow truly independent sensing of the two arm cavities.
- Independent velocity damping of arm cavities can be done when they are not resonant for the main carrier field.
- Dichroic coatings break the degeneracy of acquisition and detection finesesses.

- Green light + wedged optics allows excellent isolation of the arm cavities from other degrees of freedom, and helps to isolate the arms from each other.

With these benefits, the basic plan would be to lock the arms first using the green laser, then lock the short degrees of freedom in the same manner as is already done at the 40 m.

### 8.7.1.1 Envisioned lock acquisition procedure

At each end station, the green laser will be phase modulated, and the field injected into the arm cavity through the ETM. With the ITM having a highly reflective coating for green light, this system now forms a low-finesse, overcoupled cavity, and a standard PDH based length sensing and control scheme can be easily applied, with the feedback to the green laser frequency, which must be a fast actuator (a PZT). This fast actuator combined with a low-finesse cavity will make for tremendously simple lock acquisition. The feedback loop should only be limited by the range of the frequency actuator, which should be at least several tens of MHz. Such a range corresponds to many free-spectral ranges of the arm cavity.

Now the green laser is resonant in the arm cavity; the transmitted field (exiting the ITM toward the BS) can be picked off and directed to a photodetector, where it can be heterodyned with the frequency-doubled PSL light. The beat frequency is then exactly twice the difference between the resonant frequency of the arm cavity and the optical frequency of the PSL; this is exactly what we want for lock acquisition. The linear range of this signal will be limited only by the bandwidth of the photodetector used for heterodyning. The linear range, expressed as the number of wavelengths  $n$ , should be the PD bandwidth ( $\Delta f$ ) divided by the cavity free-spectral range  $\nu_{FSR}$ , which of course is much larger than the linear range of a PDH signal  $\lambda/4\mathcal{F}$ :

$$n = \frac{\Delta f}{\nu_{FSR}} \gg \frac{1}{4\mathcal{F}}, \quad (8.8)$$

where we are considering  $\mathcal{F}$  the finesse for the PSL ( $\lambda = 1064\text{ nm}$ ) light.

With this broad linear signal, the arm length can simply be velocity damped with gentle length actuation until it is no longer fluctuating with respect to the PSL light. Once the arm is under length control, it can be held stably at a point near the carrier resonance. With the arm lengths held such that they fluctuate much less than a fringe, they will not disturb the signals for the short DOFs (MICH, PRCL, SRCL), control of which can be easily acquired using the techniques described in section 8.6.

Once control of the short DOFs has been achieved, the full IFO is under control, and techniques similar to those described in Step B and onward in section 8.6 can be used to bring the IFO to the operating point. Alternatively, it may also be possible to use the green light sensing chain to control the arm cavities independently while the offset is reduced; this might be possible if the initial

lock stage is done at low laser power, thus avoiding significant radiation pressure effects. Radiation pressure effects can also be avoided by appropriately locking the SRCL away from its own nominal operating point (detuning it), and adjusting this offset in concert with the arm offsets to eliminate any optical spring in the DARM degree of freedom. Such a procedure is conceivable as the sensing scheme for the SRCL in Advanced LIGO has been designed to allow the SRC to be operable at multiple detunings, and to be able to switch between these detunings in lock.

### 8.7.1.2 Advantages of this technique

With an understanding of the technique, the advantages relative to the procedure in Step A of 8.6 become apparent:

- **Using green light:** breaks the degeneracy of cavity finesse for lock acquisition and GW detection; highly reflective ITMs isolates arm cavities from flashing in the short DOFs; highly reflective ITM plus the optic wedge angle serves to isolate arm cavities from flashing in the other arm cavity.
- **A secondary laser:** allows the creation of a length signal with a broad linear range. This would permit effective velocity damping of the cavity, eliminating the need for actuators that can acquire lock before the cavity has swept through a single fringe. With this the concerns outlined in section 8.2 can be sidestepped.
- **Two secondary lasers:** allow the two arms to be locked independently, both with a frequency control technique followed by velocity damping. Moreover, independent signals for the two arms allows the choice of locking to any point in the two dimensional CARM + DARM configuration space.

### 8.7.1.3 Alternative Technique

It is possible that this technique will be adversely affected by the green light transmitted through the ITM resonating in the short degrees of freedom. In that case, nearly the same technique can be used, by installing optical fibers that can transmit the main carrier field to the end stations. The lasers at the end station are phase locked to the PSL light, then frequency doubled. The resulting green light can then be locked to the arm cavity in the same way, with the error point of the phase-locked loop now taking the place of the frequency actuator. The feedback to the phase-locked loop error point now is the sensing signal for the arm cavity length; it can be used in the same way to velocity damp the arm cavity. In this case, all the sensing for the arm takes place at the end station, and so the high reflectivity (for green light) of the ITM will effectively isolate the arm from the short degrees of freedom. The main drawback of this scheme is the need for a 4 km optical fiber, which

can introduce substantial noise. The fiber system would thus require a setup to cancel phase noise induced by the fiber, such as the system devised in [95].

## 8.8 Discussion

The lock acquisition development work at the 40 m will provide significant advantages to Advanced LIGO commissioning, not only from the training of personnel, but also from the lessons learned and the techniques developed. In this chapter we have described a lock acquisition technique which differs in approach from that taken in initial LIGO, while extending it to another dimension: signal recycling.

This technique, rather than going directly from the uncontrolled state to the operating point, goes from the uncontrolled state to an acquisition point where the signals are naturally mostly diagonal, and then in a controlled process migrates to the operating point.

We have also described the steps necessary to make this technique directly applicable to Advanced LIGO, which will require additional hardware in order to reach the acquisition point. The first versions of this additional hardware will be commissioned at the 40 m in the coming year.

## Chapter 9

# Measurement of Laser and Oscillator Noise Couplings in RF/DC Readout

An experiment was performed at the Caltech 40 m prototype interferometer to study the relative merits of RF/DC readout, to gain experience with the DC readout technique, and to validate the modeling tools used in interferometer design studies. The work involved design of the output optical system (already described in chapter 5), commissioning the system, and making calibrated coupling measurements for laser and oscillator noise.

### 9.1 DC Readout Experiment

Two sets of measurements are presented. One set of measurements, in section 9.2, were taken with the interferometer in a power-recycled Fabry-Pérot Michelson configuration. This can be done simply by radically mis-aligning the signal recycling mirror, which then just behaves as a lossy element rather than a mirror. This was done to study DC readout in preparation for Enhanced LIGO.

The second set of measurements, in section 9.3, were taken with the interferometer in a detuned RSE configuration. This was to study one potential operating mode of Advanced LIGO. These measurements are all in the anti-spring configuration, because it is easier to lock (cf. section 8.6.2).

The purpose of the experiment is not necessarily to demonstrate that DC is unequivocally better than RF readout; what we are doing is validating our simulation and theory, and to search for unanticipated, significant problems with the technique which is planned for Advanced LIGO.

The laser amplitude noise measurements will show that DC readout appears to be worse than RF readout; this is actually the case for the 40 m with its relatively short arms. Extrapolating to a LIGO interferometer, which is 100 times longer, DC readout will have significant advantages due to the increased storage time of the carrier light in the interferometer.

The measurements below  $\sim 100$  Hz are typically not indicative of the real coupling; there is too much noise in the interferometer to get a solid measurement of the couplings at these low frequencies. In addition, some of the measurements around 1.5 and 4 kHz are similarly untrustworthy due to suspected mechanical resonances at those frequencies which create excess noise in DARM. This is unfortunate, as the RSE peak is near that frequency, and it would be good to have a clear understanding of how noises actually couple in that frequency region.

### 9.1.1 Noise Injections

The noise couplings were all measured by doing a swept sine measurement, injecting a sine wave into the noise source and coherently demodulating the DARM error signal. The goal is to understand (through simulation) the linear coupling; this is why swept sine injections are done rather than injecting broadband noise.

Nonetheless, it is highly unlikely that the coupling will be perfectly reproduced by the modeling: we are injecting a signal into one port of a system with many (more than  $\sim 20$ ) degrees of freedom; not all of these are controlled at DC, and so they can vary over the course of a single measurement (which takes many minutes). The simulation only includes 6 servo loops, and the configuration does not vary over the course of the swept sine calculation. Getting the coupling level roughly correct with an approximately right frequency response is a success.

The rest of this section is a description of the noise injections.

#### 9.1.1.1 Laser Amplitude Noise

The PSL includes an Intensity Stabilization Servo (cf. section 5.5.2) which stabilizes amplitude fluctuations of the laser light prior to its injection into the interferometer. By injecting a signal into the error point of this servo, we can introduce controlled levels of intensity fluctuations and measure the transfer function from laser intensity noise to the gravitational wave readout channel. Laser amplitude noise, laser power noise, and laser intensity noise all relate to the same quantity, the amplitude variation in the primary source laser field; measurements are typically quoted in relative intensity noise (RIN), which is the fractional power variation:  $\frac{\Delta P}{P} = 2 \frac{\Delta E}{E}$ . The results for laser amplitude noise are quoted in meters/RIN, with meters referring to DARM motion ( $m_{DARM}$ ).

#### 9.1.1.2 Laser Frequency Noise

The noise coupling was measured in this case by injecting a signal at the error point of the Common Mode Servo (cf. section 5.7), inducing a frequency mismatch between the laser light and the CARM degree of freedom; the signal was then coherently demodulated in the gravitational wave channel to determine the transfer function. Calibrating the injected signal into Hz is done by either calibrating

the common mode servo error signal (the case for section 9.2) or by simultaneously demodulating the signal sent to the (already calibrated) frequency actuator (the VCO; cf. section 5.7 and figure 5.4). The results for laser frequency noise are quoted in meters/Hz.

### 9.1.1.3 Oscillator Noise

A IFR2023A signal generator is used as the source signal for the RF modulation sidebands on the laser light, and the same oscillator signal is then used in demodulating the signal. These signal generators enable external modulation of the signal (in amplitude, phase, and frequency) via a BNC input; a signal was applied to this input to inject a noise source. For the oscillator amplitude noise, the injections were calibrated into oscillator RIN using the output mode cleaner as a RF field selector. With the IFO in a simple Michelson configuration, the OMC can be set to resonate (thus transmit) only an RF sideband. The transmitted power then yields a measurement of the RF oscillator amplitude noise. For oscillator phase noise, the calibration in the IFR2023A manual was used.

The results are quoted in meters/RIN and meters/ $\phi$ , for oscillator amplitude and phase noise, respectively. In section 9.2, these results show the true oscillator noise coupling for a power recycled interferometer, which as expected is significantly lower for DC readout, although not zero.

In section 9.3, the measurements for oscillator phase noise coupling will have a different meaning; since *different* signal generators are used to produce the RF sidebands and the electronic local oscillators in the double demodulation setup (cf. section 5.6.1), the noise injection does not appear in both the RF sideband and electronic local oscillator, but only for the DDM signals; thus coupling through the short degree of freedom loops can be exaggerated. The single demodulation signals still have a clear interpretation.

## 9.2 Power Recycled Fabry-Pérot Michelson Interferometer

These results provided an early test of DC readout for Enhanced LIGO, which is currently operating at improved sensitivity relative to initial LIGO (cf. section 4.4). They were previously reported in [96]. The oscillator noise measurements are of the  $f_1$  (33 MHz) oscillator, which is used to extract the gravitational wave signal, the power recycling cavity length, and the Michelson length. The common arm length is sensed with  $f_2$  (166 MHz, a non-resonant sideband in this configuration); oscillator noise for  $f_2$  was not measured.

### 9.2.1 Simulation

The measured transfer functions are presented along with simulation results from the frequency-domain interferometer simulation tool Optickle [58] (cf. appendix F); these simulation results do

include the effect of control loops. We compare the results from this simulation for laser frequency and intensity noise with the measured transfer functions from the interferometer in both a DC readout configuration and an RF readout configuration. The design parameters for the input test mass and power recycling mirror power transmissivities, which most affect the interferometer dynamics, are  $T_{ITM} = 0.005$  and  $T_{PRM} = 0.07$ ; the actual values of the interferometer optics are unknown (there is no metrology data). For modeling laser noise couplings, of greatest interest are the mismatches between the two arm cavities. The round trip loss mismatch has been independently measured to be 20 ppm (from an average of  $\sim 160$  ppm) and the ITM transmissivity mismatch is 9%, which is large, but consistent with measurements of the cavity pole frequencies. In LIGO, the mismatch is less than 2%. Analytical forms for the laser noise couplings can be found in appendix C. The DARM offset in DC readout is 25 picometers.

## 9.2.2 Laser Amplitude Noise

These measurements (figure 9.1) agree well with the modeled results; as predicted for the 40 m interferometer, the coupling of intensity noise is much larger in the DC readout scheme. For kilometer-scale interferometers, this coupling will be greatly reduced by the increased light storage time of the system, while the coupling for the RF readout scheme will be largely unchanged.

### 9.2.2.1 DC Readout

The DC readout coupling shown in this plot is the obvious one: at zero frequency, with no other dynamical changes, the intensity noise coupling must be just the DARM calibration factor (in meters/Watt). In other words, changing the input power changes the output power. The frequency response is purely due to the coupled cavity transfer function (cf. equation (3.67)), along with two poles at the arm cavity pole frequency (cf. equation (3.62)) which are from the differential arm cavity reflectivity. Together, that is one pole at  $\omega_{cc}$  and another at  $\omega_c$  (cf. equation (4.2)). The pole at  $\omega_c$  is canceled by the zero at  $\omega_c$  in the DARM sensing function, so the total coupling is falling like  $f$  everywhere above the coupled cavity pole.

### 9.2.2.2 RF Readout

The RF readout coupling has three slopes. At low frequency (below 300 Hz) is technical radiation pressure noise coupling through the arm cavity finesse imbalance (cf. equation (4.2)); since the arms have different gain, they experience different power buildup and consequently a differential radiation pressure. Note that this is actually a displacement noise, not a sensing noise, since the mirrors are being physically buffeted; it is also of course present in DC readout, but hidden by the dominant coupling. The noise coupling above 300 Hz is actually sensing noise; it is due to a residual,

unsuppressed DARM offset equivalent to 1 pm; amplitude noise on the RF sidebands beats against the resulting static carrier field. The turn up at 1.6 kHz is due to the pole in the response of DARM at that frequency, which is the arm cavity pole.

### 9.2.3 Laser Frequency Noise

In both RF and DC readout, the main coupling path is through the arm cavity finesse imbalance (cf. equation (4.2)), which couples frequency noise directly into the phase quadrature, and is falling like  $f^{-1}$  above the coupled cavity pole frequency. In addition, in RF readout, frequency noise on the RF sidebands beat against a static carrier field (due to the contrast defect), which creates a larger noise coupling at high frequencies. At the 40 m, these two paths cross at about 1 kHz.

The measured results (figure 9.2) agree with the model above  $\sim 1$  kHz, but there remains a significant unexplained discrepancy at lower frequencies, which is almost certainly due to coupling through the auxiliary loops. The high frequency (where the coupling is mostly optical, and not loop-based) behavior appears well modeled, however, and implies that DC readout will provide a real advantage within the gravitational wave detection band when employed in large-scale detectors, as the primary coupling path will be much reduced due to the significantly lower coupled-cavity pole frequency.

### 9.2.4 Oscillator Phase Noise

As the RF modulation sidebands are not filtered by the interferometer, any phase noise on the oscillator should appear in both the RF photocurrent which is the product of optical heterodyning and the electronic local oscillator with which the RF photocurrent is further heterodyned to baseband. In this final stage of mixing, oscillator phase noise should cancel and disappear from the signal; in practice, for reasons which are partially understood, it does not. For LIGO this was a limiting noise source above  $\sim 1$  kHz during 2004. It is not known whether the solution currently in use (lower noise oscillators) will be feasible for Advanced LIGO.

In the DC Readout scheme, the RF sidebands are not used for gravitational wave signal extraction, and thus have a much reduced opportunity to pollute the signal; potential coupling routes include (1) noise impressed onto auxiliary degrees of freedom (e.g., CARM or the Michelson degree of freedom) which can then couple to the DARM signal and (2) direct sideband leakage through the OMC (which should nominally reject them). Refer to figure 9.3 for the results of measurements showing a significant improvement for DC readout above 200 Hz.

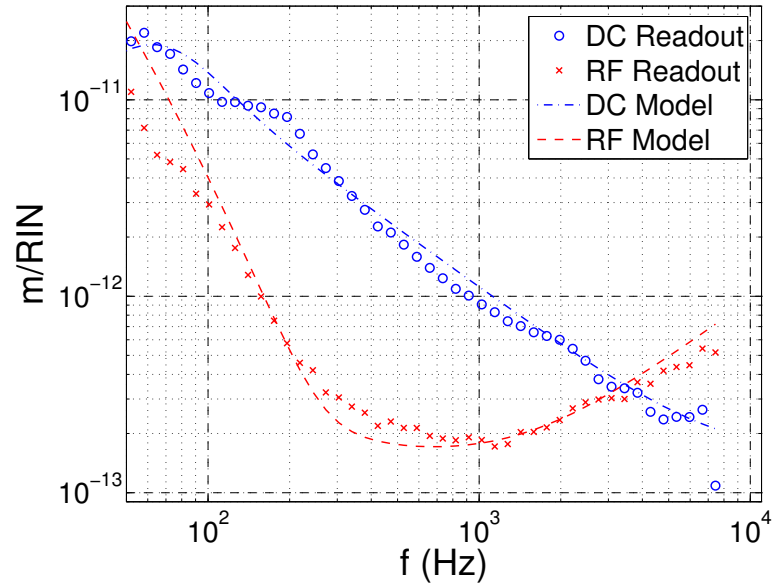


Figure 9.1: Laser intensity noise coupling for the 40 m Fabry-Pérot Michelson interferometer with power recycling. The dots indicate experimental data while the dashed lines indicate the results of numerical simulation.

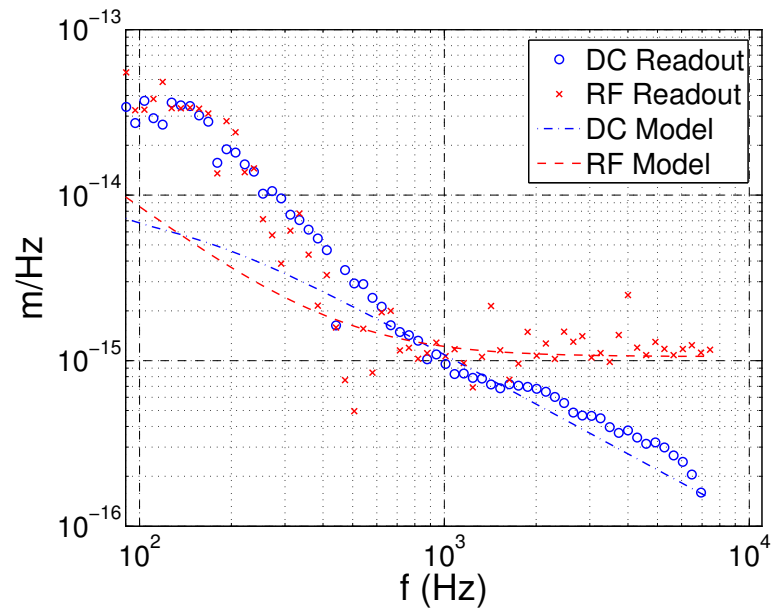


Figure 9.2: Laser frequency noise coupling for the 40 m Fabry-Pérot Michelson interferometer with power recycling. The dots indicate experimental data while the dashed lines indicate the results of numerical simulation.

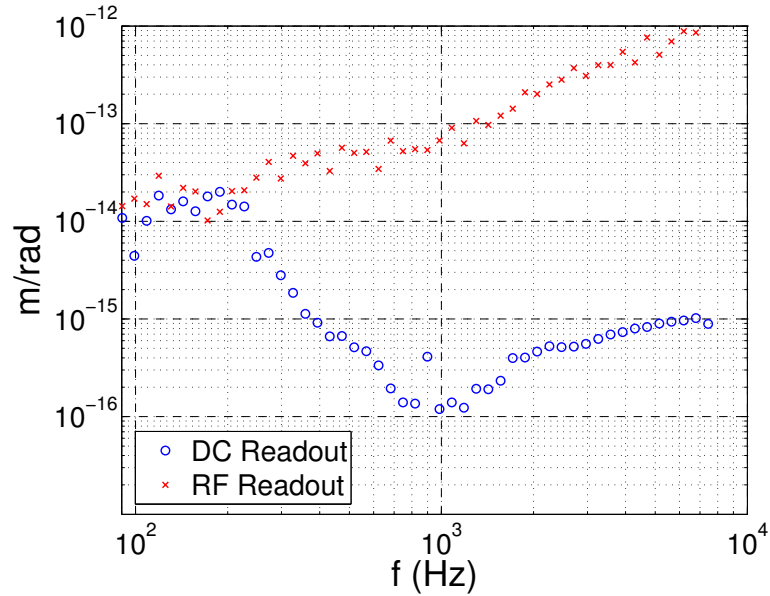


Figure 9.3: Oscillator phase noise coupling for the 40 m Fabry-Pérot Michelson interferometer with power recycling. The dots indicate experimental data.

### 9.2.5 Oscillator Amplitude Noise

In the RF readout scheme, the electronic mixer used in demodulating the RF photocurrent is saturated by its local oscillator, and so any amplitude noise on the oscillator used to generate the RF modulation sidebands appears as a gain modulation. If there is a residual, static offset in the signal, then this amplitude noise can appear directly; otherwise it appears bilinearly with the DARM signal. In the DC readout scheme, the RF modulation sidebands are used for sensing and control of auxiliary degrees of freedom, and so noise on these sidebands can couple indirectly to DARM. Additionally, as the RF modulation sidebands extract power from the carrier, any amplitude fluctuations on the sidebands correspond to amplitude fluctuations on the carrier, which can manifest as intensity noise. Direct RF sideband leakage through the OMC can also contribute. Refer to figure 9.4 for the results of measurements showing a significant improvement for DC readout.

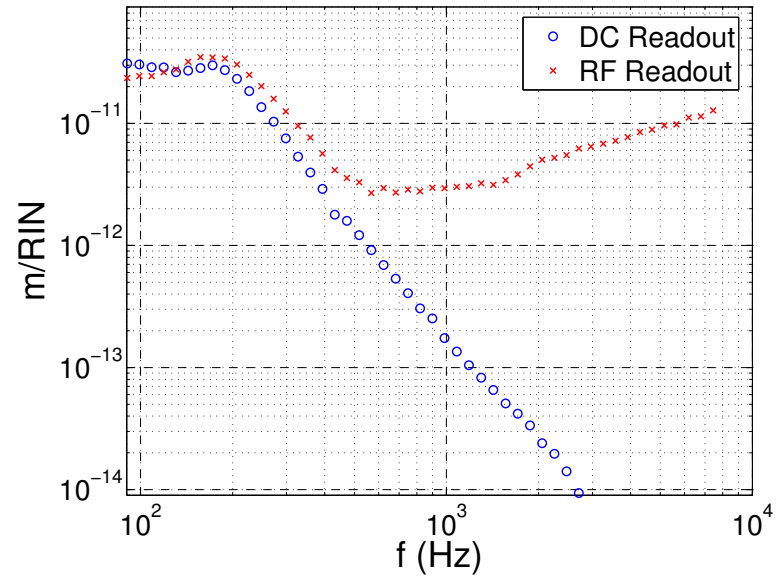


Figure 9.4: Oscillator amplitude noise coupling for the 40 m Fabry-Pérot Michelson interferometer with power recycling. The dots indicate experimental data.

## 9.3 Detuned RSE Interferometer

The same laser and oscillator noise coupling measurements were conducted as for a power recycled interferometer. The detuned interferometer uses two sets of RF sidebands; there are oscillator noise measurements for each. The oscillator noise measurements were done by injecting noise into the signal generators used to generate the RF sidebands, but not the ones that generate the electronic local oscillators for the DDM signals (at  $f_2+f_1$  and  $f_2-f_1$ ). This should not matter for oscillator amplitude noise (as the mixers should still be driven to saturation), but it does mean that oscillator phase noise will not directly cancel for the DDM signals. This is a meaningful result for a signal generation setup like the one used at the 40 m; in the future, however, the plan for the 40 m [97] is to use a single crystal oscillator in conjunction with a set of frequency multipliers to generate the electronic and optical local oscillators.

### 9.3.1 Length Offsets

A truly vexing aspect of the LSC scheme described in chapter 6 is the inevitable presence of offsets in the various error signals, a consequence of the imbalanced sidebands that result from having a detuned signal cavity and imperfect knowledge of demodulation phase (cf. section 6.3.3). These error signal offsets are different from those in a power-recycled interferometer, which are unintentional and depend on physical asymmetries, many of which can be measured and are stationary. In contrast, in a detuned interferometer, the error signal offsets depend on the microscopic state of the interferometer and on demodulation phase in a cyclical way that makes them difficult to accurately pin down. Moreover, they can vary with interferometer alignment, which is not actively controlled at the 40 m; a set of automatic alignment scripts is used during the bootstrapping (cf. section 8.5) to set the DC alignment, but this is not a perfect method for a reproducible alignment. The final result is that the positions of the optics can be displaced from their nominal, designed positions by rather alarming amounts: up to a few picometers for the ETMs and a few nanometers for the BS, PRM, and SRM. Since all the RF sidebands are imbalanced, these offsets can affect any length degree of freedom. These length offsets can severely disrupt our understanding of how laser and oscillator noises can couple to the gravitational wave signal. These noises couplings can vary strongly with microscopic offsets because, in principle, the interferometer has been designed with symmetries such that these noises cancel. The offsets ruin the symmetry and thus the cancellation.

#### 9.3.1.1 Cyclical dependencies

There is, to my knowledge, no simple way to measure the various length offsets accurately enough to remove them; because of the sensing scheme, they cannot be measured unless the interferometer is fully locked, and the detailed response of the interferometer depends on the offsets. It is thus a

chicken-and-egg problem, although not as bad the lock acquisition problem. One possible solution is of course to explore the offset space and find the place of lowest noise coupling. This is sometimes done with one to two alignment degrees of freedom in initial and Enhanced LIGO. However, by adding the length offsets, we increase the dimensionality of the space that must be explored. Moreover, since the offsets can change, this process would need to be repeated regularly. This is onerous.

### 9.3.1.2 Mode cleaner length

In addition, the input mode cleaner may not be completely resonant for the RF sidebands, although it is always resonant for the carrier. A macroscopic length change of  $100\ \mu\text{m}$  can have a significant effect on noise couplings. The regular fluctuations in mode cleaner length are known to be greater than this amount, and so this represents another significant source of uncertainty. The ultimate source of this fluctuation is poorly understood, but it probably has to do with thermal expansion in the laboratory floor and the seismic stack which supports MC2 (cf. figure 5.1). This does not have anything to do with the interferometer detuning; it is because the mode cleaner itself does not have long term stability, and the problem is exacerbated by the high RF modulation frequencies (the  $f_2$  sidebands must pass on the mode cleaner's 15th FSR). This problem could be circumvented by automating a mode cleaner length measurement, and doing it once or twice a day, but this has not yet been done.

### 9.3.1.3 Effect on DARM calibration

It is worth commenting that all these length offsets do not significantly degrade our ability to understand how the interferometer responds to gravitational waves: that depends more on the actuators and the photodiodes, so the calibration of the device (cf. chapter 7) is not really at risk. This is because unlike the noise sources, which are supposed to cancel, the signal is supposed to add; small changes thus do not have a large effect. In any case, for the conduction of searches for gravitational waves it is necessary for the calibration to be continuously tracked and measured regularly. We could track the noise couplings in the same manner as the calibration is tracked, but this would unnecessarily take up either observation time or observation bandwidth, an unattractive proposition.

## 9.3.2 Simulation

The simulation in this configuration is using the looptickle extension for Optickle (see appendix F), which includes linear control loops. The loops have proved crucial to understanding the noise couplings, as the pure optical coupling (analytically described in appendix C) does not explain any

of the measured couplings.

### 9.3.2.1 Feedback and Offsets

The simulations are closed loop; the DARM offset is actually set by the simulation (its nominal value is 25 pm), by ensuring that the OMC transmitted power is near its actual in lock value of  $\sim 1.5$  mW. The actual DARM offset then changes with the MICH offset (as it does in the real interferometer, since DARM is servo-ed to keep the OMC transmitted power constant). This actually helps explain something which was puzzling in the real interferometer: sometimes the control hand-off of DARM to DC readout would not work. It is not difficult to understand why the transition did not work if one realizes there can be carrier light at the asymmetric port which is not due to a DARM offset—the DARM length sensing based on the OMC transmitted power has too little gain and as a result the DARM loop is unstable. At the time, an offset in the RF DARM loop (in the other offset direction) was suspected, but it is now clear that a MICH offset could also have been the problem.

There are then 5 offsets which are unknown (and which can vary between each measurement trace, as they will vary from lock to lock): CARM, MICH, PRCL, SRCL, and the mode cleaner length, a five-dimensional space. In RF readout, there can also be a DARM offset, for a sixth dimension. This offset space was explored through simulation by hand in the following ranges: CARM  $\pm 3$  picometers (and DARM in RF readout),  $\pm 200$  microns for the mode cleaner length, and  $\pm 3$  nanometers for MICH, PRCL, and SRCL. For the short degrees of freedom, this level is determined by inspecting figure 6.2, where we can see that length offsets approximately scale as 1 nm/degree of demodulation phase error. For the 40 m with DDM signals  $\pm 3$  nanometers is actually a conservative limit. Nonetheless, the simulated noise couplings vary radically (by more than an order of magnitude, with significant changes in the frequency response) for offsets of this magnitude. The control loops in the simulation are automatically compensated to keep the UGFs approximately at the actual value in the real interferometer (about 100 Hz for the short loops, 180 Hz for DARM, and several kHz for CARM). The shown simulated couplings are ‘eyeball’ fits to the data—the simulation is far too slow for an automated fitting mechanism. The simulations do not perfectly match the measured data, but they do give an indication of the likely coupling mechanisms.

### 9.3.3 The simulated noise traces

The simulation results include multiple traces and are overlaid on the same plot with the measured data.

**The red circles** indicate the measured coupling level.

**The dash-dot line** indicates the optical coupling of the noise source, which excludes the effect of any control system.

**The solid line** is the total coupling in the presence of the control loops.

**The dotted lines** indicate the contributions to the total coupling from sensing noise in the individual control loops. The total coupling is not necessarily the coherent (nor quadrature) sum of all the shown couplings, however; it would be if the loops were totally decoupled, but they are not, as already discussed in section 6.4.1.1. These traces are helpful in understanding the coupling routes, however.

### 9.3.3.1 Effects not included

Not shown are any couplings which may be due to spatial higher-order modes, which are not modeled. Nonetheless, it can be seen that the measured couplings in most cases are reasonably well estimated by the closed-loop simulations, but not by the open-loop simulations.

### 9.3.3.2 Auxiliary loop coupling

There is a general theme to the oscillator noise plots: the oscillator noise couplings in DC readout are primarily due to their appearance as sensing noise in the auxiliary degrees of freedom. The proper implementation of feedforward correction (cf. section 6.4.2) should dramatically reduce these noise couplings.

There are analytic formulae for laser noise couplings in appendix C, along with plots; these are not shown here because they cannot account for offsets in the auxiliary degrees of freedom.

## 9.3.4 Laser Amplitude Noise

In a detuned RSE interferometer laser amplitude noise couplings are not as simple as in a non-recycled interferometer, because the signals (and noises) appear in all quadratures, in a frequency dependent way. The main coupling path is similar to a power recycled interferometer; input power fluctuations reach the signal cavity (i.e., the asymmetric side of the beamsplitter) in the same way, but the signal recycling cavity then reinjects these fluctuations into the asymmetric mode (with a quadrature rotation). The total response is then a combination of the coupled cavity transfer function and the DARM opto-mechanical response. The actual signal referred coupling level depends on the readout quadrature.

### 9.3.4.1 DC Readout

This simulation agrees qualitatively with the measurement in figure 9.5, but underestimates it in the region from 150 Hz to 1 kHz; this is due to an underestimate in the simulation of the actual MICH noise that results from laser intensity noise. There is also an interesting ripple in the measured data above 1 kHz that cannot be reproduced in the simulation. The closed loop coupling is larger

than the optical coupling everywhere; at high frequencies it can be seen that the CARM servo is contributing—this is amplitude noise that appears as sensing noise in the CARM servo, which then generates frequency noise.

Ideally, this coupling would be distinctly different for DARM offsets in opposite directions. The DARM offset changes sign, and so for one direction it should add to the finesse imbalance coupling, while in the other direction it should cancel at the crossover frequency (a few kHz for the 40 m). This coupling was measured in the two directions; there were only small differences between the two measurements. Whatever behavior is causing the ripple in the response above 1500 Hz obscures the cancellation effect.

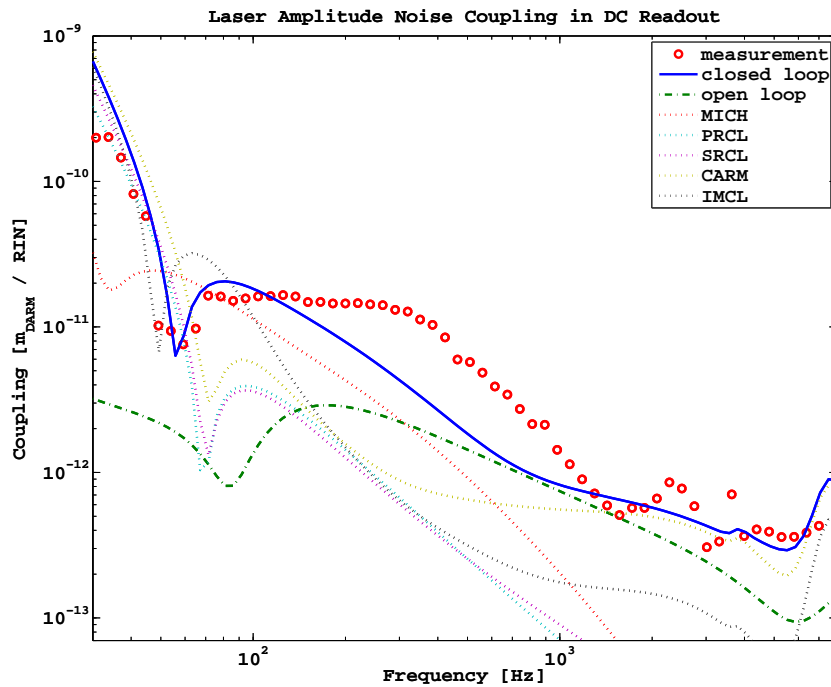


Figure 9.5: Laser amplitude noise coupling for the 40 m detuned RSE interferometer with DC readout. The circles indicate the measured coupling; the dash-dot lines indicate a numerical simulation of the coupling including only optical effects; the solid line is a numerical simulation including control loops.

### 9.3.4.2 RF Readout

In figure 9.6 we see reasonable agreement, but this particular coupling varies wildly — other measurements (not shown) of this coupling were nearly  $100\times$  worse in the region from 200 Hz to 1 kHz. At low frequencies the main effect is technical radiation pressure noise from the finesse imbalance, which crosses the coupling due to the residual DARM offset at about 300 Hz. The fluctuations observed in this coupling may be due to changing residual DARM offsets from night to night (not due to a lack of servo gain, but rather signal offsets due to the RF sideband imbalance).

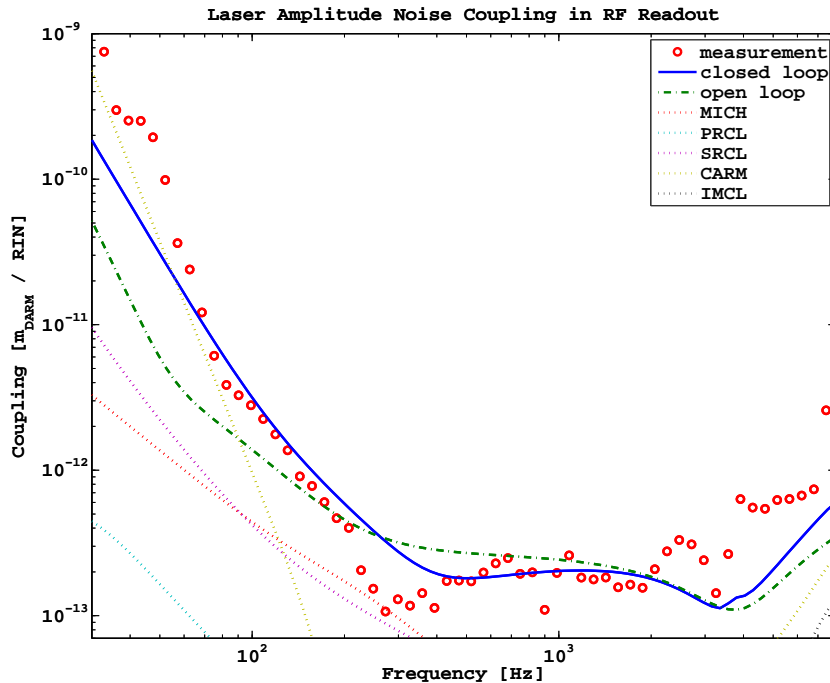


Figure 9.6: Laser amplitude noise coupling for the 40 m detuned RSE interferometer with RF readout. The circles indicate the measured coupling; the dash-dot lines indicate a numerical simulation of the coupling including only optical effects; the solid line is a numerical simulation including control loops.

### 9.3.5 Laser Frequency Noise

Similarly to laser amplitude noise, the coupling path to the signal cavity is the same as a non-recycled interferometer, and then the detuned signal cavity re-injects noise into the asymmetric mode. The resulting noise appears in all quadratures, with a quadrature dependent frequency response. These simulations are computed without the frequency stabilization servo, since the noise injection is at the error point of the servo.

#### 9.3.5.1 DC Readout

In figure 9.7 we have reasonable agreement, with the contribution from MICH nearly equal to the raw optical coupling. The turn towards a flat response near 1 kHz is due to the MICH length offset (about 4 nm)—this noise coupling is a main reason why DC readout uses a DARM offset rather than a MICH offset to create the local oscillator field. In this case, the DARM offset is actually increased to 40 pm to compensate the carrier field at the asymmetric port resulting from the MICH offset. There is some structure above 1 kHz (particularly the discontinuity near 4 kHz) which is still not explained, however. This measured coupling is greater than that expected purely from the DARM offset, loss imbalance, and finesse imbalance by a factor about 8 below 1 kHz, up to a factor of about

20 at 5 kHz.

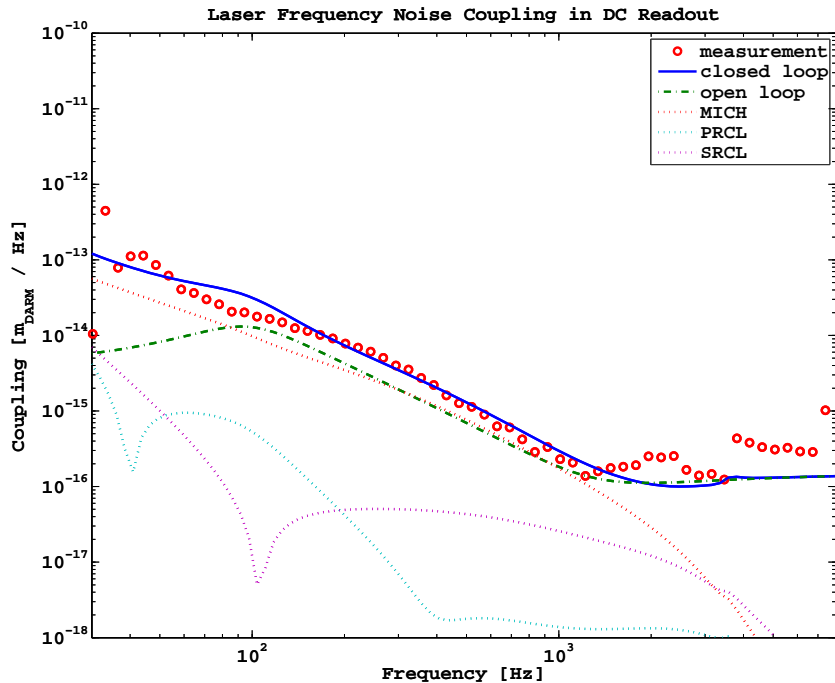


Figure 9.7: Laser frequency noise coupling for the 40 m detuned RSE interferometer with DC readout. The circles indicate the measured coupling; the dash-dot lines indicate a numerical simulation of the coupling including only optical effects; the solid line is a numerical simulation including control loops.

### 9.3.5.2 RF Readout

In figure 9.8, this coupling level depends mostly on the mode cleaner macroscopic length offset (200 microns), which shifts the local oscillator field used in RF off-resonance in the mode cleaner, increasing frequency noise coupling through that RF sideband. An offset in MICH (4 nm) also contributes significantly. Couplings due to the finesse imbalance and the loss imbalance are about  $5\times$  below those due to these offsets.

### 9.3.6 Oscillator Phase Noise

This is a noise coupling of great interest, as it surprisingly limited the LIGO sensitivity for a time. It has been essentially unpredictable. In both DC readout and RF readout, the coupling is dominated by the auxiliary loop coupling. The two oscillators have different, but important roles: the  $f_1$  oscillator is only used as part of the DDM signals, and it thus can only contribute through the auxiliary loops. The  $f_2$  sideband also creates noise in the auxiliary loops; it is also used as the sensor for the laser frequency stabilization and as the local oscillator in RF readout. As a reminder,

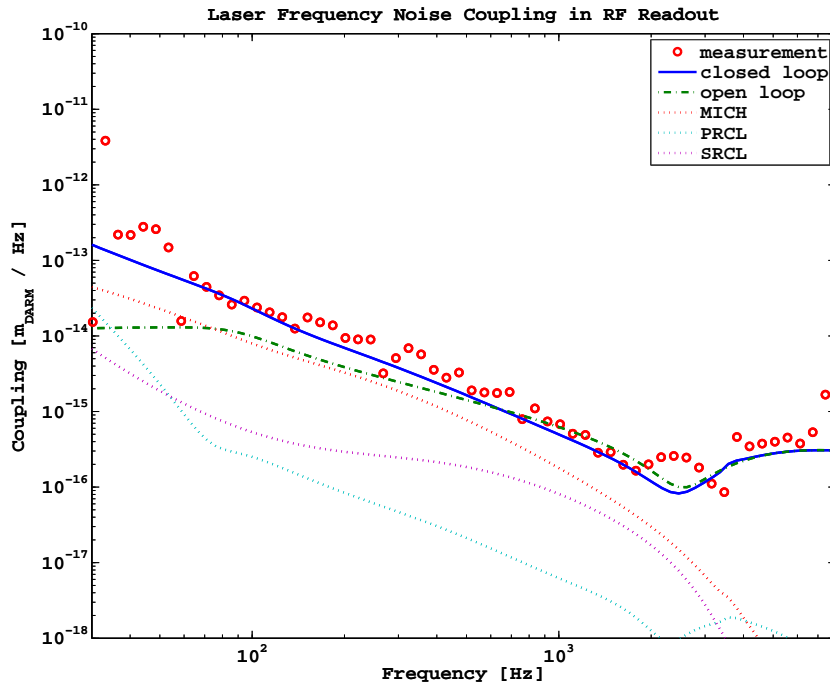


Figure 9.8: Laser frequency noise coupling for the 40 m detuned RSE interferometer with RF readout. The circles indicate the measured coupling; the dash-dot lines indicate a numerical simulation of the coupling including only optical effects; the solid line is a numerical simulation including control loops.

the coupling of this noise to the DDM-sensed loops (MICH, PRCL, SRCL) is probably unique to the 40 m scheme, which uses different signal generators for modulation and demodulation.

### 9.3.6.1 DC Readout $f_1$

This coupling, shown in figure 9.9, is not well explained by the simulation, but it is within an order of magnitude. The optical coupling cannot be seen, as it is below the  $y$ -axis limits. The dominant coupling is due MICH, and the measured level of MICH noise (not shown) actually explains the DARM coupling. The simulation, however, fails to capture accurately the amount of noise in MICH actually generated by  $f_1$  oscillator phase noise.

### 9.3.6.2 DC Readout $f_2$

In figure 9.10 we see that the dominant coupling is due, unsurprisingly, to the auxiliary control loops. Below 1kHz, the coupling is primarily due to MICH, and above 1kHz is due to the common mode servo. The actual level of the common mode servo (i.e., frequency noise) coupling depends critically on the input mode cleaner length. It is actually *worse* than the measured coupling when the mode cleaner is exactly resonant for the  $f_2$  sideband; these modeling results are for a mode cleaner length that 200 microns shorter than nominal, within the known range of length deviation.

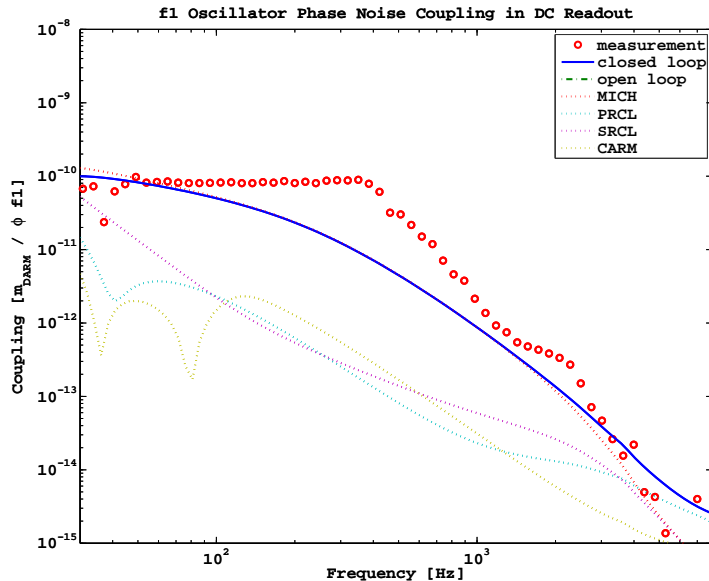


Figure 9.9:  $f_1$  oscillator phase noise coupling for the 40 m detuned RSE interferometer with DC readout. The circles indicate the measured coupling; the dash-dot lines indicate a numerical simulation of the coupling including only optical effects; the solid line is a numerical simulation including control loops.

This corresponds to a frequency offset from resonance for the  $f_2$  sideband of  $\sim 700$  Hz, which is not likely to be noticed unless the mode cleaner length measurement procedure is carried out. If the mode cleaner length is 200 microns longer than nominal, the coupling gets even worse than when it is exactly resonant. The pure optical coupling can just be seen in the bottom right corner of the plot—this coupling is from the OMC, which is off-resonant for the  $f_2$  sideband and so acts as a phase-noise to power-noise converter.

### 9.3.6.3 RF Readout $f_1$

In figure 9.11 there is also no optical coupling for  $f_1$  oscillator phase noise, since the  $f_2$  sideband is used as the local oscillator. The dominant coupling is through the MICH loop, which is well captured by the simulation in this case.

### 9.3.6.4 RF Readout $f_2$

In figure 9.12, again the MICH loop dominates the coupling at low frequencies. At 1 kHz, both the optical coupling and coupling through the common mode servo become dominant, with the relationship between the two contributing to the details of the response. The measured coupling appears to fit the open-loop simulation better than the closed-loop simulation above 1 kHz.

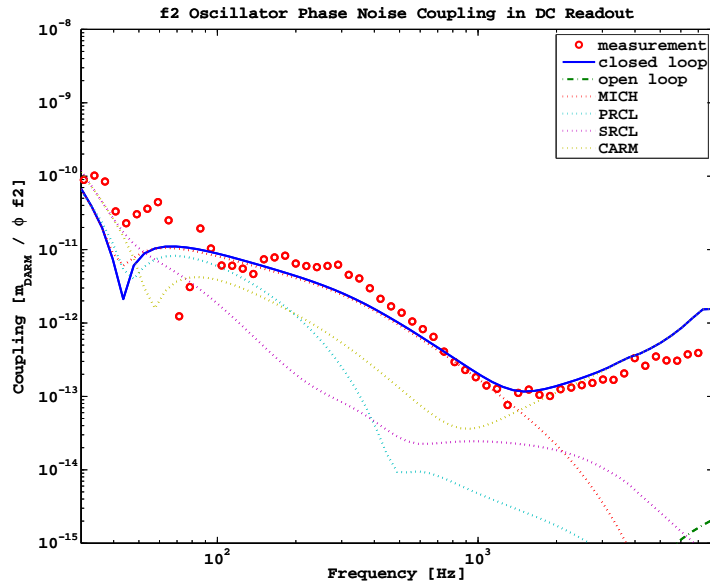


Figure 9.10:  $f_2$  oscillator phase noise coupling for the 40m detuned RSE interferometer with DC readout. The circles indicate the measured coupling; the dash-dot lines indicate a numerical simulation of the coupling including only optical effects; the solid line is a numerical simulation including control loops.

### 9.3.7 Oscillator Amplitude Noise

In DC readout, there is a direct coupling mechanism, as amplitude noise on the oscillator must create amplitude noise on the carrier, since the RF sidebands are ‘stealing’ power from the carrier (cf. chapter 4). This effect is responsible for the pure ‘optical’ coupling seen in the DC readout simulations. The dominant coupling, however, is due to auxiliary loops.

In RF readout, there is also the gain modulation as discussed in chapter 4. In both cases, noise can also couple through the auxiliary loops.

#### 9.3.7.1 DC Readout $f_1$

In figure 9.13 we see another strong disagreement between the measurement and the simulation. The measurement coherence is poor above 2kHz and below 100 Hz, but the simulation still underestimates the true coupling in the middle frequency region where the coherence is good. Not shown on this plot is the measured MICH coupling, which is much larger than in the simulation and mostly explains the large coupling to DARM. The simulation is not accurately capturing the noise coupling path to MICH, which remains unexplained. The optical coupling is from the laser intensity noise that results from oscillator amplitude noise and appears higher than the measured coupling from 1 to 2 kHz. This discrepancy is partly due to a cancellation effect (e.g., by the MICH loop, as the blue line shows), but does not explain all the cancellation.

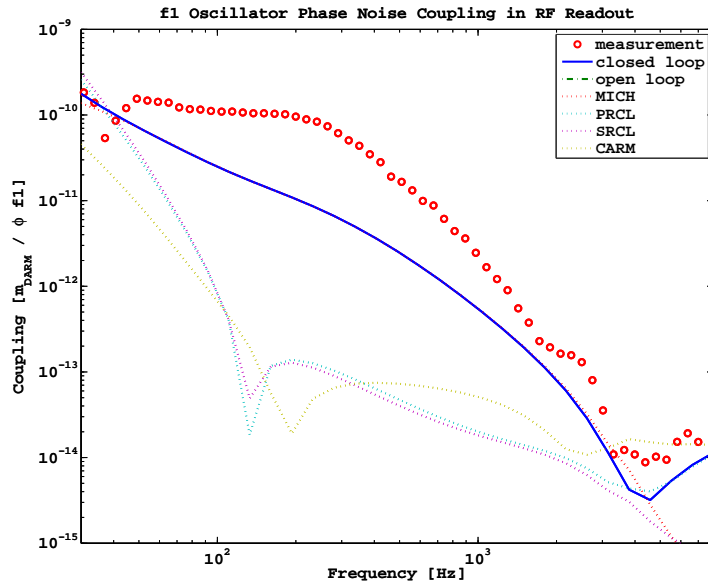


Figure 9.11:  $f_1$  oscillator phase noise coupling for the 40 m detuned RSE interferometer with RF readout. The circles indicate the measured coupling; the dash-dot lines indicate a numerical simulation of the coupling including only optical effects; the solid line is a numerical simulation including control loops.

### 9.3.7.2 DC Readout $f_2$

In figure 9.14 it is clear what is happening in this coupling—at low frequencies the MICH loop is dominating, while above 1 kHz the contributions are the direct mechanism (intensity noise) and the effect on the common mode servo.

### 9.3.7.3 RF Readout $f_1$

This coupling (figure 9.15), again is dominated by MICH loop noise. The measurement coherence is poor above 3 kHz, where the optical path should begin to be dominant.

### 9.3.7.4 RF Readout $f_2$

$f_2$  oscillator amplitude noise coupling in RF readout, in figure 9.16, is clearly underestimated everywhere by the simulation. The measured coupling everywhere is about  $10\times$  larger than the simulation, although the shape appears similar. For this coupling, we would expect the direct optical path to be large, as this is the RF sideband used as the optical local oscillator in the RF readout scheme. In addition there is a contribution from MICH below a few hundred Hz, but ultimately this measurement cannot be explained by the effects included in this simulation.

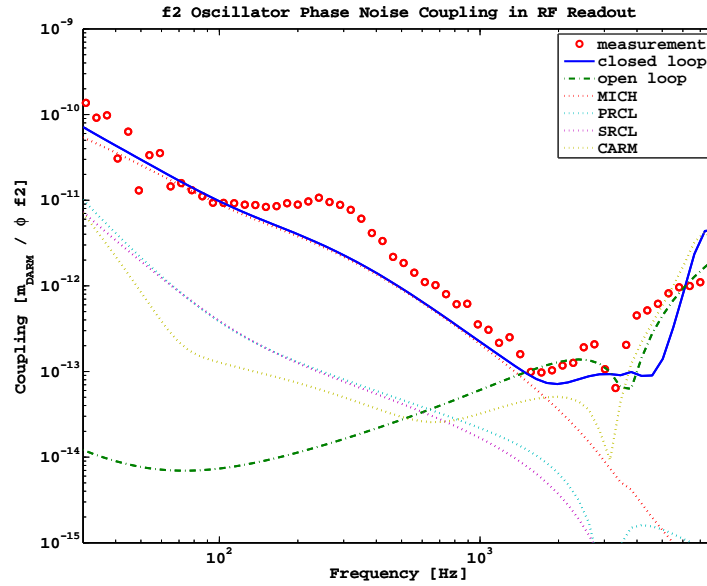


Figure 9.12:  $f_2$  oscillator phase noise coupling for the 40 m detuned RSE interferometer with RF readout. The circles indicate the measured coupling; the dash-dot lines indicate a numerical simulation of the coupling including only optical effects; the solid line is a numerical simulation including control loops.

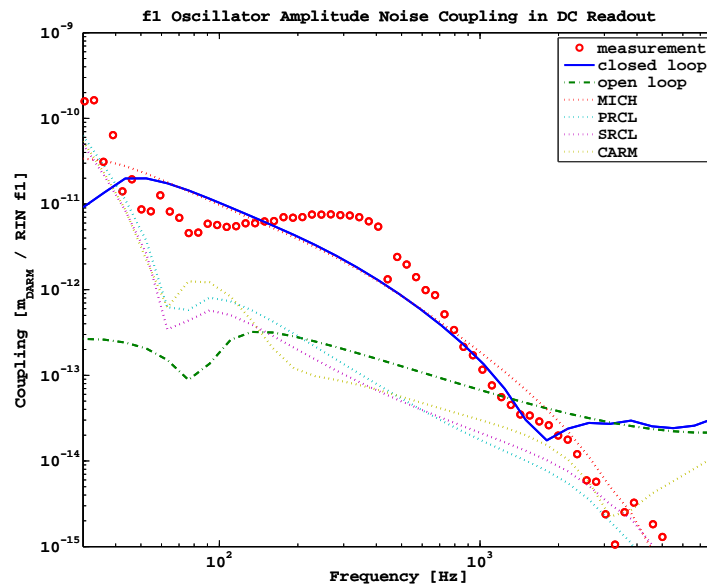


Figure 9.13:  $f_1$  oscillator amplitude noise coupling for the 40 m detuned RSE interferometer with DC readout. The circles indicate the measured coupling; the dash-dot lines indicate a numerical simulation of the coupling including only optical effects; the solid line is a numerical simulation including control loops.

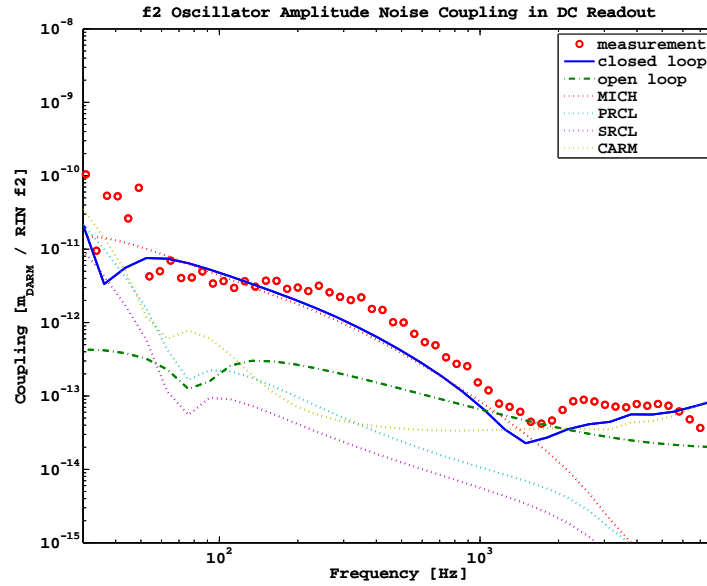


Figure 9.14:  $f_2$  oscillator amplitude noise coupling for the 40 m detuned RSE interferometer with DC readout. The circles indicate the measured coupling; the dash-dot lines indicate a numerical simulation of the coupling including only optical effects; the solid line is a numerical simulation including control loops.

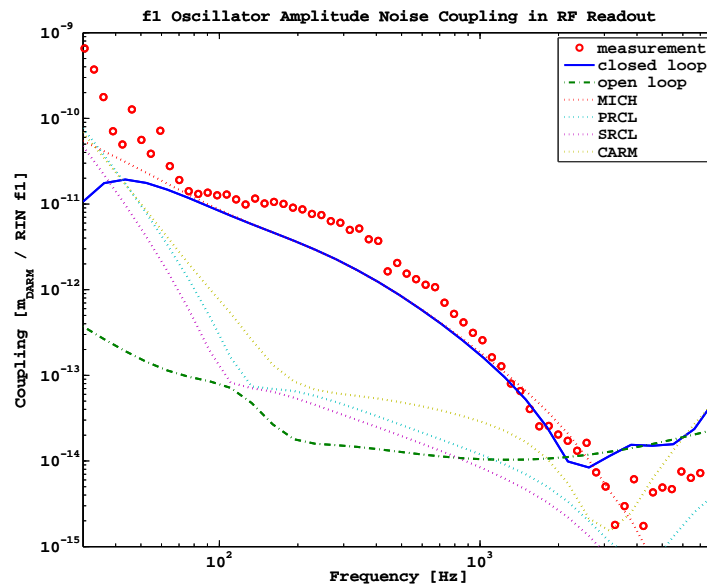


Figure 9.15:  $f_1$  oscillator amplitude noise coupling for the 40 m detuned RSE interferometer with RF readout. The circles indicate the measured coupling; the dash-dot lines indicate a numerical simulation of the coupling including only optical effects; the solid line is a numerical simulation including control loops.

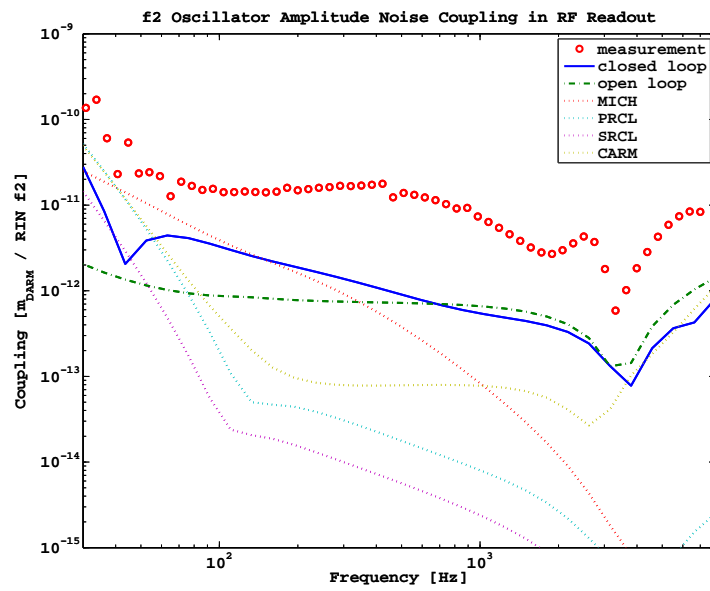


Figure 9.16:  $f_2$  oscillator amplitude noise coupling for the 40 m detuned RSE interferometer with RF readout. The circles indicate the measured coupling; the dash-dot lines indicate a numerical simulation of the coupling including only optical effects; the solid line is a numerical simulation including control loops.

## 9.4 Conclusions

We have carried out an experiment to characterize a DC readout scheme on a suspended-mass power-recycled Fabry-Pérot Michelson interferometer, using a seismically isolated in-vacuum output mode cleaning cavity along with an in-vacuum photodetector. In this experiment, we demonstrated that the laser noise couplings in RF/DC readout schemes behave generally as expected and that oscillator noise couplings are significantly reduced in the DC readout scheme. These results were an important initial test of the DC readout system for Enhanced LIGO, which then served as an OMC system *noise prototype* for Advanced LIGO.

We also made measurements of noise couplings in an Advanced LIGO configuration, where we found that the relative merits of RF and DC readout were obscured by other design choices in the LSC scheme: namely the reliance on unbalanced sidebands for length signal information. We have seen that it is a bad idea to build asymmetries into the interferometer length sensing scheme. A better scheme would ensure that the interferometer noise couplings paths are limited to uncontrollable (but hopefully independently measurable) physical imperfections. This is important because it *decouples* the asymmetries, allowing them to be individually determined, which has the very important result of *reducing the dimensionality* of the problem. Moreover, such noise couplings are static and predictable, which makes them significantly easier to deal with.

The key lessons learned from this experiment are related to those learned about the LSC scheme in general (cf. chapter 6):

**Design for bootstrapping.** It is crucially important to be able to determine signal characteristics (especially any offsets) without using the whole interferometer. The signals should be accurately characterizable using simple subsystems of the interferometer. The bootstrapping process described in section 8.5 is only just good enough to roughly determine the offsets. LSC schemes need to be designed with this in mind; otherwise noise couplings can have surprising levels.

**Design for variance in couplings.** We have seen noises, especially oscillator noises, can vary significantly with unanticipated changes in configuration. Since these couplings can vary by more than an order of magnitude from their predictions, wide safety margins must be used so they do not limit the final sensitivity.

These prescriptions, while conservative, will help to prevent unexpected noise coupling levels in advanced detectors.

## Chapter 10

# A Directional Cross-Correlation Search for Stochastic Gravitational Waves Using Data from the Fifth LIGO Science Run

This chapter describes a search for gravitational waves using data from the fifth LIGO science run, which took place between December 1, 2005 and September 30, 2007. These results use data from the LIGO detectors, but have not been reviewed or endorsed by, and do not represent the scientific opinion of, the LIGO Scientific Collaboration.

### 10.1 Stochastic Gravitational Waves

A stochastic background of gravitational radiation may be comprised of radiation from processes originating in the Big Bang, or it may arise from a large number of superposed signals from astrophysical sources [18, 98]. The optimal strategy for detecting an isotropic stochastic background was described in [99], and LIGO presented the first results using this technique in [100] and recently reported reaching a significant milestone in [101]. This method also forms the basis for detection techniques for stochastic gravitational waves which are not isotropic in origin, such as might be due to a large number of weak sources that are not individually discernible, but come from the same sky location, or anisotropies which could be of cosmological origin. A method for detecting anisotropies in the stochastic background was presented in [102], which focused on spherical harmonics; the implementation of this spherical harmonic technique is reported in [103]. A point source analysis, called the *radiometer*, was proposed in [104], and the first implementation was reported in [71, 105]. The first application to data of the radiometer technique was in [106], which presented results from the fourth LIGO science run. These results included a broadband map of the gravitational wave sky and a frequency resolved search targeting the suspected pulsar Sco-X1.

This chapter presents results using the radiometer technique on data from the fifth LIGO science run, which was much longer and more sensitive than S4. In particular we target Sco-X1, the nearest 15 globular clusters and the galactic center, which are promising locations to contain multiple, weak, superposed sources and to contain unmodeled sources. In addition, an untargeted survey of the sky was carried out.

In section 10.2 we review the general principles of the detection strategy.

## 10.2 Detecting stochastic gravitational waves

We make the following assumptions about the characteristics of a stochastic signal:

- stationary
- stochastic, zero mean, broadband, and Gaussian
- much smaller than the noise in the detectors.

To describe a stochastic source of gravitational waves, we treat the complex strain amplitude  $h_A(f, \hat{\Omega})$  (for  $\hat{\Omega} \equiv (\text{Right Ascension, Declination})$ ) as a random variable with zero mean, where the wave vector for  $h_A(f, \hat{\Omega})$  is  $\vec{k} = 2\pi f \hat{\Omega}/c$ . Then for stochastic, stationary gravitational waves the expectation value of the fields is

$$\langle h_A^*(f, \hat{\Omega}) h'_A(f', \hat{\Omega}') \rangle = H_A(f) P(\hat{\Omega}) \delta^2(\hat{\Omega}, \hat{\Omega}') \delta_{AA'} \delta(f - f'), \quad (10.1)$$

where  $P(\hat{\Omega})$  is the power distribution of the source and  $H_A(f)$  is the two-sided power spectral density in polarization  $A$ , and the delta functions have their usual interpretation. We have assumed that the source power spectrum is separable in frequency and sky location. We simultaneously drop the polarization label and move to a one sided spectrum  $H(f)$ , which is then the signal strength *assuming an unpolarized source*:

$$H(f) = 4H_A(f) \text{ for } A = +, \times. \quad (10.2)$$

One factor of two is from the move from two-sided to one-sided, and the other is from the sum over polarizations. We can convert this to an energy flux by [106],

$$F_{GW} = \frac{c^3 \pi}{4G} \int_{f_{min}}^{f_{max}} H(f) f^2 df. \quad (10.3)$$

It is the power spectrum  $H(f)$  that we want to detect. Because the signal is random, broadband, and smaller than the noise, it is indistinguishable from detector noise, unless it is present in two detectors.

This suggests an analysis strategy that involves cross-correlating the outputs of two detectors (whose noises must be assumed to be uncorrelated) over long time periods. We first describe the strategy for an isotropic background ( $P(\hat{\Omega}) = 1$ ), which is interesting for cosmological reasons ([107], [108], [98]), and which is easily extended to the directional analysis. Isotropic analyses are typically quoted as  $\Omega_{gw}(f)$ , which is the fractional energy density of gravitational waves, relative to the critical energy density of the universe, per unit logarithmic frequency interval. For an isotropic background,  $\Omega_{gw}(f)$  is related to  $H(f)$  by [109]

$$\Omega_{gw}(f) = \frac{8\pi^3}{3H_0^2} f^3 H(f), \quad (10.4)$$

where  $H_0$  is the Hubble constant.

### 10.2.1 Isotropic strategy

We define  $s_i(t)$  as the output of detector  $i$  at time  $t$ , which can be expressed as a sum of the strain sensed by the detector and any noise in the detector:

$$s_i(t) = h_i(t) + n_i(t). \quad (10.5)$$

We make the reasonable assumptions that the noise in the two detectors is uncorrelated, and the noise in each detector is uncorrelated with the signal in the other detector. We can enforce that the noise is also zero mean by high-pass filtering. Then, working in the frequency domain (so  $\tilde{s}_i(f)$  is the Fourier transform of  $s_i(t)$ ), we can write down the cross-correlation,

$$Y = \int_{-\infty}^{\infty} df' \int_{-\infty}^{\infty} df \tilde{s}_1^*(f) \tilde{s}_2(f) \tilde{Q}(f) \delta_T(f' - f), \quad (10.6)$$

where  $\delta_T(f' - f)$  is a finite time ( $T$ ) delta function approximation, and  $T$  is the observation time. We have defined the optimal filter,

$$\tilde{Q}(f) \equiv \frac{1}{N} \frac{\gamma(f)H(f)}{P_1(f)P_2(f)}, \quad (10.7)$$

in which  $P_i(f)$  is the power-spectral density of the output (assumed to be noise dominated) from detector  $i$ ,  $H(f)$  is the power spectrum of the signal (equation (E.7)),  $N$  is a normalization, and  $\gamma(f)$  is an overlap reduction function which describes the geometric configuration of the detectors:

$$\gamma(f) = \frac{1}{2} \sum_A \int_{S^2} d\hat{\Omega} e^{i2\pi f \hat{\Omega} \cdot \Delta \vec{x}/c} F_1^A(\hat{\Omega}) F_2^A(\hat{\Omega}), \quad (10.8)$$

where  $\Delta \vec{x} = \vec{x}_1 - \vec{x}_2$  is the separation vector between the two detector sites, and  $F_i^A(\hat{\Omega})$  is the response of the  $i$  detector to waves of polarization  $A = (+, \times)$  coming from direction  $\hat{\Omega}$ . The integration is

over the two-sphere  $S^2$  (the surface of the sky). Usually this overlap reduction function is normalized (with a factor of  $\frac{5}{4\pi}$ ) so that  $\gamma(f) = 1$  for co-aligned and co-located identical detectors; we omit this normalization here, in anticipation of the directional search in section 10.2.3.

The filter  $\tilde{Q}(f)$  is optimal in the sense that it maximizes the SNR for source spectrum  $H(f)$ ; since we do not know in advance what  $H(f)$  is (in principle it can be predicted for a given cosmological model [99]), the usual strategy is to define several versions of  $H(f)$  (templates) and repeat the analysis for each one. In LIGO, we use  $H(f) \propto f^\beta$ ,

$$H(f) = H_\beta \left( \frac{f}{100 \text{ Hz}} \right)^\beta, \quad (10.9)$$

with attention focused on  $\beta = 0$  (a constant strain spectrum) and  $\beta = -3$  (a constant  $\Omega_{gw}$ ). Following [99], we define a scalar product,

$$(A, B) = \int_{-\infty}^{\infty} A^*(f)B(f)P_1(f)P_2(f) df. \quad (10.10)$$

Then, with the assumptions outlined so far (stationary Gaussian noise uncorrelated between the detectors, and uncorrelated with and larger than the signal), the expectation value of  $Y$  (over random instantiations of the random noise and the random signal) is [99, 109]

$$\langle Y \rangle = T(Q, \frac{\gamma H}{P_1 P_2}), \quad (10.11)$$

and its variance is

$$\sigma_Y^2 \equiv \langle Y^2 \rangle - \langle Y \rangle^2 \approx \frac{T}{4}(Q, Q). \quad (10.12)$$

We choose the normalization  $N$  so that the expectation value of  $Y$  is

$$\langle Y \rangle = H_\beta. \quad (10.13)$$

$Y$  thus has units of strain squared per Hertz. The signal-to-noise ratio (SNR) is

$$\text{SNR} = \frac{Y}{\sigma}, \quad (10.14)$$

which we note grows with the integration time  $T$  as  $\sqrt{T}$ .

## 10.2.2 Segmenting Data and Optimal Combination

There are several wrinkles to the analysis described above, which include the non-stationarity of the detector noise spectra  $P_i(f)$ , computational resource limits, and the bias resulting from using the same data to determine a result and its variance. A strategy to address the first two concerns

was also presented in [99]. This strategy centers around breaking the data streams into time-based segments (usually 60 seconds). An estimate for  $Y_i$  and  $\sigma_i$  is formed for each segment (indexed by  $i$ ), and these estimates are then combined optimally. The optimal combination is given by a weighted average, with the weights chosen to maximize the signal-to-noise ratio. In [99] it is shown that the optimal weights are the reciprocals of the variance estimates:

$$\hat{Y} = \frac{1}{N} \sum_i Y_i \sigma_i^{-2}, \quad (10.15a)$$

$$N = \sum_i \sigma_i^{-2}, \quad (10.15b)$$

$$\sigma^{-2} = N = \sum_i \sigma_i^{-2}. \quad (10.15c)$$

The same strategy of segmenting the data can also help with the third concern: a bias can arise when the same data is used to estimate a cross-power spectrum and a power spectrum from the same data [110], and would thus appear in the result from equation (10.15), where the cross-correlation estimator and the variance of that estimator are computed from the same data. To circumvent this, the  $\sigma_i$  terms in equation (10.15) can be replaced with quantities calculated for the neighboring time segments, as illustrated in figure 10.1, to yield  $\hat{\sigma}_i$ . This  $\hat{\sigma}_i$  is called the *theoretical sigma*, and is computed by averaging the power spectra from neighboring segments, calculating the optimal filter, and then using equation (10.12) to estimate the variance. This does not entirely eliminate the bias, but it does reduce it to one that depends solely on the signal strength. If the assumptions in section 10.2 hold, then this residual bias can be ignored. The *naive sigmas*, calculated with the data from the current segment, are also recorded for use in a data analysis veto (in section 10.4.3.2). There is a further wrinkle—we also window the data (usually with a Hann window), and thus effectively discard half the data. Because of this, equation (10.15) is not the exact one used in the analysis. The segments are instead combined in an overlapping manner to recover the sensitivity lost due to

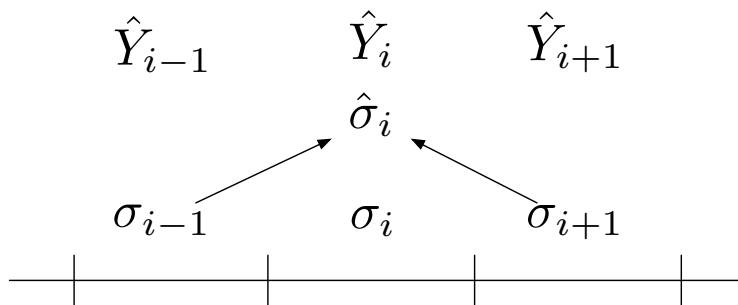


Figure 10.1: The estimate of the variance for each data segment is calculated using data from neighboring time segments to avoid biasing the estimator.

windowing. The details of this procedure are in [111].

### 10.2.3 Gravitational Wave Radiometry

The discussion in section 10.2 describes the optimal strategy for averaging the contributions to the gravitational wave signal at the detectors from all sources within the measurement bandwidth, using an optimal filtering strategy. One can form an alternative filter that specifically (and optimally) targets certain portions of the sky from which stochastic gravitational waves may originate. Such a technique would not be limited to signals of cosmological origin (or other isotropic signals), but would be useful for *any* signals which can be described by the traits in section 10.2: constant, random, broadband, and weak.

We now want to find a source with  $P(\hat{\Omega}) \neq 1$ , and so we generalize equation (10.11),

$$\langle Y \rangle = T \left( Q, \frac{4\pi}{5} \frac{\int_{S^2} d\hat{\Omega} \gamma_{\hat{\Omega}} P(\hat{\Omega}) H}{P_1 P_2} \right), \quad (10.16)$$

where we have a new direction dependent overlap reduction function which is just the integrand of equation (10.8),

$$\gamma_{\hat{\Omega}}(t, f) = \frac{1}{2} \sum_A e^{i2\pi f \hat{\Omega} \cdot \Delta \vec{x}/c} F_1^A(\hat{\Omega}) F_2^A(\hat{\Omega}). \quad (10.17)$$

This overlap reduction is also sidereal time dependent through both  $\Delta \vec{x}/c$  and  $F_i^A(\hat{\Omega})$ .

For the case of a point source  $P(\hat{\Omega}) = \delta^2(\hat{\Omega}, \hat{\Omega}')$  we have a  $\hat{\Omega}$  and time dependent optimal filter for a point source at sky direction  $\hat{\Omega}$ ,

$$\tilde{Q}_{\hat{\Omega}}(t, f) = \frac{1}{N} \frac{\gamma_{\hat{\Omega}}(t, f) H(f)}{P_1(f) P_2(f)}, \quad (10.18)$$

where  $t$  is the sidereal time. The direction dependent strain power estimate is

$$\langle Y_{\hat{\Omega}} \rangle = T \left( \tilde{Q}_{\hat{\Omega}}, \frac{\gamma_{\hat{\Omega}} H}{P_1 P_2} \right), \quad (10.19)$$

and the variance is

$$\sigma_{Y_{\hat{\Omega}}}^2 \approx \frac{T}{4} (\tilde{Q}_{\hat{\Omega}}, \tilde{Q}_{\hat{\Omega}}). \quad (10.20)$$

The optimal filter is thus calculated individually for each segment  $i$  and each direction  $\hat{\Omega}$ . It is only calculated once per segment, which introduces an error because the value must change over the course of the segment. The time  $t$  chosen is mid-segment; the remaining error is second order and is of size

$$\frac{Y_{err}(T_{seg})}{Y} \simeq O \left( \left[ \frac{2\pi f d}{c} \frac{T_{seg}}{1 \text{ day}} \right]^2 \right), \quad (10.21)$$

where  $d$  is the detector separation. For the values used in the search ( $T_{seg} = 60$  sec), this error is less than 1%.

### 10.2.4 The Point Spread Function

The radiometer search described in section 10.2.3 is optimal for point sources, where optimality again means that it yields the maximum SNR for a given source strain  $H(f)$ . This does not mean that it maximally avoids contamination with signal from other directions; there is significant covariance between different sky locations. This can be seen in the point spread function (PSF), which is the result of this covariance. Figure 10.2 is an example of the point spread function, with five injected sources at different locations to illustrate how the PSF changes with sky location. This is computed by injecting a strong source at a chosen location into simulated data (noise), and calculating the radiometer response across the whole sky. The detailed structure of the PSF will vary with sky position and frequency of the source. Because the radiometer algorithm depends on sidereal variations in the antenna acceptance to provide direction discrimination, in theory the PSF should not vary with right ascension of the source, although it will vary with declination. Its angular size will in general be smaller for higher frequency sources. A lower limit can be placed on the size of the point spread function by assuming diffraction limited detection of the gravitational waves, which limits the resolving power of an instrument by the familiar formula,

$$\theta \approx \frac{\lambda}{D}. \quad (10.22)$$

For gravitational waves where  $c = \lambda f$ , when  $f_{GW} = 500$  Hz and  $D = 3000$  km, this yields  $\theta \approx 12^\circ$ . This means the resolution of the radiometer is limited to something of order  $\sim 400$  independent points in the sky, a number which has been estimated in [71].

## 10.3 Analysis Pipeline

The basic strategy for computing the cross-correlation estimator is to parcel the data into 60 second segments and compute the estimate and variance for each segment; this is shown in figure 10.3. Also shown in figure 10.3 is the option to not perform the sum over frequencies at this stage: the  $Y_{\hat{\Omega}}$  for each frequency bin can be written down separately. This is called the ‘narrowband’ search. The individual segments are then back from the disk and optimally combined into a final estimate, depicted in figure 10.4; the separation of calculation and optimal combination are to permit vetoing of specific segments after the analysis (cf. section 10.4.3.2). Figure 10.4 actually shows the whole pipeline, and figure 10.3 represents one block in figure 10.4.

The analysis described here was carried out on the LIGO Data Grid (LDG) Caltech cluster. This

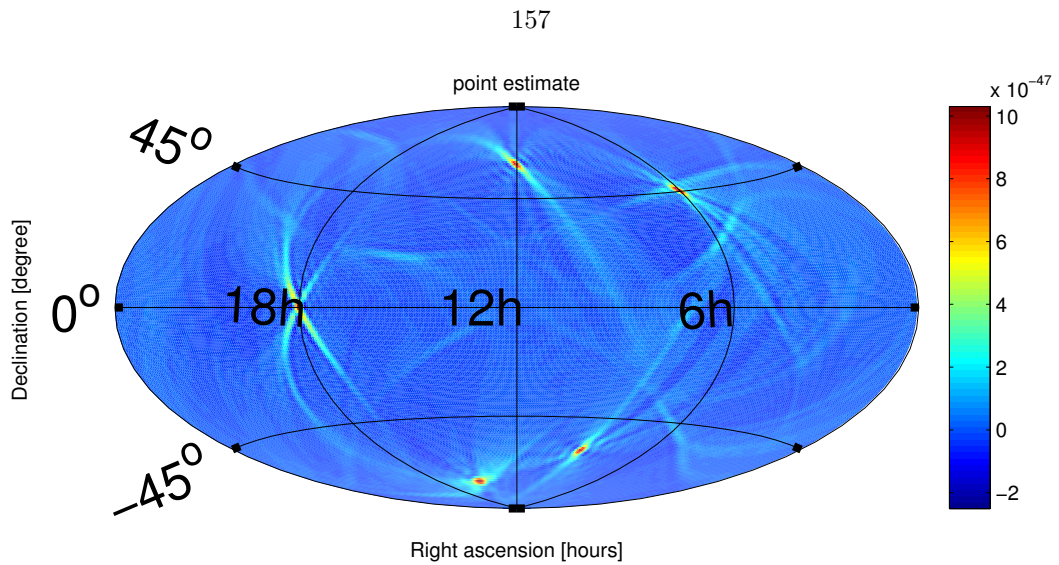


Figure 10.2: An example of a radiometer point spread function. Five strong broadband sources are injected, which can clearly be seen in the hotspots. Of note are the tails, which vary in orientation and magnitude with source declination.

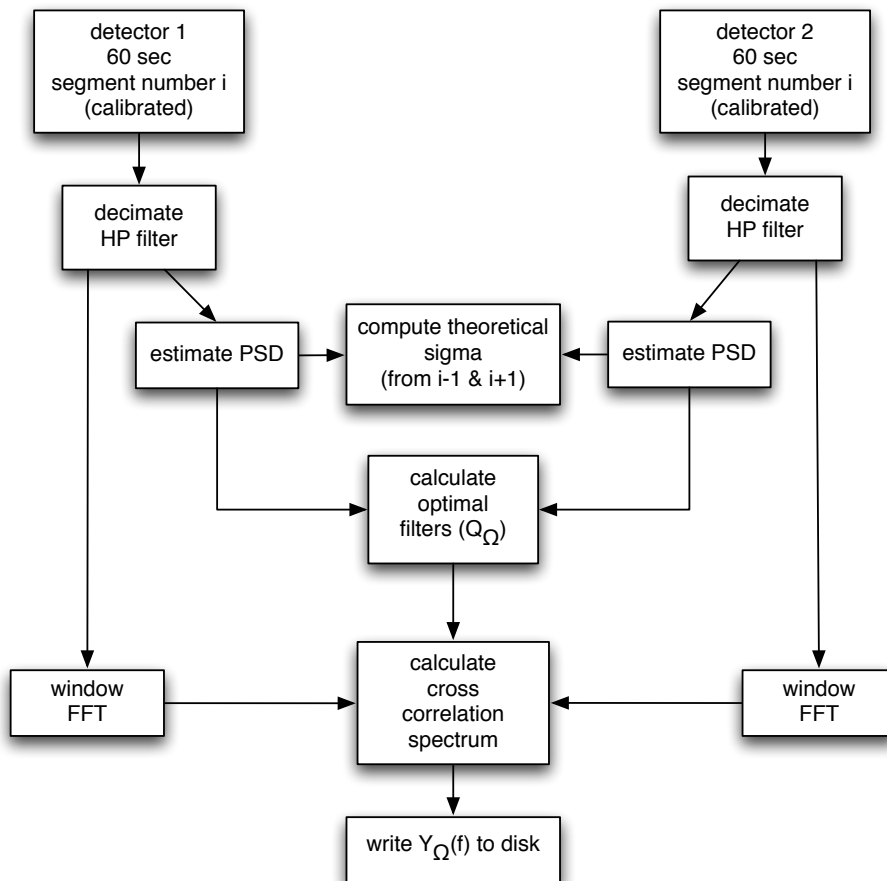


Figure 10.3: The radiometer analysis of a 60 second segment. The data is read, decimated, high-pass filtered, and then the analysis of section 10.2.3 is applied. This whole diagram is also represented as ‘run analysis jobs’ in figure 10.4.

300+ node system is managed by a Condor system [112] for large scale computing, using its directed acyclic graph (DAG) option to execute the whole pipeline. DAG configurations allow automated execution of fairly sophisticated distributed pipelines. Here, the DAG is used to parcel the data into time periods (we will use calendar months as an example); for each month, a DAG will oversee the computation of the  $Y_{\hat{\Omega}}(f)$ , the optimal combination of all segments from that month, and then deletion of all the intermediate data products. Without this deletion, the analysis would place burdensome demands on the cluster. The analysis is not CPU intensive—computer constraints are in the RAM of the individual cluster nodes, as well as disk I/O in loading the recorded strain data into memory. For the narrowband searches, computing an estimate and a sigma for each frequency bin, for each sky location (about 400), for each 60 second segment in a year of coincident data requires on the order of 10TB of data storage:

$$\left(\frac{1000 \text{ Hz}}{0.25 \text{ Hz}}\right) \times (400 \text{ points}) \times (5 \times 10^5 \text{ segments}) \times (2 \text{ numbers}) \times (8 \text{ bytes}) \rightarrow 10 \text{ TB}. \quad (10.23)$$

We do not save all this data; instead we run the full analysis (including optimal combination) for intermediate lengths of time (such as a week or a month), and only save those values to disk (cf. figure 10.4). The whole S5 run takes about 4 days to complete on the cluster, a significant fraction of which is reading the strain data, writing/reading back the intermediate data products (the result for each 60 second segment), and deleting the intermediate data products. The total CPU time is a few hundred hours.

## 10.4 Limits on Gravitational Waves

This section contains results placing limits on the strength of gravitational waves coming from several sky directions. To interpret the maps, it is useful to keep in mind what they represent: they are visualizations of a set of measurements, assumed to be mutually independent for the calculation (even though we know they are not independent), and then placed in a map: the map, however, is heavily blurred by the PSF. The first actual ‘pictures’ of the gravitational wave sky will be the clean maps produced in a spherical harmonic basis and presented in [113] (along with some of these results), with the caveat that these pictures are dominated by detector noise.

### 10.4.1 Detection

Although this chapter only places limits on gravitational waves, it is necessary to discuss how we would actually determine a detection. In the strong signal case, a detection would be obvious: it would stand out clearly with a large SNR (like 10 or more). In the weak signal case, we must distinguish between the statistical variations in the SNR which are due to detector noise and those

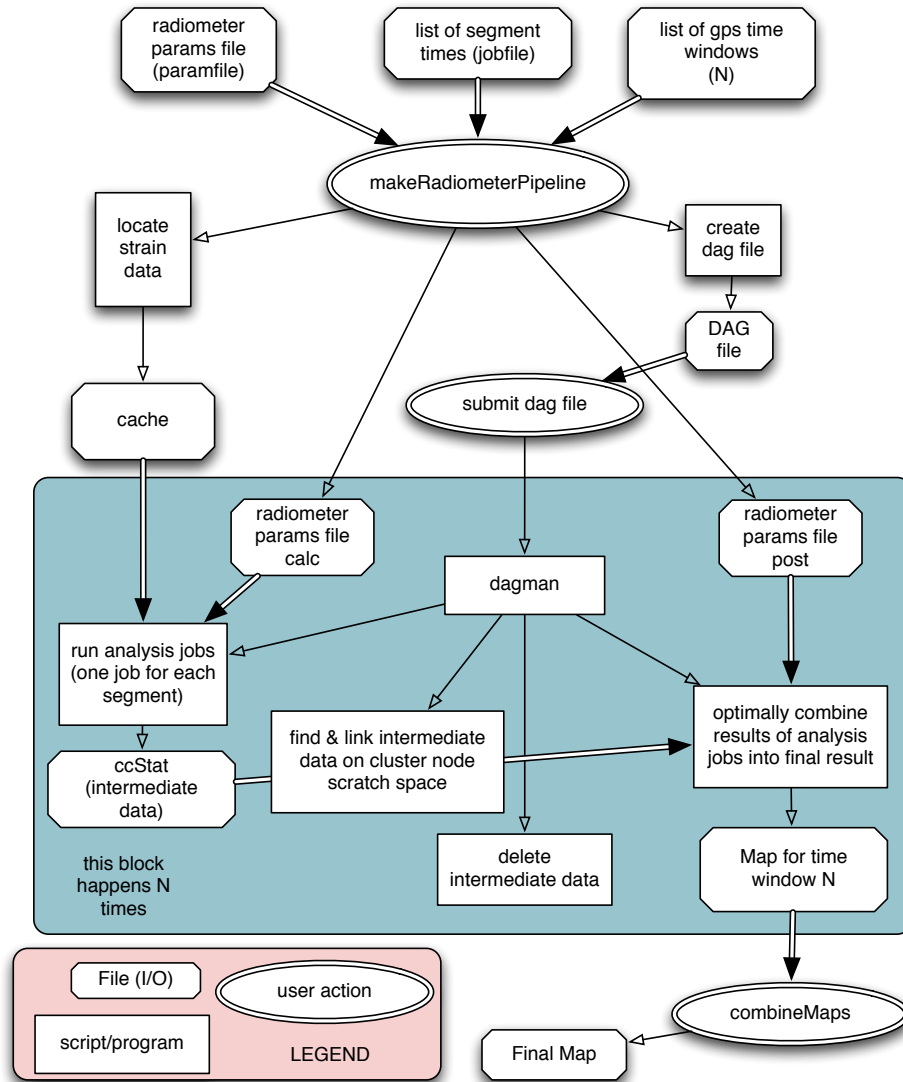


Figure 10.4: The radiometer pipeline. The user provides three input files: (1) a parameters file suitable for the stochastic analysis; (2) a list of science mode (SM) segments, selected for the appropriate level of data quality (i.e., a jobfile); (3) a list of  $N$  gps time pairs. The radiometer pipeline script produces a Condor DAG file. Submitting this DAG to Condor produces a list of radiometer maps, one for each of the  $N$  gps time pairs. The block ‘run analysis jobs’ is depicted in figure 10.3, while the ‘optimal combination’ block is computing the modified version of equation (10.15) for overlapping segments.

which are due to signals.

In the absence of signal, the point estimate  $Y$  is a zero mean signal; for a detector with Gaussian noise, then, the SNR will have a standard normal distribution. The simplest detection strategy is then just to compare the SNR distribution (in time, frequency, or sky location) to a standard normal distribution, via some statistical test. For a distribution over sky location, the pixels will be correlated by the PSF. If the two distributions are compatible, then the results are consistent with no signal. This is the basic approach taken in this chapter, using one-sample Kolmogorov-Smirnov tests for normality (using the MATLAB function `kstest`). Also used are maximum likelihood estimates for Gaussian fits to the observed SNR distributions; if these fall within  $1-\sigma$ , we declare the result consistent with no signal.

Note that the initial LIGO detector noise in reality is neither Gaussian nor stationary. However, since in this search we integrate over time and (for sky maps) signal frequency, the resulting distribution is demonstrably close to Gaussian, except for the outliers. Distinguishing outliers due to instrumental noise from those due to signal is an outstanding problem in all LIGO analyses.

We can create more rigorous detection thresholds in a straightforward manner using: (1) injections to estimate the analysis sensitivity; and (2) time shifting the detector output streams to estimate the background of signal-like events.

Fake signals can be injected into the recorded data stream at analysis time (software injections) or into the detector during operation (hardware injections). By comparing the recovered results with the injected signal, we can determine the efficiency of the search. There have not been any hardware injections of directional stochastic signals, so we must rely on software injections.

We also need confidence that any possible detections are significant; in order to do this, we need an understanding of the detector noise. The detectors are complicated devices, with non-stationary and non-Gaussian noise. The method for background estimation is time shifting the detector output streams before applying any analysis. This technique is expected to remove any stochastic signal present but preserve the statistics of the noise, and so it yields an estimate of the background. Of course, this time shifting method depends on noise sources between the two detectors being truly uncorrelated; this is assumed to be the case for the L1-H1 pair (separated by 3000 km).

Together these techniques can be used to set detection thresholds by comparing analysis results to the actual detector noise and sensitivity statistics, rather than assumed Gaussian distributions. This is the subject of current (and future) work for the radiometer analysis. A preliminary set of injections and time-shifted analysis has been done, however, as a sanity check on the results in this chapter.

## 10.4.2 The Data

The analyzed data are from the fifth LIGO Science Run (S5), and spans the period from December 1, 2005 to September 30, 2007. The data are represented as calibrated strain ( $h(t)$ , with version V3 calibration—see [114] for details) data, with a typical sensitivity as shown in figure 10.5. The data is segmented into 60 second intervals, high-passed at 32Hz, decimated to 4096 Hz, Hann windowed, and a cross-correlation analysis is performed on each segment. The segments are then combined into the final result, using a modified version of equation (10.15). The windowing effectively discards half the data, so to maintain the sensitivity, the segments are actually overlapped using the procedure described in detail in [111]. The total number of 60 second segments analyzed for the globular cluster search is 818392; of these, 8406 (1.03%) were vetoed by the  $\delta\sigma$  cut (more in section 10.4.3.2). The total remaining is about 281 days of observation time.

## 10.4.3 Data Quality

We determine and apply various data quality flags, which describe certain aspects of the detector environment for the time the flag is set. For example, a flag such as `H1:PRE_LOCKLOSS_30_SEC:v99` indicates the period encompassing 30 seconds before the H1 interferometer loses lock; the interferometer may be experiencing some instabilities during this period (which eventually cause the lock loss), and so we can exclude this data a priori. A standard set of data quality flags was applied to remove periods when, e.g., a signal was being injected (stochastic or otherwise) or a saturation was detected somewhere in the interferometer. These are the same flags used in the isotropic analysis in [101], and are appropriate for the types of results presented here, which are focused on long integration times. A search focused on shorter integration times (such as a short or medium duration transient search, discussed in section 10.6) might apply a slightly different set of data quality flags.

### 10.4.3.1 Frequency Masking

Frequencies corresponding to pulsar injections, power line harmonics, or other known instrumental lines, are masked in the analysis; these frequencies do not contribute to the final result. The mask is done in the calculation of the optimal filter. The frequency bins masked are listed in table 10.1. For the radiometer search, this eliminates  $36 \times 0.25$  Hz bins, which is about 0.05% of the total bandwidth.

### 10.4.3.2 Delta-Sigma Cut

The technique for estimating the variance described in section 10.2.2 and illustrated in figure 10.1 also allows a simple, final, data quality cut in addition to the ones described in this section. This cut, known colloquially as the delta-sigma cut, involves comparing the naive estimate of the variance

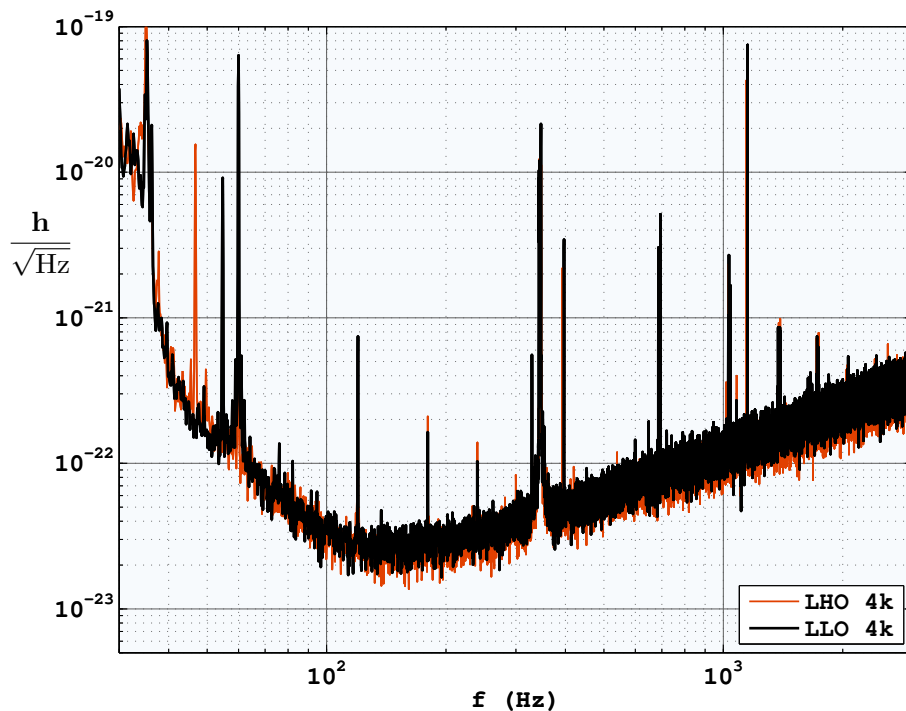


Figure 10.5: Representative strain noise curves from the 4 km LIGO detectors during the fifth LIGO science run.

for a given segment ( $\sigma_i$  in figure 10.1) to the theoretical value ( $\hat{\sigma}_i$ ). If  $\frac{\sigma_i}{\hat{\sigma}_i} > \Delta\sigma$  for any segment  $i$ , that segment is simply excluded from the analysis. This cut removes periods of excess detector noise, and for the results presented here, a threshold of  $\Delta\sigma = 1.2$  removed approximately 1% of the data which was not already excluded by the data quality flags.

#### 10.4.4 Posterior Distributions and Upper Limits

For the cases where a previous result exists (the sky map in section 10.4.5 and the Sco-X1 targeted search in section 10.5.1), that previous result is used as a Bayesian prior in forming the new upper limit. In this case, the prior results are from LIGO's fourth science run and so are indexed by an  $S_4$ .

For a previous cross-correlation estimate  $Y_{S_4}$  (with variance  $\sigma_{S_4}^2$ ), we can form the posterior distribution of the true value of  $Y$  (called  $x$  here) as a Gaussian:

$$p(x) = 0 \quad \text{for } x < 0, \quad (10.24)$$

$$p(x) = \frac{1}{\Gamma_{S_4}} \exp\left(\frac{-(x - Y_{S_4})^2}{2\sigma_{S_4}^2}\right) \quad \text{for } x \geq 0, \quad (10.25)$$

<b>f</b>	<b>nBins</b> (0.25Hz)
52.75*	1
60	1
108.75*	1
120	1
148*	3
180	1
193.5*	3
240	1
265.5*	1
300	1
360	1
376*	3
420	1
480	1
501.25*	3
540	1
575.25*	1
600	1
763.75*	1
849*	1
1220.75*	3
1400.75*	5

Table 10.1: The frequencies (and number of bins) masked in the S5 radiometer and narrowband radiometer analyses. The frequencies corresponding to injected pulsars have been marked with an asterisk.

where  $\Gamma_{S4}$  is a normalization. Then we can use that as the prior distribution for a new measurement of  $Y$ . Then for the current measurement  $Y_i$  we can form a likelihood for  $x$  (the true value of  $Y$ ) marginalized over the calibration uncertainty,

$$L(x) = 0 \quad \text{for } x < 0, \quad (10.26)$$

$$L(x) = \frac{1}{\Gamma_i} \exp\left(\frac{-(x - Y_i)^2}{2\sigma_i^2 + Y_i^2 c^2}\right) \quad \text{for } x \geq 0, \quad (10.27)$$

where  $c$  is a fractional calibration uncertainty (10% in this analysis), which we have simply included as contributing to the total variance. Then the Bayesian posterior distribution for the S5 result is the likelihood times the prior,

$$P(x) = L(x)p(x), \quad (10.28)$$

and the confidence level  $\mu$  upper limit on the true value of  $Y$ ,  $x_\mu$ , is given by the value of  $x$  where the cumulative distribution function (CDF) of the posterior  $P(x)$  is the desired confidence level:

$$\mu = \int_0^{x_\mu} P(x) dx. \quad (10.29)$$

## 10.4.5 Gravitational Wave SkyMap

Figure 10.6 shows the results of a radiometer analysis using data from S5. A broadband point estimate, integrated over the frequencies from 50 Hz to 1.8 kHz, is computed for each square degree of the sky (so there are a total of  $360 \times 181$  points). This strongly oversamples the sky, since the resolution is limited to about 400 points. The resulting SNR distribution over sky location will be highly correlated.

Figure 10.6(a) is a SNR map of the S5 run for a flat source strain spectrum. This map is constructed by dividing the point estimate for each sky location (not shown) by the theoretical sigma for the same location (figure 10.6(d)). Figure 10.6(b) is a 90% confidence upper limit from the S5 run for a flat source strain spectrum, using the corresponding result from the S4 run ([106]) as a Bayesian prior as described in section 10.4.4. The upper limit varies from  $2.1511 \times 10^{-50} \text{ Hz}^{-1}$  at RA 17.07 h, Declination  $53^\circ$  to  $2.0121 \times 10^{-49} \text{ Hz}^{-1}$  at RA 23.33h, Declination  $6.0^\circ$ . Figure 10.6(c) is a histogram of the SNR map (figure 10.6(a)). Also shown on this plot are a maximum likelihood Gaussian estimate for the distribution (green solid), along with an ideal Gaussian (red solid) and  $\pm\sigma$  deviations (red dashed), for a distribution with 400 independent points (which is approximately the resolution of the radiometer for a constant  $H(f)$ ). The maximum likelihood estimate is within the  $\pm\sigma$  bounds; the SNR distribution also passes a Kolmogorov-Smirnov test comparing it to the normal distribution for 400 effective degrees of freedom, at  $\alpha = 0.05$ .

Because the noise cannot be distinguished from the standard normal distribution, we conclude the results are consistent with no signal. Figure 10.6(d) is the theoretical sigma, which is the sensitivity level. The variation in sensitivity with declination is a natural consequence of the detector antenna pattern (cf. section 10.2.4, equation (10.17)). The variation with right ascension is a bit different. Ideally, the sensitivity will not vary with right ascension; in reality, the detectors work better (lower noise, more stability) during the night when anthropogenic noise is at minimum. Since the radiometer is an earth-rotation aperture synthesis technique and the sensitivity varies during a single day this breaks the symmetry with respect to right ascension. This day-night asymmetry will be smoothed as the earth orbits the sun; since S5 was not exactly two calendar years, some portions of the sky got better coverage than others, resulting in the residual asymmetry. A further contribution comes from the changes in the level of detector day-night asymmetry during the course of the run: it got better as the run progressed.

### 10.4.5.1 Injection

To show what a signal would look like, a strong point source, with strength  $H(f) = 5 \times 10^{-49} \text{ Hz}^{-1}$  was injected at RA = 6h, Decl =  $-45^\circ$ . This strength is smaller than the tightest upper limit set during the S4 analysis (which was  $8.5 \times 10^{-49} \text{ Hz}^{-1}$ , [106]). It is clearly visible as a dominant hotspot

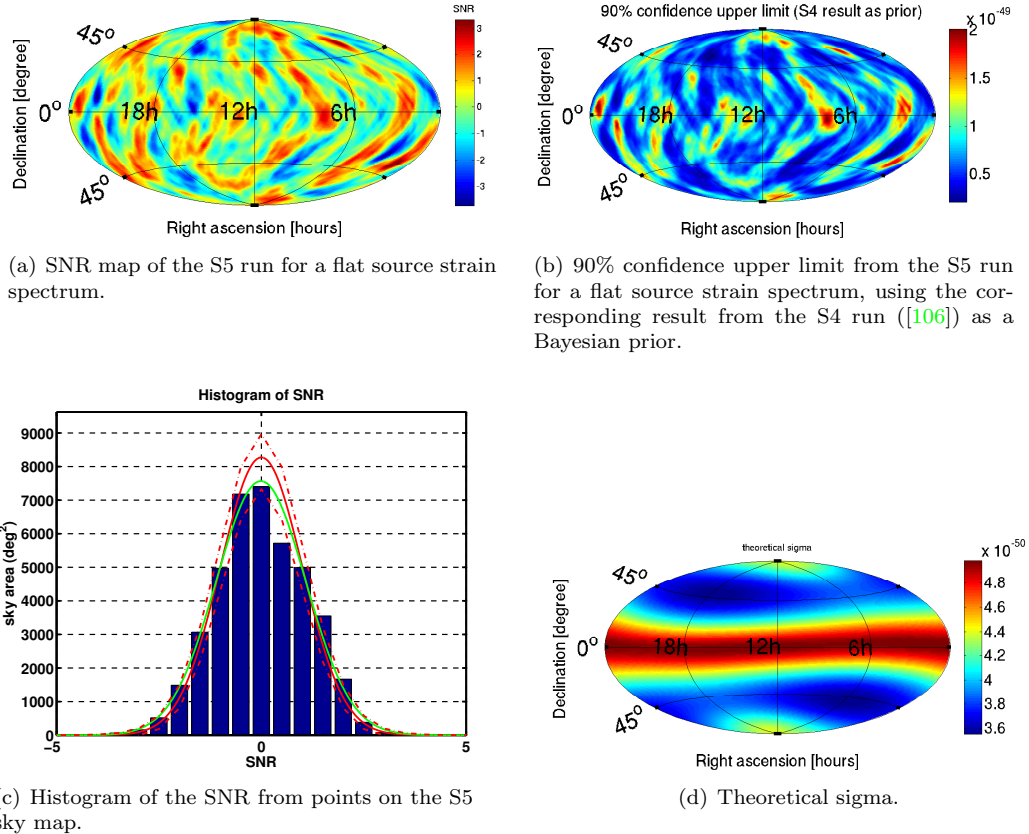


Figure 10.6: Results for the radiometer search from S5 assuming a flat source strain spectrum ( $H(f) = \text{const}$ ). Refer to the text (section 10.4.5) for a description.

in the resulting SNR map in figure 10.7. It also significantly distorts the SNR distribution over the sky, creating a long tail at positive SNR, and causing the maximum likelihood estimate Gaussian to lie well outside the  $\pm\sigma$  bounds of the ideal Gaussian.

## 10.5 Frequency and Location Resolved Searches

By breaking up the integral in equation (10.10) we can refrain from integrating over the whole measurement bandwidth. This frequency resolved search is called a narrowband radiometer. Here we use it to present limits on several interesting astrophysical targets.

### 10.5.1 Upper Limit on gravitational waves from Sco X1

Low mass x-ray binaries (LMXBs) are binary systems with a neutron star and a companion low-mass star; the companion (or donor) object is accreting matter onto the neutron star, driving its spin. The accreting matter will drive the spin frequency until some process radiates away the angular momentum of the accreting matter. In the case that gravitational waves provide the torque balance,

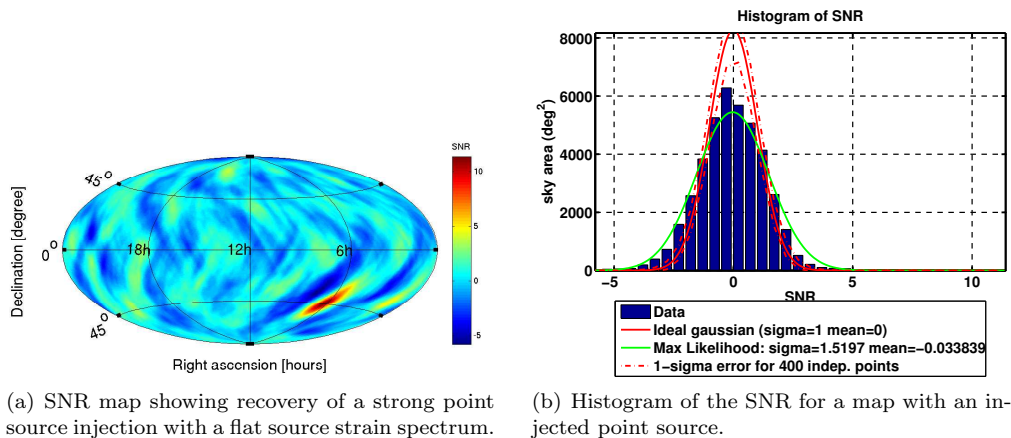


Figure 10.7: A broadband point source with power spectrum  $H(f) = 5 \times 10^{-49} \text{ Hz}^{-1}$  was injected at RA = 6h, Decl =  $-45^\circ$ . It is clearly recovered, and the resulting SNR distribution vs. sky direction shows a long tail in the positive SNR direction and significant deviation from the standard normal distribution (the actual levels in the tail cannot be seen in the plot, but the x-axis limits are set according to the maximum SNR values). The injected source strength is approximately one-half the tightest upper limit set during the S4 run ([106]).

then the energy radiated in gravitational waves is related to the x-ray radiated energy by [115]

$$F_{GW} \approx \frac{f_{spin}}{f_{Kepler}} F_X, \quad (10.30)$$

where  $f_{spin}$  is the spin frequency and  $f_{Kepler}$  is the final orbital frequency of the accreting matter. Sco-X1 is the most luminous LMXB and so makes an interesting target for a narrowband search. The radiometer is a useful method since it makes a minimal amount of assumptions, and we do not know the spin frequency.

Upper limits from Sco-X1 in the frequency band from 50 Hz to 1 kHz are presented in  $6941 \times 0.25$  Hz frequency bins in figure 10.8 and in [113]. In the absence of signal, the frequency bins will all be independent; these results are consistent with no signal. The power spectrum used in the optimal filter is a constant  $H(f)$ . The SNR distribution passes a Kolmogorov-Smirnov test for a Gaussian distribution with 6941 degrees of freedom (the number of frequency bins), failing to reject the null hypothesis at  $\alpha = 0.05$ . The upper limit in figure 10.8 has used the corresponding result from the S4 run [106] as Bayesian prior (cf. section 10.4.4); the new limit surpasses the previous result by a factor of about 5.

### 10.5.2 The Galactic Center

The center of our Milky Way galaxy represents another promising target. It is at (RA = 17h 45m 40.04s, Dec = -29 deg 00 min 28.1s) at a distance of about 7.6 kpc. It contains a supermassive black hole [116] and an intense compact radio source (Sagittarius A\*, which is probably the black

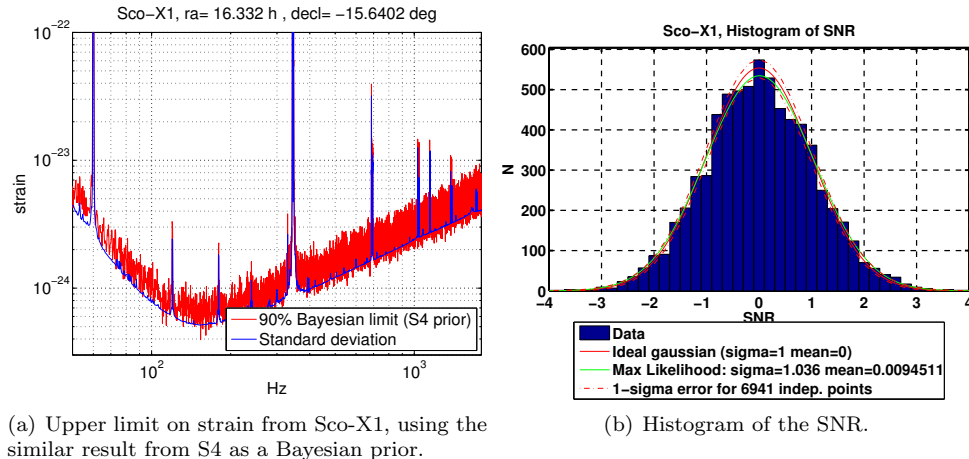


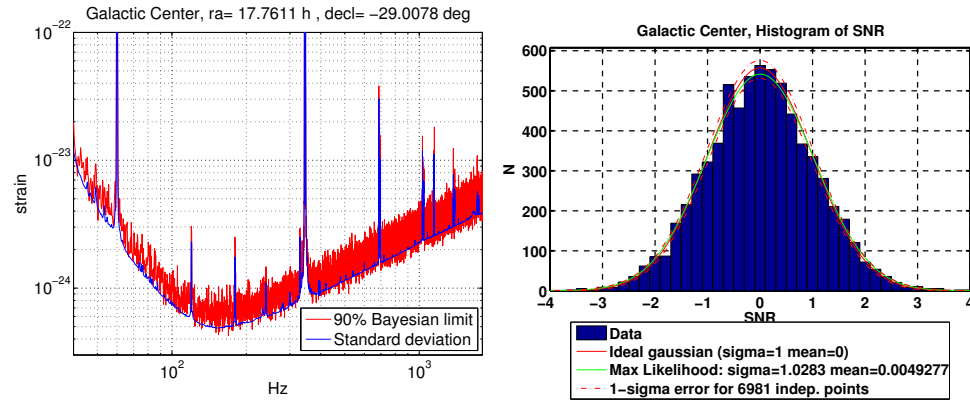
Figure 10.8: Limits on gravitational radiation from Sco-X1.

hole accretion disk) and many thousands of stars in a narrow angular band [117]. It is, moreover, behind the zone of avoidance which makes it difficult to observe with optical, infrared, or soft x-ray telescopes due to the intervening interstellar dust. Detection of gravitational waves from object infalling to the central supermassive black hole or orbiting it is unlikely at the audio frequency band of ground based detectors ([118], [119]), but it is still an interesting target for the radiometer due to the sheer number of objects at a close distance, within a limited angular region on the sky. These could from a stochastic signal, as it would be a large number of unresolved sources. Figure 10.9 presents upper limits on gravitational waves emanating from the galactic center in the frequency band from 40 Hz to 2 kHz (6981 bins); the results are consistent with no signal, and the SNR distribution passes a KS test at  $\alpha = 0.05$ , failing to reject the null hypothesis that the distribution is standard normal.

### 10.5.3 Globular Clusters

Globular clusters are spherical agglomerations of stars bound by gravity, typically containing from  $10^4$  to  $10^7$  stars, with a typical half-radius (the radius containing half the mass of the cluster) of ten parsecs [120]. So for globular clusters closer than 5kpc, most of the mass is contained in a region on the sky of angular size  $\sim 10'$ , which makes them interesting targets for radiometer analyses.

Their high density of stars makes globular clusters promising candidates to hold relativistic binary systems [120], but it also makes them an interesting target for a radiometer search for two simple reasons: they hold a lot of stars in a relatively small patch of the sky, and some of them are pretty close. Because the radiometer is optimal for point sources of a stochastic nature, it is a good tool for targeting unmodeled sources of a compact size on the sky, and globular clusters are good candidates for containing such sources—especially for containing a number of superposed incoherent sources. This situation is similar to that of the galactic center.



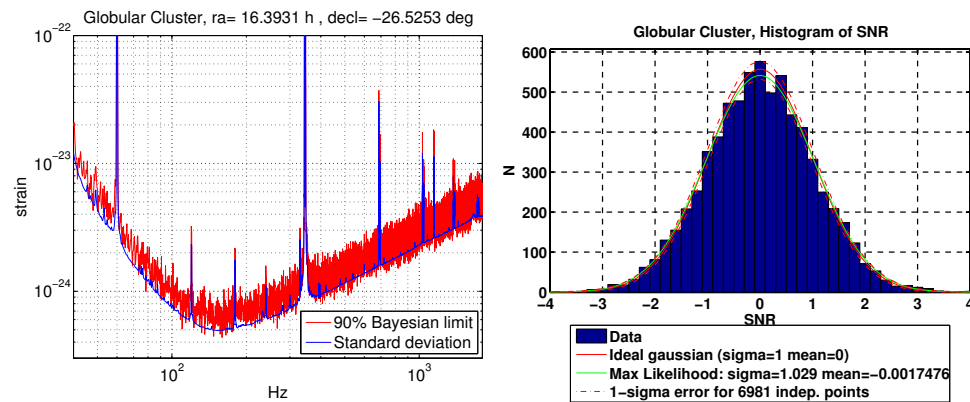
(a) Upper limit (90% confidence level) on strain from the galactic center. The standard deviation bins is the theoretical sigma. (b) Histogram of the SNR in 0.25 Hz frequency from the galactic center. The histogram shows data points (blue bars) and a fitted ideal gaussian (red line) with parameters  $\sigma=1$  and  $\text{mean}=0$ . The maximum likelihood fit (green line) has  $\sigma=1.0283$  and  $\text{mean}=-0.0049277$ . A dashed red line indicates the 1-sigma error for 6981 independent points.

Figure 10.9: Limits on gravitational radiation from the galactic center.

There are about 150 globular clusters in the Milky Way, and 15 of these which are closer than 5 kpc are listed in table 10.2.

In this section I present 90% confidence upper limits on strain, binned by frequency, for each of these globular clusters. These limits were set using data from S5.

For all the clusters, the results are consistent with no signal. The SNR distribution for each cluster passes a Kolmogorov-Smirnov test comparing it to the standard normal distribution with a  $\alpha = 0.05$ , with the number of degrees of freedom equal to the number frequency bins. Table 10.3 also shows the integrated point estimate for each cluster (the total strain power), the integrated sigma, the KS statistic, and the asymptotic p-value of the SNR distribution. The p-value is returned from the MATLAB routine used to perform the KS-test; it represents the probability of observing this data set, or one with stronger deviations from the null-hypothesis distribution (in this case standard normal).



(a) Upper limit on strain from GC1.

(b) Histogram of the SNR.

Figure 10.10: Results from GC1.

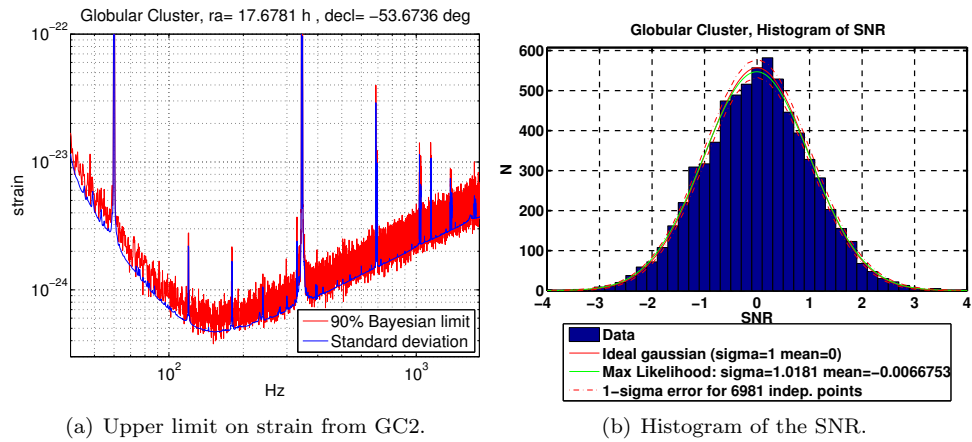


Figure 10.11: Results from GC2.

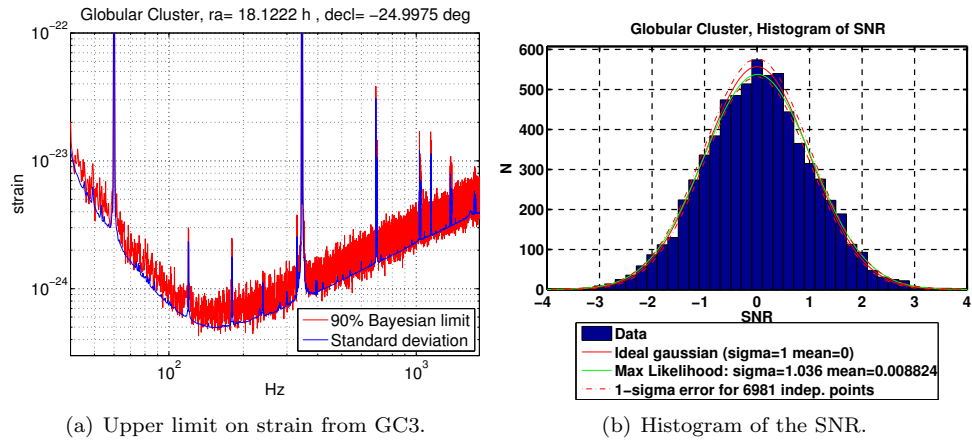


Figure 10.12: Results from GC3.

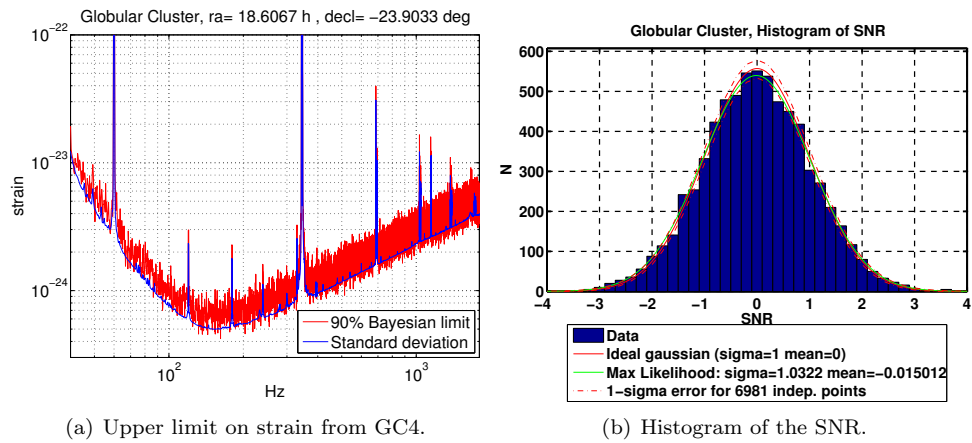


Figure 10.13: Results from GC4.

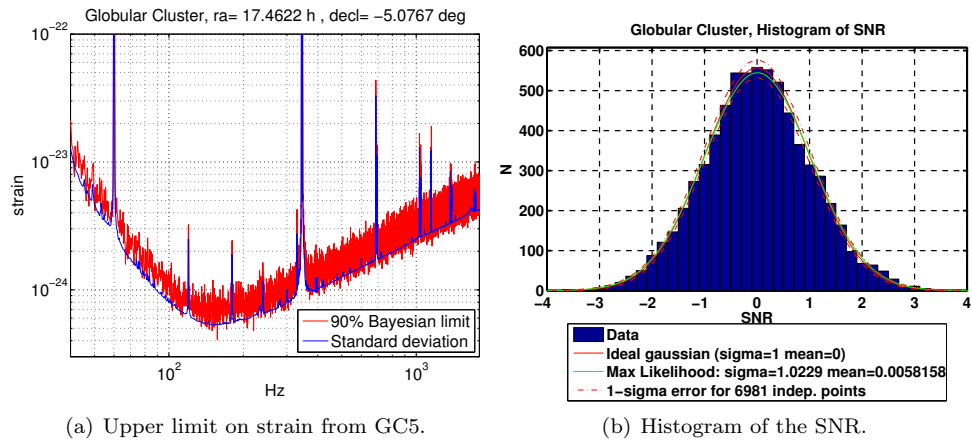


Figure 10.14: Results from GC5.

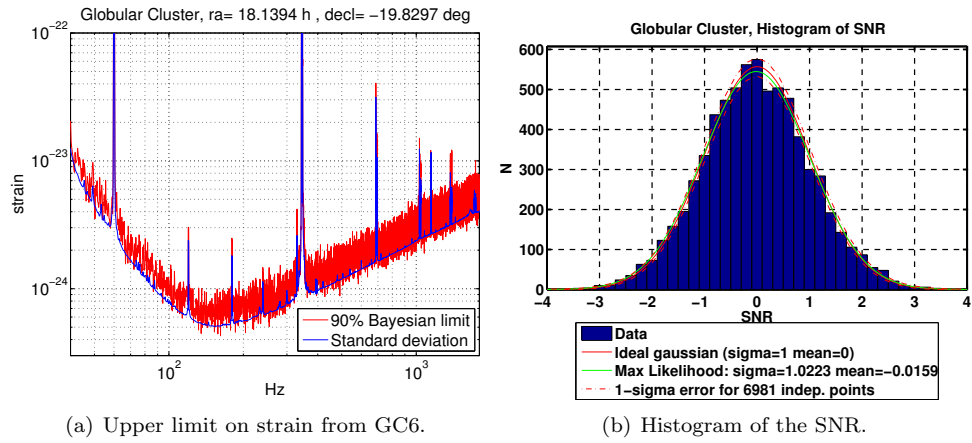


Figure 10.15: Results from GC6.

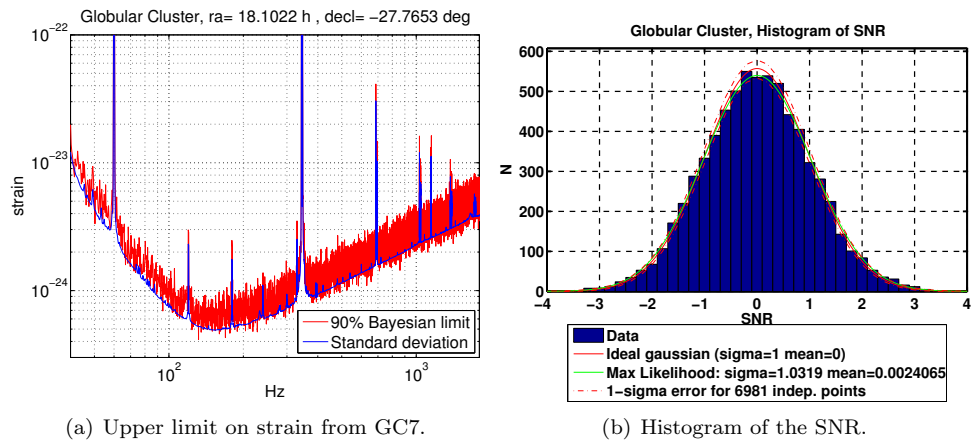


Figure 10.16: Results from GC7.

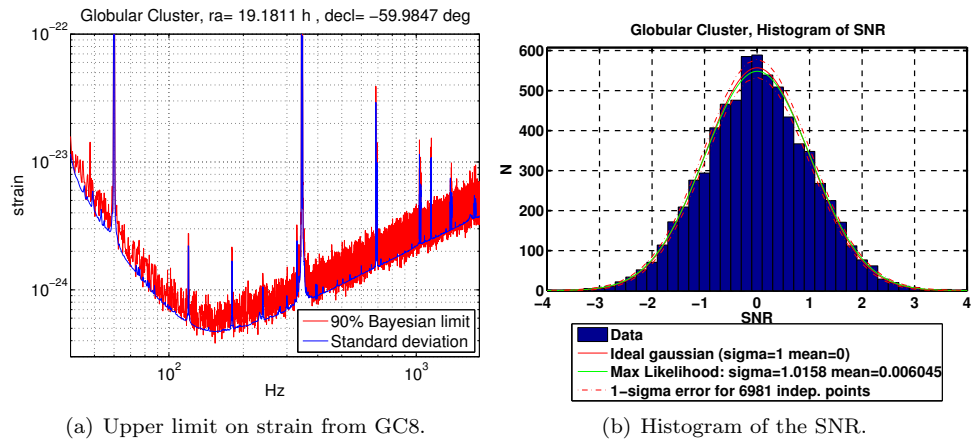


Figure 10.17: Results from GC8.

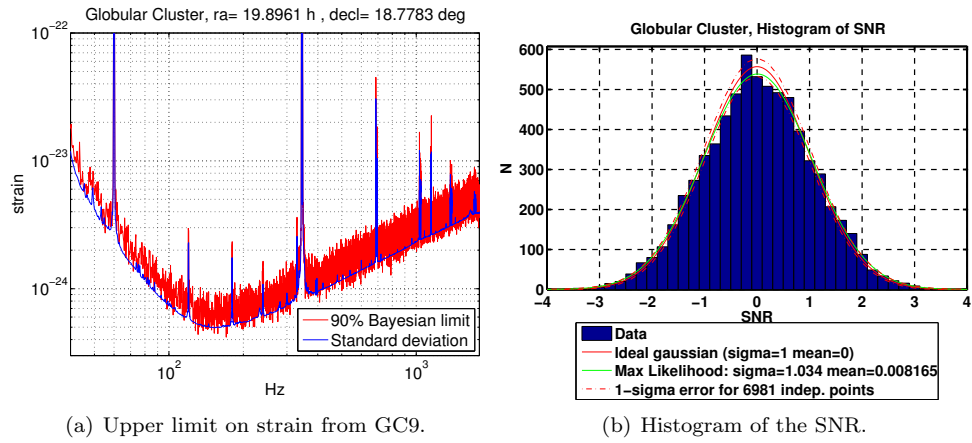


Figure 10.18: Results from GC9.

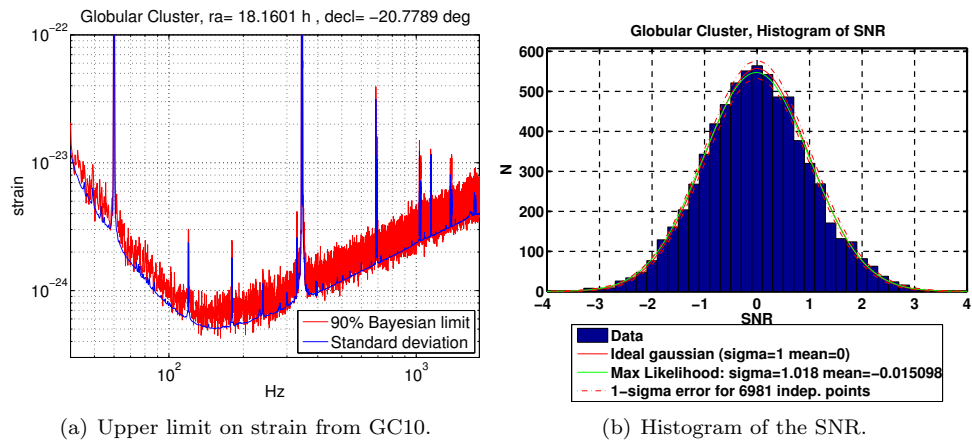


Figure 10.19: Results from GC10.

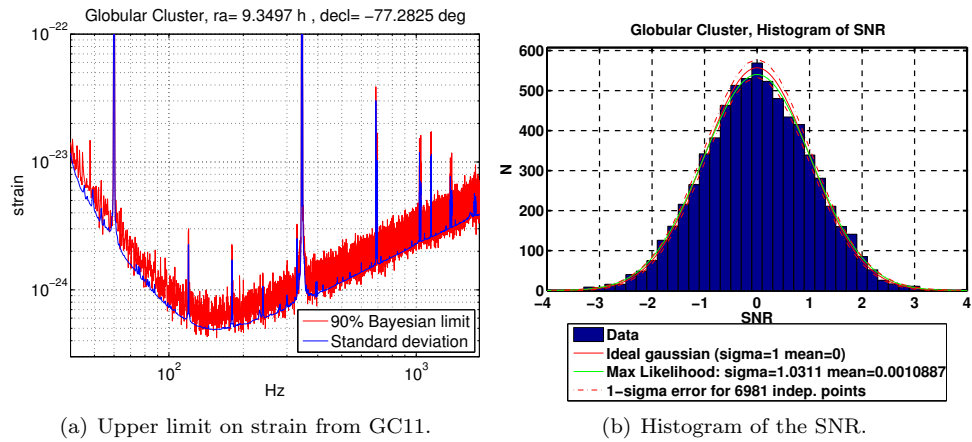


Figure 10.20: Results from GC11.

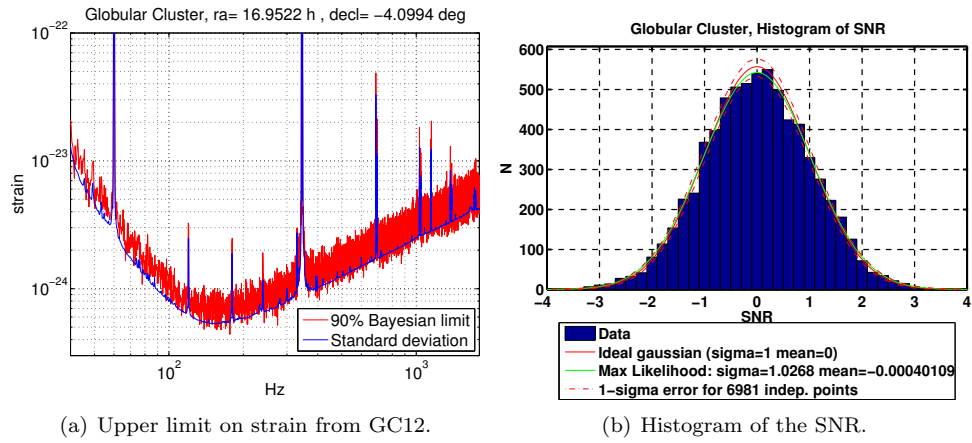


Figure 10.21: Results from GC12.

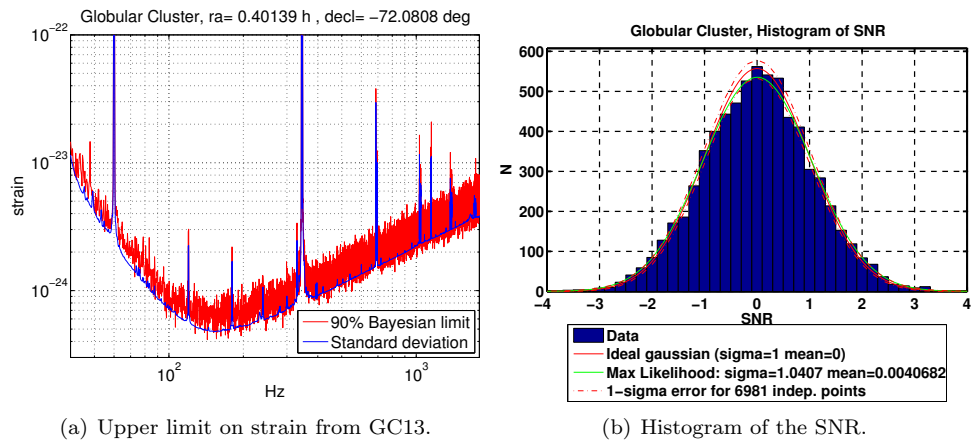


Figure 10.22: Results from GC13.

Cluster Name	Right Ascension	Declination	Distance (kpc)
NGC 6121	16 23 35.	-26 31 31	2.2
NGC 6397	17 40 41	-53 40 25	2.3
NGC 6544	18 07 20.	-24 59 51	2.7
NGC 6656	18 36 24.	-23 54 12	3.2
NGC 6366	17 27 44.	-05 04 36	3.6
2MASS-GC01	18 08 21.8	-19 49 47	3.6
NGC 6540	18 06 08.	-27 45 55	3.7
NGC 6752	19 10 52.0	-59 59 05	4
NGC 6838	19 53 46.	+18 46 42	4
2MASS-GC02	18 09 36.5	-20 46 44	4
E 3	09 20 59.	-77 16 57	4.3
NGC 6254	16 57 08.	-04 05 58	4.4
NGC 104	00 24 05	-72 04 51	4.5
Terzan 12	18 12 15.	-22 44 31	4.8
NGC 6218	16 47 14.	-01 56 52	4.9

Table 10.2: The globular clusters targeted for analysis. This list includes all known globular clusters closer than 5 kiloparsecs.

Object	$\text{Hz}^{-1}$	$\sigma$	p-value	KS statistic
NGC 6121	$4.21 \times 10^{-50}$	$4.32 \times 10^{-50}$	0.76	0.007999
NGC 6397	$-7.02 \times 10^{-50}$	$3.90 \times 10^{-50}$	0.28	0.011844
NGC 6544	$-3.81 \times 10^{-50}$	$4.37 \times 10^{-50}$	0.09	0.014854
NGC 6656	$-8.23 \times 10^{-50}$	$4.41 \times 10^{-50}$	0.21	0.012678
NGC 6366	$-3.95 \times 10^{-52}$	$5.02 \times 10^{-50}$	0.48	0.010026
2MASS-GC01	$-8.50 \times 10^{-50}$	$4.57 \times 10^{-50}$	0.13	0.013957
NGC 6540	$-4.33 \times 10^{-50}$	$4.27 \times 10^{-50}$	0.38	0.010823
NGC 6752	$-6.20 \times 10^{-50}$	$3.94 \times 10^{-50}$	0.44	0.010372
NGC 6838	$-1.21 \times 10^{-50}$	$4.35 \times 10^{-50}$	0.14	0.013839
2MASS-GC02	$-8.09 \times 10^{-50}$	$4.54 \times 10^{-50}$	0.19	0.012901
E 3	$5.04 \times 10^{-50}$	$4.22 \times 10^{-50}$	0.12	0.014117
NGC 6254	$-3.47 \times 10^{-50}$	$5.03 \times 10^{-50}$	0.39	0.010782
NGC 104	$1.23 \times 10^{-51}$	$4.06 \times 10^{-50}$	0.42	0.010524
Terzan 12	$-7.30 \times 10^{-50}$	$4.46 \times 10^{-50}$	0.74	0.008133
NGC 6218	$-7.62 \times 10^{-50}$	$5.03 \times 10^{-50}$	0.04	0.016794

Table 10.3: Summary of results from surveyed point sources. Included are the total strain power estimate (not an upper limit), the sigma for that estimate, the asymptotic p-value for Kolmogorov-Smirnov statistic, and the KS statistic.

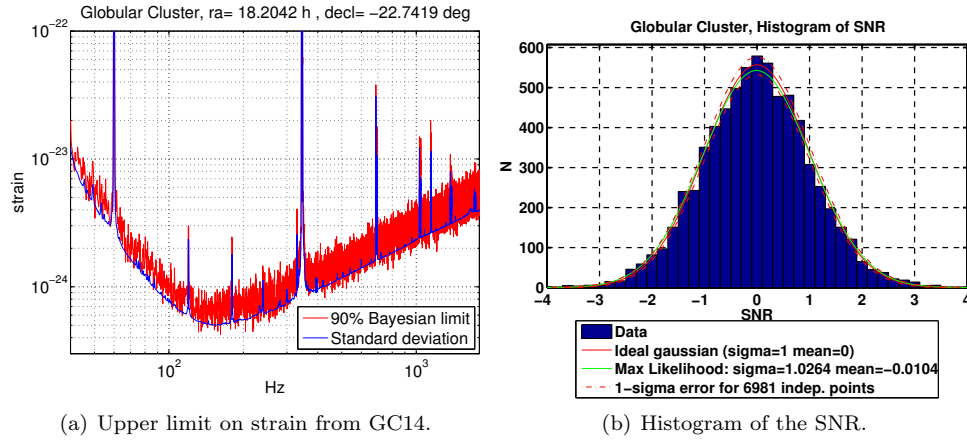


Figure 10.23: Results from GC14.

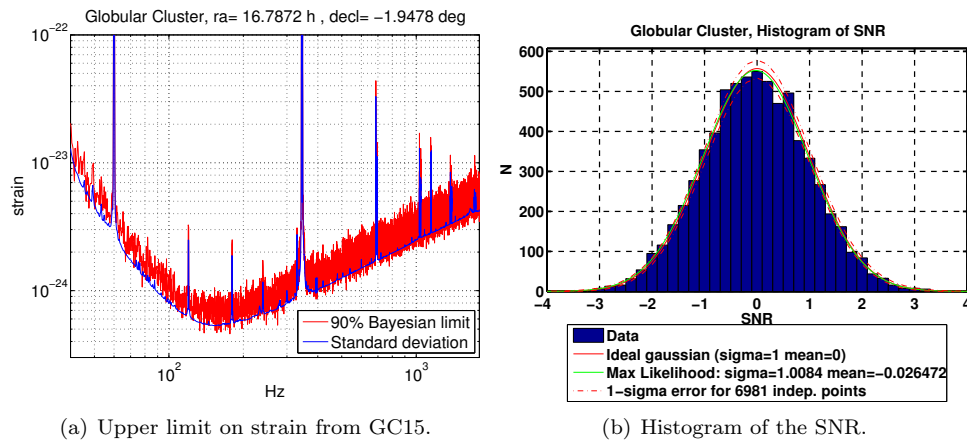


Figure 10.24: Results from GC15.

### 10.5.4 Untargeted Narrowband Search on the Whole Sky

In addition to the targeted searches described above, an untargeted frequency-binned search was also carried out. This search targeted the 768 sky locations which are the pixel locations in the HEALpix decomposition of the sphere [121]; HEALpix was chosen both for the equal area and isolatitude nature of the decomposition (although no use has yet been made of the second feature). This number of pixels oversamples the sky by a factor of about 2; it is thus a reasonable tiling to search the whole sky, without excessive redundancy. Somewhat less data was used in this search than the others described earlier: only 565381 60 second segments, of which 5716 (1.011%) were vetoed. This corresponds to 194 days of observation time.

A narrowband search was performed for each pixel with a frequency spacing of 1 Hz, in the band from 50 Hz to 1 kHz. Visualization of the data is somewhat problematic, since it is 768 spectra or  $\sim 900$  skymaps. Moreover, the PSF will correlate different sky locations, so a simple KS-test cannot be performed on the whole data set. Treating each pixel location separately, however, we can perform a KS-test on the SNR distribution at each pixel. The SNR distributions from 29 of these directions fail the test at an  $\alpha = 0.05$ . For a true Gaussian underlying distribution, we would expect  $19.2 \pm 4.3$  rejections (determined using a simple Monte Carlo with the same MATLAB KS-test routine), so this result would represent a 1% outlier; however the analysis has also been run with time-shifted data streams (meaning non-physical results). In the two time shifted analyses (with 30 ms and 350 ms time shifts), 26 and 29 directions failed at  $\alpha = 0.05$ . This indicates that the SNR distribution with frequency is not actually Gaussian (not a big surprise), and so deviations from Gaussianity alone will not lend great confidence to a claim of detection. Taking this analysis further will thus require better estimation of the background (as discussed in section 10.4.1).

Nonetheless, we list these directions in table 10.4, which includes the right ascension and declination, the maximum and minimum SNR, the frequency bins with the maximum and minimum SNR, and the asymptotic p-value. Visual inspection of the spectra reveals no obvious outliers. The next step would be a closer examination of all the measurements above an interesting SNR threshold, but this has not yet been done.

### 10.5.5 Injection

Again, to show what a strong signal would look like, a strong point source was injected at RA = 6h, Decl =  $-45^\circ$ , with a strain power spectrum of  $H(f) = 8 \times 10^{-48} \text{ Hz}^{-1}$  in the band from 100 Hz to 200 Hz, and  $1 \times 10^{-50} \text{ Hz}^{-1}$  outside that band. This strong injection, at a level below what would have been seen in S4, is clearly recovered, as can be seen in figure 10.25. Shown are the measured strain power spectrum  $H(f)$  and the SNR as a function of frequency, along with a histogram of the SNR. The histogram shows a strong deviation from the standard normal, and the SNR as a function

RA [h]	DECL [deg]	$SNR_{max}$	$f_{max}$	$SNR_{min}$	$f_{min}$	p value
11	72.3876	4.36	688	-6.56	62	0.021
7.5	54.3409	4.43	57	-3.79	54	0.004
17.5	54.3409	3.93	316	-5.94	62	0.017
0.42857	48.1412	4.33	77	-4.08	70	0.007
22.7143	48.1412	3.88	77	-3.35	298	0.020
21	35.6853	4.77	95	-2.90	465	0.017
23.625	19.4712	3.78	122	-4.77	70	0.008
1.5	14.4775	4.73	69	-5.3	75	0.013
18.75	14.4775	4.66	232	-3.66	63	0.005
0.375	9.5941	4.75	54	-4.67	214	0.004
15.75	4.7802	3.72	58	-3.87	234	0.016
18	4.7802	3.96	92	-3.31	77	0.025
6.375	0	3.41	796	-4.56	55	0.009
7.125	0	3.78	77	-4.95	55	0.003
15.375	0	3.97	58	-3.53	444	0.020
6.75	-4.7802	3.71	99	-4.70	55	0.015
2.625	-9.5941	3.25	70	-5.67	62	0.007
18	-14.4775	3.74	86	-4.92	77	0.010
10.125	-19.4712	3.05	54	-5.51	62	0.014
14.625	-19.4712	4.69	77	-5.31	54	0.010
15.375	-30	4.17	77	-5.37	54	0.006
21	-35.6853	4.08	66	-3.08	618	0.008
8.625	-41.8103	3.91	974	-3.24	57	0.024
19.875	-41.8103	3.03	722	-3.45	77	0.013
22.5	-54.3409	4.70	62	-3.32	685	0.005
19	-72.3876	5.30	62	-3.27	73	0.013
4.5	-78.2841	6.35	62	-3.65	86	0.016
13.5	-78.2841	4.55	62	-3.97	100	0.013
16.5	-78.2841	3.45	93	-3.97	978	4.2e-05

Table 10.4: Results from a un-targeted narrow band search of the sky

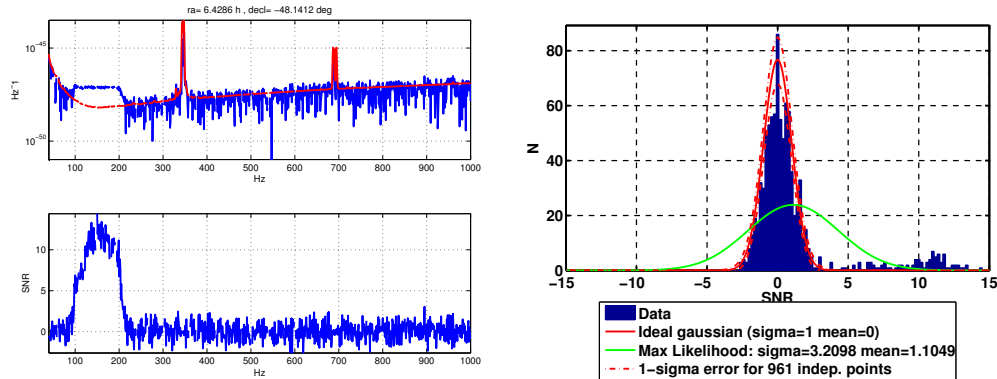
of frequency shows a clear bump at the frequencies of the injected signal. None of the sky directions in the untargeted narrowband search looked anything like this injection; they all appear similar to the results from the globular clusters and the galactic center, with the power spectrum close to the theoretical sigma at all frequencies.

## 10.6 Future Work

This section describes several possible extensions to this analysis.

### 10.6.1 Detection Thresholding

The first clear work is set clear detection thresholds through more systematic sensitivity analysis and background estimation (cf. section 10.4.1), by performing large sets of injections and large sets of time shifted analyses. The current implementation is not well suited to doing large numbers of injections (because the full pipeline is run for each injection or each time-shift), but the necessary



(a) Recovered strain power spectrum and SNR near direction of an injected point source.

(b) Histogram of the SNR from direction near an injected point source.

Figure 10.25: An injected point source is clearly recovered. The point source was injected at  $RA = 6h$ ,  $Decl = -45^\circ$ . This figure shows the recovered result at the nearest pixel in the HEALpix 768 pixel decomposition (see section 10.5.4). In (a, top), the injected power spectrum can be clearly seen over the sensitivity level (blue). In (a, bottom) the SNR shows a clear clustering of high values at the frequencies of the injection. In (b) the histogram of the SNR in frequency bins shows clear deviations from a standard normal distribution, with many outliers at high SNR.

modifications to carry out an analysis like this should be straightforward.

### 10.6.2 Multi-baseline Radiometry

In May of 2007 the LIGO and Virgo collaborations agreed to share data. This makes possible a three-detector network with multi-baseline radiometry. The theoretical foundations for such a network based approach have been laid in [103], but it remains to be implemented with data. This has not been done for data from S5 (which partially overlapped with the first Virgo science run), but it should be done for future coincident data taking runs.

### 10.6.3 Transient Searches

A natural extension to the radiometer analysis is a time dependent search, for stochastic signals which might have a shorter duration than two years. Such a search would essentially be a burst search: a search for unmodeled, short duration signals. There is already a burst search for signals with duration less than 1 second, but no search has yet been done for signals with duration of minutes to weeks. Candidates for such a search include starquake relaxations ([122], [123]) or other processes in isolated neutron stars ([124], [125]). In addition, core-collapse supernovae and both long and short gamma ray bursts are potential sources [126]. A search for one-day timescale bursts is already underway, but not yet mature enough for inclusion in this thesis. A key aspect of such a search will be the development of statistical methods for interpretation, similar to those already discussed in section 10.4.1 and section 10.6.1.

### 10.6.4 Clustering

The narrowband injection (cf. section 10.5.5) hints at another extension, which is to use a clustering analysis. The narrowband search allows a decomposition into three spaces: time, frequency, and location. We can calculate point estimates  $Y_{\hat{\Omega},t,f}$  and variances  $\sigma_{\hat{\Omega},t,f}$  for each direction, time bin, and frequency bin, and look in the resulting data for clusters of high SNR, which would then be examined more carefully. Such clusters would allow us to search directly for correlations in the SNR distributions over frequency, space, or time. This would clearly yield a more powerful search in the case that a signal appears in a few adjacent bins, which physically is of course more likely than a particular source signal being randomly distributed over frequency, time, or location.

## 10.7 Discussion

We have presented the results of a search for stochastic gravitational waves arising from specific directions using a year of coincident data from LIGO's fifth science run. These results include two searches over the whole sky, one frequency-binned at 1 Hz dependent and one integrated over the frequencies 40 Hz to 2 kHz. There were no detections. In addition, results were presented which placed limits on gravitational radiation in the frequency band from 50 Hz to 1 kHz for Sco-X1, the brightest LMXB. These are the most sensitive limits placed on Sco-X1 to date. Limits were placed on gravitational radiation from the galactic center and the 15 nearest globular star clusters in the band from 40 Hz to 2 kHz. These are the first such results for these targets. Finally, an untargeted narrowband search of 768 sky locations was carried out.

We have also presented several clear future directions for the future of this analysis technique, which are expected to be carried out soon.

## Chapter 11

# Summary and Conclusion

We have introduced the motivations for adding a signal recycling mirror to the Advanced LIGO configuration, and discussed the resulting possible sensitivity improvements and the increase in system complexity.

We have demonstrated the viability of a length sensing and control scheme for a detuned RSE interferometer that uses a pair of non-cascaded frontal phase modulations in conjunction with optical heterodyning to provide a matrix of discriminants. This demonstration and prototyping effort has already proven useful; the various pitfalls encountered prompted significant changes to the Advanced LIGO design. Some of the resulting changes include the switch to broadband RSE, the reduction of modulation frequencies, and the reduction of the finesse of the arm cavities. These changes will simplify the operation and commissioning of Advanced LIGO, which will enable Advanced LIGO to begin observation sooner; this will in turn allow the earlier detection of gravitational waves (if they have not already been detected) and an earlier beginning to gravitational wave astronomy.

We also developed an automated calibration procedure for a detuned RSE interferometer, which showed that the more complicated optical response of a detuned interferometer will not only make interferometer operation more difficult, but will also require much more effort to accurately calibrate.

We developed the first lock acquisition protocol for a suspended-mirror interferometer with five length degrees of freedom, a critical step in the development of the second generation of interferometric gravitational wave detectors. This protocol will form the basis for lock acquisition in Advanced LIGO, but significant work is still required before the Advanced LIGO lock acquisition protocol can be declared ready—in particular, a better scheme to reach the acquisition point, which places minimal demands on the test mass actuators, must be demonstrated. This is the subject of current work at the 40 m, using significant extra optical hardware (secondary lasers) dedicated purely to lock acquisition. This will be the first demonstration of such a subsystem dedicated purely to lock acquisition.

We measured light source noise couplings, making a comparison with modeling for these noise couplings using the two gravitational wave signal extraction techniques known as RF and DC read-

out. These measurements revealed the difficulty of accurately predicting these noise couplings, and will inform the choices of interferometer topology, readout technique, and most importantly, control scheme for future gravitational wave detectors. In particular, a LSC scheme in which error signal offsets are sensitive to first order to parameters which can only be measured in *coupled* optical systems makes it extremely difficult to accurately determine, at DC, the microscopic positions of the interferometer optics. This does not significantly affect our ability to control or calibrate the detector, but it does profoundly impact our ability to predict light source noise couplings, which depend critically on cancellation effects. Thus, LSC schemes need to be designed in such a manner that unpredictable parameters (such as demodulation) can be measured straightforwardly; furthermore, the scheme should be designed so that errors in these parameters will not lead at first order to length offsets. We have also seen that, in DC readout, the light source noises can couple strongly through the auxiliary control loops. We conclude that LSC schemes for signal recycled interferometers must include feedforward loop correction. Without these changes, much more conservative estimates of light source noise couplings must be used, with correspondingly tighter constraints on the design of the light source itself.

Lastly, a search was performed for stochastic gravitational waves using the data from LIGO's fifth science run. This search set the tightest (and first) upper limits on stochastic gravitational waves from the directions of the galactic center and the fifteen nearest globular clusters. Future extensions to this search were outlined.

The prototyping efforts at the 40 m have yielded significant contributions to the Advanced LIGO design effort and thus to the gravitational wave detection community. Advanced LIGO is currently under construction, with installation in the coming year. Once operational, Advanced LIGO is expected to open the field of gravitational wave astronomy.

## Appendix A

# Acronyms

AOM	Acousto-optic modulator
ASC	Alignment Sensing and Control
BS	Beam Splitter
BSC	Barbecue Sauce Container
CARM	Common Arm
CLG	Closed Loop Gain
CM	Common Mode
DARM	Differential Arm
DOF	Degree of Freedom
DRFPMI	Dual Recycled Fabry Perot Michelson Interferometer
DRM	Dual Recycled Michelson
EOM	Electro-optic modulator
ETM	End Test Mass
FP	Fabry-Pérot
FPMI	Fabry Perot Michelson Interferometer
FSR	Free Spectral Range
FSS	Frequency Stabilization Servo
FWHM	Full Width at Half Maximum
GGN	Gravity Gradient Noise
GW	Gravitational Wave(s)
IMC	Input Mode Cleaner
ISC	Interferometer Sensing and Control
ISS	Intensity Stabilization Servo

ITM	Input Test Mass
LIGO	Laser Interferometer Gravitational Wave Observatory
LSC	LIGO Scientific Collaboration
LSC	Length Sensing & Control
LTI	Linear Time Invariant
MC	Mode Cleaner
MICH	Michelson
OL	Optical Lever
OLG	Open Loop Gain
OMC	Output Mode Cleaner
OOC	Output Optic Chamber
PCIX	Peripheral Component Interconnect Extended
PDH	Pound-Drever-Hall
PRC	Power Recycling Cavity
PRFPMI	Power Recycled Fabry Perot Michelson Interferometer
PRM	Power Recycled Michelson (Interferometer)
PRM	Power Recycling Mirror
PSL	Pre-Stabalized Laser
QND	Quantum Non-Demolition
RC	(Frequency) Reference Cavity
RSE	Resonant Sideband Extraction
SNR	Signal to Noise Ratio
SOS	Second Order Section
SOS	Small Optic Suspension
SQL	Standard Quantum Limit
SRC	Signal Recycling Cavity
SRM	Signal Recycling Mirror
SUS	Suspension
TLA	Three Letter Acronym
UGF	Unity Gain Frequency
VME	Versa Module Eurocard
WFS	Wave Front Sensor
XARM	X-Arm
YARM	Y-Arm



## Appendix B

# Quantum Noise in RSE interferometers

As discussed in [44], the ultimate source of the quantum noise in an interferometer is from vacuum fluctuations entering the asymmetric port. Computing the quantum noise in an interferometer, then, requires computing the input-output relations for the asymmetric port, which are essentially a two-photon version of equation (3.14). These input-output relations were first presented in [127] for non-signal recycled interferometers and extended in [61] to include signal-recycled interferometers. In both cases, the input-output operators are written as quadrature fields  $\mathbf{a}$  (the input) and  $\mathbf{b}$  (the output). For a signal recycled interferometer, they are

$$\begin{pmatrix} b_1 \\ b_2 \end{pmatrix} = \frac{1}{M} \left[ e^{2i\beta} \begin{pmatrix} C_{11} & C_{12} \\ C_{21} & C_{22} \end{pmatrix} \begin{pmatrix} a_1 \\ a_2 \end{pmatrix} \right], \quad (\text{B.1})$$

where  $\beta = -\arctan \frac{\omega_a}{\omega_c}$  is the phase delay in the arm cavities,

$$M = 1 + r_s^2 e^{4i\beta} - 2r_s e^{2i\beta} \left( \cos 2\phi + \frac{\mathcal{K}}{2} \sin 2\phi \right), \quad (\text{B.2})$$

$$C_{11} = C_{22} = (1 + r_s^2) \left( \cos 2\phi + \frac{\mathcal{K}}{2} \sin 2\phi \right) - 2r_s \cos 2\phi, \quad (\text{B.3})$$

$$C_{12} = -t_s^2 (\sin 2\phi + \mathcal{K} \sin^2 \phi), \quad (\text{B.4})$$

$$C_{21} = t_s^2 (\sin 2\phi - \mathcal{K} \sin^2 \phi), \quad (\text{B.5})$$

$$(\text{B.6})$$

and  $\mathcal{K}$  is a radiation pressure coupling term,

$$\mathcal{K} = \frac{8I_{bs}}{mL^2} \frac{\omega_0}{\omega_a^2(\omega_c^2 + \omega_a^2)}, \quad (\text{B.7})$$

where  $I_{bs}$  is the power illuminating the beamsplitter and  $m$  is the mass of the test masses.

Note for the special case of  $r_s = 0, t_s = 1, \phi = 0$  (no signal mirror), these relations reduce to equation (3.14). The signal part of  $\mathbf{b}$  is given by, for strain signal  $h$ ,

$$\begin{pmatrix} b_1 \\ b_2 \end{pmatrix} = \frac{1}{M} \left[ \sqrt{2\mathcal{K}t_s} e^{i\beta} \begin{pmatrix} D_1 \\ D_2 \end{pmatrix} \frac{h}{h_{SQL}} \right], \quad (\text{B.8})$$

where the signal coupling terms are

$$D_1 = -(1 + r_s e^{2i\beta}) \sin \phi, \quad (\text{B.9})$$

$$D_2 = -(-1 + r_s e^{2i\beta}) \cos \phi, \quad (\text{B.10})$$

and  $h_{SQL}$  is the free-mass standard quantum limit:

$$h_{SQL} = \sqrt{\frac{8\hbar}{m\omega_a^2 L^2}}. \quad (\text{B.11})$$

The total output  $\mathbf{b}$  is the sum of the signal and the quantum noise,

$$\begin{pmatrix} b_1 \\ b_2 \end{pmatrix} = \frac{1}{M} \left[ e^{2i\beta} \begin{pmatrix} C_{11} & C_{12} \\ C_{21} & C_{22} \end{pmatrix} \begin{pmatrix} a_1 \\ a_2 \end{pmatrix} + \sqrt{2\mathcal{K}t_s} e^{i\beta} \begin{pmatrix} D_1 \\ D_2 \end{pmatrix} \frac{h}{h_{SQL}} \right]. \quad (\text{B.12})$$

The quantum noise level can be calculated by setting  $\mathbf{a}$  to the vacuum field ( $\frac{1}{2}$ ) in equation (B.1) to get  $\Delta\mathbf{b}$ , the portion of the output signal due to noise. This noise level can then be calibrated in units of strain by setting  $h = 1$  in equation (B.8) to get  $\mathbf{b}^s$  and dividing to get the noise spectral density in units of strain:

$$\frac{\Delta\mathbf{b}}{\mathbf{b}^s}. \quad (\text{B.13})$$

This is the amplitude of  $h$  for which the quantum noise limited SNR is 1.

A more complete set of relations that includes additional quantum noise terms due to photodetector, signal recycling cavity, and arm cavity losses can be found in [61]; for other interferometer configurations, [128] presents a framework for numerical simulation of arbitrary interferometer configurations using the two-photon formalism by conveniently writing down the two-photon analogues of equation (3.9). This framework can be used to calculate the input-output relations at a given port, as well as all the cross-couplings between ports. It is thus a more general way to calculate quantum noise arising from all the losses in an interferometer. This framework has been implemented as a general interferometer simulation tool in the C programming language by the lead author of [128], and also in MATLAB as a parallel branch (now defunct) of Optickle (cf. appendix F) by me.

**Heterodyne detection** For heterodyne detection (see [72] for a complete discussion), if we let  $D_{\pm}$  be the upper and lower RF sideband amplitudes and  $\phi_D$  the demodulation phase, then the effective local oscillator field amplitude is

$$D_0 \equiv |D_+ e^{-i\phi_D} + D_- e^{i\phi_D}|, \quad (\text{B.14})$$

and the detection quadrature is

$$\zeta \equiv \frac{\pi}{2} + \arg(D_+ e^{-i\phi_D} + D_- e^{i\phi_D}). \quad (\text{B.15})$$

Then the PD output at  $\omega_a$  is

$$PD = D_0 \left[ E_{\zeta}(\omega_a) + \frac{|D_+|}{D_0} E_{\zeta_+}^{2\Omega_m} + \frac{|D_-|}{D_0} E_{\zeta_-}^{-2\Omega_m} \right], \quad (\text{B.16})$$

where

$$\zeta_{\pm} \equiv \pm\phi_D + \frac{\pi}{2} + \arg D_{\pm}, \quad (\text{B.17})$$

and the terms at  $E_{\zeta_{\pm}}^{\pm 2\Omega_m}$  are noise arising from the heterodyne detection process. These terms are responsible for the classical ‘cyclostationary’ noise. Quantum mechanically, they are vacuum fields at  $\pm 2\Omega_m$  which are mixed to  $\Omega_m$  by the square-law photodetection process, and so are present in the RF photocurrent which gets demodulated.

## Appendix C

# Laser Noise Coupling Formulae

An analytical comparison of susceptibility to laser noise in RF/DC readout schemes was carried out for signal recycled interferometers in [52]. This appendix summarizes some of the most important results presented there.

### C.1 Asymmetries and Couplings

Laser noise couples to the signal port through interferometer asymmetries. These asymmetry parameters, and their names, are listed here; the asymmetries refer to mismatches between the two arm cavities unless otherwise specified. The beamsplitter imbalance is  $\sigma \equiv r_{bs}^2 - t_{bs}^2$ .

### C.2 Laser noise coupling to asymmetric port

Laser noises will couple to the asymmetric port through interferometer asymmetries. We are primarily concerned with the differential arm cavity reflectivity:

$$\Delta r_c = \frac{\xi}{1 + s_c} + \frac{2s_c}{(1 + s_c)^2} \frac{\Delta \mathcal{F}}{\mathcal{F}} + \frac{2i}{(1 + s_c)^2} \frac{\omega_0 \Delta L_-}{\omega_c L}. \quad (\text{C.1})$$

Asymmetry	Name
$\xi$	contrast defect
$\frac{\Delta \mathcal{F}}{\mathcal{F}}$	arm cavity finesse imbalance
$\sigma$	beamsplitter imbalance
$\frac{\Delta m}{m}$	mass imbalance
$\frac{\Delta \omega_c}{\omega_c}$	arm cavity-pole mismatch

Table C.1: Interferometer asymmetries that contribute to laser noise couplings.

This analysis ignores the input mode cleaner. We write the Fourier components of the laser noise fields as the quadrature fields  $l_1$  and  $l_2$ ; at the input to the interferometer these are

$$\begin{aligned} l_1 &= \frac{E_{in}}{\sqrt{2}} \frac{\delta P}{2P}, \\ l_2 &= \frac{E_{in}}{\sqrt{2}} \frac{2\pi}{\omega_a} \delta\nu, \end{aligned} \tag{C.2}$$

where the laser RIN is as usual  $\frac{\delta P}{P}$  and the laser frequency noise in Hz is  $\delta\nu$ . Using the results from [42], we can write the fields due to laser noise at the *asymmetric side of the beamsplitter* as  $a_1$  and  $a_2$ :

$$\begin{aligned} a_1 &= -\frac{\pi\delta\nu}{\sqrt{2}\omega_a} \frac{2}{(1+s_{cc})(1+s_c)} \frac{\omega_0\Delta L_-}{\omega_c L} \\ &\quad + \frac{1}{4\sqrt{2}} \frac{\delta P}{P} \left\{ \frac{\xi}{1+s_{cc}} + \frac{2s_c}{(1+s_{cc})(1+s_c)} \frac{\Delta\mathcal{F}}{\mathcal{F}} \right\}, \\ a_2 &= \frac{\pi\delta\nu}{\sqrt{2}\omega_a} \left\{ \frac{\xi}{1+s_{cc}} + \frac{2s_c}{(1+s_{cc})(1+s_c)} \frac{\Delta\mathcal{F}}{\mathcal{F}} \right\} \\ &\quad + \frac{1}{4\sqrt{2}} \frac{\delta P}{P} \frac{1}{(1+s_{cc})(1+s_c)} \left\{ \frac{2\omega_0\Delta L_-}{\omega_c L} \right. \\ &\quad \left. + \mathcal{K}(1+s_c)^2 \times \left[ \sigma + \frac{\Delta\omega_c/\omega_c}{(1+s_c)^2} + \frac{\Delta m}{2m} \right] \right\}. \end{aligned} \tag{C.3}$$

Note that these are the noise fields normalized by the symmetric field amplitude ( $g_{pr}E_{in}$ ); they are the laser noise fields around the carrier. This also includes noise due to radiation pressure, which is not included in [42] but is in [52]. However, this equation does not include the effect of radiation pressure noise due to frequency noise, which will appear when the arm cavities are differentially detuned (as they will be for DC readout). This effect can be significant when the circulating power is very large.

The gravitational wave signal field at the asymmetric side of the beamsplitter appears only in the phase quadrature:

$$\begin{pmatrix} a_1^{sig} \\ a_2^{sig} \end{pmatrix} = g_{pr}E_{in} \frac{\sqrt{2}\omega_0\delta L_-}{L\omega_c(1+s_c)} \begin{pmatrix} 0 \\ 1 \end{pmatrix}. \tag{C.4}$$

The total field at the output port, usually called  $\mathbf{b}$ , is the sum of these two fields, multiplied by a matrix that describes the effect of the signal recycling cavity on the fields:

$$\begin{pmatrix} b_1 \\ b_2 \end{pmatrix} = \frac{t_s g_{pr} E_{in}}{M} \begin{pmatrix} D_{11} & D_{12} \\ D_{21} & D_{22} \end{pmatrix} \left[ \begin{pmatrix} 0 \\ 1 \end{pmatrix} \frac{\sqrt{2}\omega_0\delta L_-}{L\omega_c(1+s_c)} + \begin{pmatrix} a_1 \\ a_2 \end{pmatrix} \right]. \tag{C.5}$$

The matrix  $\frac{\mathbb{D}}{M}$  relates the fields at the asymmetric side of the beamsplitter to the fields at the output

port (the back of the SRM). For a non-signal-recycled interferometer,  $\frac{\mathbb{D}}{M}$  is the identity matrix. For a signal recycled interferometer,  $\mathbb{D}$  is

$$D_{11} = (1 - r_s e^{2i\beta}) \cos \phi - r_s e^{2i\beta} \mathcal{K} \sin \phi, \quad (\text{C.6})$$

$$D_{12} = -(1 + r_s e^{2i\beta}) \sin \phi, \quad (\text{C.7})$$

$$D_{21} = (1 + r_s e^{2i\beta}) \sin \phi - r_s e^{2i\beta} \mathcal{K} \cos \phi, \quad (\text{C.8})$$

$$D_{22} = (1 - r_s e^{2i\beta}) \cos \phi. \quad (\text{C.9})$$

$M$  is a common term that has been pulled out; it is given by

$$M = 1 + r_s^2 e^{4i\beta} - 2r_s e^{2i\beta} \left( \cos 2\phi + \frac{\mathcal{K}}{2} \sin 2\phi \right). \quad (\text{C.10})$$

Setting  $r_s = 0$  and  $\phi = 0$  yields the identity matrix, as expected.

The fields  $\mathbf{b}$  must then be combined with an optical local oscillator (whether heterodyne or homodyne). In DC readout, this is the homodyne local oscillator. It is whatever static carrier field is at the output port. This will be the sum of a field due to the contrast defect, which is from a reflectivity imbalance and so is in the amplitude quadrature,

$$\begin{pmatrix} a_1^\xi \\ a_2^\xi \end{pmatrix} = \frac{g_{pr} E_{in}}{2\sqrt{2}} \begin{pmatrix} 1 \\ 0 \end{pmatrix} \xi, \quad (\text{C.11})$$

and a field due to the total DARM offset  $\Delta L_-$ ,

$$\begin{pmatrix} a_1^{L-} \\ a_2^{L-} \end{pmatrix} = \frac{g_{pr} E_{in}}{2\sqrt{2}} \begin{pmatrix} 0 \\ 1 \end{pmatrix} \frac{\sqrt{2}\omega_0 \Delta L_-}{L\omega_c}, \quad (\text{C.12})$$

which is in the phase quadrature. The DARM offset is the result (sum) of several effects: (1) the intentional offset, as part of a DC readout technique; (2) a residual offset from finite limited DARM loop gain; (3) the contrast defect  $\xi$  being re-injected in the interferometer by the signal cavity, causing a radiation pressure offset. There is also a slowly (below 1 Hz) varying  $\Delta L_-^{rms}$  which is due to many factors in the control system; this can also be included, but properly the effect due to this slow variation should be calculated separately and added in quadrature (in the root-square-sum sense, not the quadrature-field sense). It is excluded from the calculations here. Regardless, the output field depends on the actual location of the mirrors, which is  $\Delta L_-$  by definition. We can then write the static field at the output port as the sum of the fields at the asymmetric side of the beamsplitter (due to  $\xi$  and  $\Delta L_-$ ), multiplied by a zero-frequency ( $\omega_a = 0$ ), no radiation pressure

( $\mathcal{K} = 0$ ) limit of  $\frac{\mathbb{D}}{M}$ :

$$\begin{pmatrix} B_1 \\ B_2 \end{pmatrix} = \frac{g_{pr} E_{in}}{2\sqrt{2}} \frac{t_s}{M_{free}} \left[ \begin{pmatrix} (1 - r_s) \cos \phi \\ (1 + r_s) \sin \phi \end{pmatrix} \xi + \begin{pmatrix} (1 + r_s) \sin \phi \\ (1 - r_s) \cos \phi \end{pmatrix} \frac{\sqrt{2}\omega_0 \Delta L_-}{L\omega_c} \right], \quad (\text{C.13})$$

where we have written a capital  $\mathbf{B}$  to signify that this is a *static* field.  $M_{free}$  is a zero-frequency no radiation pressure limit of  $M$ :

$$M_{free} = 1 + r_s^2 - 2r_s \cos 2\phi. \quad (\text{C.14})$$

The PD signal for homodyne detection is the inner product of the local oscillator field  $\mathbf{B}$  and the signal+noise field  $\mathbf{b}$ ,

$$PD = \mathbf{B} \cdot \mathbf{b}, \quad (\text{C.15})$$

where the  $\cdot$  indicates an inner product. This is the signal in DC readout. The detection quadrature depends on the relative amplitudes of the fields due to  $\xi$  and  $\Delta L_-$ . To prevent variance in the readout quadrature,  $\Delta L_-$  should be larger than  $\Delta L_-^{rms}$ . It is also possible that  $\xi$  could be a time varying quantity (e.g., differential alignment fluctuations, differential heating causing mode mismatch, etc). This could be a particular problem if  $\xi$  fluctuates around zero, which will cause the biggest change in the homodyne angle in the case of a large  $\Delta L_-$ . If this is the case, it might be necessary to purposely introduce an artificial imbalance to stabilize the homodyne angle.

The RF local oscillator in a heterodyne scheme can be written as

$$\begin{pmatrix} B_1^{RF} \\ B_2^{RF} \end{pmatrix} = \aleph E_{in} \begin{pmatrix} \sin \zeta \\ \cos \zeta \end{pmatrix}, \quad (\text{C.16})$$

where the  $\aleph$  is a pre-factor that describes the effective local oscillator amplitude at the signal port (see [72] for details); an exact value is not necessary for calculating signal-referred noise couplings. Note that these are not quadrature fields at  $\omega_0 \pm \Omega_m$ ; they are equivalent quadrature fields at the carrier frequency, after photodetection and demodulation; see Appendix B of [52] for details.

If the RF sidebands are unbalanced (the case for a detuned interferometer), then any detection quadrature  $\zeta$  can be chosen by adjusting the demodulation phase. If the sidebands are balanced, only  $\zeta = \pi/2$  can be detected.

The noise (due to source laser noise) on the RF sideband fields, at  $\omega_a$  is:

$$\begin{pmatrix} b_1^{RF} \\ b_2^{RF} \end{pmatrix} = \aleph E_{in} \left[ \frac{2\pi\delta\nu}{\omega_a} \begin{pmatrix} -\cos \zeta \\ \sin \zeta \end{pmatrix} + \frac{\delta P}{2P} \begin{pmatrix} \sin \zeta \\ \cos \zeta \end{pmatrix} \right]. \quad (\text{C.17})$$

This is written assuming that the RF sideband fields are not significantly filtered by the interferometer, so noise travels directly to the detection port.

The PD output in RF readout is then

$$PD = \mathbf{B}^{\text{RF}} \cdot \mathbf{b} + \mathbf{B} \cdot \mathbf{b}^{\text{RF}}. \quad (\text{C.18})$$

The key distinction between RF readout and DC readout can be seen to be the noise on the RF sidebands. In general, both noises will be dependent on the detection quadrature; also, in a detuned interferometer, both laser amplitude and frequency noise appear in both output quadratures.

The following figures show the individual contributions of laser noise couplings from the imbalances listed in table C.1. Mass imbalance is not shown, since it appears in the same manner as a beamsplitter imbalance (cf. equation (C.3)). The total coupling is the linear sum of the individual couplings: this means there can be cancellations, which depend on the relative signs of the imbalances. This can be seen in figure C.1, where the coupling from the finesse imbalance cancels that from the DARM offset (which is included in all the traces in the DC readout plots, necessarily) at two frequencies.

Figure C.1 shows the contributions to the laser amplitude noise coupling of the imbalances in DC readout; the imbalance level is shown in the legend. These are typical levels for the 40 m. The DARM offset provides the dominant imbalance above 100 Hz, while technical radiation pressure noise dominates below 100 Hz.

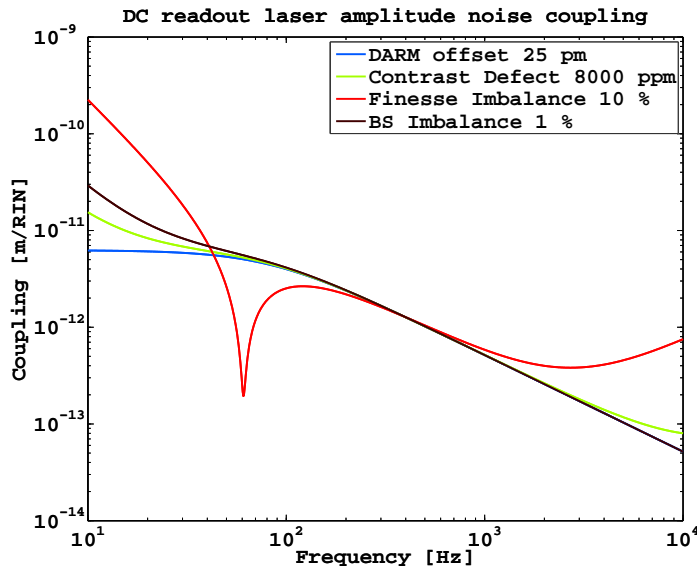


Figure C.1: Laser Amplitude Noise Coupling Paths in DC Readout.

Figure C.2 shows the contributions to the laser amplitude noise coupling of the imbalances in RF readout; the imbalance level is shown in the legend. These are typical levels for the 40 m. The arm cavity finesse imbalance appears to be the most important contributor here.

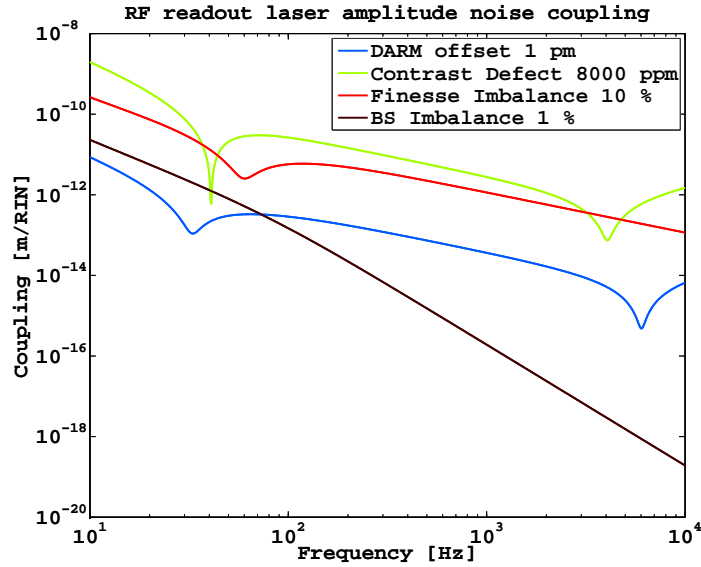


Figure C.2: Laser Amplitude Noise Coupling Paths in RF Readout.

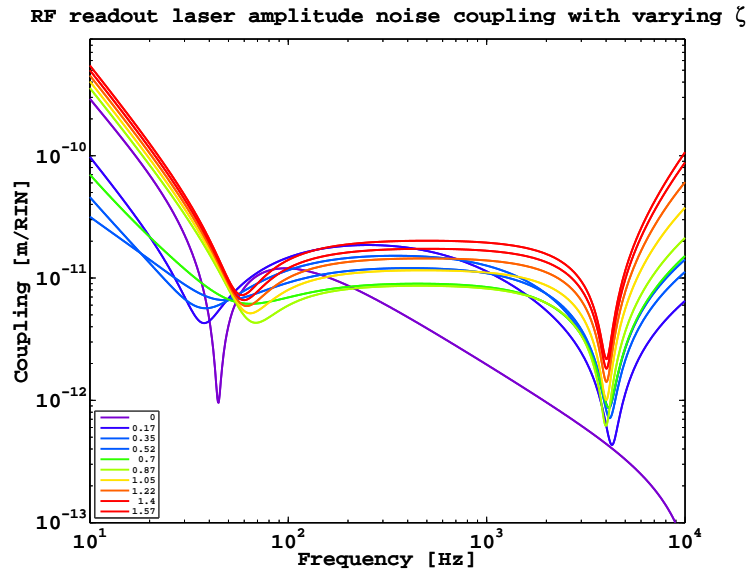
Figure C.3: Laser Amplitude Noise Coupling in RF Readout varies with the readout quadrature  $\zeta$ .

Figure C.4 shows the contributions to the laser frequency noise coupling of the imbalances in DC readout; the imbalance level is shown in the legend. These are typical levels for the 40 m. The DARM offset provides the dominant imbalance everywhere.

Figure C.5 shows the contributions to the laser frequency noise coupling of the imbalances in RF readout; the imbalance level is shown in the legend. These are typical levels for the 40 m. The arm cavity finesse imbalance dominates above  $\sim 20$  Hz, while the contrast defect dominates below  $\sim 20$  Hz.

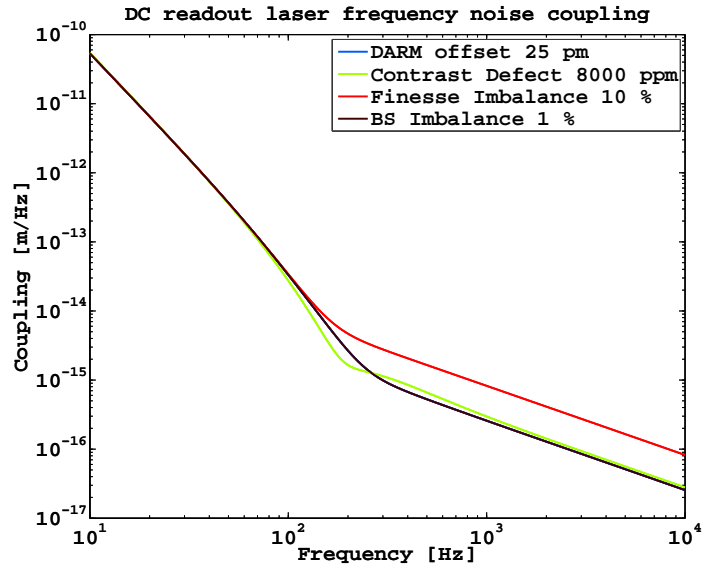


Figure C.4: Laser Frequency Noise Coupling Paths in DC Readout.

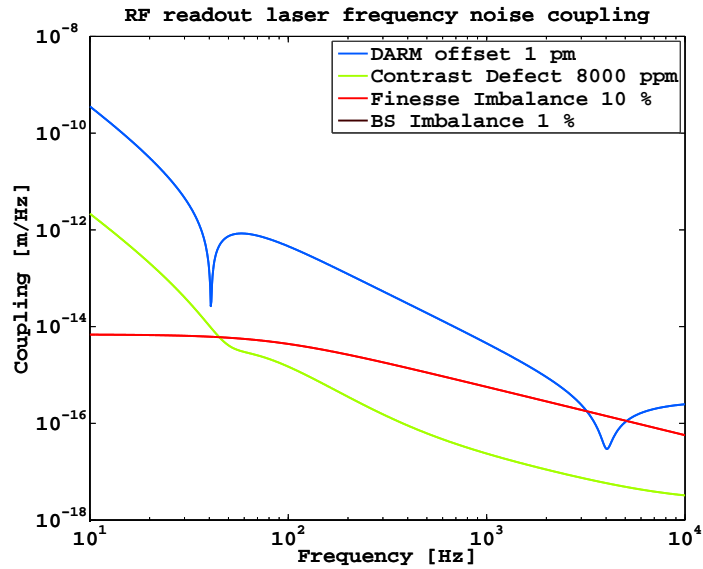


Figure C.5: Laser Frequency Noise Coupling Paths in RF Readout.

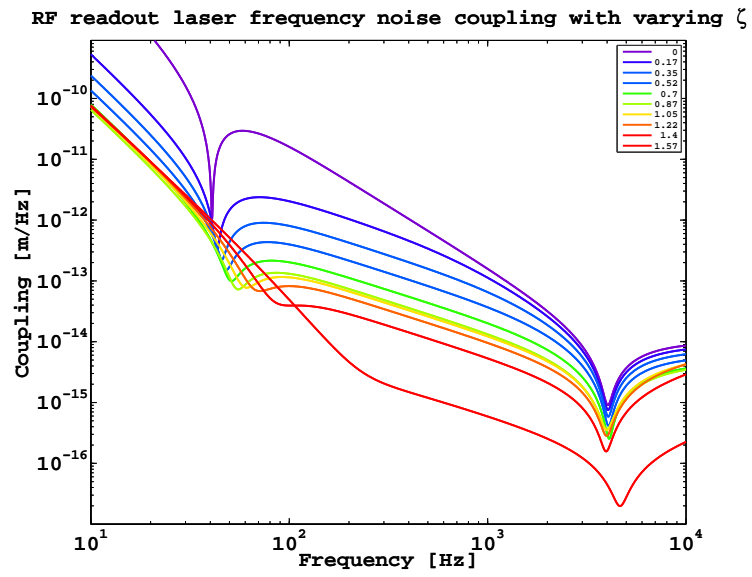


Figure C.6: Laser Frequency Noise Coupling in RF Readout varies with the readout quadrature  $\zeta$ .

## Appendix D

# Resonant Cavity Formulae

### D.1 Statics

Referring to figure D.1, at equilibrium, the fields inside the cavity satisfy the set of equations ,

$$\begin{aligned}
 E_1 &= E_{inc} + E_4 r_i, \\
 E_2 &= E_1 e^{ikL}, \\
 E_3 &= E_2 r_e, \\
 E_4 &= E_3 e^{ikL}, \\
 E_t &= E_2 t_e, \\
 E_r &= -E_{inc} r_i + E_4 t_i.
 \end{aligned}
 \tag{D.1}$$

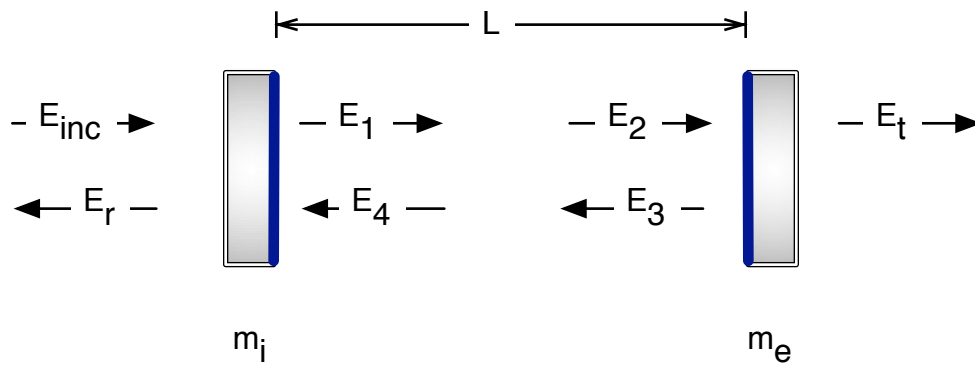


Figure D.1: Indexed fields in a resonant cavity

Solving this set of equations for  $E_r$ ,  $E_t$ , and  $E_{circ} = E_1$ , in terms of  $E_{inc}$  and  $L$ , we get

$$E_{circ} = \frac{E_{inc}t_i}{1 - r_i r_e e^{2ikL}}, \quad (\text{D.2})$$

$$E_r = -E_{inc}r_i + E_{circ}r_e t_i e^{2ikL} = -E_{inc} \left[ r_i - \frac{r_e t_i^2 e^{2ikL}}{1 - r_e r_i e^{2ikL}} \right], \quad (\text{D.3})$$

$$E_t = E_{circ} e^{ikL} t_e = \frac{E_{inc} t_i t_e e^{ikL}}{1 - r_i r_e e^{2ikL}}. \quad (\text{D.4})$$

When the resonance condition

$$\begin{aligned} kL &= n\pi, \\ L &= \frac{n}{2}\lambda, \end{aligned} \quad (\text{D.5})$$

is satisfied, the field circulating in the cavity builds resonantly.

Making the substitution  $e^{2ikL} = e^{2in\pi} = 1$ , and focusing on the lossless case ( $r^2 + t^2 = 1$ ), we can examine the behavior in three situations

**Overcoupled cavity:**  $r_i < r_e$ . In this case, the reflected field is dominated by the circulating field resonating in the cavity, which leaks out through the input mirror. This field has opposite sign to the prompt reflection, and so the sign of the field reflected from the cavity changes when the cavity is resonant.

**Undercoupled cavity:**  $r_i > r_e$ . In this case, the reflected field is dominated by the field promptly reflected from the input mirror.

**Critically coupled cavity:**  $r_i = r_e$ . For a critically coupled cavity, the promptly reflected field is cancelled by the leakage field, and there is zero reflection. This situation is described as an impedance matched cavity.

## D.2 Equilibrium Frequency Response

This discussion follows [49]. If we write the input field as  $E_{in} = e^{i(\omega_0 + \omega_a)t}$ , then the field inside the cavity is

$$E_{circ} = \frac{\sqrt{1 - r_i^2}}{1 - r_i r_e e^{-2i(\omega_a \frac{l}{c} + \phi)}} E_{in}, \quad (\text{D.6})$$

where  $l$  is the cavity length,  $\omega_a$  is the audio frequency deviation from resonance, and  $\phi$  is the phase deviation from resonance. In reflection and transmission we have

$$E_{refl} = r_i E_{in} - r_e \sqrt{1 - r_i^2} e^{-2i\omega_a \frac{l}{c}} E_{circ}, \quad (\text{D.7})$$

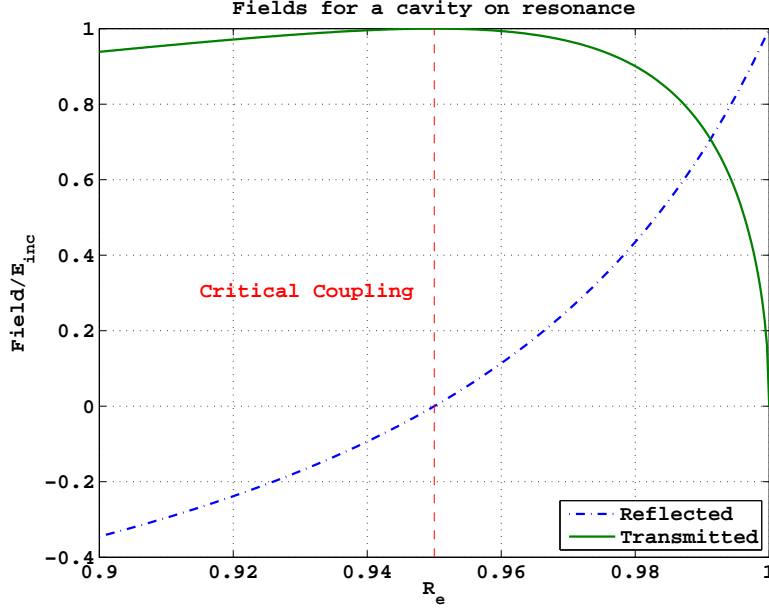


Figure D.2: Reflected and transmitted field amplitudes relative to the incident field amplitude for a lossless, resonant Fabry-Pérot cavity as a function of end-mirror reflectance, when the input mirror reflectance is  $R_i = 0.95$ . The vertical dashed line indicates critical coupling, where the reflection goes to zero.

and

$$E_{trans} = \sqrt{1 - r_e^2} e^{i\omega_a \frac{l}{c}} E_{circ}. \quad (\text{D.8})$$

We can write the cavity pole,

$$\omega_c \equiv \frac{c}{2l} \frac{1 - r_i r_e}{\sqrt{r_i r_e}}, \quad (\text{D.9})$$

and define

$$s_c \equiv \frac{i\omega_a}{\omega_c}. \quad (\text{D.10})$$

Then when  $\frac{\omega_a}{2\pi} \ll \frac{c}{2l}$  the cavity transfer functions are

$$\frac{E_{circ}}{E_{in}} = \left[ \frac{\sqrt{1 - r_i^2}}{1 - r_i r_e} \frac{1}{1 + s_c} - 2ik\delta l \frac{r_i r_e \sqrt{1 - r_i^2}}{(1 - r_i r_e)^2} \frac{1}{(1 + s_c)^2} \right], \quad (\text{D.11})$$

$$\frac{E_{refl}}{E_{in}} = \left[ r_c \frac{1 + \frac{s_c}{r_c}}{1 + s_c} + 2i \frac{r_c' k \delta l}{(1 + s_c)^2} \right], \quad (\text{D.12})$$

$$\frac{E_{trans}}{E_{in}} = \frac{\sqrt{1 - r_i^2} \sqrt{1 - r_e^2}}{1 - r_i r_e} \left[ \frac{1}{1 + s_c} - ik\delta l \frac{1 + r_i r_e}{1 - r_i r_e} \frac{1}{(1 + s_c)^2} \right], \quad (\text{D.13})$$

where

$$r_c = \frac{r_i - r_e}{1 - r_i r_e}, \quad (\text{D.14})$$

and

$$r'_c = \frac{(1 - r_i^2)r_e}{(1 - r_i r_e)^2} = \frac{-i}{E_{in}} \frac{c}{2l} \frac{dE_{refl}}{d\omega_a}, \quad (\text{D.15})$$

are the arm cavity reflectivity and the derivative of the reflectivity at resonance.

It should be noted that these transfer functions apply to a single frequency. Care must be employed when using them for an off-resonant case ( $\delta l \neq 0$ ) to compute phase modulation transfer functions (because in this formalism, where we typically work in the phasor basis such that  $\omega_0 = 0$ , phase modulations appear at both positive and negative frequencies).

### D.3 Coupled Cavities

For a single cavity we can define a cavity operator:

$$G(\omega_a, \omega_c, r_c) \equiv r_c \frac{1 + \frac{s_c}{r_c}}{1 + s_c}, \quad (\text{D.16})$$

which is the complex, frequency dependent reflectivity of the cavity near resonance. Then, for a three-mirror cavity such as in figure 3.7 we can write down the field inside a cavity whose back mirror is another cavity on resonance by replacing  $r_e$  with  $G$ :

$$E_{circ}^{cc} = \frac{\sqrt{1 - r_r^2}}{1 - r_r G e^{-2i(\omega_a \frac{l}{c} + \phi_r)}} E_{in}, \quad (\text{D.17})$$

where  $\phi_r$  now denotes the round trip phase in the input cavity. From here on we will consider the input cavity as a recycling cavity, in reference to LIGO, and assume it to be much shorter than the arm cavity.  $r_r$  is thus the amplitude reflectivity of the recycling mirror. For a LIGO arm cavity (which is overcoupled) on resonance,  $G$  has opposite sign from the bare reflectivity of the input mirror  $r_i$ ; this means that the maximum field amplitude in the combined cavities will occur when the recycling cavity is anti-resonant for the carrier ( $\omega_a = 0$  and  $\phi_r = 0$ ). So, we can write the amplitude recycling gain as

$$g_r = \frac{\sqrt{1 - r_r^2}}{1 - r_r G(0, \omega_c, r_c)} = \frac{t_r}{1 - r_r r_c}. \quad (\text{D.18})$$

The transfer function from the back of the recycling mirror to the front of the recycling mirror is then

$$\frac{E_{circ}^{cc}}{E_{in}} = g_r \frac{1 + s_c}{1 + s_{cc}}, \quad (\text{D.19})$$

when

$$s_{cc} = i \frac{\omega_a}{\omega_{cc}}, \quad (\text{D.20})$$

$$\omega_{cc} = \frac{1 + r_r r_c}{1 + r_r} \omega_c, \quad (\text{D.21})$$

# Appendix E

## Feedback

### E.1 Linear Control: Loopology

The techniques of linear control involve taking an *error signal* received from a *sensor*, altering it with a *filter*, then applying the filtered signal to an *actuator* which operates on the *plant* to be controlled. The error signal is a signal proportional to the deviation of the system from its *operating point*.

This relationship, and a representative loop, is shown in figure E.1. Linear control theory applies when all the components of such a feedback loop can be described (or approximated) as linear time invariant (LTI) systems. Generally, this applies to the work done in this thesis.

It is common in LTI systems for the output of one system to be fed into another system. The output of a given LTI system is a convolution of the input to the system with a representative kernel; it is thus often convenient to work in the frequency domain (generally the Laplace domain, but the Fourier domain can be sufficient when the steady state response is the only response of interest), where cascaded convolutions take the form of simple multiplication. For each LTI system, the relationship of the input to the output is called the *transfer function*.

The open loop gain (OLG)  $G$  of a system is the cascaded transfer function going once around the loop. For the loop shown in figure E.1,  $G$  is the product of the elements in the loop  $G = FAPS$ , where  $F$  represents the transfer function of the feedback filter,  $A$  that of the actuator,  $P$  that of the plant, and  $S$  that of the sensor. Laplace domain algebra allows us to write  $tp3 = F \times tp2$ , and so the transfer function of  $tp2$  to  $tp3$  is given by the quotient,

$$\frac{tp3}{tp2} = F. \tag{E.1}$$

A disturbance (indicated by  $EXC$ ) injected into the loop at the summing point will be added to itself after going once around the loop, and so will be suppressed by the gain of the loop if the loop is set up in a negative feedback configuration. Injecting a signal at  $EXC$ , then, the signals present

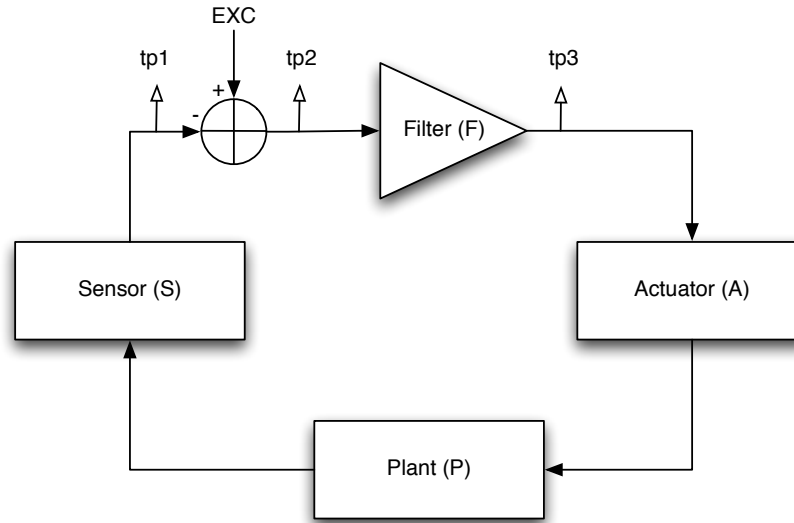


Figure E.1: Schematic idealization of a canonical feedback loop.

at the three testpoints  $tp1$ ,  $tp2$ , and  $tp3$ , are given by

$$\begin{aligned} tp1 &= G \times tp2, \\ tp2 &= EXC - tp1, \\ tp3 &= F \times tp2. \end{aligned}$$

Solving this system yields the transfer function from  $EXC$  to  $tp2$ , which is known as the closed loop gain:

$$CLG \equiv \frac{tp2}{EXC} = \frac{1}{1+G}; \quad (\text{E.2})$$

and the transfer function from  $EXC$  to  $tp3$ , sometimes called the *forward loop gain*:

$$FLG \equiv \frac{tp3}{EXC} = \frac{F}{1+G}. \quad (\text{E.3})$$

The closed loop gain can be thought of as a transfer function from outside the loop to inside the loop: when signals are injected into the loop, they are immediately multiplied by the closed loop gain. Thus, for frequencies where the open loop gain is large ( $G \gg 1$ ), the injected signal is strongly suppressed. This suppression appears immediately after the injection point, which can have unwanted effects if noise is injected at certain points in the loop. For example, when the injection point is inside the sensor, a signal is applied to the plant so that the injection at the sensor is canceled; this means that, while noise in the sensor is suppressed, it is done so at the cost of increased noise in the plant. For this reason, a second, out-of-loop sensor is often used. This out-of-

loop sensor is connected to the plant but the signals derived from it are not used for feedback, so it can be used as an independent monitor of residual noise in the plant.

## E.2 Servo Stability

Concomitant with the issue of feedback is stability. A servo system is said to be stable if disturbances to the system do not grow with time as a result of the feedback mechanism. Considering only the steady state response, this condition implies that the closed loop gain must not be infinite at any frequency. Inspection of equation E.2 reveals that such an infinity will occur if the open loop gain  $G$  approaches  $-1$ . This means that the *phase delay* of the open loop gain must be less than  $-180^\circ$  at the unity gain frequency (UGF, where  $\|G\| = 1$ ) in order for a feedback loop to be stable. This condition applies to the steady state response of the system.

The dynamical response must also be stable (i.e., perturbations must not grow with time), which implies that all of the poles of the closed loop gain must be in the left-hand side of the s-plane.

### E.2.1 Bode gain-phase relationship

For real systems, the Bode gain-phase relationship (a special form of the Kramers-Kronig relations for systems responding to a force) describes the relationship between the amplitude and phase of the frequency response of a system. One important consequence of this relationship is that for a system whose frequency response can be characterized by  $f^\alpha$ , the phase delay (or advance) is approximately  $90^\circ \times \alpha$ .

$$\text{Mag}(f) \propto f^\alpha \rightarrow \text{phase}(f) \propto 90^\circ \times \alpha. \quad (\text{E.4})$$

Thus, for each increase (or decrease) in the slope of the open loop gain, the phase is advanced (or delayed) by ninety degrees. This generalization provides the useful rule that for a servo loop to be stable, the open loop gain at the UGF must be declining with a slope of approximately  $-1$ . So, for  $f$  near  $f_0$ , when  $\|G(f_0)\| = 1$ ,

$$G(f) \propto f^{-1}. \quad (\text{E.5})$$

### E.2.2 Conditional Stability

The heuristic stability condition in E.2 is surprisingly general. For simple loops, with only one unity gain frequency (UGF), as long as the phase delay at the UGF is less than  $-180^\circ$ , the loop can be stable. The phase delay can go beyond this limit as long as it returns before the gain reaches unity. Such systems are said to be conditionally stable. This is in contrast to unconditionally stable systems, where the phase delay never goes beyond  $-180^\circ$ . Most loops in the length control systems

of a complex interferometer are conditionally stable, as this allows the aggressive filtering necessary for high gain at low frequencies, where the bulk of the noise occurs.

### E.3 Servo Bandwidth

Given the reality of LTI systems, it is not possible to have infinitely fast response times in a loop such as that shown in figure E.1, and there is thus a maximum useful frequency. The *bandwidth* of a servo loop is generally taken to mean the frequency at which the magnitude of the open loop gain,  $G$ , is unity. This frequency is then known as the unity gain frequency (UGF). Typically, the response of the system is decreasing at higher frequencies, and so the unity gain frequency is the highest frequency at which the servo system can be thought of as doing useful work.

### E.4 Feedback Filter Design

The feedback filter  $F$  is an important component, because it is the part of the loop that is most easily modified. The plant, sensor, and actuator are all to some degree determined by the problem (i.e., what needs to be controlled); the filter can then take whatever form is necessary to give the loop the proper shape. There are three common traits a filter should meet:

**Make the loop stable.** The first object of filter design is to make the loop stable. If the loop would not be stable with a unity gain feedback filter, then the filter should be tailored to make the loop stable.

**High open loop gain where the plant is noisy.** After ensuring stability, the feedback filter should be tailored so that the open loop gain of the system is high at frequencies where the plant is noisy. This is to increase the suppression factor of the loop where it is most needed.

**Low open loop gain where the plant is quiet.** It is also a good idea to have low open loop gain (much less than unity) where the plant is quiet. This is to prevent the loop from imposing sensor noise onto the plant.

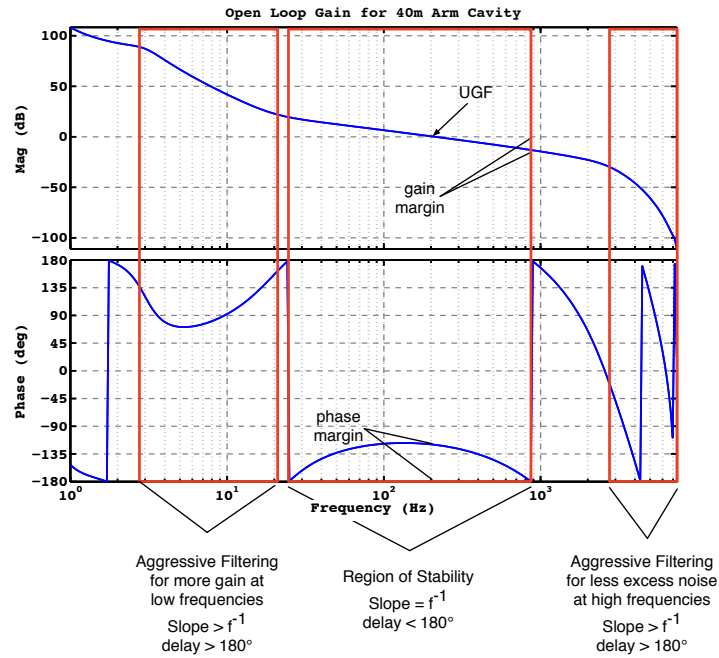
#### E.4.1 MIMO control

For a multiple-input multiple-output (MIMO) system, we replace the algebra of section E.1 with matrix algebra. Then for the example  $2 \times 2$  system in figure E.3, the closed loop gain of the system is

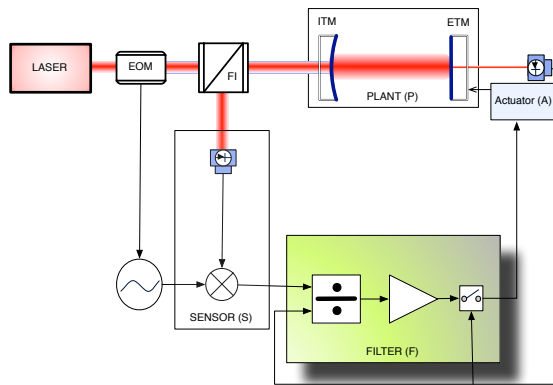
$$\mathbf{C} = \left[ \mathbf{I} + \mathbf{HP} \right]^{-1}. \quad (\text{E.6})$$

This implies that

$$\mathbf{b} = \mathbf{C} \mathbf{X} - \mathbf{a}. \quad (\text{E.7})$$

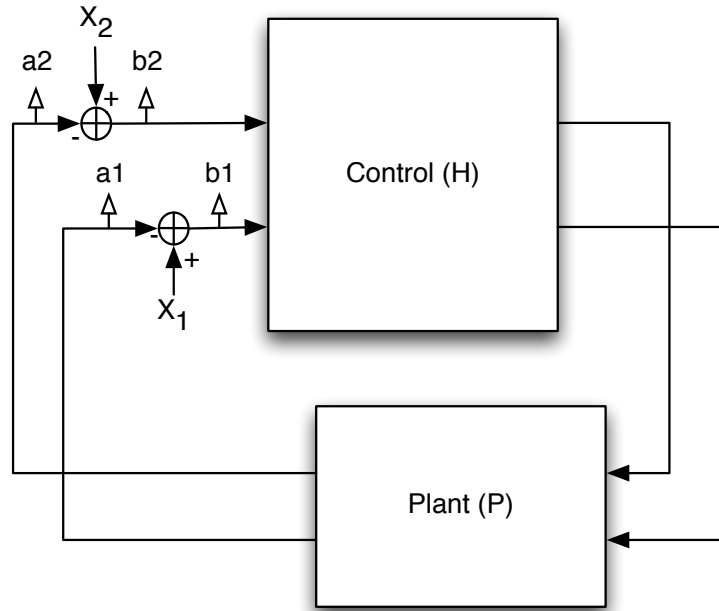


(a) Example Bode plot of the open loop gain for a 40 m arm cavity.



(b) The feedback loop used to control a Fabry-Pérot cavity near resonance.

Figure E.2: (a) This loop is conditionally stable, with a phase bubble extending from 30 Hz to 900 Hz, and the unity gain frequency at 200 Hz near the phase maximum. (b) This loop shows a Pound-Drever-Hall technique with power normalization and loop triggering. The shadowed elements are digital.

Figure E.3: A  $2 \times 2$  MIMO control system

It is easy to see that if the matrix product  $\mathbb{H}\mathbb{P}$  is diagonal, then  $\mathbb{C}$  will also be diagonal. In that case, noise injected at  $X_1$  will not appear at  $a_2$  (or  $b_2$ ). Generally, we will have non-diagonal plants, and so the ideal situation is to choose  $\mathbb{H}$  to be proportional to the inverse of  $\mathbb{P}$ , at every frequency.

#### E.4.1.1 Cross Coupling

For a  $2 \times 2$  system, it is not hard to write down the ‘open loop gain’ of loop 1 explicitly in the case where  $H$  is diagonal, but  $P$  is not. In that situation, we have

$$G_{11} = H_1 P_1 - \frac{H_1 H_2 P_{12} P_{21}}{1 + H_2 P_{22}}, \quad (\text{E.8})$$

where we see that the open loop gain of loop 1 can be heavily influenced by loop 2, and vice versa.

# Appendix F

## Interferometer Modeling

### F.1 Modeling Tools

A suite of modeling tools for the study of interferometric gravitational wave detectors has been developed by the gravitational wave detection community. While none of these tools can, by itself, provide a complete picture, the appropriate use of several of the tools which provide complementary information can be used to guide the design and operation of an interferometer. The list presented here is not intended to be complete, but rather to describe briefly some of the major tools available. A generic review of the methods (how to build the field matrix and invert it, signal creation, etc.) is in [129].

#### F.1.1 FINESSE

FINESSE [130, 131] is a frequency domain interferometer simulation tool based on the LISO circuit simulation engine. It can simulate an arbitrary collection of optics including the transverse profile of circulating beams using a Hermite-Gauss spectral decomposition, but it does not account for radiation pressure effects. All calculations are done in the frequency domain, and so transient effects cannot be studied.

#### F.1.2 GWINC

GWINC (formerly known as Bench) is a top-level optimization tool for interferometer design. It is designed to calculate the effect of displacement noises resulting from various sources which may not be opto-mechanical in origin, such as thermal and seismic noise, on the astrophysical sensitivity of an interferometric gravitational wave detector. Detailed information about interferometer operation is not included in this model, but it is an excellent tool for estimated the impact on astrophysical sensitivity of a given noise source. For the most part, it is a noise calculator, and uses analytical formulae for noise couplings when such formulae exist.

### F.1.3 Optickle

Optickle [58] is a frequency domain interferometer simulation tool, written in Matlab. Like Finesse, it can simulate an arbitrary interferometer configuration, but it can also simulate radiation pressure effects. Simulation of transverse profile is limited to the first set of transverse modes (TEM01 and TEM10), which allow a simulation of the effects of radiation pressure on the angular orientation of the optics (to study, i.e., the effects of Sidles-Sigg instabilities [132]). The angular instabilities were not considered in this thesis.

There are actually two programs called Optickle, which are essentially different branches. The first one was described above, and was written by Matt Evans; all the simulation results presented in this thesis are from this program (or the looptickle extension, next section). The second program called Optickle, written by me, is a MATLAB implementation of the two-photon simulation framework described in [128]. It should in principle thus correctly calculate the quantum noise in an interferometer. Development was abandoned because it is much slower and more memory intensive. Matt's Optickle is much faster and has a nicer interface, and now the looptickle extension has made it a truly powerful tool.

### F.1.4 Looptickle

Looptickle is a set of extensions, written in Matlab by Stefan Ballmer, which allow a closed loop analysis by adding feedback to an Optickle model. Optickle calculates the frequency dependent sensing matrix  $\mathbb{M}$ , and looptickle can then be used to construct a frequency dependent feedback matrix  $\mathbb{H}$ . Then the closed loop gain of the system (the response to disturbances) is given simply by inverting the matrix,

$$\mathbb{I} + \mathbb{H}\mathbb{M}, \tag{F.1}$$

which is the same thing as equation (E.2), but now with matrices (MIMO) rather than simple transfer functions (SISO). This allows us to simulate the effect of cross-talk in the control loops.

### F.1.5 E2E: End to End

E2E is a time domain simulation which is designed to mimic many aspects of an interferometer. Building, using, and correctly interpreting the model is nearly as difficult as building an actual interferometer, but it is probably cheaper.

### F.1.6 FFT

FFT [133] is a full-field relaxation code which simulates the modal structure (i.e., the transverse profile) of the beam in a cavity. It is not the Fast-Fourier-Transform.

## F.2 MATLAB code

### F.2.1 The RSE response function

```

function E = RSEtf(f,rs,ts,Titm,m,Larm,phi,zeta,Ibs)
% E = RSEtf(Tsr,Titm,m,Larm,phi,zeta,Ibs)

c=299792458;
lambda = 1.064e-6;
omega_0 = 2*pi*c/lambda;
hbar = 1.0546e-034;
omega_c = c/2/Larm * (1 - sqrt(1-Titm)) / ( sqrt(sqrt(1-Titm)) );
omega_a = 2*pi*f;
beta = -atan( omega_a./omega_c );
L = Larm;

i = sqrt(-1);

K = (8*Ibs/m/L^2) * omega_0./omega_a.^2 .* 1./(omega_c^2 + omega_a.^2);

numer = ts *exp(i*beta).*( (1-rs*exp(2*i*beta))*cos(zeta)*cos(phi) ...
- (1+rs*exp(2*i*beta))*sin(zeta)*sin(phi));

denom = 1 + rs^2*exp(4*i*beta) - ...
2*rs*exp(2*i*beta) .* (cos(2*phi) + K/2*sin(2*phi));

E = numer./denom .* sqrt(2*Ibs * omega_0^2 ./ (omega_c^2 + omega_a.^2));

```

# Bibliography

- [1] A. Abramovici, W. E. Althouse, R. W. P. Drever, Y. Gursel, S. Kawamura, F. J. Raab, D. Shoemaker, L. Sievers, R. E. Spero, K. S. Thorne, R. E. Vogt, R. Weiss, S. E. Whitcomb, and M. E. Zucker. LIGO: The Laser Interferometer Gravitational-Wave Observatory. *Science*, 256(5055):325–333, 1992.
- [2] H. Luck and the GEO600 Team. The GEO600 project. *Classical and Quantum Gravity*, 14(6):1471–1476, 1997.
- [3] VIRGO Collaboration. The VIRGO Project: A wide band antenna for gravitational wave detection. *Nuclear Instruments and Methods in Physics Research Section A: Accelerators, Spectrometers, Detectors and Associated Equipment*, 289(3):518–525, 1990.
- [4] K. Tsubono. 300m laser interferometer gravitational wave detector (TAMA300) in Japan. In *Gravitational Wave Experiments Proc. 1st Edoardo Amaldi Conf.*, pages 112–114, Singapore, 1995. World Scientific.
- [5] The Advanced LIGO project: <http://www.ligo.caltech.edu/advLIGO/>.
- [6] A. Einstein. Die grundlage der allgemeinen relativitätstheorie (the foundation of the general theory of relativity). *Annalen der Physik*, 1916.
- [7] F. W. Dyson, A. S. Eddington, and C. Davidson. A determination of the deflection of light by the sun’s gravitational field, from observations made at the total eclipse of May 29, 1919. *Philosophical Transactions of the Royal Society of London. Series A, Containing Papers of a Mathematical or Physical Character*, 220(571-581):291–333, 1920.
- [8] C. M. Will. The confrontation between general relativity and experiment. *Living Reviews in Relativity*, 9:3, 2005.
- [9] J. D. Jackson. *Classical Electrodynamics*. Number 0-471-30932-X. Wiley, 1998.
- [10] K Schwarzschild. Über das gravitationsfeld eines massenpunktes nach der einstein’schen theorie. *Sitzungsberichte der Königlich Preussischen Akademie der Wissenschaften*, 1:189–196, 1916.

- [11] R. P. Kerr. Gravitational field of a spinning mass as an example of algebraically special metrics. *Physical Review Letters*, 11(5):237–238, 1963.
- [12] F. Pretorius. Evolution of binary black-hole spacetimes. *Physical Review Letters*, 95(12):121101, 2005.
- [13] C. W. Misner, K. S. Thorne, and J. A. Wheeler. *Gravitation*. W. H. Freeman and Co., 1970.
- [14] K. S. Thorne. Gravitational waves. *arXiv*, (gr-qc/9506086), 1995.
- [15] K. S. Thorne. *Three Hundred Years of Gravitation*, pages 330–458. Cambridge University Press, 1987.
- [16] R. A. Hulse and J. H. Taylor. Discovery of a pulsar in a binary system. *Astrophysical Journal*, 195:L51–L53, 1975.
- [17] J. M. Weisberg and J. H. Taylor. Relativistic binary pulsar B1913+16: Thirty years of observations and analysis. *ASP Conference Series*, 328:25, 2005.
- [18] M. Maggiore. Stochastic backgrounds of gravitational waves. *arXiv*, (gr-qc/0008027), 2000.
- [19] A. J. Farmer and E. S. Phinney. The gravitational wave background from cosmological compact binaries. *Monthly Notices of the Royal Astronomical Society*, 346:1197–1214, 2003.
- [20] L. Bildsten. Gravitational radiation and rotation of accreting neutron stars. *Astrophysical Journal*, 501:L89, 1998.
- [21] D. I. Jones and N. Andersson. Gravitational waves from freely precessing neutron stars. *Monthly Notices of the Royal Astronomical Society*, 331(1):203–220, 2002.
- [22] LIGO Scientific Collaboration. Einstein@home search for periodic gravitational waves in early S5 LIGO data. *Physical Review D (Particles, Fields, Gravitation, and Cosmology) Rev. D*, 80(4):042003, 2009.
- [23] L. Blanchet. Gravitational radiation from post-newtonian sources and inspiralling compact binaries. *Living Reviews in Relativity*, 9(4), 2006.
- [24] LIGO Scientific Collaboration. Search for gravitational waves from low mass compact binary coalescence in 186 days of LIGO’s fifth science run. *Phys. Rev. D*, 80(4):047101, Aug 2009.
- [25] C. D. Ott, A. Burrows, E. Livne, and R. Walder. Gravitational waves from axisymmetric, rotating stellar core collapse. *The Astrophysical Journal*, 600(2):834–864, 2004.
- [26] LIGO Scientific Collaboration. Implications for the origin of GRB 070201 from LIGO observations. *The Astrophysical Journal*, 681(2):1419–1430, 2008.

- [27] C. Cutler and K. Thorne. In N. T. Bishop and D. M. Sunil, editors, *General Relativity and Gravitation*, page 72. World Scientific, 2002.
- [28] LIGO Scientific Collaboration. Search for gravitational-wave bursts in the first year of the fifth LIGO science run. *Physical Review D (Particles, Fields, Gravitation, and Cosmology)*, 80(10):102001, 2009.
- [29] LIGO Scientific Collaboration. Search for high frequency gravitational-wave bursts in the first calendar year of LIGO’s fifth science run. *Physical Review D (Particles, Fields, Gravitation, and Cosmology)*, 80(10):102002, 2009.
- [30] LIGO-VIRGO Collaboration. Rate predictions for compact binary coalescence events. Technical Report LIGO-P0900125, California Institute of Technology, 2010.
- [31] J. Weber. Detection and generation of gravitational waves. *Physical Review*, 117(1):306–313, 1960.
- [32] R. Weiss. Electromagnetically coupled broadband gravitational antenna. *Mass. Inst. Technol. Res. Lab. Electron. Q. Rep.*, 105:54–76, 1972.
- [33] R. Adhikari. *Sensitivity and Noise Analysis of 4km Gravitational Wave Antennae*. Ph.D. thesis, Massachusetts Institute of Technology, 2004.
- [34] Saulson P R. *Fundamentals of Interferometric Gravitational Wave Detectors*. World Scientific, Singapore, 1994.
- [35] R. Adhikari, P. Fritschel, and S. Waldman. Enhanced LIGO. Technical Report T060156, California Institute of Technology, 2006.
- [36] F. D. Ryan. Accuracy of estimating the multipole moments of a massive body from the gravitational waves of a binary inspiral. *Physical Review D (Particles, Fields, Gravitation, and Cosmology)*, 56(4):1845–1855, 1997.
- [37] S. A. Hughes. Gravitational waves from extreme mass ratio inspirals: challenges in mapping the spacetime of massive, compact objects. *Classical and Quantum Gravity*, 18(19):4067–4073, 2001.
- [38] R. Abbott, R. Adhikari, G. Allen, D. Baglino, C. Campbell, D. Coyne, E. Daw, D. DeBra, J. Faludi, P. Fritschel, A. Ganguli, J. Giaime, M. Hammond, C. Hardham, G. Harry, W. Hua, L. Jones, J. Kern, B. Lantz, K. Lilenkamp, K. Mailand, K. Mason, R. Mittleman, S. Nayfeh, D. Ottaway, J. Phinney, W. Rankin, N. Robertson, R. Scheffler, D. H. Shoemaker, S. Wen, M. Zucker, and L. Zuo. Seismic isolation enhancements for initial and Advanced LIGO. *Classical and Quantum Gravity*, 21(5):S915–S921, 2004.

- [39] G. M. Harry, H. Armandula, E. Black, D. R. M. Crooks, G. Cagnoli, J. Hough, P. Murray, S. Reid, S. Rowan, Peter Sneddon, Martin M. Fejer, Roger Route, and Steven D. Penn. Thermal noise from optical coatings in gravitational wave detectors. *Applied Optics*, 45(7):1569–1574, 2006.
- [40] H. B. Callen and T. A. Welton. Irreversibility and generalized noise. *Physical Review*, 83(1):34–40, 1951.
- [41] V. B. Braginsky, M. L. Gorodetsky, F. Y. Khalili, A. B. Matsko, K. S. Thorne, and S. P. Vyatchanin. Noise in gravitational-wave detectors and other classical-force measurements is not influenced by test-mass quantization. *Physical Review D (Particles, Fields, Gravitation, and Cosmology)*, 67(8):082001, 2003.
- [42] J. B. Camp, H. Yamamoto, S. E. Whitcomb, and D. E. McClelland. Analysis of light noise sources in a recycled Michelson interferometer with Fabry–Perot arms. *Journal of the Optical Society of America A*, 17(1):120–128, 2000.
- [43] M.W. Regehr. *Signal Extraction and Control for an Interferometric Gravitational Wave Detector*. Ph.D. thesis, California Institute of Technology, 1994.
- [44] C. M. Caves. Quantum-mechanical noise in an interferometer. *Physical Review D (Particles, Fields, Gravitation, and Cosmology)*, 23(8):1693–1708, 1981.
- [45] I.S. Gradshteyn and I. M. Ryzhik. *Table of Integrals, Series, and Products*. Academic Press, 6th edition, 2000.
- [46] L. Schnupp. Internal modulation schemes. Presented at the European Collaboration Meeting on Interferometric Detection of Gravitational Waves, Sorrento, Italy., 1988.
- [47] A. E. Siegman. *Lasers*. University Science Books, 1986.
- [48] H. Kogelnik and T. Li. Laser beams and resonators. *Applied Optics*, 5(10):1550–1567, 1966.
- [49] D. Sigg. Frequency Response of the LIGO interferometers. Technical Report T970084-00 D, LIGO, 1997.
- [50] M. Rakhmanov, J. D. Romano, and J. T. Whelan. High-frequency corrections to the detector response and their effect on searches for gravitational waves. *Classical and Quantum Gravity*, 25(18):184017, 2008.
- [51] R. W. P. Drever, J. L. Hall, F. V. Kowalski, J. Hough, G. M. Ford, A. J. Munley, and H. Ward. Laser phase and frequency stabilization using an optical resonator. *Applied Physics B: Lasers and Optics*, 31(2):97–105, 1983.

- [52] K. Somiya, Y. Chen, S. Kawamura, and N. Mio. Frequency noise and intensity noise of next-generation gravitational-wave detectors with RF/DC readout schemes. *Physical Review D (Particles, Fields, Gravitation, and Cosmology)*, 73(12):122005, 2006.
- [53] B. L. Schumaker and C. M. Caves. New formalism for two-photon quantum optics. II. Mathematical foundation and compact notation. *Physical Review A (Atomic, Molecular, and Optical Physics)*, 31(5):3093–3111, 1985.
- [54] C. M. Caves and B. L. Schumaker. New formalism for two-photon quantum optics. I. Quadrature phases and squeezed states. *Physical Review A (Atomic, Molecular, and Optical Physics)*, 31(5):3068–3092, 1985.
- [55] P. Willems. Thermal compensation in the LIGO gravitational-wave interferometers. In *Adaptive Optics: Methods, Analysis and Applications*. Optical Society of America, 2009.
- [56] B. J. Meers. Recycling in laser-interferometric gravitational-wave detectors. *Physical Review D (Particles, Fields, Gravitation, and Cosmology)*, 38(8):2317–2326, 1988.
- [57] J. Mizuno. *Comparison of optical configurations for laser-interferometric gravitational-wave detectors*. Ph.D. thesis, Universitat Hannover, 1995.
- [58] M. Evans. Optickle. Technical Report T070260, LIGO, 2007.
- [59] A. Buonanno and Y. Chen. Optical noise correlations and beating the standard quantum limit in advanced gravitational-wave detectors. *Classical and Quantum Gravity*, 18(15):L95–L101, 2001.
- [60] A. Buonanno and Y. Chen. Signal recycled laser-interferometer gravitational-wave detectors as optical springs. *Physical Review D (Particles, Fields, Gravitation, and Cosmology)*, 65(4):042001, 2002.
- [61] A. Buonanno and Y. Chen. Quantum noise in second generation, signal-recycled laser interferometric gravitational-wave detectors. *Physical Review D (Particles, Fields, Gravitation, and Cosmology)*, 64(4):042006, 2001.
- [62] V. B. Braginsky, M. L. Gorodetsky, and F. Ya. Khalili. Optical bars in gravitational wave antennas. *Physics Letters A*, 232(5):340 – 348, 1997.
- [63] O. Miyakawa, R. Ward, R. Adhikari, M. Evans, B. Abbott, R. Bork, D. Busby, J. Heefner, A. Ivanov, M. Smith, R. Taylor, S. Vass, A. Weinstein, M. Varvella, S. Kawamura, F. Kawazoe, S. Sakata, and C. Mow-Lowry. Measurement of optical response of a detuned resonant sideband extraction gravitational wave detector. *Physical Review D (Particles, Fields, Gravitation, and Cosmology)*, 74(2):022001, 2006.

- [64] K. Ogata. *Modern Control Engineering*. Number 978-0136156734. Prentice Hall, 2009.
- [65] J. Bechhoefer. Feedback for physicists: A tutorial essay on control. *Reviews in Modern Physics*, 77(3):783–836, 2005.
- [66] K. A. Strain, G. Muller, T. Delker, D. H. Reitze, D. B. Tanner, J. E. Mason, P. A. Willems, D. A. Shaddock, M. B. Gray, C. Mow-Lowry, and D. E. McClelland. Sensing and Control in Dual-Recycling Laser Interferometer Gravitational-Wave Detectors. *Applied Optics*, 42(7):1244–1256, 2003.
- [67] J. E. Mason and P. A. Willems. Signal extraction and optical design for an advanced gravitational-wave interferometer. *Applied Optics*, 42(7):1269–1282, 2003.
- [68] P. Fritschel, R. Bork, G. González, N. Mavalvala, D. Ouimette, H. Rong, D. Sigg, and M. Zucker. Readout and control of a power-recycled interferometric gravitational-wave antenna. *Applied Optics*, 40(28):4988–4998, 2001.
- [69] K. Kawabe, L. Matone, and J. Betzwieser. Excess noise mechanism in LIGO output mode cleaner. Technical Report LIGO-T040158-00-D, California Institute of Technology, 2004.
- [70] P. Fritschel. Output mode cleaner design. Technical Report LIGO-T040018-00-D, California Institute of Technology, 2004.
- [71] S. Ballmer. *LIGO interferometer operating at design sensitivity with application to gravitational wave radiometry*. Ph.D. thesis, Massachusetts Institute of Technology, 2006.
- [72] A. Buonanno, Y. Chen, and N. Mavalvala. Quantum noise in laser-interferometer gravitational-wave detectors with a heterodyne readout scheme. *Physical Review D (Particles, Fields, Gravitation, and Cosmology)*, 67(12):122005, 2003.
- [73] D. Ugolini, S. Vass, and A. Weinstein. Measurement of seismic motion at 40m and transfer function of seismic stacks. Technical Report LIGO-T000058, California Institute of Technology, 2000.
- [74] R. Bork, R. Abbott, D. Barker, and J. Heefner. An overview of the LIGO control and data acquisition system. In H. Shoae, editor, *Proceedings ICALEPCS 2001 (San Jose)*, pages 19–23, 2001.
- [75] EPICS, the Experimental Physics and Industrial Control System: <http://www.aps.anl.gov/epics/>.
- [76] B. W. Barr, O. Miyakawa, S. Kawamura, A. J. Weinstein, R. Ward, S. Vass, and K. A. Strain. Control sideband generation for dual-recycled laser interferometric gravitational wave detectors. *Classical and Quantum Gravity*, 23(18):5661–5666, 2006.

- [77] A. Araya, A. Telada, K. Tochikubo, S. Taniguchi, R. Takahashi, K. Kawabe, D. Tatsumi, T. Yamazaki, S. Kawamura, S. Miyoki, S. Moriwaki, M. Musha, S. Nagano, M. Fujimoto, K. Horikoshi, N. Mio, Y. Naito, A. Takamori, and K. Yamamoto. Absolute-length determination of a long-baseline fabry-perot cavity by means of resonating modulation sidebands. *Applied Optics*, 38(13):2848–2856, 1999.
- [78] O. Miyakawa, S. Kawamura, B. Abbott, R. Bork, P. Fritschel, L. Goggin, J. Heefner, A. Ivanov, F. Kawazoe, C. Mow-Lowry, A. Ourjountsev, S. Sakata, M. Smith, K. A. Strain, R. Taylor, D. Ugolini, S. Vass, R. Ward, and A. Weinstein. Sensing and control of the advanced LIGO optical configuration. volume 5500, pages 92–104. SPIE, 2004.
- [79] A. Weinstein. Advanced LIGO optical configuration and prototyping effort. *Classical and Quantum Gravity*, 19(7):1575–1584, 2002.
- [80] B. Abbott, G. Billingsley, L. Jones, R. Karwoski, J. Romie, M. Smith, D. Ugolini, S. Vass, and A. Weinstein. Conceptual design of the 40 meter laboratory upgrade for prototyping a advanced LIGO interferometer. Technical Report LIGO-T010115, California Institute of Technology, 2001.
- [81] G. Muller, T. Delker, D. B. Tanner, and D. Reitze. Dual-recycled cavity-enhanced Michelson interferometer for gravitational-wave detection. *Applied Optics*, 42(7):1257–1268, 2003.
- [82] D. A. Shaddock, M. B. Gray, C. Mow-Lowry, and D. E. McClelland. Power-recycled Michelson interferometer with resonant sideband extraction. *Applied Optics*, 42(7):1283–1295, 2003.
- [83] J. E. Mason. *Signal Extraction and Optical Design for an Advanced Gravitational Wave Interferometer*. Ph.D. thesis, California Institute of Technology, 2001.
- [84] M. Evans. *Lock Acquisition in Resonant Optical Interferometers*. Ph.D. thesis, California Institute of Technology, 2002.
- [85] S. Haykin. *Adaptive Filter Theory (4th Edition)*. Prentice Hall, 2001.
- [86] R. Adhikari, G. Gonzalez, M. Landry, and B. O’Reilly. Calibration of the LIGO detectors for the First LIGO Science Run. *Classical and Quantum Gravity*, 20(17):S903–S914, 2003.
- [87] A. Buonanno and Y. Chen. Scaling law in signal recycled laser-interferometer gravitational-wave detectors. *Physical Review D (Particles, Fields, Gravitation, and Cosmology)*, 67(6):062002, 2003.
- [88] L. Lindblom. Optimal calibration accuracy for gravitational-wave detectors. *Physical Review D (Particles, Fields, Gravitation, and Cosmology)*, 80(4):042005, 2009.

- [89] J. Camp, L. Sievers, R. Bork, and J. Heefner. Guided lock acquisition in a suspended Fabry-Perot cavity. *Optics Letters*, 20:2463–2465, December 1995.
- [90] M. Evans, N. Mavalvala, P. Fritschel, R. Bork, B. Bhawal, R. Gustafson, W. Kells, M. Landry, D. Sigg, R. Weiss, S. Whitcomb, and H. Yamamoto. Lock acquisition of a gravitational-wave interferometer. *Optics Letters*, 27(8):598–600, 2002.
- [91] VIRGO Collaboration. The variable finesse locking technique. *Classical and Quantum Gravity*, 23(8):S85–S89, 2006.
- [92] L. Barsotti. *The control of the Virgo interferometer for gravitational wave detection*. Ph.D. thesis, University of Pisa, 2006.
- [93] R. Abbott, R. Adhikari, S. Ballmer, L. Barsotti, M. Evans, P. Fritschel, V. Frolov, G. Mueller, B. Slagmolen, and S. Waldman. AdvLIGO interferometer sensing and control conceptual design. Technical Report LIGO-T070247-01-I, California Institute of Technology, 2007.
- [94] O. Miyakawa, R. Ward, R. Adhikari, B. Abbott, R. Bork, D. Busby, M. Evans, H. Grote, J. Heefner, A. Ivanov, S. Kawamura, F. Kawazoe, S. Sakata, M. Smith, R. Taylor, M. Varvella, S. Vass, and A. Weinstein. Lock acquisition scheme for the advanced LIGO optical configuration. *Journal of Physics: Conference Series*, 32:265–269, 2006.
- [95] L. Ma, P. Jungner, J. Ye, and J. L. Hall. Delivering the same optical frequency at two places: accurate cancellation of phase noise introduced by an optical fiber or other time-varying path. *Optics Letters*, 19(21):1777–1779, 1994.
- [96] R. L. Ward, R. Adhikari, B. Abbott, R. Abbott, D. Barron, R. Bork, T. Fricke, V. Frolov, J. Heefner, A. Ivanov, O. Miyakawa, K. McKenzie, B. Slagmolen, M. Smith, R. Taylor, S. Vass, S. Waldman, and A. Weinstein. dc readout experiment at the Caltech 40m prototype interferometer. *Classical and Quantum Gravity*, 25(11), 2008.
- [97] R. Adhikari, Y. Aso, S. Ballmer, R. Bork, J. Miller, S. Vass, R. Ward, A. Weinstein, A. Brooks, and D. Yeaton-Massey. Upgrade of the 40m interferometer. Technical Report LIGO-T080074, California Institute of Technology, 2008.
- [98] B. Allen. The stochastic gravity-wave background: Sources and detection. *arXiv*, (gr-qc/9604033), 1996.
- [99] B. Allen and J. D. Romano. Detecting a stochastic background of gravitational radiation: Signal processing strategies and sensitivities. *Physical Review*, D59:102001, 1999.
- [100] LIGO Scientific Collaboration. Analysis of first LIGO science data for stochastic gravitational waves. *Physical Review D (Particles, Fields, Gravitation, and Cosmology)*, D69:122004, 2004.

- [101] LIGO-VIRGO Collaboration. An upper limit on the stochastic gravitational-wave background of cosmological origin. *Nature*, 460(7258):990–994, 08 2009/08/20/print.
- [102] B. Allen and A. C. Ottewill. Detection of anisotropies in the gravitational-wave stochastic background. *Physical Review D (Particles, Fields, Gravitation, and Cosmology)*, D56:545–563, 1997.
- [103] E. Thrane, S. Ballmer, J. D. Romano, S. Mitra, D. Talukder, S. Bose, and V. Mandic. Probing the anisotropies of a stochastic gravitational-wave background using a network of ground-based laser interferometers. *Physical Review D (Particles, Fields, Gravitation, and Cosmology)*, 80(12):122002, 2009.
- [104] R. Weiss and A. Lazzarini. Proposal for a targeted search for stochastic gravitational waves. Technical Report LIGO-T040140-00-Z, California Institute of Technology, 2004.
- [105] S. W. Ballmer. A radiometer for stochastic gravitational waves. *Classical and Quantum Gravity*, 23(8):S179–S185, 2006.
- [106] LIGO Scientific Collaboration. Upper limit map of a background of gravitational waves. *Physical Review D (Particles, Fields, Gravitation, and Cosmology)*, 76(8):082003–11, 2007.
- [107] X. Siemens, V. Mandic, and J. Creighton. Gravitational wave stochastic background from cosmic (super)strings. *Physical Review Letters*, 98:111101, 2007.
- [108] L. R. Price and X. Siemens. Stochastic Backgrounds of Gravitational Waves from Cosmological Sources: Techniques and Applications to Preheating. *Physical Review D (Particles, Fields, Gravitation, and Cosmology)*, 78:063541, 2008.
- [109] LIGO Scientific Collaboration. Analysis of first LIGO science data for stochastic gravitational waves. *Physical Review D (Particles, Fields, Gravitation, and Cosmology)*, 69(12):122004, 2004.
- [110] A. Lazzarini. Bias from power spectrum measurement in parameter estimation for the stochastic gravitational wave background. Technical Report LIGO-T040128-02-E, California Institute of Technology, 2006.
- [111] A. Lazzarini and J. Romano. Use of overlapping windows in the stochastic background search. Technical Report T040089-00-Z, California Institute of Technology, 2004.
- [112] The Condor research project for high throughput computing: <http://www.cs.wisc.edu/condor/>.

- [113] LIGO Scientific Collaboration. A directional search for unmodeled persistent gravitational waves with LIGO. *in preparation*, 2010.
- [114] X. Siemens, B. Allen, J. Creighton, M. Hewitson, and M. Landry. Making  $h(t)$  for LIGO. *Classical and Quantum Gravity*, 21:S1723–S1736, 2004.
- [115] R.V Wagoner. Gravitational radiation from accreting neutron stars. *The Astrophysical Journal*, 1984.
- [116] S. S. Doeleman, J. Weintroub, A. E. E. Rogers, R. Plambeck, R. Freund, R. P. J. Tilanus, P. Friberg, L. M. Ziurys, J. M. Moran, B. Corey, K. H. Young, D. L. Smythe, M. Titus, D. P. Marrone, R. J. Cappallo, D. C. J. Bock, G. C. Bower, R. Chamberlin, G. R. Davis, T. P. Krichbaum, J. Lamb, H. Maness, A. E. Niell, A. Roy, P. Strittmatter, D. Werthimer, A. R. Whitney, and D. Woody. Event-horizon-scale structure in the supermassive black hole candidate at the galactic centre. *Nature*, 455(7209):78–80, 09 2008.
- [117] Rainer Schodel et al. The structure of the nuclear stellar cluster of the Milky Way. *arXiv*, (astro-ph/0703178), 2007.
- [118] M. Freitag. Gravitational waves from stars orbiting the sagittarius a\* black hole. *The Astrophysical Journal Letters*, 583(1):L21–L24, 2003.
- [119] C. O. Lousto. Infall of a particle into a black hole as a model for gravitational radiation from the galactic center. *Modern Physics Letters*, A12:1879–1882, 1997.
- [120] M. J. Benacquista. Relativistic binaries in globular clusters. *Living Reviews in Relativity*, 9(2), 2006.
- [121] K. M. Gorski, E. Hivon, A. J. Banday, B. D. Wandelt, F. K. Hansen, M. Reinecke, and M. Bartelmann. HEALPix: A framework for high-resolution discretization and fast analysis of data distributed on the sphere. *The Astrophysical Journal*, 622(2):759–771, 2005.
- [122] C. A. van Eysden and A. Melatos. Gravitational radiation from pulsar glitches. *Classical and Quantum Gravity*, 25(22):225020 (24pp), 2008.
- [123] A. Melatos, C. Peralta, and J. S. B. Wyithe. Avalanche dynamics of radio pulsar glitches. *The Astrophysical Journal*, 672(2):1103–1118, 2008.
- [124] A. Melatos and L. Warszawski. Superfluid vortex unpinning as a coherent noise process, and the scale invariance of pulsar glitches. *arXiv*, (09042998), 2009.
- [125] A. Melatos and C. Peralta. Gravitational Radiation from Hydrodynamic Turbulence in a Differentially Rotating Neutron Star. *arXiv*, (09111609), 2009.

- [126] C. Ott. Sources of long bursts of gravitational radiation. Presented at a Stochastic Group IM Pipeline Telecon, 2010/01/18.
- [127] H. J. Kimble, Y. Levin, a. B. Matsko, K. S. Thorne, and S. P. Vyatchanin. Conversion of conventional gravitational-wave interferometers into quantum nondemolition interferometers by modifying their input and/or output optics. *Physical Review D (Particles, Fields, Gravitation, and Cosmology)*, 65(2):022002, 2001.
- [128] T. Corbitt, Y. Chen, and N. Mavalvala. Mathematical framework for simulation of quantum fields in complex interferometers using the two-photon formalism. *Physical Review A (Atomic, Molecular, and Optical Physics)*, 72(1):013818, 2005.
- [129] A. Freise and K. Strain. Advanced Optics for Gravitational Wave Detection. *arXiv*, (gr-qc/09093661), 2009.
- [130] Finesse: An interferometer simulation: <http://www.gwoptics.org/finesse/>.
- [131] A. Freise. *The Next Generation of Interferometry: Multi-Frequency Optical Modelling, Control Concepts and Implementation*. Ph.D. thesis, Universitat Hannover, 2003.
- [132] J. A. Sidles and D. Sigg. Optical torques in suspended Fabry-Perot interferometers. *Physics Letters A*, 354(3):167 – 172, 2006.
- [133] J.-Y. Vinet, P. Hello, C.N. Man, and A. Brillet. A high accuracy method for the simulation of non-ideal optical cavities. *J.Phys. I (Parisa)*, 2(7):1287–1303, 1992.